Thermophysics 2014 - Conference Proceedings

19th International Meeting of Thermophysical Society

8th to 10th October 2014

Podkylava, Slovak Republic

Slovak Academy of Sciences in Bratislava

Book cover design: Vladimír Dvonka, Michal Veselý

Printed by: Brno University of Technology, Faculty of Chemistry, 2014

ISBN: ISBN 978-80-214-5034-9

HISTORY OF CONFERENCE

The first workshop was organized by ***prof. Stefan Barta*** on January 22, 1996 at the Department of Physics, Faculty of Electrical Engineering and Information Technology at the Slovak University of Technology in Bratislava. The Termophysic's meetings have been established as periodical meetings of scientists working in the field of investigation of thermophysical properties of materials and the problems of heat transfer and measurement of thermophysical and other transport properties of materials.

The Thermophysics as the working group of the Slovak Physical Society was established on the meeting at the Department of Thermophysics of the Slovak Academy of Sciences in Bratislava on June 13, 1997. The aim of the constitution of the working group is to exchange actual information in the field of heat transfer phenomena.

Dr. Ludovit Kubicar acted as the coordinator of the group and organized meetings at the Institute of Physics of the Slovak Academy of Sciences in Bratislava in the years - 1997, 1998 and 1999.

Then ***Dr. Libor Vozar*** from Faculty of Natural Sciences at the Constantine the Philosopher University in Nitra coordinated the activities of the society for the years 2000, 2001 and 2002. The workshops were organized in Nitra, in Račková dolina and Kočovce, respectively.

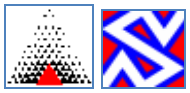

Next years, the Thermophysics workshop was held in Kočovce again. ***Dr. Peter Matiasovsky***, working for the Institute of Construction and Architecture at the Slovak Academy of Sciences in Bratislava, being the chairman of Thermophysical Society for the years 2003, 2004 and 2005 was taking the chair of the workshops.

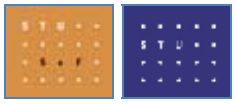

Since 2006 to 2008, the Thermophysics workshop took place in Kocovce, whereas ***Dr. Jozefa Lukovicova*** from research group at the Department of Physics of Faculty of Civil Engineering at the Slovak University of Technology in Bratislava was taking the chair of the workshops.

Since 2009 to 2011, the Thermophysics workshop was held in Valtice. ***Prof. Oldrich Zmeskal*** (working at the Institute of Physical and Applied Chemistry and Centre of Material Research at the Faculty of Chemistry of the Brno University of Technology in Brno) and ***prof. Robert Cerny*** (working at the Department of Materials Engineering and Chemistry at the Faculty of Civil Engineering of the Czech Technical University in Prague) were taking the chairs of the workshops.

Dr. Vlastimil Bohac, IP SAS, Bratislava, Slovak Republic in cooperation with co-organizers (***prof. Zmeskal*** and ***prof. Cerny***) has taken the chairmanship for the years 2012-2014. Since 2012, the Thermophysics workshop is held in Guesthouse Adam in the village of Podkylava. Guesthouse Adam is surrounded in picturesque hilly region covered with hamlets and caters to all groups' visitors and tourists. The guesthouse was built with the financial support of the European Union funds and has begun its operation in May 2006.

ACKNOWLEDGMENT

Publication of this book was financially supported by the Czech Ministry of Education, Youth and Sports, under project No LO1211.

The organizers would like to thank the Slovak Physical Society for their financial support of the conference arrangement and invited lectureres.

$$k = \frac{q}{\Delta T / L}$$

$$\alpha = \frac{k}{\rho C_p}$$

TA Instruments provides the widest range of tools for **thermal conductivity**, **thermal diffusivity**, and **specific heat capacity.** Highly accurate, versatile tools for polymers, ceramics, composites, insulation materials, metals, and much more.

- Laser Flash Analysis (ASTM E1461)
- Heat Flow Meter (ASTM C518)
- Guarded Heat Flow Meter (ASTM E1530)
- Guarded Hot Plate (ASTM C177)

TA

www.tainstruments.com

Committees

INTERNATONAL SCIENTIFIC COMMITTEE

Vlastimil Bohac, Institute of Physics SAC, Bratislava, SLOVAK REPUBLIC
Robert Cerny, Faculty of Civil Engineering CTU, Prague, CZECH REPUBLIC
Dariusz Gawin, Department of Building Physics & Building Materials, Technical University of Lodz, Lodz, POLAND
Hans-Peter Ebert, Bavarian Center for Applied Energy Research, Würzburg, GERMANY
John Grunewald, Faculty of Architecture, Dresden University of Technology, Dresden, GERMANY
Shuichi Hokoi, Department of Architecture and Architectural Engineering, Faculty of Engineering, Kyoto University, Kyoto, JAPAN
Ludovit Kubicar, Institute of Physics SAC, Bratislava, SLOVAK REPUBLIC
Xinying Lu, Department of Civil Engineering, Tsinghua University, Beijing, CHINA
Zbysek Pavlik, FCE CTU, Prague, CZECH REPUBLIC
Bimal Kumar Sarkar, Department of Physics, Galgotias University, Greater Noida, INDIA
Jay Sanjayan, Faculty of Engineering & Industrial Sciences, Swinburne University of Technology, Hawthorn, AUSTRALIA
Henryk Sobczuk, Faculty of Environmental Engineering, Lublin University of Technology, Lublin, POLAND
Oldrich Zmeskal, Faculty of Chemistry BUT, Brno, CZECH REPUBLIC

ORGANIZING COMMITTEE

Vlastimil Bohac, SAS, Bratislava, Slovak Republic
Oldrich Zmeskal, FCH BUT, Brno, Czech Republic
Zbysek Pavlik, FCE CTU, Prague, Czech Republic
Viliam Vretenar, SAS, Bratislava, Slovak Republic
Danica Fidrikova, SAS, Bratislava, Slovak Republic
Marian Markovic, SAS, Bratislava, Slovak Republic
Tomas Bzatek, FCH BUT, Brno, Czech Republic

Invited Speaker

Dr. Silas E. Gustafsson

POSITION
Retired leader of the research group, which used to work on thermal transport properties at the Department of Physics, Chalmers University of Technology, Gothenburg, Sweden. presiding chairman of the private company Hot Disk AB, which is recognised as an official research organisation by the Swedish Government.

PUBLICATIONS
some 80 scientific papers to his name

COLLABORATED WITH THE FOLLOWING RESEARCH ORGANIZATIONS
Departments and Foundations at Chalmers University of Technology (Sweden)
Aerospace Research Laboratories at Wright Patterson Air Force Base (USA)
Dowty Electronics Ltd. (United Kingdom)
Universtität des Saarlandes (Germany)
Universtität Ulm (Germany)
Stord/Haugesund College (Norway)
Quaid-i-Azam University (Pakistan)
University of Rajasthan (India)
The Royal Institute of Technology Stockholm (Sweden)
The Slovak Academy of Sciences (Slovakia)
The Hokkaido National Industrial Research Institute (Japan)
Oak Ridge National Laboratory (USA), and Hot Disk AB (Sweden)

PAPER PRESENTED
Possible Ways of Measuring the Thermal Transport Properties of Anisotropic Materials

CONTACT
www.hotdiskinstruments.com

Invited Speaker

Prof. Olivier Fudym

POSITION

full Professor in Heat Transfer, Ecole des Mines d'Albi, Toulouse-University.
head of the program "Inverse Methods and Energy Efficiency" at the Research Center RAPSODEE (Mines Albi & CNRS)
head of the Master program "Eco-Activities and Energy

EDUCATION

Ph.D. in Energetics from the University of Toulouse in 1994.
HDR, „Habilitation a Diriger les Recherches", from the University of Bordeaux in 2005

SCIENTIFIC AREA

worked on integrated renewable energy projects in Ecuador as a cooperation assistant in a research center, then in France as an engineer in an electricity company.
specialist of analytical and hybrid methods in heat transfer modelling and its implementation in the field of inverse problems for infrared images processing applied to thermal characterization methods: thermal diffusivity mapping, reactive flow in microfluidics, infrared tracking…
supervisor of 11 Ph.D. students

MEMBERSHIP

member of the scientific committee of the French Heat Transfer Society (SFT) since 2009
member of the Scientific Council of International Centre for Heat and Mass Transfer (ICHMT)
member of scientific and organization committees of several national and international conferences.
expert reports on different scientific projects for governmental organizations
reviewed manuscripts for 12 scientific journals

PUBLICATIONS

author of 34 articles in refereed journals
author of 63 refereed national and international conferences

OTHER ACTIVITIES

organized an advanced school on thermal measurements and inverse techniques
presented five invited Lectures and co-edited a book on inverse methods in heat transfer

RESEARCH FIELDS

Inverse methods in heat transfer
Thermal Characterization in heterogeneous media
Infrared thermography, thermal images processing
Analytical Methods in heat transfer, integral transforms and thermal quadrupoles
Optimization and stochastic modelling

PAPER PRESENTED

Bayesian inverse methods for the thermal characterization of heterogeneous materials

Invited Speaker

Prof. Jerzy Bodzenta

POSITION
Silesian University of Technology
Institute of Physics - Centre for Science and Education
Head of the Division of Applied Physics
Gliwice, Poland
Jerzy.Bodzenta@polsl.pl

EDUCATION/PROFESSIONAL QUALIFICATIONS

2008 Professorship in Technical Sciences
2001 D.Sc. (habilitation) in Electronics, the Institute of Fundamental Technological Research PAS, Warsaw, Poland
1990 Ph.D. in Electronics, the Institute of Fundamental Technological Research PAS, Warsaw, Poland
1985 M.Sc. in Electronics, Lviv Politechnic National University, Lviv, Ukraine

RESEARCH AREAS

Photothermal and photoacoustic measurements
Methods for thermal properties measurement of electronic materials and structures
Determination of thermal properties of thin films and complex materials
Scanning thermal microscopy
Spatially resolved thermal measurements
Analytical and numerical modelling of thermal measurements

PUBLICATIONS AND DISSEMINATION OF RESULTS

2 books
2 textbooks for students
123 published papers (60 from JCR database)
147 conference presentations (7 invited)
11 invited lectures in scientific institutions
2 patents

OTHER ACTIVITIES

Member of scientific committees of international conferences
Guest editor of the International Journal of Thermophysics
Chairman of the Workshop on Photoacoustics and Thermal Wave Methods
Head of 11 scientific and research projects

PAPER PRESENTED

Quantitative thermal measurements with nanofabricated thermal probes

Table of Contents

Possible Ways of Measuring the Thermal Transport Properties of Anisotropic Materials (Key lecture)

Silas E. Gustafsson

Thermetrol AB, Klyvsagagatan 29,Gothenburg, SWEDEN,SE-41679,
email: silas.gustafsson@thermetrol.se

Abstract: *Transient methods for measuring thermal transport properties have attracted an increased interest over the last couple of decades. There are a number of reasons for this interest, which will be highlighted and discussed. Because of this interest quite a large number of different methods have been developed and are routinely used at different laboratories and some of these methods are even available commercially. The focus of the lecture will be on the Transient Hot Strip and the Hot Disc methods and will end with a discussion on the recently developed Slab Pulse Transient Hot Strip or Micro Strip method, which is designed for studies of μm thin layers of anisotropic materials*

Keywords: *transient hot strip, transient hot disc, anisotropy, thin layers*

Quantitative thermal measurements with nanofabricated thermal probes (Key lecture)

Jerzy Bodzenta

Institute of Physics – Centre for Science and Education, Silesian University of Technology
Krzywoustego 2, 44-100 Gliwice, Poland, email: Jerzy.Bodzenta@polsl.pl

Abstract: *Scanning thermal microscopy (SThM), invented in 1986 by Williams and Wickramasinghe, is a scanning technique allowing imaging of either temperature distribution (in passive mode) or the thermal conductivity distribution (in active mode) at the sample surface. With increasingly common use of resistive nanofabricated thermal probes (NTP) the spatial resolution of imaging is better than 100 nm. A development of the SThM has led to work out methods for quantitative thermal measurements making use of SThM equipment. The main reason for which these methods did not become popular is a relatively low dynamic range of measured signal. In a case of dc measurement in air 2-3 orders of magnitude change of the thermal conductivity of the sample causes typically less than 10% change of measured signal. For this reason methods offering high sensitivity to signal changes are developing. They typically base on lock-in signal detection which assures effective noise suppression. The development of new measuring method can be divided into two stages. The first one is an analysis of limitations caused by a character of heat transport in a probe-sample system. Because of relatively complex geometry of the system it is often carried out by the use of numerical modelling. Another possibility is to use electrical analogies of the heat flow. It was shown that both mentioned methods can be useful in analysis of the probe-sample system and give results which are in good agreement with experimental data. The second stage of elaboration of the measuring method is working out of experimental procedure. To make use of advantages of dc and ac techniques a method in which the NTP is driven by a sum of dc and ac currents was proposed. In this case the probe voltage is a sum of dc component and three harmonics with diminishing amplitudes. In practise, determination of amplitude and phase of ω or 2ω components can be used for measurement of the thermal conductivity of the sample. Measurements carried out for reference samples and various thin films confirmed usefulness of proposed method. Detailed description of research carried out by our group can be found in Refs [1-4].*

Keywords: *quantitative thermal measurement, spatially resolved measurement, scanning thermal microscopy (SThM), nanofabricated thermal probes*

References

[1] J. BODZENTA, M. CHIRTOC, J. Juszczyk, Reduced thermal quadrupole heat transport modeling in harmonic and transient regime scanning thermal microscopy (SThM) using nanofabricated thermal probes, J. Appl. Phys. **116** (2014) 054501.

[2] J. BODZENTA, J. JUSZCZYK, M. CHIRTOC, Quantitative scanning thermal microscopy based on determination of thermal probe dynamic resistance, Rev. Sci. Instrum. **84** (2013) 093702.

[3] J. JUSZCZYK, M. KRZYWIECKI, R. KRUSZKA, J. BODZENTA, Application of scanning thermal microscopy for investigation of thermal boundaries in multilayered photonic structures, Ultramicroscopy **135** (2013) 95-98.

[4] A. KAŹMIERCZAK-BAŁATA, M. KRZYWIECKI, J. JUSZCZYK, P. FIREK, J. SZMIDT, J. BODZENTA, Application of scanning microscopy to study correlation between thermal properties and morphology of $BaTiO_3$ thin films, Thin Solid Films **545** (2013) 217-221.

Bayesian inverse methods for the thermal characterization of heterogeneous materials (Key lecture)

Olivier Fudym

Université de Toulouse; Mines Albi; CNRS; Centre RAPSODEE, Campus Jarlard, F-81013 Albi cedex 09, France, olivier.fudym@mines-albi.fr, France, e-mail: olivier.fudym@mines-albi.fr

Abstract: *The need for specific thermal characterization methods is often driven by the sample, according to both the structure and geometry. For instance, in the case of highly anisotropic composite materials, the samples may be quite thin, which prevents to make use of the widespread transient characterization methods designed to be used with some electro-resistive probe heating the sample with a semi-infinite thickness assumption. In that case, it is still possible to implement the same kind of methods with a convenient finite sample model. Unfortunately, the thermal parameters to be retrieved may result to be correlated and/or have a low sensitivity coefficient, which yields a quite poor expectation for their simultaneous estimation. Another family of measurement methods is based of infrared thermal images processing, where some local thermal parameters are to be retrieved, such as the local thermal diffusivity.*

In this lecture we propose some estimation methods for the thermal characterization of heterogeneous materials, such as the simultaneous estimation of both the in-plane and in-depth thermal conductivities of thin highly orthotropic composite materials, or for local thermal diffusivity mapping. These thermal parameters are estimated within a bayesian frame by a Monte Carlo Markov Chain (MCMC) method, implemented with a Metropolis Hastings algorithm. The Bayesian approach offers the possibility to obtain the posterior probability distribution for each estimated parameter through adding some prior information.

Different kind of samples are analysed in this lecture, from fiber layers to carbon nanotubes composites, which aim to present some different in-plane/transverse ratio, correlation and sensitivity levels.

Keywords: *thermal conductivity, orthotropic materials, Hot Disk, Metropolis Hastings, Bayesian methods*

Barrier-cluster-heating model and photoluminescence quenching in disordered semiconductors

Ivan Baník, Gabriela Pavlendová

Departmen of Physics, Faculty of Civil Engineering, Slovak University of Technology, Slovakia, 81368 Bratislava, Radlinského 11, e-mail: ivan.banik@stuba.sk

***Abstract**: It is known from experiment, that a strong electric field about 10^7 Vm^{-1} decreases a photoluminescence level in non-crystalline semiconductors. This fact is sometimes interpreted in such a way that the field by its stregth causes the decay („dissociation") of bound exciton pairs and thus prevents the photoluminescent radiant recombination. However, the center of the respective mechanism is - from our point of view - somewhere else. In submitted article this effect is clarified by barrier-cluster-heating model of a non-crystalline substance. It is based on assumption that the strong electric field increases production of free electrons during an optical absorption process. Free electrons are created optically by mechanism of multi-tunneling through potential barriers. These electrons afterwards stimulate (as catalyzers) non-radiation recombination of electron-hole pairs. In consequence the decrease occurs at the photoluminescence level. The presented approach enables to create a unified view of the suppression of fotoluminescence in disordered semiconductors due to several factors. In addition to the electric field the fotoluminescence is suppressed by the temperature rise (Street Law) and also the energy increase of photons in high energies (decreasing part of the PLE characteristics). In all mentioned cases, it is the analogous mechanism associated with the fact that the relevant factor increases the production of free electrons and their catalytic action disposes bound e-h pairs. Free electrons stimulate nonradiative transitions of eh pairs.However, our view does not exclude the above mentioned possibility that a strong field contributes also to the decay (disociation) of bound e-h couples. Barrier-cluster-heating model allows explanation of full range of optical phenomena in non-crystalline semiconductors.*

Keywords: photoluminescence, field effect, quenching, barrier-cluster-heating model, disordered semiconductor, a-Si:H

1. Introduction

The physical principle of optical phenomena in non-crystalline semiconductors has not been fully understood yet [1-6]. It appears that a barrier-cluster-heating model of a non-crystalline semiconductor is able to explain several significant phenomena in non-crystalline semiconductors [7-11]. Up to now, it was used in the explanantion of origin and features of exponential tails in optical absorption, in physics of electroabsorption and photoluminescence and in some other optical connections. The strong electric field decreases the level of photoluminescent radiation. This experimental fact is sometimes interpreted in such a way that strong electric field contributes to the decay of bound exciton pairs and thus prevents the photoluminescent radiant recombination. In our opinion the suppression of photoluminiscence is caused by different mechanism. The most important determinant of electric field influence is - as we suppose - the fact that strong electric field increases the probability of the *s*-fold tunnelling of electrons through potential barriers during absorption,

which results in the increase of production of free electrons and thus, suppression of photoluminescence

2. Barrier-cluster-heating and optical phenomena in disordered semiconductors

The barrier-cluster model comes out from the assumption that potential barriers exist in a non-crystalline semiconductor, which separate certain nanoregions – nanoclusters and in this way, they hinder the transport of the carriers at the margin of the conduction or valence bands [7-11]. The barriers also influence significantly the optical absorption at the optical absorption edge. It is caused firstly by their inducing a strong electron-phonon interaction, which results in the fact that on optical transition, apart from the energy of a photon, an electron can also take the energy of a phonon and thus, on such a transition, the total of energy taken by an electron equals the sum of the photon and phonon energies. Another important factor - as far as influence of barriers is concerned - is that the absorption of light in the region of the optical absorption edge at low temperatures is usually connected with tunneling of carriers through the potential barrier. Due to this, the absorption process is influenced by barriers.

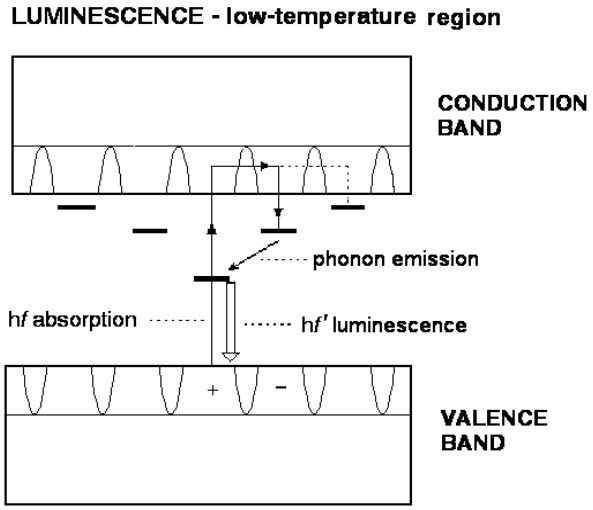

Fig. 1 Mechanism of photoluminescence from the point of view of the BCH model

Physical nature of photoluminescence

A possible concept of physical nature of photoluminescence in chalcogenide glasses at low temperatures from point of view of the barrier-cluster-heating model is depicted in Fig. 1. An electron in the course of optical transition, connected with tunneling, gets to an adjacent or a nearly region on an energy level, which is below the peak level of potential barriers. At lower temperatures, the excited electron after an optical transition, will pass on the lowest energy levels of a given localization region. It will be free only within its own localization region. Its wave function would be localized practically in its own micro-region between the neighboring barriers. Due to Coulomb interaction and the poorly penetrable potential barrier between them, a bound state of such an *e-h* couple arises. As a consequence, a new energy level is formed in the forbidden band. Let us assign this level formally to that localization region where the electron rests. This level will be below the bottom of the conduction band. Levels of this kind will arise not only in the neighboring nanoregion (cluster), but also

in the more distant regions. The height of these levels will depend on the distance from the "motherly" nanoregion (for the sake of simplification, we suppose that the hole did not move). With increasing distance, these levels will approach the bottom of the conduction band. In Fig. 1 several these levels are depicted on both sides of the hole (in one-dimensional model). These levels create a kind of "funnel" of levels. A new energy level will appear not only in adjacent nanoregions but also in the original mother nanoregion in which the hole rests. The electron level in the mother region is the lowest one from among all levels of the funnel. However, discrete levels of excited states in a given region also belong to each level of the funnel, as the lowest energy level of the given localization region. (These levels are not shown in the diagram). At low temperatures, an optically excited electron will, with high probability, gradually get back to the mother region of the hole. Such an approach is connected to gradual tunneling and diffusion. At that, the approaching jumps "region-by-region", are connected to an interaction with phonons. Without phonons, such process would not be possible. These approaching processes are in principle not radiant. An electron loses gradually a considerable part of its energy in them. In the last phase of approach, a non-radiant transition occurs to its own localization region. In this region, radiant optical recombination of the *e-h* pair occurs, connected with emission of a luminescence photon, whose energy is considerably lower than that of photons of the exciting radiation. A distinct Stokesian shift will occur. If there were no other disturbing processes, a stationary state with a relatively high level of luminescence would establish quickly. In fact, this corresponds rather well to a real situation in the first phase of irradiation. However, the state of a high luminescence begins to impair and weaken rather quickly.

Free electrons as stimulators of non-radiant recombinations

When irradiating a non-crystalline semiconductor by a flux of photons at low temperatures under conditions described above, free electrons are practically formed in materials substantially only by a multi-tunneling of a little part of electrons, which performed the optical transition. The slow rise of concentration of free electron is caused by the relatively low probability of multi-tunneling process. The concentration of free electrons in semiconductor stabilizes only after a long time, when dynamical equilibrium of two mutually opposing effects establishes, i.e. the process of arising of free electrons and the process of their annihilation by joining holes through which, new bound *e-h* pairs are created. When explaining the laws of photoluminescence on the basis of the barrier-cluster-heating model, an extremely significant assumption is important in our considerations, namely that free electrons, by their effect, stimulate the non-radiant recombination of bound *e-h* pairs (as a kind of a catalyst), and thus, they reduce the number of radiant transitions. So, ultimately, free electrons markedly influence the luminescence process. The free electron remains free after such individual catalyst process and continues triggering non-optical transitions, acting as a catalyst.

Mechanism of free electrons origin

The source of free electrons in a non-crystalline matter during photo-irradiation at low temperatures is a manifold tunneling of a small electron fraction at the process of the optical absorption connected with tunneling (Fig. 1). For this mechanism is essential that majority of electrons execute at the optical transition a tunneling through one potential barrier. Some electrons drive a tunnel *s*-time across s-barriers consecutively at the optical transition. In this manner electrons overrun a long distance from their original region and become free.

Electron will be no longer bounded with a hole by the Coulomb force. In our model it is assumed that free electrons then activate non-radiate transitions of bounded pairs *e-h*. These will not contribute to the luminescence. According to [7,8] the probability *p* of a single-event tunneling of such a particle will be proportional to the expression

$$p \sim \exp(-A\Delta W) \tag{1}$$

where A is the barrier's parameter and ΔW – the energy deepness of the level at which the tunneling takes place measured from the peak of barriers. For probability p^s multi-tunneling of electron through *s* barrier, we can write

$$P^s \sim \exp(-As.\Delta W) \tag{2}$$

The probability of creation of a free electron will be proportional to the expression (2).

Remark: In [8-10] the fatigue effect, generalized Street's law and PLE-charakteristic was derived outgoing from the assumption described hereinbefore.

3. Influence of a strong electric field on photoluminescence

Strong electric field – as it is known from experimental observations – depresses the level of photoluminescence in non-crystalline semiconductors. From the barrier-cluster-heating model viewpoint this effect is connected with the influence of the field which increases number of free electrons. Those electrons during process of optical absorption become free due to the multiple tunneling across barriers. Increased number of free electrons (stimulating non-radiate recombination) implicates a lowering of radiate recombination number and simultaneously a level lowering of the luminescence.

Influence of an electric field on a process of multiple tunneling of electrons

Effect of the field on a process of multiple tunneling in the strong electric field affecting the energy of an electron also during tunneling through the potential barriers. This state is depicted In Fig. 2. The energy of a moving electron in the direction of acting electric force increases, consequently tunneling of the electron is in progress gradually still on higher energy level. This way probability of a tunnel transition through the next barrier gradually increases.

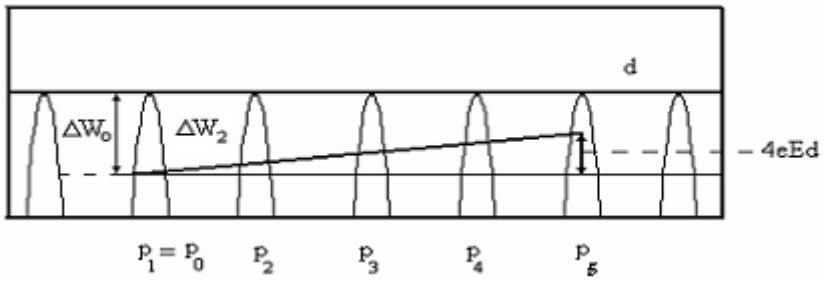

Fig. 2 Multiple tunneling of an electron in the direction of acting electric force

At the motion of the electron in opposite direction (against the acting electric force) the state will be opposite. The electron energy will decrease; consequently the decrease of probability of each next tunneling will appear. Let us analyze the situation shown in Fig. 2. The

probability p_0 of a tunnel transition through the first one of the potential barriers can be expressed by [7, 8]

$$p_o \approx \exp(-A\Delta W_o) \tag{3}$$

where A represents a parameter of the barrier and $\Delta W_o = \Delta W_1$ - the energy depth (measured from the level of barrier's peak) at which the tunneling takes place. The next tunnel transitions through barriers in a given field will be under way in successive steps on levels $\Delta W_o - eEd$ (=ΔW_2), $\Delta W_o - 2eEd$, $\Delta W_o - 3eEd$,…. $\Delta W_o - seEd$. Here s are actual number of barriers. It holds for corresponding probabilities of tunnel transition

$$p_1 = p_o \sim \exp(-A\Delta W_o) \tag{4}$$

$$p_2 \sim \exp(-A(\Delta W_o - eEd)) = p_o \exp(AeEd) \tag{5}$$

$$p_3 \sim \exp(-A(\Delta W_o - 2eEd)) = p_o \exp(2AeEd) \tag{6}$$

$$p_s \sim \exp(-A(\Delta W_o - (s-1)eEd)) = p_o \exp((s-1)AeEd) \tag{7}$$

Probability of multiple tunneling

Probability of the multiple tunnel transition P_s through all s barriers will be

$$P_s = p_1 p_2 p_3 \ldots p_s \tag{8}$$

or, in accordance with relations (4-7)

$$P_s \sim p_o^{\,s} \exp(0{,}5.AeEd(s-1)s) \tag{9}$$

Then probability of the multiple tunneling can be written as

$$P_s \sim B_1 \exp(B_2 E) \tag{10}$$

where, taking into account relations (3, 9)

$$B_1 = p_o^{\,s} = B_1 = \exp(-As\Delta W_o) \tag{11}$$

$$B_2 = \frac{As(s-1)ed}{2} \tag{12}$$

Analogical relations could be obtained for electron tunneling in opposite direction to acting electric force. Such relations differ in sign of electric field intensity. Instead of the relation (10) following one would be obtained

$$P_s' \sim B_1 \exp(-B_2 E) \tag{13}$$

Remark: In three dimensional case (3D) the state is more complex. Here we consider 1D case.

Effect of **a field on free electron concentration**

An electron at an optical transition connected with multi tunneling can pass a long distance from a hole in two ways (in 1D case) – at the tunneling: in the direction of an acting electric force or in the opposite direction. In the first case the field evokes an increase of probability of that tunneling, in the second one the probability decreases (in comparison to situation

when field is not present). Further, we show that both changes do not compensate each other. From analysis it follows that a strong electric field increases the probability of multi-tunneling as a result. For mean probability of multi-tunneling trough the s - barriers provided the strong electric field is present can be taken the arithmetical average of probabilities (10) and (13)

$$\frac{P_s(+) + P_s(-)}{2} = \frac{B_1 \exp(B_2 E) + B_1 \exp(-B_2 E)}{2} \tag{14}$$

where $P(+) = P_s$ denotes the probability of multi-tunneling in the direction of an acting electric force and $P(-) = P'_s$ denotes the probability of multi-tunneling in the opposite direction. If electric field is not present ($E = 0$) from relation (14) one obtains

$$\frac{P_s(0) + P_s(0)}{2} = P_s(0) = B_1 \tag{15}$$

This relation determines the mean value of multi-tunneling probability in the absence of the field.

Let us suppose that the condition for the creation of free electron by optical absorption is tunneling of an electron 1 through some specific number of "s" barriers. The number of optically produced number of free electrons per unit time (the generation factor) in the absence of the field we denote by the symbol G (0), in the presence of the field $G(E)$. For $G(0)$ according to [7-10] equation (16) is valid, so that, taking (14) into account we can write

$$G(0) = \left(\frac{dn}{dt}\right)_{E=0} = C \exp\left[-A(hf + CT)\right] \tag{16}$$

$$G(E) = \left(\frac{dn}{dt}\right)_{E\neq 0} = G(0).\frac{1}{2}\left[\exp(B_2 E) + \exp(-B_2 E)\right] \tag{17}$$

Assuming that for recombination is valid

$$R = \left(\frac{dn}{dt}\right)_{rec} = C.n^2 \tag{18}$$

For the equilibrium concentration of free electrons in the presence, respectively. absence of the field can be written

$$G(E) = R, \qquad G(0) = R \tag{19}$$

From above written equations the concentrations $n(0)$, $n(E)$) of free electrons for both.cases can be calculated .We get:

$$n(0) = \sqrt{C}\ \left[\exp\left[-0{,}5.A(hf + CT)\right]\right] \tag{20}$$

$$n(E) = n(0)\left[\frac{1}{2}\left[\exp(B_2 E) + \exp(-B_2 E)\right]\right]^{\frac{1}{2}} \tag{21}$$

Effect of a field on photoluminescence

Intensity I of photoluminescence in steady state is dependent on the free electron

concentration *n*. According to [8, 10] it holds

$$I \sim \frac{C_x}{C_y + C_z n} \tag{22}$$

where C_y a C_z are constants. If $C_y << C_z n$ (at steady state) then (23)

$$I \sim \frac{C_x}{C_z n} \sim \frac{1}{n} \tag{24}$$

Under that condition for photoluminescence intensity can according to (20, 21) be writen

$$\frac{I}{I_o} = \frac{n(0)}{n(E)} \tag{25}$$

where $I = I(E)$ is the photoluminescence intensity at the presence of the field and $I_o = I(0)$ without of the field. One obtains from (20, 21, 25)

$$I = I_o \frac{2}{\left[\exp(B_2 E) + \exp(-B_2 E)\right]^{\frac{1}{2}}} \tag{26}$$

This relation determines the dependence of PL intensity on the electric field in 1D-case.

Three-dimensional case

In reality, a tunneling process in a non-crystalline semiconductor is 3D. The upper obtained result holds for 1D-case. Then, there is a need for correction in 3D case. A detail analysis showed, that the quantity B_2 has to be changed in a 3D-case by the quantity twice less. It is due to the fact that after passing a distance *d* in a random direction (from point O(0,0,0) to the point $B(x \geq 0, y, z)$) *x*-coordinate of an electron (assuming *x* is parallel to the field) changes at average only about *d*/2. Then *d* should be replaced simply by *d*/2. This implies that the average change in potential energy of an electron in the field *E* will be *eEd*/2. In 3D case

$$I = I_o \frac{2}{\left[\exp(B_2 E) + \exp(-B_2 E)\right]^{\frac{1}{2}}} \tag{27}$$

where

$$B_2 = \frac{As(s-1)ed}{4} \tag{28}$$

Weak electric fields

In the case of weak electric fields the exponential functions in (27) can expand into (well convergent) Taylor series. If we cut the series after quadratic terms in *E*, we obtain

$$I = I_o \frac{1}{\sqrt{1 + 0{,}5\, B_2^{\,2} E^2}} \quad \text{or approximately} \quad I = I_o\left(1 - 0{,}25\, B_2^{\,2} E^2\right) \tag{29a,b}$$

where the relation (28) holds for B_2. Under these conditions the intensity of photoluminescence decreases quadratic with electric field intensity *E*. But the relation (27) is more general.

Strong electric fields

In the case of strong electric fields exp(B_2E) >> exp(-B_2E). Relation (27) takes the form

$$I = I_o \frac{1}{\sqrt{\exp(B_2 E)}} \ , \ I = I_o \exp(-0{,}5.B_2 E) \tag{30}$$

In this area of the fields photoluminiscence declines exponentially with the field strength E.

4 Discussion - a brief confrontation with the experiment

Quadratic decrease in the PL level (equation (29b)) in the case of chalcogenide glasses was already published [5, 6]. This type of dependence in the low fields occurs also in the case of a-Si: H. In the strong fields (up to 3.10^7.Vm-1) was in hydrogenated amorphous silicon [12] recorded an exponential decline, which can be expressed by an empirical relationship

$$I = I_o \exp(-\gamma E) \tag{31}$$

with the value of the constant γ = 3,1.10-6 V-1.cm ($3{,}1.10^{-8}$ V^{-1}.cm). More detailed confrontation of the presented model with experiments will be published in [16]. It will also be shown there, that the value of the constant γ in equation (31) corresponds quite well with the value provided by our model. Numerical evaluations based on the relations (24, 25) offered a relative good agreement with experimental data published e.g. in [12]. Another dependencies , regarding the effect of the field on photoluminescence, which are in reasonably good agreement with the experiment based on BCH model will be given in [13] .

5. Conclusion

Submitted material shows that the barrier-cluster-heating model is able in an acceptable way to explain the essence of electric field action on photoluminescence level in non-crystalline semiconductors. Described mechanism of photoluminescence and heating of the nanoregions at nonradiative recombination allows also explaining of the weak absorption tail formation and also why photoinduced changes (photo-expansion) correlated with photoconductivity and anti-correlated with photoluminescence.

Acknowledgement

The research has been supported by grant VEGA 1/0184/14, Slovakia

References

[1] TANAKA, K. - SHIMAKAWA, K. *Amorphous Chalcogenide Semiconductors and Related Materials,* (Springer, 2011), p. 200-300, (2011).

[2] MALINOVSKY, V.K. – SUROVTSEV, N.V. Chalcogenide Letters, Vol.9, No.2, p.79-84, (2012).

[3] POPESCU, M. Disordered chalcogenide optoelectronic materials: phenomena and applications, *Journ. Optoelectr. Adv. Mater.* Vol. 7, No. 4, p.2189–2210, (2005).

[4] MOTT, N.F. – DAVIS, E.A. *Electron processes in non-crystalline materials,* Clarendon Press, Oxford (1979).

[5] BRODSKY, M.H. *Amorphous semiconductors,*Springer Verlag Berlin, Heidelberg, New York (1979). (Amorfnyje poluprovodniky, Mir, Moskva, 1982).

[6] SHIMAKAWA, K. – KOLOBOV, A.V. – ELLIOTT, R. Adv. Phys. 44, 475 (1995).

[7] BANIK, I. Journ. of Non-Crystalline Solids 353, p.1920-11924, (2007).

[8] BANIK, I. Journ. of Optoelectr. and Adv.Materials, Vol. 11, No. 12, p.1915-1930, (2009).

[9] BANIK, I. Journ. of Optoelectr. and Adv.. Materials, Vol. 14, No. 9- 10, p.711 – 716, (2012).

[10] BANIK, I. – POPESCU, M. Journ. of Optoelectr. and Adv. Materials, Vol. 15, No. 11-12, p.1179-1189, (2013).

[11] BANIK, I. Proc. Thermophysics, Podkylava 2013, ed. O. Zmeškal, p. 32-39, (2013).

[12] MUSCHIK, T. – SCHWARS, R. , 0160-8371/88/000-0191 IEEE Adv. Tech. p.191-195, (1988).

[13] BANIK, I. will be published.

Thermal properties of cement based composites with incorporated crushed waste polypropylene

Zbyšek Pavlík, Martina Záleská, Milena Pavlíková, Lukáš Fiala, Robert Černý

Department of Materials Engineering and Chemistry, Faculty of Civil Engineering, CTU Prague, Thákurova 7, 166 29 Praha 6 – Dejvice email: pavlikz@fsv.cvut.cz

Abstract: *For the improvement of energy efficiency of buildings, there is necessary to focus on advanced technical solution of building design resulting in building envelopes with high thermal resistance and sufficient thermal stability. Specific attention must be paid not only to the design of building envelopes, but also to the thermal insulation of buildings subsoil. Here, new materials improving the thermal insulation properties of concrete can find use.*

Cement-based composites are characterized by their good mechanical properties but they often lack a thermal insulation capability. On this account, the possibility of recycling crushed waste polypropylene (CWPP) coming from PP tubes production as lightweight aggregate instead of sand in the manufacturing of the cement-based composites with improved thermal insulation properties is researched in the paper. This material should find application as light-weight concrete for spread layer of floor structure, whereas the developed material will be used as dry mixture of binder, plastic and sand, and will be produced on building site. The application of (CWPP) results in an improvement of thermal insulation properties of the developed composite. The obtained results present good fundamentals for further studies aimed at an advanced design of composite materials with enhanced thermal insulation function.

Keywords: *crushed waste polypropylene, cement-based composite, lightweight aggregate, thermal properties*

1. Introduction

In the last decades, due to the increasing cost of raw materials and the continuous reduction of natural resources, the recycling of industrial waste or by-products has become an interesting option for the building industry. Fly ash, demolition waste, bottom ash from municipal solid waste incineration, silica fume, ground granulated blast furnace slag can be considered common materials in the construction industry now. Concrete is beyond question the most important building material. Its worldwide annual production is presently more than 10 billion tons [1], and one can expect rapid increase of its manufacturing in the near future especially in the developing countries whose economies rapidly grow. Instead of the concrete excellent mechanical and durability properties that are the main reasons for its usage, its production brings several harmful secondary effects to the human society and environment. Except high amount of CO_2 emission released within the clinker productions, there is the vast amount of natural resources needed to produce such high amount of building material each year. On this account, taking into account the sustainability principles, there is necessary to take advantage of secondary-raw materials coming from industry for concrete production. Application of any industrial waste or/and by-product for concrete manufacturing represents a tremendous saving of energy and has important environmental benefits.

A substantial growth in the consumption of plastic is observed all over the world in recent years, which has led to huge quantities of plastic-related waste [2]. Annual consumption of plastics in Western Europe is about 60 million tons, which results in about 23 million tons of plastics waste. The EU Packing and Packaging Waste Directive (2004/12/CE) had the objective to reclaim or incinerate (using energy recovery) at least 60 wt% of packaging waste and to recycle between 55 wt% and 85 wt% of it [3]. The use of this type of waste in the construction field may represent an effective solution both to the problem of reducing the environmental impact of plastics and to the development of an increasingly sustainable building industry. On this account, recycling of plastic waste to produce new materials like concrete or mortar appears as one of the best solution for disposing of plastic waste, due to its economic and ecological advantages. A review on the use of plastic waste in preparation of cement mortar and concrete preparation is already available [4]. However, several important properties such as pore size distribution, thermophysical properties, durability performance of cement mortar and concrete containing plastic as aggregate were not discussed before due to lack of available information. Data were provided only for some of properties, where plastic was used as fibrous content in concrete and therefore the amount incorporated was very low in comparison to its use as aggregate or filler [3]. On this account, the possibility of recycling crushed waste PP coming from PP tubes production as lightweight aggregate instead of sand in the manufacturing of the cement-based composites with improved thermal insulation properties is researched in the paper. This material should find application as light-weight concrete for spread layer of floor structure, whereas the developed material will be used as dry mixture of binder, plastic and sand, and will be produced on building site. The main aim of the presented research is to optimize the plastic waste addition in terms of physical, mechanical and thermal performance of the resulting cement-based composite.

2. Experimental

2.1 Studied materials

Within the experimental testing, basic physical and thermal properties of crushed waste PP coming from PP tubes production were accessed at first. The PP waste was then used as partial natural aggregate replacement in cement-based composite mix design. The sized silica sand was mixed from three types of sand in ratio 1:1:1 and was delivered by Heidelberg Cement Group, Brněnské písky Ltd., affiliated company Bratčice, Czech Republic. The grain size curve of the applied sand is given in Figure 1. The natural aggregate was substituted with the plastic waste at weight dosages of 10, 20, 30, 40, and 50%, whereas the reference mixture without plastic addition was studied as well. The composites were prepared with Portland cement CEM I 42.5 R. Composition of tested composites is given in Table 1.

Table 1: Composition of tested composites

Material		Mref	MP10	MP20	MP30	MP50
Portland cement CEM 42.5 R	g	450	450	450	450	450
PP waste	g	-	135	270	405	675
Natural aggregate – I, II, III type	g	1350	1215	1080	945	675
Water	ml	280	280	225	225	180
Water/cement ratio	-	0.6	0.6	0.5	0.5	0.4

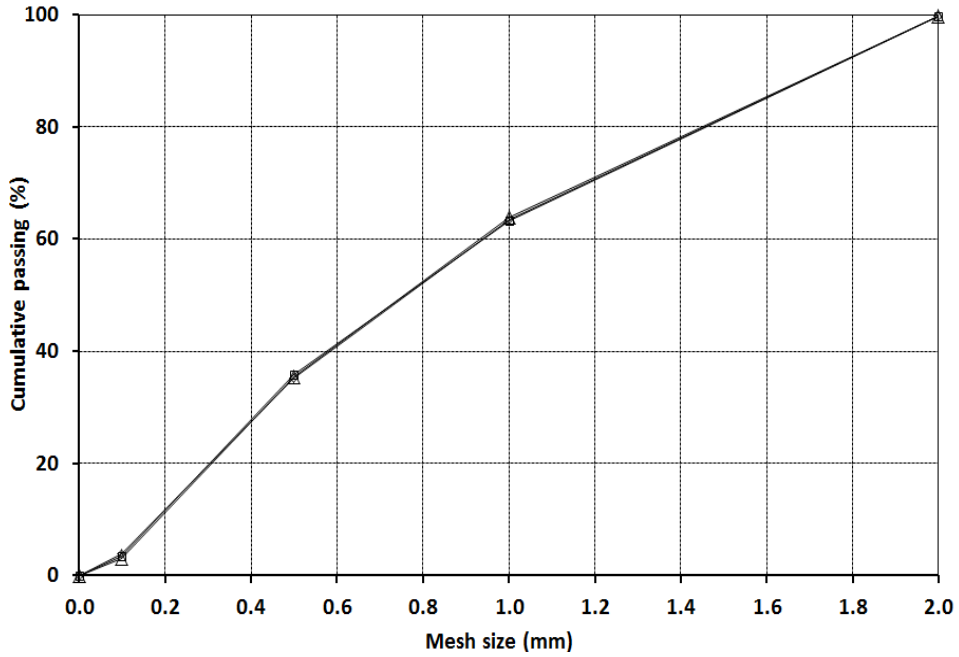

Figure 1: Grain-size curve of used mixed sand.

2.2 Basic material properties of PP aggregate

For the PP waste, measurement of grain-size curve, powder density, matrix density, and pores size distribution was done. The grain size analysis was realized using standard sieve method using sieves of the following mesh dimensions: 0.063; 0.125; 0.25; 0.5; 1.0; 2.0; 4.0; 8.0; 16.0; 31.5; and 63.0 mm. Results of grain-size sieve analysis are given in Figure 2.

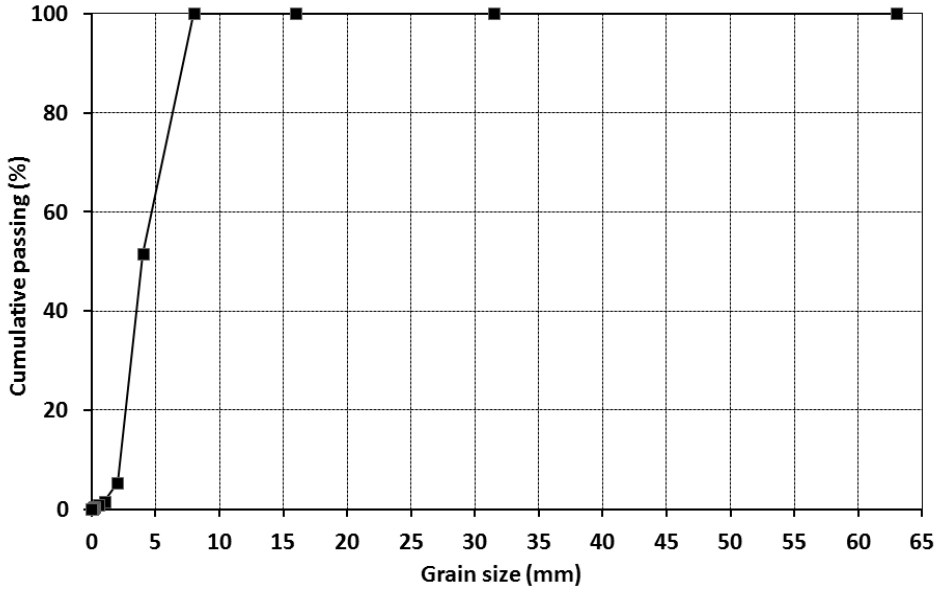

Figure 2: Grain-size curve of PP waste.

We can see that 100% of particles were smaller than 8 mm what is beneficial for incorporation into the composition of the light-weight composites.

Powder density was measured in dependence on compacting time. During the measurement, the PP waste was put into the graduated cylinder and compacted using the vibration exciter. From the know mass of the sample in cylinder and its volume, powder density was evaluated. Matrix density was measured by helium pycnometry using apparatus Pycnomatic ATC (Thermo Scientific). The accuracy of the gas volume measurement using this device is ± 0.01% from the measured value, whereas the accuracy of used analytical balances is ± 0.0001 g.

2.3 Basic physical properties of tested materials

Among the basic material properties, bulk density, matrix density and total open porosity were determined. Bulk density was accessed on the gravimetric principle from measured sample size using digital length meter and its dry mass. For this measurement, 5 cubic samples of side 100 mm were used. The matrix density was determined also on helium pycnometry principle. On the basis of bulk density and matrix density measurements, the total open porosity was calculated [5]. The relative expanded uncertainty of applied testing method was 5%.

2.4 Thermal properties

In order to evaluate the effect of plastic aggregate application on improvement of thermal insulation properties, thermal conductivity λ (W/mK), thermal diffusivity a (m^2/s) and volumetric heat capacity C_v (J/m^3K) were measured. Together with thermal properties of researched composites, heat transport and storage properties were measured also for plastic aggregate. Here, the measurements were performed in dependence on powder density.

For our measurements, the commercially produced device ISOMET 2114 (Applied Precision, Ltd.) was used as a representative of transient impulse methods. The reproducibility of ISOMET 2114 for thermal conductivity measurement is 3% of reading + 0.001 W/mK and for volumetric heat capacity 3% of reading + 1·103 J/m^3K. The measurement accuracy is given in the following table.

Table 2: Measurement accuracy of ISOMET 2114

Measurement	Measurement range	Accuracy
Thermal conductivity	0.015 - 0.70 W/mK	5 % of reading + 0.001 W/mK
	0.7 – 6.0 W/mK	10 % of reading
Volumetric heat capacity	4.0·104 - $4.0 \cdot 10^6$ J/m^3K	15 % of reading +1.103 J/m^3K
Temperature	-20 .. +70°C	1°C

The measurements were done on dry materials. The composite samples (cubic, with a side dimension of 70 mm) were measured using surface probe. For the measurement of PP aggregates, needle probe was used. Here, the measurements were realized in a graduated cylinder in dependence on compacting time having a relation to material powder density.

For the tested materials, thermal transmittance (U-Value) and thermal resistance (R-Value) were calculated assuming the thickness of composites layer 0.1 m. Thermal resistance of composite layer was calculated using Eq. (1)

$$R = \frac{d}{\lambda_{eff}}, \tag{1}$$

where R (m²K/W) is thermal resistance, d (m) material thickness and λ_{eff} (W/mK) measured effective thermal conductivity of studied material. Thermal resistance of the whole structure is expressed as

$$R_T = R_{si} + R + R_{se}, \tag{2}$$

where R_T (m²K/W) is total thermal resistance of structures within the heat transfer, R_{si} (m²K/W) thermal resistance for the heat transfer at interior surface (for floor structure 0.17 m²K/W) and R_{se} (m²K/W) thermal resistance for the heat transfer at exterior surface (for winter period 0.04 m²K/W). Thermal transmittance U (W/m²K) was calculated from Eq. (3)

$$U = \frac{1}{R_T}. \tag{3}$$

3. Results and discussion

Basic physical properties of tested materials are summarized in Table 3. With increasing amount of applied PP aggregate the material porosity systematically increases. This effect is highly positive from the point of view of better thermal insulation properties of the developed composites. The plastic modified composites can be classified as lightweight concrete (according to the standard ČSN EN 206-1), since their bulk densities reach values at the interval 800 – 2000 kg/m³.

Table 3: Basic physical properties of tested composites

Material	Bulk density (kg/m³)	Matrix density (kg/m³)	Total open porosity (% m³/m³)
Mref	2 064	3 121	33.9
MP10	1 798	2 779	35.3
MP20	1 620	2 554	36.6
MP30	1 358	2 384	43.0
MP50	953	2 060	53.8
PP aggregate	-	905	-

Thermal properties of PP aggregate and developed composites are given Tables 4, 5. One can see that with increasing powder density, thermal conductivity of PP waste aggregate increased, as well as its volumetric heat capacity. However, the differences in thermal conductivity values were very small, typically in the range of measuring error. On the other

hand, with longer time of compaction, decline in thermal diffusivity values was measured. The data measured for tested composites revealed the positive effect of PP aggregate incorporation on the moderation of heat transport. The increasing amount of PP aggregate in composites composition led to a substantial decrease of thermal conductivity. For example, 50% replacement of natural aggregate gave thermal conductivity that was about 85% lower, as compared to the reference material. This finding is highly promising for an application of the developed composite in thermal insulation layers of floor structures. For this PP highly modified material, the promising thermo-technical parameters were also calculated. Assuming the thickness of material MP50 0.1 m, one third of required thermal resistance value for the floor structure in contact with subsoil was reached.

Table 4: Thermal properties of PP aggregate

Compaction time (s)	Volume after compaction (ml)	Powder density (g/cm^3)	λ (W/mK)	C_v (10^6 J/m^{3}K)	a (10^{-6} m^2/s)
0	980	0.382	0.098	0.240	0.408
10	880	0.425	0.098	0.272	0.358
20	860	0.435	0.098	0.279	0.351
30	840	0.445	0.100	0.258	0.389
60	840	0.445	0.100	0.258	0.389
90	830	0.451	0.101	0.296	0.337
120	820	0.456	0.102	0.297	0.336
180	820	0.456	0.105	0.299	0.336
240	800	0.467	0.108	0.322	0.310

Table 5: Thermal properties of composites

Material	λ (W/mK)	C_v (10^6 J/m^{3}K)	a (10^{-6} m^2/s)	U (W/m^{2}K)	R (m^{2}K/W)
Mref	1.614	1.745	1.128	16.129	0.062
MP10	1.451	1.671	0.831	14.493	0.069
MP20	1.096	1.458	0.656	10.990	0.091
MP30	0.649	1.431	0.445	6.494	0.154
MP50	0.233	0.421	0.553	2.331	0.429

4. Conclusions

Experimental results presented in this paper provided information on the thermal performance of the developed composites with incorporated PP aggregate. The assessment of thermal transport and storage properties of plastic waste represents a novel information for the design and development of lightweight composites aimed at the thermal stability

improvement of buildings. The application of PP results in an improvement of thermal insulation properties. The obtained results present good fundamentals for further studies aimed at an advanced design of composite materials with enhanced thermal insulation function.

Acknowledgment

This research has been supported by the by the Ministry of Education, Youth and Sport of the Czech Republic, under project No SGS14/174/OHK1/3T/11. The authors are also grateful to the company FV Plast, a.s., Czech Republic that provided the PP waste.

References

[1] MEYER, C. The greening of the concrete industry. In *Cement and Concrete Composites*. 2009. 31. p. 601-605. ISSN 0958-9465

[2] SAIKIA, N. – JORGE DE BRITO, J. Use of plastic waste as aggregate in cement mortar and concrete preparation: A review. In *Construction and Building Materials*. 2012. 34. p. 385-401. ISSN 09500618

[3] IUCOLANO F., B. – LIGUORI, B. – CAPUTO, D. – COLANGELO, CIOFFI, R. Recycled plastic aggregate in mortars composition: Effect on physical and mechanical properties. In *Materials and Design*. 2013. 52. p. 916-922. ISSN 0261-3069

[4] SIDDIQUE R. – KHATIB, J. – KAUR, I. Use of recycled plastic in concrete: a review. In *Waste Managemen*t. 2008. 28. p. 1835–52. ISSN 0956-053X

[5] PAVLÍKOVÁ, M. – PAVLÍK, Z. – KEPPERT, M. – ČERNÝ, R. Salt transport and storage parameters of renovation plasters and their possible effects on restored buildings'walls. In *Construction and Building Materials*. 2011. 25(3). p. 1205-1212. ISSN 09500618

Experimental assessment of hygrothermal function of a brick building envelope exposed to winter climatic conditions

Zbyšek Pavlík, Jan Fořt, Robert Černý

Czech Technical University in Prague, Faculty of Civil Engineering, Department of Material Engineering and Chemistry, Thákurova 7, Prague 6, Czech Republic
email: pavlikz@fsv.cvut.cz

Abstract: *Experimental assessment of hygrothermal function of a newly developed hollow brick based building envelope with foam polyurethane cavity filler is done in the conditions of difference climate. For the measurement, sophisticated climatic chamber system is used that allows simulation of interior as well as of exterior climatic conditions and thus semi-real climatic loading of the tested structure. Within the performed experiment, the Prague winter climatic conditions are simulated on exterior side of the envelope, whereas the constant interior climatic conditions corresponding to the residential houses are set. The evaluation of hygrothermal performance of a researched brick envelope is done on the basis of relative humidity and temperature profiles measured along the cross section of the hollow brick block.*

The obtained results show a good hygrothermal performance of the analysed brick building envelope. From the point of view of utilization of the obtained data in building practice, one can conclude that the current developments in the production of ceramic brick blocks proceed in a proper direction. The application of foam PU cavity filler is found to lead to a substantial improvement of thermal properties of the brick block as compared with air-filled cavities. This finding represents useful information for the producers of building ceramics, as well as for the future research that can be focused on finding or development of optimal cavity filling materials.

Keywords: *hollow brick block, polyurethane cavity filler, hygrothermal function, difference climate conditions, thermal conductivity, improvement of thermal performance.*

1. Introduction

Present age lays great emphasis on decrease of energy consumption for buildings conditioning, e.g. energy for heating in cold year period and energy for air conditioning in hot year seasons. Environmental protection and achieving sustainable development requires energy efficient solutions and energy conservation in buildings. The high demands on thermal insulation function of buildings led to the construction of passive and low energy buildings that are known to outperform conventional buildings in terms of living conditions and energy efficiency due to their heat recovery, good thermal insulation, and the overall optimization of the house [1].

There are number of technical standards and recommendations on the proper indoor temperature and relative humidity of buildings. According to [1], [2] the internal temperature is the best to be kept between 20 - 26 °C and the indoor relative humidity between 30% and 60%.

In order to meet the above given requirements on low energy consumption for buildings operation and to keep optimal conditions of interior climate, new sophisticated thermal insulation materials and systems are under development and testing.

Hollow bricks are used extensively in the construction of building envelopes because of their enhanced thermal insulation properties, attributed mostly to the presence of air holes. Concerning the mode of heat transport in hollow bricks, it is generally accepted that overall heat transfer trough the cavity is due to the convective, conductive and radiative transfers [3], [4] whereas this heat transport can be reduced by thermal insulation fillers of the cavities [5], [6]. On this account, a new type of hollow brick with original cavities arrangement and with foam PU cavity filler is studied in the paper.

2. Experimental details

Studied hollow brick

The hollow brick with internal cavities filled by recycled foam PU was designed for application in single layer thermal insulation masonry having a width of 500 mm. The view of the cross-section of researched hollow brick is given in Fig. 1. Similar brick body arrangement we studied in [7], where we accessed the thermal conductivity of brick block having cavities filled by polystyrene balls.

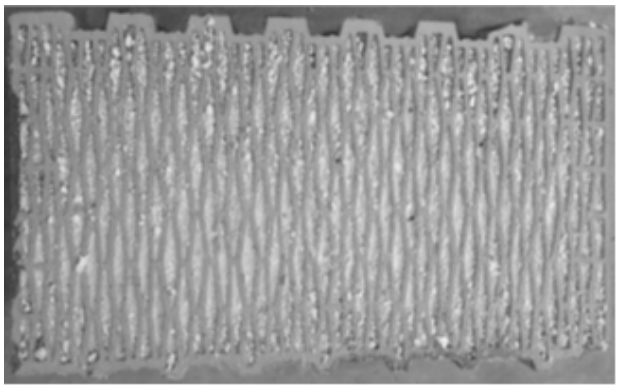

Figure 1: The view of the cross-section of the researched hollow brick block

Basic physical properties of the brick body we measured in [8]. Here, the bulk density was accessed from the measurement of sample size by digital length meter and its dry mass. The matrix density was determined on helium pycnometry principle. The total open porosity was then calculated from the bulk density and matrix density. In [8] we determined also thermal conductivity of the brick ceramic body, whereas the measurements were performed in dependence on moisture content from the dry state to the water fully saturated state using impulse measurement technique. The basic properties of the brick body are given in Table 1. Moisture dependent thermal conductivity is presented in Table 2.

Table 1: Basic physical properties of the brick body

Bulk density (kg/m^3)	Matrix density (kg/m^3)	Total open porosity (-)
1 389	2 830	50.9

Table 2: Thermal conductivity of the brick body

Moisture content (m^3/m^3)	Thermal conductivity (W/mK)
0.0	0.3
0.11	0.44
0.13	0.57
0.29	0.75
0.36	0.88
0.46	1.03
0.49	1.06

In above listed paper [8] we tested also reference brick block without cavity filling, brick block with polystyrene balls filled cavities and brick block with mineral wool filled cavities. On the basis of obtained data there was observed improvement of bricks thermal resistance by application of thermal insulation materials as cavity fillers. From the quantitative point of view, the best thermal insulation performance exhibited brick blocks with recycled foam PU and mineral-wool filled cavities. Their thermal conductivities were about 40% lower compared to brick block with air cavities. On this account, brick with PU filled cavities is studied, in order to approve its improved thermal insulation function.

Semi-scale experiment

Determination of hygrothermal performance of the studied hollow brick was done in the conditions of semi-scale experiment that enables testing of the whole brick block.

For the realization of the transient heat and water vapour transport experiment, the climatic chamber system originally designed in our laboratory was used [9], [10]. This system consists of two climatic chambers for simulation of relative humidity and temperature, and connecting tunnel for placing the specimen (Fig. 2).

Figure 2: Climatic chamber system

Maximum volume of the tested specimen, which is possible to be placed into the connecting tunnel, is 0.35 m^3 with surface exposed to the simulated climatic conditions of dimension 0.7 x 0.9 m. The construction of the particular chambers is based on common commercial

solutions for controlling temperature and relative humidity conditions but the solution of connections between the chambers and the tunnel and of the organization of additional admission holes for parallel measurements are designed in our laboratory. The dimension of the test space of the chambers is 0.72 x 0.72 x 0.60 m. In our case, the hollow brick of real dimension was studied.

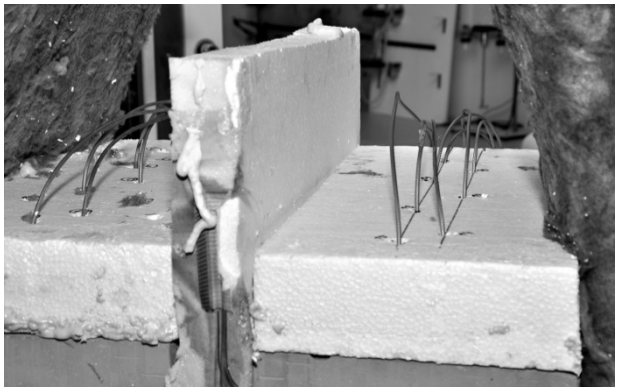

Figure 3: Sensors positioning and sample insulation

Within the experiment, the investigated brick was placed into the tunnel, and then provided with the sensors and with the additional thermal insulation consisting of polystyrene boards and polyurethane foam (Figs. 3, 4). Finally, the climatic chamber system was closed, and required temperature and relative humidity values were set. The whole experimental setup is schematically presented in Fig.5.

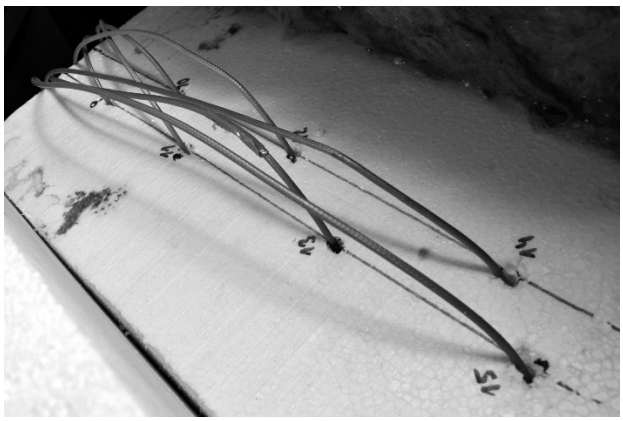

Figure 4: View of the sensors in thermal insulation board

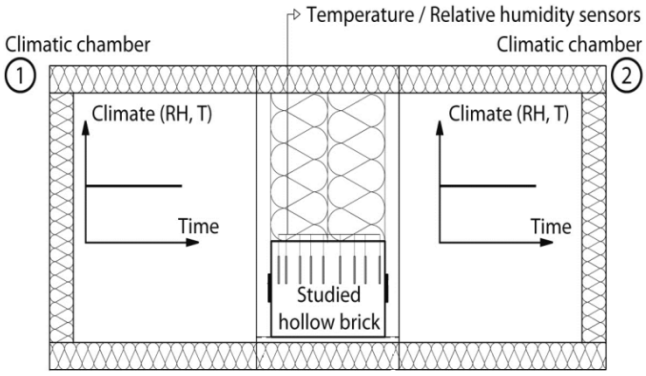

Figure 5: Scheme of the experimental setup

During the experiment, constant temperature 21 ± 0.5 °C and constant relative humidity 50 ± 2% were maintained in the interior climatic chamber. On the exterior side, there were simulated typical climatic conditions for Prague, whereas the climatic loading started with data corresponding to November 1 and the experiment was stopped with climatic data corresponding to March 31. Hence, the whole winter period, which is the most critical part of the year from the point of view of heat losses, was simulated. The airtightness of the climatic chamber system was monitored by anemometers for air flow velocity measurement. Continuous monitoring of temperature and relative humidity distribution along the hollow brick thickness was done using commercial combined sensors from Ahlborn, Germany. These sensors measure relative humidity on electrical capacity principle in the 5-98% relative humidity range with a ± 2% accuracy and temperature using NTC thermistor. The temperature measurement accuracy was for the temperature sensors applied in the measuring system ± 0.1°C.

3. Results and discussion

Climatic conditions typical for residential buildings measured in the interior climatic chamber are given in Fig. 7. We can see that both temperature and relative humidity were kept during the whole time of experiment almost constant.

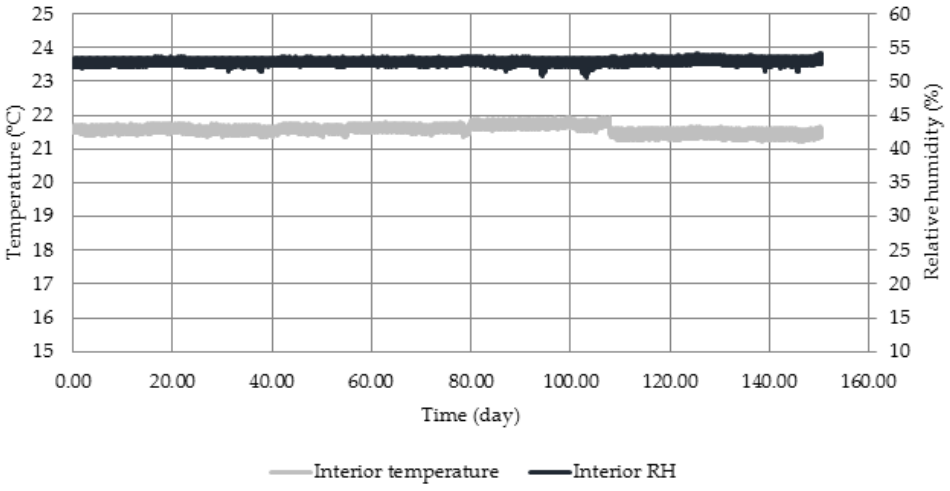

Figure 7: Interior climatic conditions

Simulated exterior climatic conditions corresponding to the time interval from November 1 to March 31 are graphed in Figs. 8, 9. Within the whole experiment, high values of relative humidity were simulated, what is typical for autumn and winter period of the year. Here, the temperature varied between -15°C and 15°C.

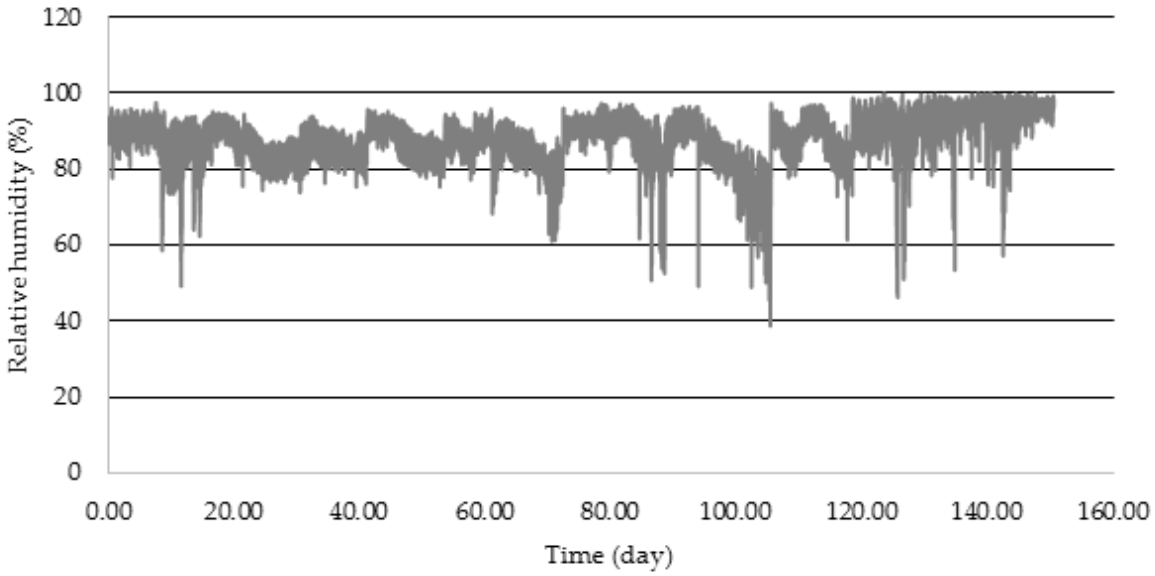

Figure 8: Exterior relative humidity

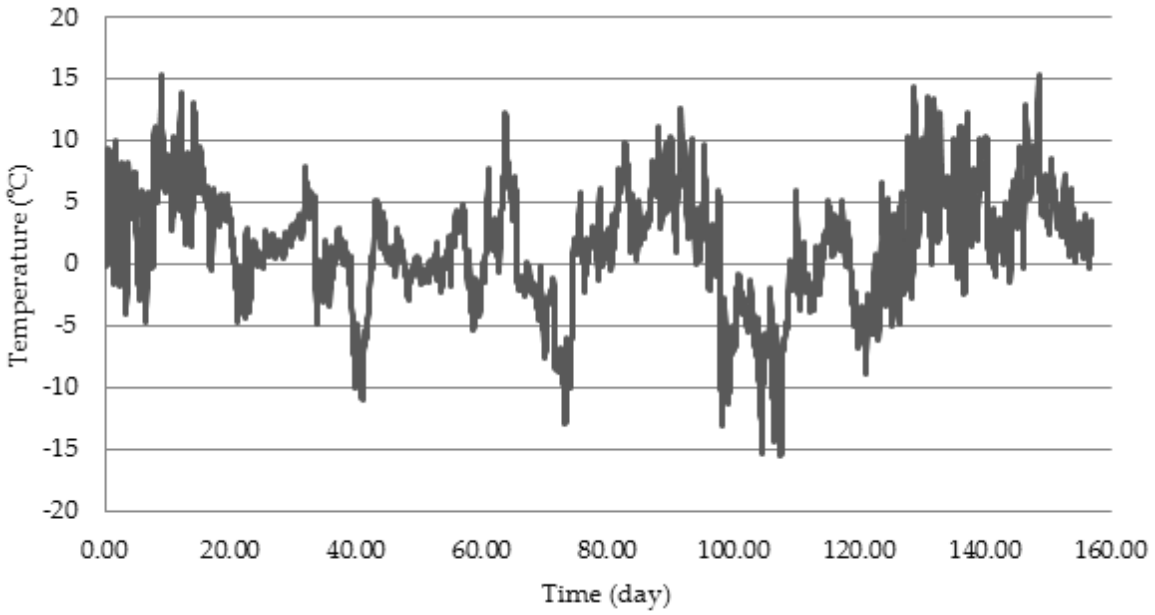

Figure 9: Exterior temperature

Temperature and relative humidity profiles measured along the brick thickness are presented in Figs. 10, 11. Looking at the temperature profiles one can observe high sensitivity of the researched brick block on the exterior temperature variations. The thermal insulation function of the brick can be considered good in general, what is promising for practical

application of the developed material in building practice. At 150 mm distance from the interior surface, there were measured temperatures of the brick about 20°C, what is very good for the conditioning of the interior climate. Basically, there were only small differences between interior temperatures and the temperatures of the brick at the distance of 150 mm from the brick surface.

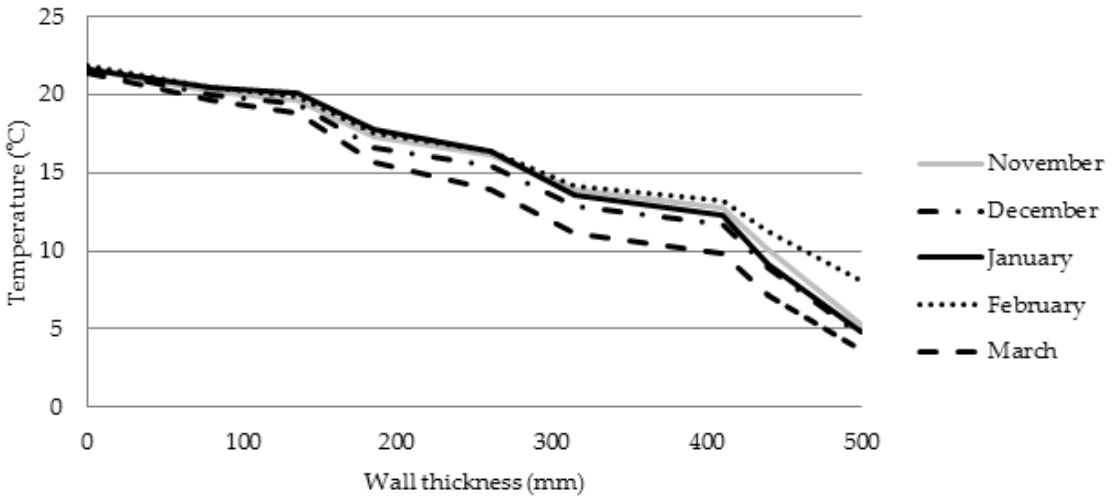

Figure 10: Temperature profiles measured along the sample thickness

Relative humidity profiles reflected the simulated relative humidity in the exterior chamber. Typically, the lowest values of relative humidity were measured for climatic loading corresponding to January and November. Here, the relative humidity values were < 60% up to 400 mm distance from the interior surface of the brick block. Relative humidity in the exterior layers of the brick was then affected by high relative humidities simulated in the climatic chamber. In December, February and March, the measured relative humidity values slightly increased and varied typically from 55 to 65%. Also in this case, the exterior side of the brick was more affected by exterior climatic conditions changes.

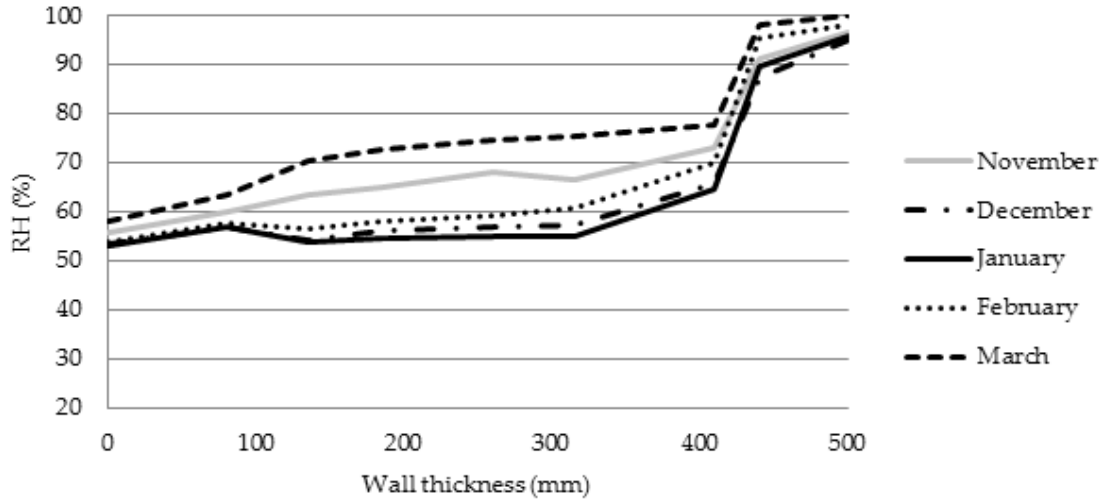

Figure 11: Relative humidity profiles measured along the brick thickness

4. Conclusions

The application of semi-scale arrangement for experimental assessment of hygrothermal performance of the newly developed hollow brick block was found to be effective way for such type of analysis. The relatively low cost of the experiment in a combination with the reasonable accuracy of measured temperature and relative humidity fields in long time interval makes good prerequisites for a widespread use of the technique.

The applied climatic loading allowed evaluation of the functionality of the tested wall segment in the winter period, which is the most critical part of the year from the point of view of the heat losses of the buildings. The obtained results revealed a very good hygrothermal performance of the brick block provided with foam PU cavity fillers.

Acknowledgement

This research has been supported by the Ministry of Education, Youth and Sport of the Czech Republic, under project No SGS14/174/OHK1/3T/11.

References

[1] MLAKAR, J. – ŠTRANCAR, J. Temperature and humidity profiles in passive building blocks. In *Building and Environment*. 2013. 60. p. 185-193. ISSN 0360-1323.

[2] WOLKOFF, P. – KJAERGAARD, S.K., The dichotomy of relative humidity on indoor air quality. In *Environmental International*. 2007. 33. p. 850-857. ISSN 0160-4120.

[3] VASILE, C. – LORENTE, S. – PERIN, B. Study of convective phenomena inside cavities coupled with heat and mass transfers through porous media – application to vertical hollow bricks – a first approach. In *Energy and Buildings*. 1998. 28. p. 199-208. ISSN 0378-7788.

[4] ANTAR, M.A. – BAIG, H. Conjugate conduction-natural convection heat transfer in a hollow brick block. In *Applied Thermal Engineering*. 2009. 29. p. 3716-3720. ISSN 1359-4311.

[5] HAZMY, M.M. Analysis of coupled natural convection-conduction effects on the heat transfer through hollow building blocks. In *Energy and Buildings*. 2006. 38. p. 515-521. ISSN 0378-7788.

[6] ZUKOWSKI, M. – HAESE, G. Experimental and numerical investigation of a hollow brick filled with perlite insulation. In *Energy and Buildings*. 2010. 42. p. 1402-1408. ISSN 0378-7788.

[7] PAVLÍK, Z. – FIALA, L., JERMAN, M. – FOŘT, J. – ČERNÝ, R. Thermal properties of contemporary lightweight cavity bricks: A semi-scale experimental study. In *Proceedings of the 2nd Central European Symposium on Building Physics*, 9-11 September 2013, Vienna, Austria, p. 733-739. ISBN 978-3-85437-321-6.

[8] PAVLÍK, Z. – FIALA, L. – VEJMELKOVÁ, E. – ČERNÝ, R. Application of effective media theory for determination of thermal properties of hollow bricks as function of moisture content. In *International Journal of Thermophysics.* 2013. 34. p. 894-908. ISSN 1572-9567.

[9] PAVLÍK, Z. – ČERNÝ, R. Experimental assessment of hygrothermal performance of an interior thermal insulation system using a laboratory technique simulating on-site conditions. In *Energy and Buildings*. 2008. 40. p. 653-678. ISSN 0378-7788.

[10] PAVLÍK, Z. – ČERNÝ, R. Hygrothermal performance study of an innovative interior thermal insulation system. In *Applied Thermal Engineering*. 2009. 29. p. 1941-1946. ISSN 1359-4311.

Thermophysics of the Sorption Storage Material CaCl2 – Zeolite Composite

Hohenauer Wolfgang, Lager Daniel

AIT - Austrian Institute of Technology GmbH

This paper has been removed.

The article originally presented here was submitted in a non-authorized version. It was not intended to be published.

This paper has been removed.

The article originally presented here was submitted in a non-authorized version. It was not intended to be published.

This paper has been removed.

The article originally presented here was submitted in a non-authorized version. It was not intended to be published.

This paper has been removed.

The article originally presented here was submitted in a non-authorized version. It was not intended to be published.

This paper has been removed.

The article originally presented here was submitted in a non-authorized version. It was not intended to be published.

This paper has been removed.

The article originally presented here was submitted in a non-authorized version. It was not intended to be published.

Measuring reliability and accuracy analysis of the hot-ball sensor

Ján Hudec[1], Peter Dieška[2], Vladimír Štofanik[1,3], Viliam Vretenár, Ľudovít Kubičár[1]

[1]Istitute of Physics SAS, Dubravska cesta 9, 845 11 Bratislava, Slovakia, kubicar@savba.sk
[2]Institute of Nuclear Science and Physical Engineering, FEI STU, Ilkovičova 3, 812 19 Bratislava, Slovakia
[3]Institute of Electronics and Photonics, FEI STU, Ilkovičova 3, 812 19 Bratislava, Slovakia

Abstract: *Hot ball method is used for measuring thermal conductivity, thermal diffusivity and specific heat. Two goals are followed, namely reliability of a measurement, and utilization of the hot ball method for monitoring regime. Certified values of distilled water and glycerol are utilized to find criterion of method reliability. Limitaions of the sensor structure considering measurement uncertainty is analysed. Structure of the sensor is searching that is suitable for mass production. Viscosity of the liquid is a limiting factor to obtain reliable data. Viscosity of distilled water seems to be a border value considering used sensor structure.*

Keywords: *Hot ball method, Thermal conductivity, Thermal diffusivity, Measurement reliability.*

1. Introduction

We use the hot-ball method for measuring thermophysical properties. The method uses of a small ball that generates a transient temperature field in its surrounding and simultaneously measures the temperature. The temperature of the ball is a measure of the thermal conductivity of the surrounding material.

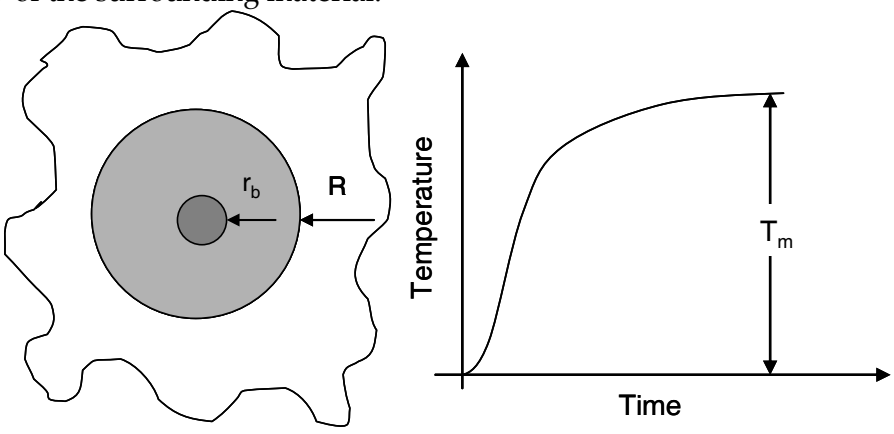

(a) *(b)*

Fig. 1 (a) Model of the hot ball and (b) temperature response for constant production of heat q = const for t > 0. Black region – hot-ball area, grey region – area penetrated by heat

A sketch of an embedded hot-ball sensor is shown in Fig 1a. A heat source in the form of a small ball starts to produce heat with a constant rate and simultaneously measures the temperature response of the surrounding medium. The temperature response stabilizes to a constant value T_m (Fig. 1b). Heat penetrates into a sphere with radius R during the

temperature stabilization to T_m. Thus, the determined thermophysical properties correspond to the material property within this sphere.

The working equation of the hot-ball sensor is based on a model, which assumes a constant heat flux q from the surface of the ball of radius r_b into the infinite medium. Then for the negligible heat capacity and high thermal conductivity of the ball, the temperature distribution within the medium is characterized by the function,

$$T(t,r_b) = T_0\left\{1 + \frac{1}{z_1 - z_2}\left[z_2 w(-iz_1\sqrt{t}) - z_1 w(-iz_2\sqrt{t})\right]\right\} \quad (1)$$

where $w(z) = e^{-z^2}\Theta^*(-iz)$, $\theta^*(u)$ is the complementary error function, $z_{1,2} = A(-1 \pm \sqrt{1-B})$, $T_0 = \frac{qr_b}{\lambda}$, $A = \frac{\lambda}{2\sqrt{k}C_s}$, $B = \frac{4C_s k}{\lambda r_b}$ and λ and k are the thermal conductivity and thermal diffusivity of the surrounding medium, respectively. Equation (1) is a solution of the partial differential equation for heat conduction for $r \geq r_b$ considering the following boundary and initial conditions:

$$T(r,0) = 0,\ -\lambda\frac{\partial T}{\partial r}\Big|_{r=r_b} + C_s\frac{\partial T}{\partial t}\Big|_{r=r_b} = P1(t)$$

where $P = q/4\pi r_b^2$ is density of heat flux at the ball surface and $T(t,\infty) = 0$. $T(t,r)$ is the temperature distribution in the surrounding material (specimen), r_b is radius of the ball, C_s is surface heat capacity of the ball calculated from the overall heat capacity C of the ball by $C_s = C/4\pi r_b^2$ and q is overall heat output of the ball and 1(t) is the step wise unit function.

2. The Hot ball sensor

The hot ball sensor consists of two main electrical components: a heating element and a thermometer. The heater used as a source for generation of the temperature field. The thermometer used for measuring temperature response to this heating. Both these parts are glued into a metallic ball. Diameter of the ball is up to 3 mm. Simple schematic of the hot-ball sensor's structure is shown in Fig. 2a. Example of how a real hot-ball sensor can look is in Fig. 2b.

(a) *(b)*

Fig. 2: a – schematic of hot ball, b – photo of real hot ball

A typical measurement is shown in Fig. 3. The measuring procedure consists of the specimen's temperature measurement representing the baseline, switching on the heating and simultaneously scanning the ball temperature. When the ball temperature stabilizes, the heating is interrupted and a period of temperature equilibration follows. After stabilization of the specimen temperature to the value prior to heat generation, the next measurement starts. The repeatability rate of the measurements depends on the thermal conductivity, and it ranges for liquids from 60 s up to 1000 s.

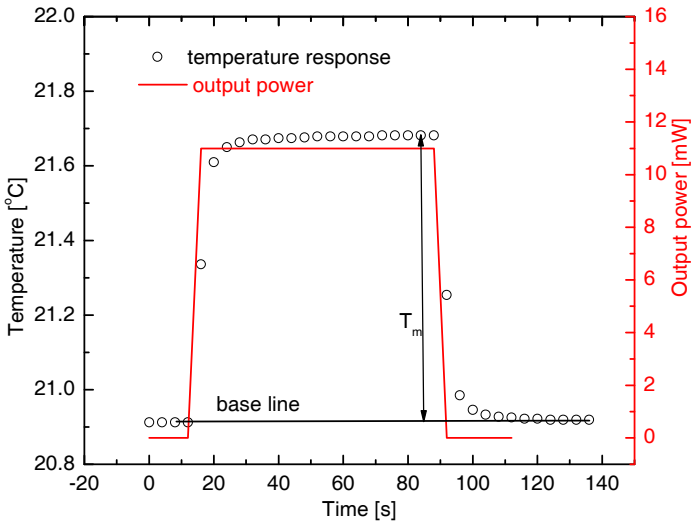

Fig. 3.: Temperature response and heat output of the sensor. Liquid: water λ = 0.58 W m-1 K-1.

3. Experiment

Hot ball sensor is fixed into the vessel made of aluminium. The vessel filled with the corresponding certified liquid [2]. A wireless instrument was used for experiments. The instrument performs measuring of surrounding conditions, data storing, communication and realization of a measurement [3]. Measurements were done in Climate chamber HPP 108. The critical point of the hot ball reliability lies in affecting the measured signal by structure of the hot ball. The properties of a hot ball were verified by measurement of distilled water and glycerol. Used liquids have different thermophysical properties (Table 1). The evaluated values of the radius and heat capacity of the ball found in both liquids in distilled water and glycerol are a measure of the sensor reliability,

Table 1.: Certified parameters of the used liquids

Liquid	Density [kg m^{-3}]	Thermal conductivity [W m^{-1} K^{-1}]	Thermal diffusivity [mm^2 s^{-1}]	Specific heat [J kg^{-1} K^{-1}]	Dynamic viscosity [Ns m^{-2}]
Distilled water	997	0.58	0.14	4180	0.00089
Glycerol	1260	0.29	0.095	2381	0.91

Six different output heat powers were used for measurements in the range from 2.5 to 16 mW. Three measurements were done for every heat output power. Stabilization time

between two measurements takes around 2 hours. Two parameters were determined, namely radius and the heat capacity of the sensor. All calibration measurements were done at 25 °C and 30 % environmental humidity in Climate chamber HPP 108.

4. Evaluation procedure

Output of a measurement includes characteristics of tested material, measuring parameters, surrounding environmental parameters and scans of temperature response. The temperature response has a shape shown in Fig. 1b. Model of the sensor is shown in Fig. 1a. Its mathematical representation gives equation (1). The used model of the method includes several parameters and variables.
Parameters:
r_b – radius of the hot ball [mm]. Generally unknown parameter due to not precise construction
C – heat capacity of the hot ball [J K^{-1}]. Not known parameter due to various materials used for construction.
q – overall heat output of the heater [mJ]. Precisely measured parameter
λ – thermal conductivity of the surrounding material (specimen). Searched parameter.
k – thermal diffusivity of the surrounding material (specimen). Searched parameter.
Variables (scanned experimental data T_i, t_i – see Fig. 3):
T_i - temperature [K]. Scanned value.
t_i - time [s]. Scanned value.

For fitting we use Levenberg - Marquadt procedure. Equation (1) gives us 4 unknown parameters. As some of them correlate, we calibrate hot ball using certificate liquids. In addition we are searching time window (time interval of the temperature response) in which constructed hot ball fulfils used model (Fig. 1a and boundary and initial conditions). A difference analysis is used to find the time window. For that purpose a "strobe" of the temperature is chosen in which the function (1) is fitted. The strobe is shifted along the whole temperature response. The corresponding data of δT is plotted against centre of the time of the strobe (see Fig. 5). The constant value of the δT gives us time window of the temperature response. When time window is found then we fit function (1) over the experimental points (scans) within this window. As a result of the mentioned methodology we obtain alternatively data of radius and heat capacity of the sensor during calibration or thermal conductivity and thermal diffusivity of the surrounding material (specimen) during measurement. The following assumption is made to use the mentioned procedure: Every point of the temperature response contains full information on sensor property and thermophysical properties of the surrounding material (specimen). As no evaluation procedure is known up to now how to extract the mentioned properties from one point of the temperature response, we chose a small time "strobe" of the temperature response (time interval) that allows us to use fitting procedure. Constructing of graphs of searching parameters (thermal conductivity, thermal diffusivity or alternatively radius, heat capacity and δT) as a function of centre time of a strobe we are able to determine time window in which construction of our sensor (Fig. 2b) satisfies to our model (Fig. 1a and equation (1)) with satisfactorily accuracy. It should be noted that for short times of the temperature response the structure of sensor is predominant and condition $\lambda_{sensor} \rightarrow \infty$ is not fulfilled. For

long times of the temperature response the flow of the liquid is induced. Nevertheless we note that uncertainty analysis still needs to be performed.

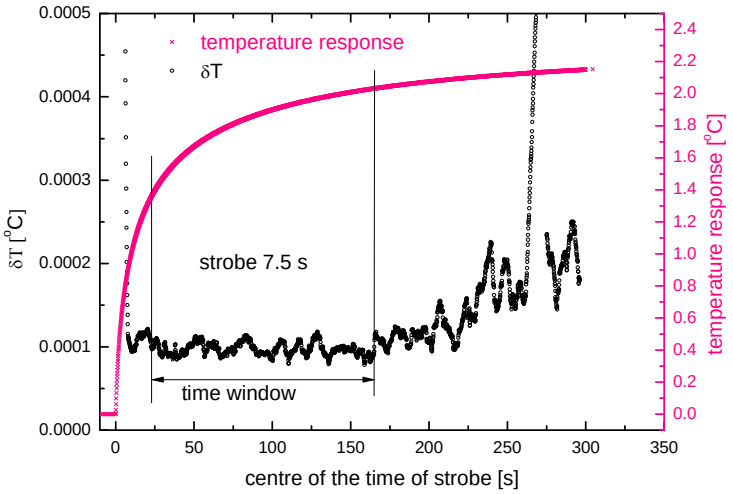

Fig. 5.: Graph of temperature response and the corresponding difference analysis of the plot. Liquid: Glycerol, output heat power 14 mW

4. Results and discussion

Data of radius and heat capacity found for sensor HB 5201 are shown in Fig. 6a and 6b. Statistics follow from a set of measured values. Values shifted far out from the mean are omitted. Data are influenced by surrounding specimen in a small extent. Considering data published in [1] it is clear, that liquids having thermal conductivity above distilled water will be influenced by measured medium in a considerable extent. Thus calibration every hot ball needs to be performed using appropriate liquids. Data shifts are caused by differences between model (Fig. 1a) and real structure of the hot ball (Fig. 2b). Clear condition $\lambda_{sensor} \rightarrow \infty$ is not fulfilled. The higher the thermal conductivity of the surrounding medium the larger data shift will be found. Dependence of the heat capacity and radius on surrounding medium is approximated by a linear function, only. Looking on data shown in [1] more calibration points needs to be used to cover these dependences by a nonlinear function.

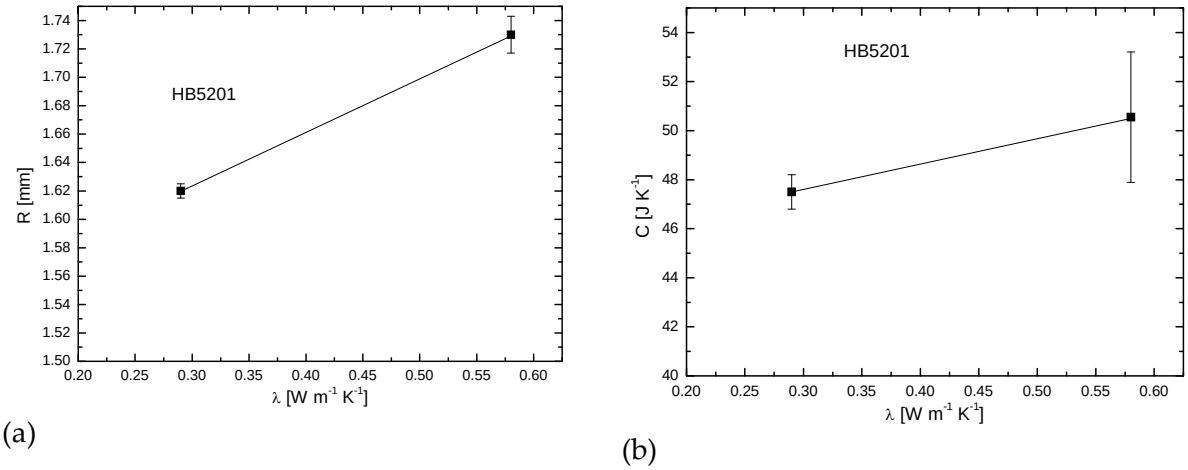

(a) (b)

Fig. 6.: Radius (a) and heat capacity (b) of the hot ball HB 5201.

Acknowledgments

This research was supported by the projects VEGA 2-0190-12 and VEGA 1/0664/14.

References

[1] KUBIČÁR, Ľ., VRETENÁR, V., ŠTOFANIK, V., BOHÁČ, V., Hot-Ball Method for Measuring Thermal Conductivity, Int. J. Thermophys., 2010, 31, 1904-1918

[2] KUBIČÁR Ľ., ANIBARO C. C., VRETENÁR V., DIEŠKA P., NOVÁK I., Monitoring of Epoxy Curing by a Thermal-Conductivity Sensor Based on the Hot-Ball Transient Method, Int J Thermophys (2012) 33:1164–1176

[3] FIDRÍKOVÁ, D., VRETENÁR, V., ŠIMKOVÁ, I., GREIF, V., VLČKO, J., KUBIČÁR, Ľ., Sensor for Monitoring the Moisture in Porous Materials, Int. J. Thermophys. 2013, DOI 10.1007/s10765-013-1493-0

Kinetics of high-temperature sintering in an illite-based ceramic body studied by thermodilatometry

Tomáš Húlan[1*], Igor Medveď[1,2], Anton Trník[1,2], Rudolf Podoba[3]

[1]Department of Physics, Faculty of Natural Science, Constantine the Philosopher University, A. Hlinku 1, 94974 Nitra, Slovakia

[2]Department of Materials Engineering and Chemistry, Faculty of Civil Engineering, Czech Technical University, Thakurova 7, 16629 Prague, Czech Republic

[3]Department of Structural Ceramics, Institute of Materials Research, Slovak Academy of Sciences, Watsonova 47, 040 01 Košice, Slovakia

*tomas.hulan@ukf.sk

Abstract: *A kinetic analysis of the sintering process in an illite-based ceramic body is studied under non-isothermal conditions using thermodilatometry. Kissinger's method and non-linear model-fitting method was adopted to provide a deeper insight into the mechanisms of this sintering. We show that it becomes rapid at the temperature ~900 °C and occurs in several overlapping steps. The apparent activation energy of the sintering process determined by the non-linear model-fitting method is 818.71 ± 0.09 and 865.32 ± 0.14 kJ/mol for the first and second step, respectively. Furthermore, the mechanism of sintering and/or crystallization seems to be heating-rate independent and governed by the thickening of the flat illitic particles.*

Keywords: *kinetics, illite, sintering, activation energy, non-linear method*

1. Introduction

The traditional ceramics gets its appreciated properties during the sintering process. Among these properties are hardness, strength in pressure, chemical resistance and, in some cases, color. In order to get the desired properties, the ceramic body has to reach a temperature high enough to enable the start of sintering and, furthermore, it has to remain at that particular temperature for a sufficiently long time.

In general, sintering proceeds are faster at higher temperatures. However, the higher is the temperature, the larger is the consumption of energy. In order to lower the production costs, one has to decide if it is more convenient to use a longer isothermal period at a lower temperature or a shorter isothermal period at a higher temperature. The knowledge of the kinetics of sintering can be very useful in such a situation. Using the kinetic parameters, one is able to predict the reaction development for long time periods or arbitrary temperature programs [3]. From a more fundamental point of view, the kinetic analysis can offer the information about the character of the processes under the study.

Illite is one of the most important constituent of raw materials for the production of the traditional ceramics. Nevertheless, its high-temperature transformation and behavior during sintering have not been explored completely up to this date. Illite is a non-expanding, dioctahedral, Al-K, mica-like mineral occurring in the clay fraction [1]. It consists of repeated tetrahedral-octahedral-tetrahedral (TOT) layers. The interlayer space is mainly occupied by potassium cations or water molecules [2]. During heating, illite overcomes (1) the drying phase (80 – 150 °C) in which physically bounded water is released, (2) the dehydroxylation

phase (400 – 700 °C) in which the structurally bounded water in the form of OH groups is connected with water molecules that are subsequently removed, and (3) the sintering phase at temperatures higher than ~950 °C. The new formed phases at high temperatures are *β*-quartz (1000 – 1300 °C), spinel (1000 – 1400 °C), and mullit (1150 – 1400 °C) [4]. Similar results were reported in [5] where, using an *in-situ* electron microscope, they observed the melt formation already at a relatively low temperature ~700 °C. After the dehydroxylation, the remaining anhydrides form a K-Al-Si glass [6]. The sintering process of an illitic-chloritic clay was studied in [7] and it was concluded that the sintering is mainly governed by the viscous flow with the apparent activation energy around 100 kJ/mol.
In comparison with kaolinite, there are, as far as we know, no data on the kinetics of high temperature processes of an almost pure illite. In this study, we use an illite-rich material and investigate its behavior during sintering by the thermodilatometric analysis (TDA). The sintering process was parametrized and we attempt at describing the mechanisms of the high temperature processes.

2. Experimental

Sample preparation and measurement

A raw material with a major content of illite (that will be referred to as illite for simplicity in the following) was first crushed, milled in a planetary ball mill Retzsch PM100, and sieved in order to obtain the particles with the dimensions less than 100 μm. A powdered illite was mixed with water and extruded into samples with a circular cross-section of diameter ~12 mm. The water content during extrusion was 36.7 wt.%. The samples were freely dried in the air in the laboratory until their moisture content was stabilized at ~2.9 wt.%. In order to reduce the thermal gradients during the heating, the diameter of the samples was reduced to 7 mm by a lathe. The samples used in the experiments had a length ~20 mm with plan-parallel bases. For the TDA measurements we used an instrument DIL 402C from Netzsch. The heating of illite was carried out at the heating rates β = 2, 5, 7, 10, and 15 °C/min from 40 to 1300 °C in an N_2 flow of 40 ml/min. The force applied to the push-rod was 0.15 N. The spacer made from a hard alumina brick was placed between a sample and the push-rod in order to distribute the push-rod pressure. The TDA measurements under every heating rate were repeated twice in order to get an average value. The chemical composition of the studied material is given in Tab. 1.

Table 1: The chemical composition of illite from Füzérradvány, Hungary (in mass%)

SiO_2	Al_2O_3	Fe_2O_3	TiO_2	CaO	MgO	K_2O	Na_2O	L.O.I.
58.0	24.0	0.6	0.05	0.38	1.70	7.85	0.10	7.3

Kinetic analysis

In general, the reaction rate (also called the sintering or crystallization rate) $d\alpha/dt$, is dependent on the temperature, T, and the reacted fraction (also called the extent of conversion), α. It is frequently described by the differential equation [8]

$$\frac{d\alpha}{dt} = k(T) f(\alpha), \tag{1}$$

where t is time, $k(T)$ is term dependent on the absolute temperature , and $f(\alpha)$ is meant to represent the reaction mechanism and is usually called the kinetic model. The temperature dependence is often considered to be of the Arrhenius type,

$$k(T) = A\exp(-E_a/RT), \tag{2}$$

where A is a pre-exponential factor (or the frequency factor), E_a is the apparent activation energy of the studied process, and R stands for the ideal gas constant. The rate equation (1) is valid only for single-step, non-overlapping processes. If the process has multiple steps or if more processes overlap, Eq. (1) has to be extended to the system of a differential equation in which each equation represents one step of the reaction with different kinetic parameters, assuming an appropriate reaction scheme (parallel, consecutive, concurrent, autocatalytic, reversible, etc.). We will assume that the sintering of illite occurs at two overlapping parallel reactions. Therefore, for their description the system of two differential equations reads

$$\frac{d\alpha_1}{dt} = A_1\exp(-E_{a,1}/RT)n_1(1-\alpha_1)[-\ln(1-\alpha_1)]^{1-1/n_1},$$

$$\frac{d\alpha_2}{dt} = A_2\exp(-E_{a,2}/RT)n_2(1-\alpha_2)[-\ln(1-\alpha_2)]^{1-1/n_2}. \tag{3}$$

The overall reaction is given as $\alpha = z\alpha_1 + (1-z)\alpha_2$, where z is the contribution of the first reaction to the total extent of reaction (we determined it as the ratio of the area under the first peak to the whole area under both peaks). As a reaction model we will consider the kinetic model of the Johnson-Mehl-Avrami (JMA) nucleation and growth which is commonly used in the kinetics of glass and ceramic sintering [9, 10],

$$f(\alpha) = n(1-\alpha)[-\ln(1-\alpha)]^{1-1/n}, \tag{4}$$

where n is the kinetic exponent and its value is characteristic for the different crystallization processes [11].

The Kissinger approach

The Kissinger method is often used in the sintering and crystallization kinetics [12, 10, 13]. This method is one of the maximum rate methods, and the apparent activation energy by this method is determined from the plot of $\ln[(T_m)^2/\beta]$ vs. $1/T$ for different heating rates, because

$$\ln\left(\frac{T_m^2}{\beta}\right) = \frac{E_a}{RT_m} + \text{const}, \tag{5}$$

where T_m is the temperature of the maximum reaction rate at the heating rate β.
The kinetic exponent can be evaluated using the Kissinger method from the shape of the reaction peak, but only if the reactions do not overlap. This is the reason why we used the Kissinger method mainly just for the evaluation of the apparent activation energy.

The non-linear model-fitting approach

To estimate the kinetic parameters E_a, A, and n, we used the non-linear method of a numerical optimization. The non-linear methods offer several advantages over the linear ones, for example, they can take into account any variation of the temperature program [8].

We decided to use the Particle Swarm Optimization (PSO) method [14] to find a minimum of the objective function. In comparison with the other methods, the PSO is less sensitive to stacking into a local minimum of the objective function instead of the global minimum. It is especially beneficial in our case when we optimize six parameters at once. The objective function itself is given by the sum of the residuals between the experimental and the theoretical (calculated) curves. The theoretical curves were evaluated as the numerical solution of the system of two ordinary differential equations (3) by using the fourth order Runge-Kutta method which is implemented as the function 'ode45()' in the programing environment Matlab®.

3. Results

Morphology by SEM

In Fig. 1a the morphology of raw illite powder is shown. It consists of aggregates of small flat particles of illite with a size less than 2 μm. After thermal treatment of illite powder at the temperature of 1050 °C we observe that the illite particles are still flat but thicker and smoother (see Fig. 1b). It seems that the thin cloven flake crystals of illite blend together and form thicker particles, most probably with an amorphous structure.

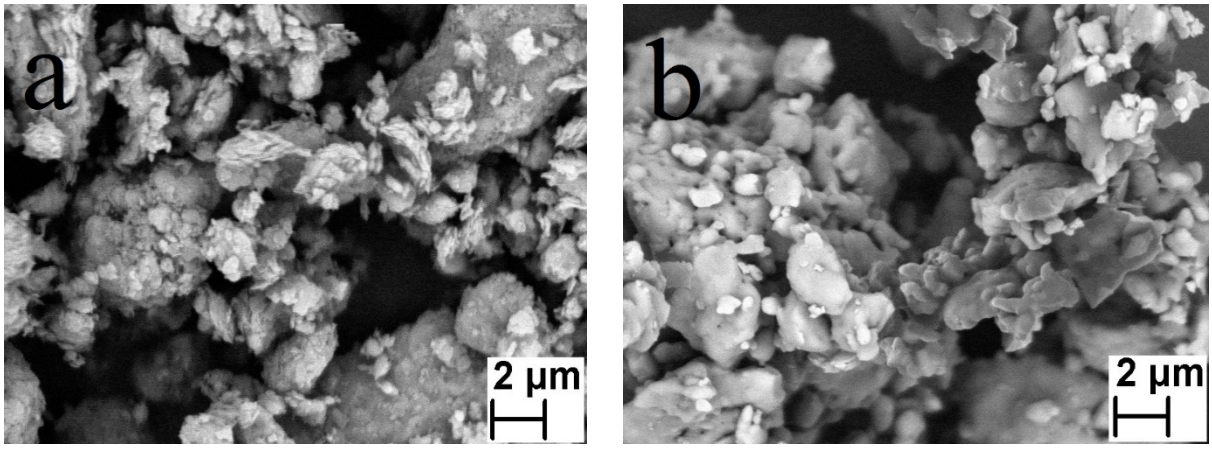

Figure 1: a) Illite particles before thermal treatment. b) Particles of the illite anhydride after thermal treatment at 1050 °C without isothermal regime.

Thermodilatometry

The relative expansion of an illite-based ceramic body run at different heating rates is shown in Figure 2a. We may observe that sintering begins at the temperature ~900 °C. The rate of the dimensions changes is depicted in Figure 2b only for temperature range 800 – 1300 °C where the sintering occurs. We may clearly recognize two partly overlapping sintering steps in the temperature region ~900 – 1220 °C.

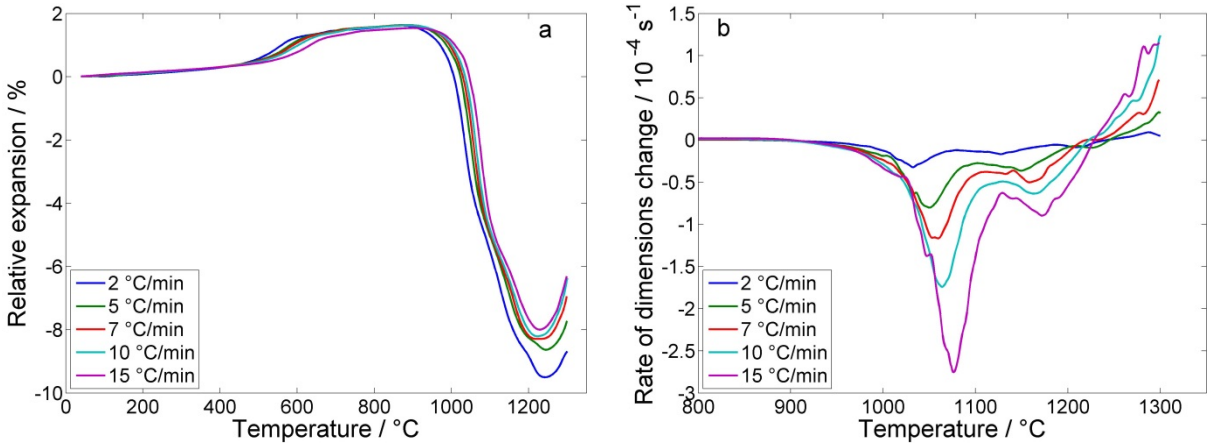

Figure 2: a) Relative expansion and b) rate of dimensions change of an illitic-based ceramic body under different heating rates.

To construct the conversion curves α vs. T, we first subtracted the baseline as it is shown in the example from Figure 3 for the case of the TDA measurement at the heating rate 2 °C/min.

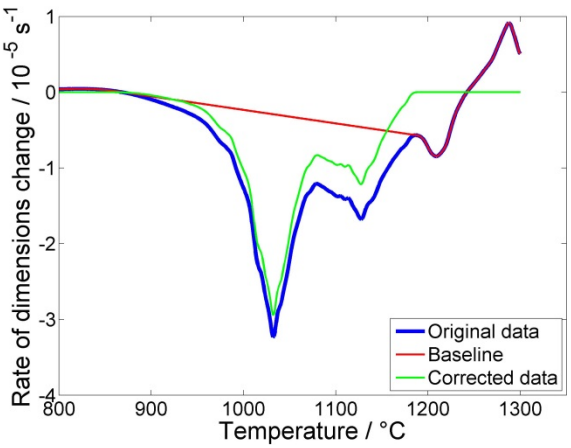

Figure 3: An example of the baseline subtraction for the heating rate 2 °C/min.

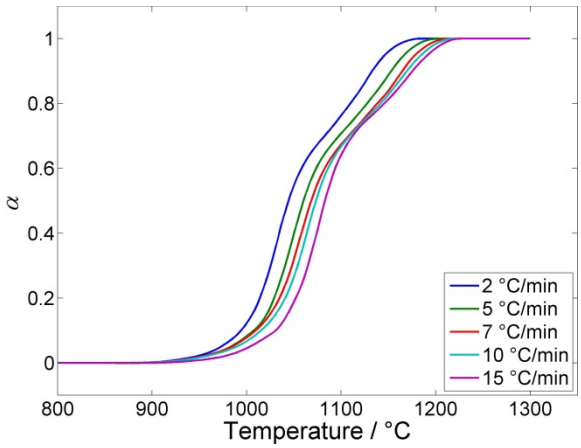

Figure 4: Conversion-temperature curves after baseline subtraction.

From the corrected curves we constructed the conversion curves (see Figure 4) as a ratio of the partial area to the total area of the peak.

Activation energy by Kissinger's method

The apparent activation energy determined by the Kissinger method is 641 ± 125 kJ/mol and 733 ± 145 kJ/mol for the first and second sintering step, respectively (see Fig. 5). A somewhat high uncertainty in the determination of the apparent activation energy is most probably caused by a not simple single-step reaction process.

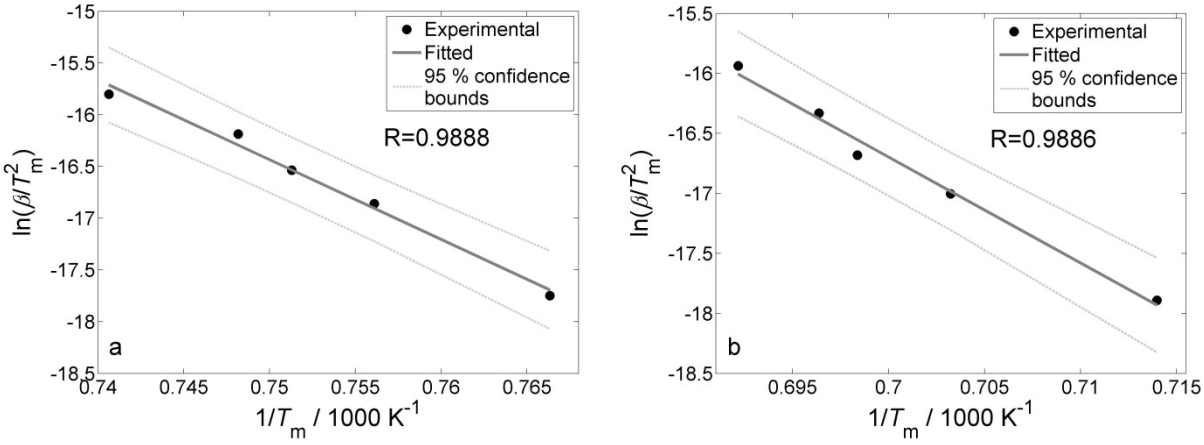

Figure 5: Kissinger's method – maximum reaction rate vs. inverse temperature for different heating rates and a) the first sintering step and b) the second sintering step.

The kinetic parameters by a simultaneous non-linear fitting of all TDA runs

If the process under consideration is independent of the heating rate, there is only one set of kinetic parameters which are able to predict the reaction progress under arbitrary temperature-time program. Therefore, it is appropriate to fit several experimental conversion curves obtained at different temperature programs simultaneously. We solved system (3) numerically, assuming suitable temperature programs. The parameters A_1, E_1, n_1 and A_2, E_2, n_2 in system (3) were optimized by the PSO algorithm in order to get the lowest possible value of the sum of squared residuals between the solution of system (3) and the experimental conversion curves from Figure 4. As starting values for the parameters E_1 and E_2, we used the results of the Kissinger method. The result of the fitting procedure is shown in Figure 6.

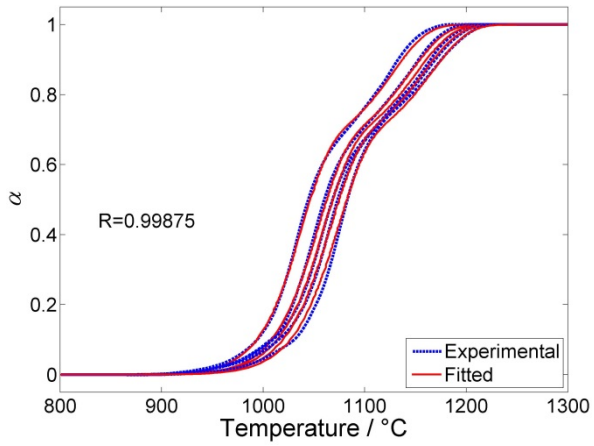

Figure 6: The result of the non-linear fitting procedure.

We obtained the apparent activation energies 818.71 ± 0.09 kJ/mol and 865.32 ± 0.14 kJ/mol, respectively. These are higher than those determined by the Kissinger method. In addition, the pre-exponential factors A_1 and A_2 were determined to be (7.648 ± 0.004) × 10^{29} s^{-1} and (3.101 ± 0.003) × 10^{29} s^{-1}, respectively. Finally, we get the values 0.6585 ± 0.0001 and 0.5583±0.0001 for the kinetic exponents n_1 and n_2, respectively, which suggest that the mechanism of both reactions is characterized by the thickening of very large plates [9]. This

is in agreement with observation of illite particles by the SEM in Fig. 1. Thus, based on the results of our kinetic analysis, we conclude that during sintering these plates become thicker probably in first step due to viscous flow (as reported in [7]) and in the second step due to the crystallization process accompanied by a further growth of particles. To confirm these results, a more detailed microstructure and mineralogical analysis should be carried out in the future.

Non-linear fitting of the individual curves

In order to examine the effect of the heating rate on the reaction kinetics, we applied the non-linear fitting method as described above also to the individual curves obtained at different heating rates. The results are summarized in Table 2. The variances in the kinetic parameters can be considered insignificant, and so we conclude that the mechanism of the illite sintering is independent of the heating rate (up to the heating rate of 15 °C/min).

Table 2: Kinetic parameters for different heating rates

β / C/min	A_1 / s^{-1}	E_1 / kJ/mol	A_2 / s^{-1}	E_2 / kJ/mol	n_1	n_2	R
2	4.913±0.003×10^{29}	812.86±0.07	4.54±0.10×10^{29}	867.44±0.49	0.6789±0.0002	0.645±0.016	1.000
5	7.477±0.006×10^{29}	817.45±0.15	8.11±0.19×10^{29}	875.59±0.60	0.6683±0.0001	0.588±0.015	1.000
7	9.258±0.010×10^{29}	820.87±0.21	7.24±0.17×10^{29}	877.62±0.89	0.6176±0.0001	0.583±0.015	0.999
10	8.135±0.006×10^{29}	819.11±0.24	3.559±0.003×10^{29}	867.59±0.36	0.6283±0.0005	0.5280±0.0004	0.999
15	6.755±0.280×10^{29}	819.23±0.20	7.493±0.309×10^{29}	874.35±0.18	0.6956±0.0003	0.5087±0.0002	0.999

4. Conclusions

A kinetic analysis of illite-base ceramic body was provided using thermodilatometry in non-isothermal conditions. In the illite sintering region, ~900 – 1200 °C, we observed at least two overlapping sintering processes. In comparison with the Kissinger method, the non-linear fitting method gives larger values of the apparent activation energy for both sintering steps: 818.71 ± 0.09 kJ/mol and 865.32 ± 0.14 kJ/mol vs. 641 ± 125 kJ/mol and 733 ± 145 kJ/mol. Based on the kinetics exponent of the JMA model, we concluded that the sintering process is governed by the thickening of the flat particles of the illite anhydride.

Acknowledgement

This work was supported by the grant VEGA 1/0646/12 from the Ministry of Education of the Slovak Republic and by the Czech Science Foundation, Project No. P105/12/G059. The authors are indebted to K. Mitterpach for technical help and to J. Biber from Inter-ILI Engineering Office (Hungary) for a supply of illite.

References

[1] J. ŚRODOŃ and D. EBERL, "Illite," *Reviews in mineralogy*, vol. 13, pp. 495-544, 1984.

[2] A. F. GUALTIERI and S. FERRARI, "Kinetics of illite dehydroxylation," *Phys Chem Minerals*, vol. 33, pp. 490-501, 2006.

[3] R. L. BLAINE and H. E. KISSINGER, "Homer Kissinger and the Kissinger equation," *Thermochimica Acta*, vol. 540, pp. 1-6, 2012.

[4] B. BOHOR, "High-temperature phase development in illitic clays," in *Clay and Clay Minerals: Proceedings of the Twelfth National Conference on Clays and Clay Minerals*, Oklahoma, 1963.

[5] R. FURLONG, "Electron diffraction and micrographic study of the high-temperature changes in illite and montmorillonite under continuos heating conditions," in *Clay and Clay Minerals. Proceedings of the Fifteenth Conference*, Pittsburg, 1967.

[6] CARROLL, C.L. et al., "Solid-state NMR characterization of the thermal transformation of Hungarian white illite," *Solid State Nuclear Magnetic Resonance,* vol. 28, pp. 31-43, 2005.

[7] A. KHALFAOUI, S. KACIM and M. HAJJAJI, "Sintering mechanism and ceramic phases of an illitic-chloritic raw clay," *Journal of European Ceramic Society,* vol. 26, pp. 161-167, 2006.

[8] S. VYAZOVKIN, A. K. BURNHAM, J. M. CRIADO, L. A. PÉREZ-MAQUEDA, C. POPESCU and N. SBIRRAZZUOLI, "ICTAC kinetics commitee recommendations for performing kinetic computations on thermal analysis data," *Thermochimica Acta,* vol. 520, pp. 1-19, 2011.

[9] J. MÁLEK, "Kinetic analysis of crystallization processes in amorphous materials," *Thermochimica Acta,* vol. 355, pp. 239-253, 2000.

[10] P. PTÁČEK, F. FRAJKOROVÁ, F. ŠOUKAL and T. OPRAVIL, "Kinetics and mechanism of three stages of thermal transformation of kaolinite to metakaolinite," *Powder Technology,* vol. 264, pp. 439-445, 2014.

[11] J. MÁLEK, "The applicability of Johnson-Mehl-Avrami model in the thermal anylisis of the crystallization kinetics of glasses," *Thermochimica Acta,* vol. 267, pp. 61-73, 1995.

[12] A. LOPES, R. MONTEIRO, R. SOARES, M. LIMA and M. FERNANDES, "Crystallization kinetics of a barium-zinc borosilicate glass by a non-isothermal method," *Journal of Alloys and Compounds,* vol. 591, pp. 268-274, 2014.

[13] A. KARAMANOV and M. PELINO, "Sinter-crystallization in the diopside-albite system. Part II. Kinetics of crystallization and sinterIng." *Journal of European Ceramic Society,* vol. 26, pp. 2519-2526, 2006.

[14] J. KENNEDY, "Particle swarm optimization," in *Encyclopedia of Machine Learning*, Springer US, 2010, pp. 760-766.

[15] A. PEREJÓN, P. E. SÁNCHEZ-JIMÉNEZ, J. M. CRIADO and L. A. PÉREZ-MAQUEDA, "Kinetic analysis of complex solid-state reactions. A new deconvolution procedure.," *J. Phys. Chem. B,* vol. 115, pp. 1780-1791, 2011.

[16] R. SVOBODA and J. MÁLEK, "Applicability of Fraser-Suzuki function in kinetic analysis of complex crystallization processes," *J Thermal Anal Calorim,* vol. 111, pp. 1045-1056, 2016.

First principles study on the Thermodynamic properties of Fe2B

Miloud Ibrir[1,*], Said Lakel[2] and Saadi Berri[1]

[1]Laboratory of Physics of Materials and its Applications, Department of Physics, Faculty of sciences, University of M'sila, Algeria.
[2]Laboratory of Metallic and Semiconducting Materials (LMSM) University of Biskra

Abstract: *Equation of state (EOS) and other thermodynamic properties of Fe2B are studied using first- principles calculations based on the plane wave full potential density functional theory method within the generalized gradient approximation (GGA) for exchange and correlation. It is demonstrated that the ratio c/a of about 1.271 is the most stable structure for the Fe2B, which is consistent with the experimental data. Through the quasi-harmonic Debye model, in which the phononic effects are considered, the dependences of the relative volume V/V0 on pressure P, cell volume V, and on temperature T, are successfully obtained. The variations of the Debye temperature θ(V), the thermal expansion α, and the heat capacity CV as a function of pressure P and temperature T, are investigated systematically in the ranges of 0-50 GPa and 0-1000 K.*

Keywords: *Equation of state, thermodynamic properties, first- principles, Fe2B, quasi-harmonic Debye model*

1. Introduction

Prediction of good thermodynamic properties of materials is the focus of solid-state science and industrial research. It is particularly the key of applying in some modern technologies which make materials undergo the ultra high-pressure and high temperature environment. For these technologies, not only the high-performance materials but also more accurate theoretical models and computational methods are needed [1].
The stable phase of Fe_2B, under ambient conditions, has a body-centered tetragonal structure of the $CuAl_2$ type with unit cell parameters of: a = 5.109 Å and c = 4.249 Å, is ferromagnetic with a magnetic moment of about 1.9 μ_B per Fe ion at 20 K and with the Curie temperature of approximately 1015 K [2, 3]. It has been reported that the Fe–B system amorphizes by rapid quenching [4] and by ion-beam mixing [5].
In our work, structure, heat capacity and thermal expansion of Fe_2B, are studied in detail by first-principles and quasi-harmonic Debye model. Since not many theoretical work on this has been published, the results obtained in this work may be useful for other groups working on or with Fe_2B.

2. Theoretical method

The zero-temperature energy calculations are performed using the WIEN2k package [6], which is based on the density functional theory. Exchange and correlation functional is given by the generalized-gradient approximation (GGA96) of Perdew et al. [7]. The PWs cut-off is used with the highly recommended condition RMTKmax = 9, where RMT is the average of the Muffin-tin spheres and Kmax is the plane waves (PWs) cut-off. The sphere radii used in the calculations are 2.17 and 1.92 a.u. for Fe and B, respectively. The k-integration over the

Brillouin zone was performed using a mesh of 10 x10x10 k-points in the irreducible wedge of the Brillouin zone. To ensure proper convergence of the self consistency calculation, the calculated total energy of the crystal converged to less than <0.5 mRy.
To investigate the thermodynamic properties of Fe_2B, the quasi-harmonic Debye model [8], is applied in which the non-equilibrium Gibbs function G*(V, P, T) can be written in the form of:

$$G^*(V; P, T) = E(V) + PV + A_{vib}[\theta(V); T] \quad (1)$$

where E(V) is the total energy per unit cell, P corresponds to the constant hydrostatic pressure condition, θ(V) is the Debye temperature, and A_{vib} is the vibrational term, which can be written using the Debye model of the phonon density of states as [9, 10]:

$$A_{vib}(\theta; T) = nkT\left[\frac{9\theta}{8T} + 3\ln\left(1 - e^{-\frac{\theta}{T}}\right) - D\left(\frac{\theta}{T}\right)\right] \quad (2)$$

where n is the number of atoms per formula unit, D(θ/T) represents the Debye integral, and for an isotropic solid, θ is expressed as [10]:

$$\theta = \frac{\hbar}{k}\left[6\pi^2 V^{\frac{1}{2}} n\right]^{\frac{1}{3}} f(\sigma)\sqrt{\frac{B_s}{M}} \quad (3)$$

where M is the molecular mass per unit cell, Bs, the Poisson σ is taken as 0.25 [13], and the adiabatic bulk modulus, is approximated by the static compressibility[9]:

$$B_s \cong B(V) = V\frac{d^2E(V)}{dV^2} \quad (4)$$

in which f(σ) is given by references 11 and 12. Therefore, the non-equilibrium Gibbs function G*(V; P, T) is a function of (V; P, T) can be minimized with respect to volume V,

$$\left[\frac{\partial G^*(V)\, P,T)}{\partial V}\right]_{P,T} = 0 \quad (5)$$

By solving Eq. (5), one can obtain the thermal equation-of-state (EOS) V(P,T). The heat capacity C_V, and the thermal expansion coefficient α are given by [14]:

$$C_V = 3nk\left[4D\left(\frac{\theta}{T}\right) - \frac{3\theta/T}{e^{\theta/T}-1}\right] \quad (6)$$

$$\alpha = \frac{\gamma C_V}{B_T V} \quad (7)$$

where γ is the Grüneisen parameter defined as:

$$\gamma = -\frac{d\ln\theta(V)}{d\ln V} \quad (8)$$

Through the quasi-harmonic Debye model, one could calculate the thermodynamic quantities of any temperatures and pressures of Fe_2B from the calculated E–V data at T=0 and P=0. By using the method above, the thermodynamic properties of Fe_2B can be successfully obtain.

3. Results and discussion

The total energy is obtained as a function of volume and fitted to the Murnaghan equation of state [15] (Fig. 1) to obtain the equilibrium lattice constant and bulk modulus. The calculated lattice cell volume and the bulk modulus are V_0= 353.96 (u.a)^3 and B = 229.34 GPa, respectively. The experimental bulk modulus is B = 194 GPa [16].

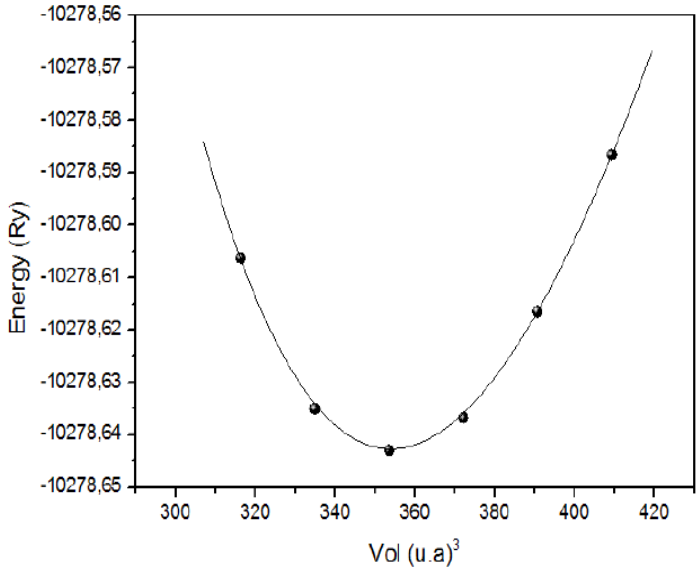

Fig. 1. Total energy as function of cell volume of Fe2B.

The thermal properties are determined in the temperature range from 0 to 1300 K, where the quasi-harmonic model remains fully valid, whereas, the pressure effect is studied in the 0–50 GPa range.

The temperature effects on the cell volume are shown in Fig. 2. The cell volume increases with increasing temperature but the rate of increase is very moderate. Furthermore, it is noted, from Fig. 3, that the relationships between bulk modulus and pressure are all nearly linear at various temperatures of 0, 300, 500, 700, and 1000 K, respectively. The bulk modulus increases with pressure at a given temperature and decreases with temperature at a given pressure.

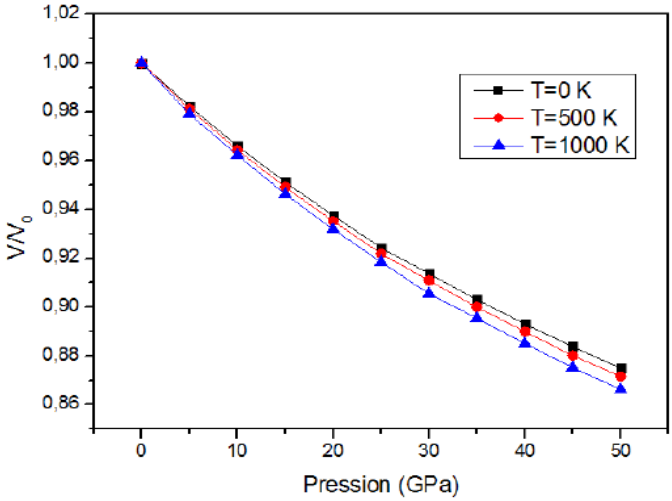

Fig. 2. Pressure and temperature dependence of the relative volume V/V0 of the Fe2B at temperatures of 0 , 500, and 1000 K, respectively.

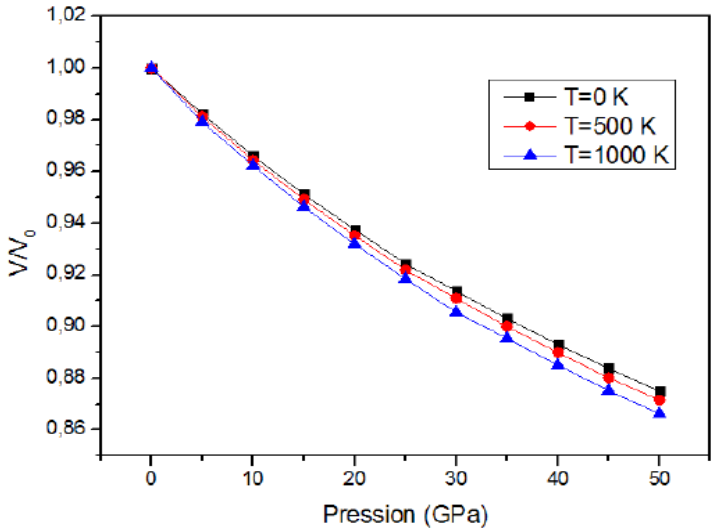

Fig. 3. Bulk modulus as a function of pressure at temperatures of 0, 300, 500, 700 and 1000 K.

The investigation on the heat capacity of crystals is a well established topic of condensed matter physics [17–19]. Knowledge of the heat capacity of a substance not only provides essential insight into its vibrational properties but also mandatory for many applications. Two famous limiting cases are correctly predicted by the standard elastic continuum theory [19]. At high temperatures, the constant-volume heat capacity Cv tends to the Petit and Dulong limit [20]. At sufficiently low temperatures, C_v is proportional to T^3 [19]. At intermediate temperatures, however, the temperature dependence of C_v is governed by the details of vibrations of the atoms. Fig. 4 represent the heat capacity, C_v (T), as function of the temperature. These two quantities indicate a sharp increase up to ~600 K which is due to the anharmonic approximation of the Debye model here. However, at higher temperature, the anharmonic effect on C_v is suppressed, and C_v is very close to the Dulong–Pettit limit, common to all solids at high temperatures. It can be seen from Fig. 3 that as pressure increases, the heat capacity C_v decreases as well as the Debye
Temperature 0 increases. The heat capacity C_v in this work is 54.06 J/mol K at zero pressure and ambient temperature. Moreover, the Debye temperature θ obtained here is 792.48 K.

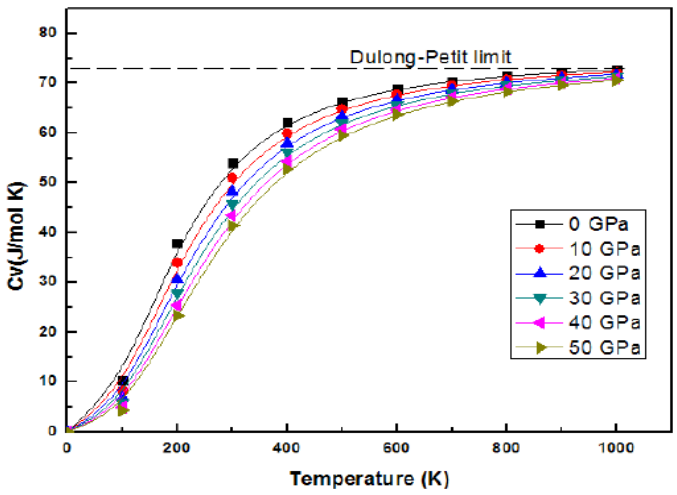

Fig. 4. Heat capacity Cv versus temperature at pressures of 0-50 GPa.

Finally, in Fig. 5, we have plotted our results for the thermal expansion coefficient α of Fe_2B. We remark that for a given pressure, α increases rapidly with temperature at low temperatures especially at zero pressure, then gradually increase slowly at higher temperatures. As pressure increases, the increasing of α with temperature becomes smaller. While for a given temperature, α decreases rapidly with increasing pressure.

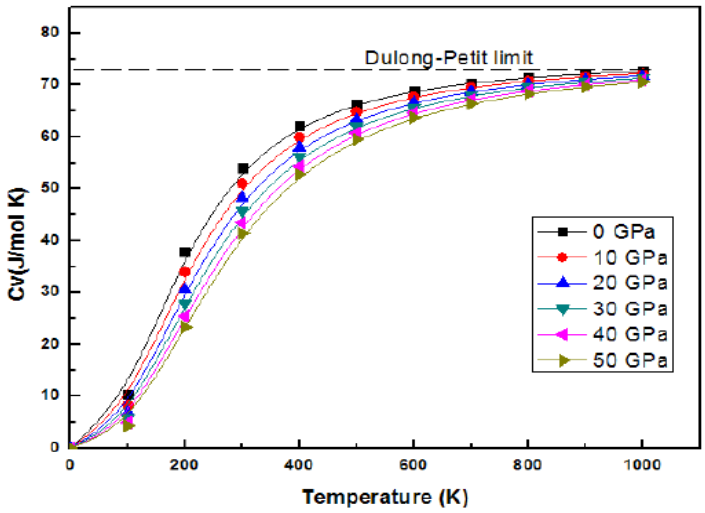

Fig. 5. The thermal espansion as afunction of temperature at pressure of 0-50 GPa.

4. Conclusion

Structural properties of Fe_2B at temperature T = 0 K have been calculated using the FP-LAPW method within the generalized-gradient approximation in the frame of density functional theory. It is found that the cell volume is in a good agreement with the few available experimental and theoretical data. The thermodynamic properties of Fe_2B are predicted using the quasi-harmonic Debye model. C_v is found to increase with temperature and is close to the Dulong–Petit limit at high temperatures. Furthermore, the thermal expansion coefficient rises with temperature and its increasing trend will get slow at high temperature and high pressure.

References

[1] YOO CS, AKELLA J, CAMPBELL AJ, MAO HK, HEMLEY RJ, Phase-diagram of iron by in-situ X-ray-diffraction - implications for earth core, *Science* 1995; **270**:1473-1475.

[2] MURPHY KA, HERSHIKOWITZ N, *Phys. Rev. B* 1973; **7**:23.

[3] PEARSON WB, *Handbook of Lattice Spacings and Structures of Metals*, Pergamon: New York; 1967.

[4] J.M. DUBOIS and Y.G.L. CAER, *Nucl. Instrum. Methods* 1982; **58**: 307.

[5] CLEMENS BM, NEUMEIER JJ, Ion-beam-mixed iron boron film, *J. Appl. Phys.* 1985; **58**:4061-4064.

[6] BLAHA P, SCHWARZ K, MADSEN G.K.H, KVASNICKA D, LUITZ J, WIEN2k, Vienna University of Technology, Vienna, Austria, 2001, http://www.wien2k.at/reg_user/textbooks/S.

[7] PERDEW JP, BURKE S, ERNZERHOF M, Generalized Gradient Approximation Made Simple. *Phys. Rev. Lett.* 1996; **77**: 3865- 3868.

[8] BLANCO MA, FRANCISCO E, LUANA V, GIBBS: isothermal-isobaric thermodynamics of solids from energy curves using a quasi-harmonic Debye model. *Comput. Phys. Commun.* 2004; **158**: 57-72.

[9] BLANCO MA, MARTIN PENDAS A, FRANCISCO E, RECIO JM, FRANCO R. Thermodynamical properties of solids from microscopic theory: applications to MgF_2 and Al_2O_3. *J. Molecular Struct. Theochem* 1996; **368**: 245-255.

[10] FLOREZ M, RECIO JM, FRANCISCO E, BLANCO MA, Martin PENDAS A. First-principles study of the rocksalt–cesium chloride relative phase stability in alkali halides. *Phys. Rev. B.* 2002; **66**:144112-144119.

[11] FRANCISCO E, RECIO JM, BLANCO MA, MARTIN PENDAS A, Costales A. Quantum-Mechanical Study of Thermodynamic and Bonding Properties of MgF_2. *J. Phys. Chem.A* 1998; **102**: 1595–1601.

[12] FRANCISCO E, BLANCO MA, SANJURJO G. Atomistic simulation of SrF_2 polymorphs. *Phys. Rev. B* 2001; **63**:094107-094116.

[13] POIRIER JP. *Introduction to the Physics of the Earth's Interior*, vol. 39, Cambridge University Press: Oxford: 2000.

[14] HILL R. The Elastic Behaviour of a Crystalline Aggregate. *Proc. Phys. Soc. London A* 1952; **65**: 349.

[15] MURNAGHAN FD. *Proc. Nat. Acad. Sci. USA* 1944; **30**: 5390.

[16] XIAO B, XING JD, FENG J, ZHOU CT, Li FY, SU W and al. A comparative study of Cr_7C_3, Fe_3C and Fe_2B in cast iron both from ab initio calculations and experiments. *J. phys. D: Appl. Phys.* 2009; **42**: 115415

[17] EINSTEIN A. Die Plancksche Theorie der Starhlang und die Theorie der spezifishen Wärme. *Ann. Phys.* 1907; **22**: 180-189.

[18] NERNST W, LINDEMANN AF, Angew Z. *Elektrochem. Phys. Chem.* 1977; **17**:817.

[19] DEBYE P, *Ann. Phys.* 1912; **39**: 789.

[20] PETIT AT, DULONG PL, *Ann. Chim. Phys.* 1819; **10** : 395.

Effect of salt contamination on drying rate of ceramic brick

Olga Koronthalyova[1], Lubomir Bagel[1]

[1]Institute of Construction and Architecture, SAS, Dubravska c. 9, SK-84503 Bratislava, Slovakia, email:usarkoro@savba.sk

Abstract: *An effect of the salt contamination on the moisture transport was studied for case of burnt clay brick with low hygroscopic ability. The analysis was limited to small salt concentration, having practically negligible effect on the material porosity but significantly increasing hygroscopic moisture content (HMC) of the brick. The simply experiment, consisting in monitoring of isothermal one-dimensional capillary uptake and following drying was carried out for salt free and salt contaminated bricks. The experimental results were compared with numerical simulation of the process of drying. On the base of the comparison the effect of salt contamination on moisture transport parameters was evaluated. The presence of salt had practically no effect on moisture diffusivity function. On the other hand, the water vapour permeability was significantly lowered by the salt crust formation.*

Keywords: *drying rate, water vapour permeability, moisture diffusivity, efflorescence, burnt clay brick*

1. Introduction

A numerical simulation is at present a common tool for determination of a hygro-thermal state of building structures. However, reliable results of numerical simulation can be obtained only on condition of using correct moisture transport and accumulation parameters. Moisture transport and accumulation parameters are commonly measured in laboratory conditions where moisture in material pores is not contaminated. In reality, an interaction between the materials in building structures and chemicals from the surrounding air or water is often present and therefore pore water frequently contains dissolved salt or different salts.

Drying of porous materials in the presence of salt is still poorly understood. This is caused by the complexity of the involved phenomena e.g., moisture and ion transport phenomena and phase transitions. The phenomena of salt efflorescence and the fact that the created salt crust can affect resultant water vapour permeability are generally well known but a quantification of this effect is rarely presented in literature. Significant increase of the water vapour resistance factor value of saline sandstones was reported for example in [1]. Similarly in [2], a decrease of water vapour permeability of ceramic brick contaminated by sodium chloride has been detected. However, the extent of the water vapour permeability decrease has depended on the actual salt crust formation. A detailed analysis of drying behaviour of ceramic brick saturated with the 15 % (kg/kg) sodium chloride solution has been presented by Gupta et al. [3], where the drying of saline brick was compared to the standard drying behaviour of water saturated materials and significant effect of the actual salt crust properties was found out. Similarly in [4] it has been shown that the actual drying rate depends on the type of the created efflorescence.

This work is focused on the effect of salt contamination on the moisture transport parameters -water vapour permeability and moisture diffusivity. Analysis is limited to sodium chloride solution of small salt concentration, having practically negligible effect on the material

porosity. Possible changes of moisture transport parameters were studied by simply experiment, consisting in monitoring of isothermal one-dimensional capillary uptake of distilled water /salt solution and following drying. Based on the comparison of the process of drying of the saline and the salt free material and its numerical simulation the effect of salt contamination on moisture transport parameters was determined.

2. Materials and methods

The tested brick is commonly used burnt clay brick produced by Slovak factory characterised by low hygroscopic ability [2, 5]. The brick is manufactured from a clay-sand mixture (the proportion of the sand ranged from 30% to 50%); the temperature of burning is 900–1000°C. Basic material parameters (bulk density, total open porosity), pore structure, mineral composition, water vapour permeability as well as water vapour adsorption isotherms of the salt free and saline (contaminated by 4% NaCl solution) bricks were determined in previous works [2, 5]. Within this work the sorption data were completed by desorption curves measurement.

The water vapour sorption curves were measured by standard gravimetric desiccator method, which consists in conditioning the samples in desiccators under constant RH and temperature (23°C) until the static equilibrium is achieved [6]. The water vapour permeability was measured by the standard cup method [7] and the specific surface area (SSA) was determined by nitrogen adsorption measurements.

The process of capillary uptake and following drying was measured on prism samples with the base of ca 34 x 26 mm and the height of ca 52 mm. The four side surfaces of the specimens were sealed by epoxy resin in order to guarantee one-dimensional moisture flow. In total, three brick samples were tested. Two were immersed into distilled water and one was immersed into 4% NaCl solution (40 g NaCl in 1000 g of distilled water). During the capillary uptake test, the depth of the sample immersion was kept at ca 2 mm. After completion of capillary uptake process, the samples were dried by the air flow (the air flow velocity was between 2.0 - 2.5 m/s) in air conditioned laboratory room (temperature of 23 ± 0.5°C and RH of 53 ± 1%). The drying was going on through both of base surfaces of the specimen. Monitoring of the water uptake and release process was done by sample weighing at appropriate time intervals. At the end of tests the samples were oven dried at temperature of 105°C in order to determine actual moisture contents of the samples.

3. Results and discussion

The basic material parameters of the tested brick D obtained from the previous measurements [2] and from the capillary uptake test are presented in Table 1.

Table 1: Basic material properties of salt free and saline brick D

NaCl content [kg/kg]	Bulk density [kg/m^3]	Density [kg/m^3]	Open porosity [-]	SSA [m^2/ g]	Absorption coefficient of water [kg/(m^2·s$^{0.5}$)]	Capillary saturation moisture content [kg/m^3]
0	1780	2752	0.30	1.13	0.17	235
0.00492	1789	2752	-	0.79	0.17	235

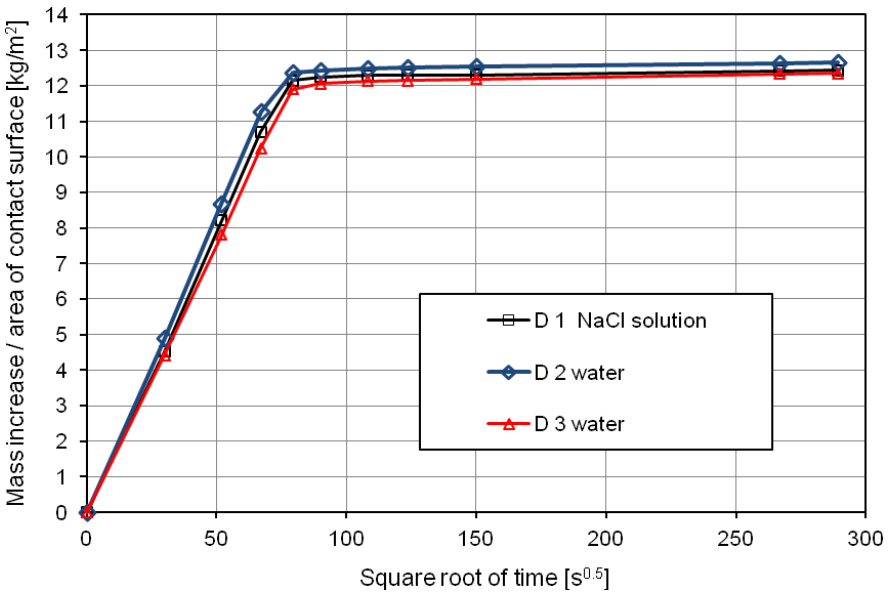

Figure 1: Comparison of capillary water absorption of ceramic brick immersed into sodium chloride solution or distilled water

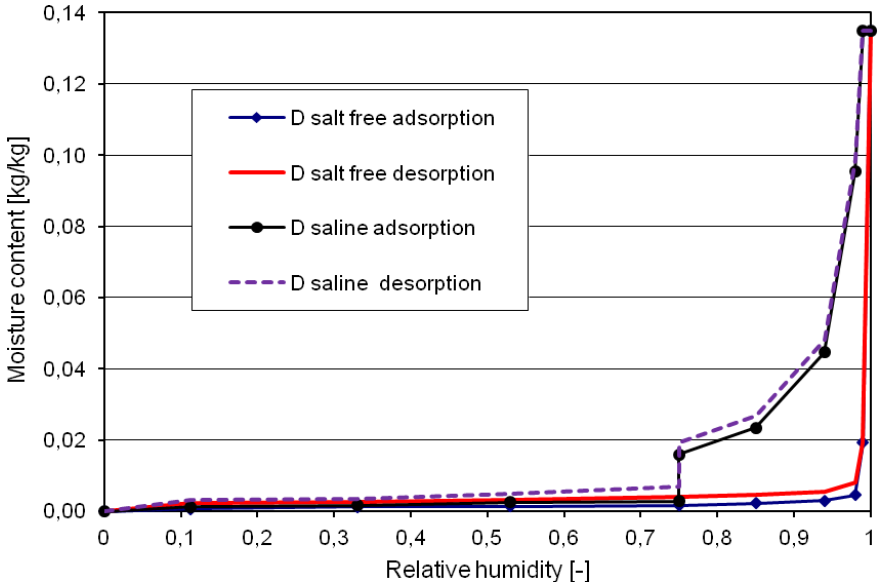

Figure 2: Water vapour adsorption and desorption curves for salt free brick and brick contaminated by 4% sodium chloride

The process of capillary water uptake is presented in Fig. 1. As can be seen from Fig. 1, the process of capillary uptake of the sample immersed in salt solution does not differ from the one of the samples immersed in distilled water. It can be explained by the small concentration of the applied salt solution. As a consequence, the same values of absorption coefficient and capillary saturation moisture content were obtained for salt free and saline bricks (Tab. 1).

The measured water vapour adsorption and desorption isotherms are shown in Fig. 2. In case of saline brick a sharp increase of adsorbed moisture can be seen at relative humidity of 0.75, which is deliquescence relative humidity of sodium chloride at temperature of 23 °C. As it has been concluded in previous work [2], this effect occurs in case of ceramic bricks with low hygroscopic ability and indicates a relative independence of the process of water adsorption by the salt and by the material. The detected hysteretic effects are not very significant. However, it should be noted that in the following comparison of the experimental and numerical results of the drying process they cannot be omitted due to very high sensitivity of the simulation results to the applied moisture storage function [8]. In case of saline bricks, the noticed hysteretic effects are slightly higher than the ones of the salt free brick.

Fig. 3 presents the monitored process of bricks drying. There was practically no constant drying rate period, as can be expected considering the fact that the drying started from capillary moisture content. During the period of the first five hours, the rate of drying was similar for all three bricks. Then, the noticeable decrease of the drying rate of the saline brick D 1, compared to the salt free bricks was observed. Simultaneously a creating of a salt crust was noticed on the both base surfaces of brick D 1. The salt crust formation had continued up to the 24th hour, when practically continuous salt crust was created on the base 1 that was in contact with water during capillary uptake test. The salt crust formed on the base 2 that was during capillary uptake test in contact with surrounding air was thinner and not continuous (Fig. 4).

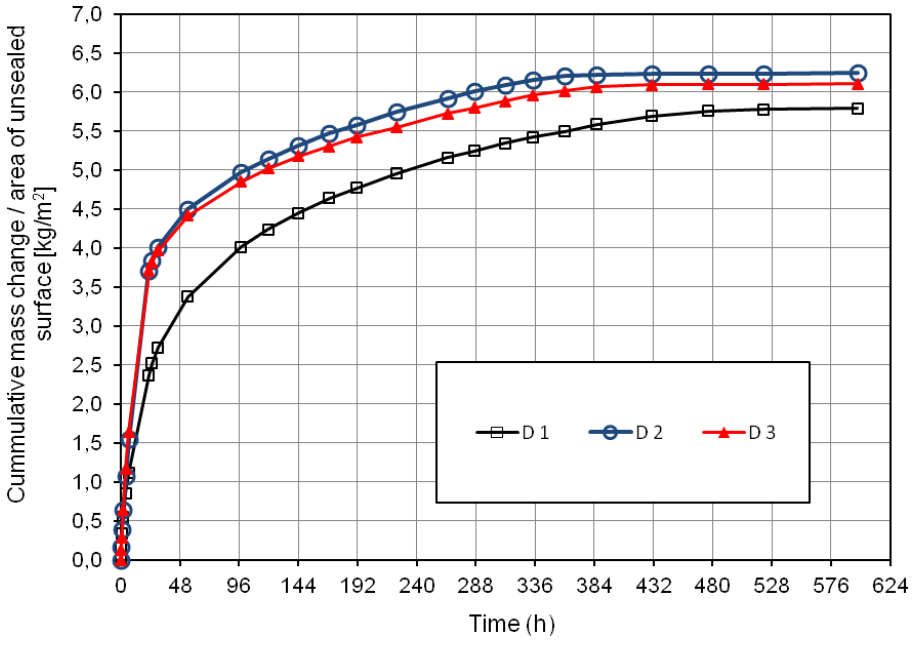

Figure 3: Process of bricks drying presented by cumulative amount of the dried out water divided by the area of base surfaces. D 1 – saline brick, D 2, D 3 – salt free bricks

The different salt crust formation on base 1 and 2 can be explained by the fact that at the beginning of the drying, moisture content was not perfectly identical within the sample and higher moisture content was near base 1, which was in contact with water. Another reason

could be the brick non-homogeneity that resulted in presence of coarser surface on the base 2 (Fig. 4). The second reason is in agreement with results presented in [4] where it was concluded that sufficiently fine porous medium is necessary for creating the crusty (blocking) efflorescence.

Figure 4: Efflorescence formed on the base 1 (left) and the base 2 (right) of brick D 1. Real dimensions of the displayed segments are of ca 12x10 mm

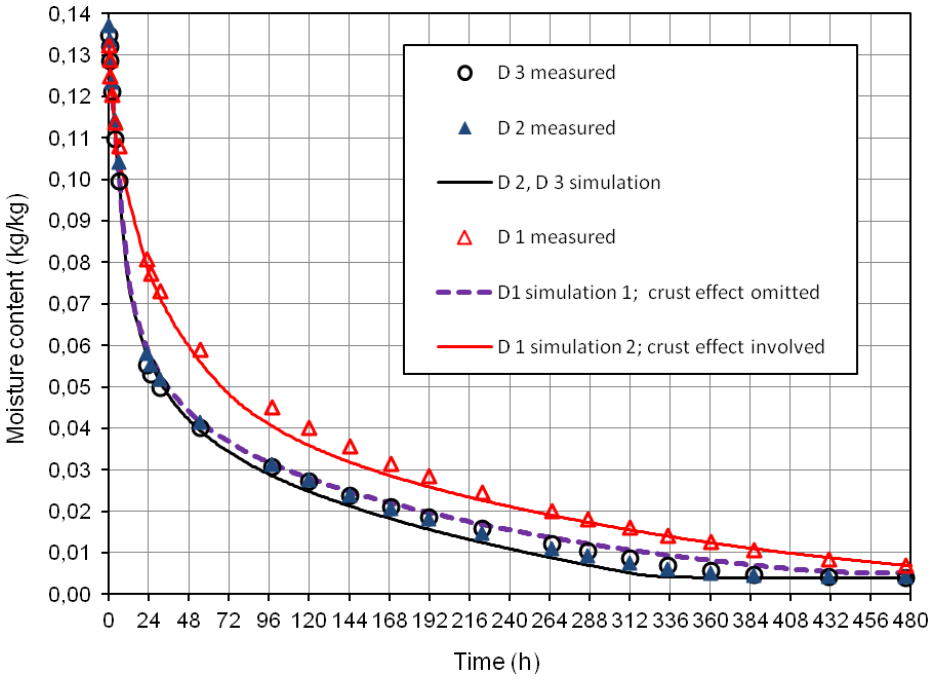

Figure 5: Time course of moisture content of the dried bricks - comparison of the measured and simulated data. D 1 – saline brick, D 2, D 3 – salt free bricks

The moisture content courses of the drying bricks are shown in Fig. 5.

Numerical simulations of the moisture content of the samples during 1D drying were done by 1-D simulation tool WUFI (version 2.2).

In the simulations, the measured desorption curves (Fig. 2) were used as moisture storage function. Within the hygroscopic range, moisture transport was characterised by water vapour

permeability. Beyond the hygroscopic range, moisture diffusivity function was used for simulation of moisture transport.

The moisture dependence of water vapour permeability of salt free and saline brick D was determined in previous work [2]. As follows from this work, in the interval of moisture contents, occurring during drying (Fig. 5), the water vapour permeability is practically constant and corresponds to the wet-cup value. The determined wet-cup water vapour resistance factor values are of 11 and 10 for salt free and saline brick D respectively [2].

In evaluation of moisture diffusivity it was supposed that its dependence on moisture content is exponential [9]:

$$D_{\mathrm{w}} = D_{w0} \cdot \exp\left(\frac{w}{w_{cap}} \cdot \log\left(\frac{D_{wcap}}{D_{w0}} \right) \right) \tag{1}$$

Where w is moisture content (kg/m^3), w_{cap} is capillary saturation moisture content (kg/m^3), D_{w0} *is* moisture diffusivity at moisture content w_0 (w_0 corresponds to moisture content at the end of hygroscopic range), $D_{w\,cap}$ *is* moisture diffusivity at capillary saturation moisture content.

$D_{w\,0}$ and $D_{w\,cap}$ were evaluated from the experimentally determined values of absorption coefficient for water and capillary saturation water content (Tab. 1), using Kunzel's simplified relation [9]:

$$D_{\mathrm{w}\,0} = \frac{3.8}{1000} \cdot \left(\frac{A}{w_{cap}} \right)^2 = 2 \cdot 10^{-9}\,\mathrm{m}^2 \cdot \mathrm{s}^{-1} \tag{2}$$

$$D_{\mathrm{w}\,cap} = 3.8 \cdot \left(\frac{A}{w_{cap}} \right)^2 = 2 \cdot 10^{-6}\,\mathrm{m}^2 \cdot \mathrm{s}^{-1} \tag{3}$$

Equation (3) gives the moisture diffusivity at capillary moisture content for the process of suction. As a rule, the process of redistribution, occurring during the drying is slower. Therefore, the redistribution moisture diffusivity at capillary water content can be approximately estimated by the value, lying one decimal power below the $D_{w\,cap}$ [9].

The air flow velocity near the sample was estimated to 2.2 m/s. On the base of the similarity relations and the Lewis relation [10] the value of the surface film coefficient for diffusion β_v = $1.5 \cdot 10^{-7}$ s/m was determined, which was used in simulations.

Comparison of the experimental and numerical results for salt free bricks shows sufficient agreement (Fig. 5). Presence of small discrepancies can be partly explained by the applied simplification in the evaluation of the moisture diffusivity – from the detailed measurements of ceramic bricks it is known that real moisture diffusivity moisture dependence is not as strictly exponential as it follows from Eq. 1, cf. for example [11]. Another reason can consist in material non-homogeneity, observable from a small difference between the moisture content courses of brick D 2 and D 3 (Fig. 5).

In case of saline brick, two simulations were done: Simulation 1 was performed using material parameters as described above, without involving the effect of salt crust. As can be seen from Fig. 5, an agreement between the simulated and measured results was obtained only for the period of first five hours, when the salt crust was not present. In simulation 2 the same material parameters were applied as in simulation 1, but the crust effect was involved by considering of additional water vapour resistances on sample bases. In reality, the creating of salt crust was a continuous process. In simulation, it was evaluated by a simplified way, using constant values for the first period from the 6th to the 24th hour and for the remaining period of the drying. The applied values of additional water vapour resistances are summarised in Tab. 2. The results of simulation 2 agree satisfactorily to the measured results (Fig. 5). It should be mentioned that the applied value of the additional water vapour resistances on the base 1 corresponds roughly to the additional water vapour resistance of salt crust observed during previous dry cup measurement on the brick D [2]. Presence of salt had relevant effect on moisture storage function of the brick. However, for the tested salt concentration, the water vapour as well as capillary water transport within the brick was not affected by presence of salt. The noticed lowering of water vapour permeability resulted from the salt crust formed of sample surface.

Table 2: Additional water vapour diffusion equivalent air layer thickness

	Period from the 6th to the 24th hour	Period from the 25th hour
Base 1	0.03 m	0.035 m
Base 2	0.004 m	0.01 m

4. Conclusions

An effect of the salt contamination on the moisture transport was studied for case of burnt clay brick with low hygroscopic ability contaminated with small salt concentration.

The measurements have shown that the process of capillary uptake is practically identical for the brick immersed into salt solution and the one immersed into distilled water. The process of drying is significantly affected by actual salt crust creation. For the tested salt concentration, the water vapour as well as capillary water transport within the brick was not affected by presence of salt. The lowering of water vapour permeability can be fully explained by presence of salt crust formed of sample surface. The salt crust formation was affected by initial moisture content at the surface that influenced the evaporation rate from the surface. It is probable that the surface roughness could have some effect as well.

In future work the effect of salt contamination on moisture transport should be verified for other types of ceramic bricks, different salt concentrations and rates of drying.

Acknowledgments

This research was supported by the Scientific Grant Agency VEGA (Grant No. 2/0145/13).

References

[1] KIESSL, K.: Bauphysikalische Einflüsse bei der Krustenbildung am Gestein alter Bauwerke. In *Bauphysik* 11(1989): 44-49.

[2] KORONTHALYOVA, O. – BAGEL, L. – KULLIFAYOVA, M. - IFKA, T. Effect of presence of salt on moisture accumulation and transport in burnt clay bricks. In *NSB 2014, 10th Nordic Symposium on Building Physics*, Editors: Jesper Arfvidsson, Lars-Erik Harderup, Anders Kumlin, Bitte Rosencrantz, Lund, Sweden, 2014, p. 443-450, ISBN: 978-91-88722-53-9 (TVBH-3061).

[3] GUPTA, S., HUININK, H. P., PRAT, M., PEL, L., & KOPINGA, K. Paradoxical drying of a fired-clay brick due to salt crystallization. In *Chemical Engineering Science*, Vol.109 (2014): 204-211.

[4] ELOUKABI, H., SGHAIER, N., BEN NASRALLAH, S., & PRAT, M. Experimental study of the effect of sodium chloride on drying of porous media: The crusty–patchy efflorescence transition. In *International Journal of Heat and Mass Transfer*, Vol. 56(2013): 80-93.

[5] KORONTHALYOVA, O. Moisture storage capacity and microstructure of ceramic brick and autoclaved aerated concrete. In *Construction and Building Materials,* Vol. 25 (2011): 879-885.

[6] EN ISO 12571:2000 Hygrothermal performance of building materials and products - Determination of hygroscopic sorption properties.

[7] EN ISO 12572:2001 Hygrothermal performance of building materials and products - Determination of water vapour transmission properties.

[8] KORONTHALYOVA, O. & MIHALKA, P. Simplified modelling of hygric performance of a hysteric building material exposed to cyclic changes of relative humidity. In *Thermophysics 2012: 17th International Meeting of Thermophysical Society,* Editor Oldřich Zmeškal, Bratislava, Institute of Physics, Slovak Academy of Science in Bratislava, 2012, p. 73-80, ISBN 978-80-214-4599-4.

[9] KUNZEL, H. M. *Simultaneous Heat and Moisture Transport in Building Components*, IRB Verlag Stuttgart 1995, ISBN 3-8167-1403-7.

[10] RADU, A., et al. Heat, air and moisture transfer terminology-parameters and concepts. Porto, FEUP ediçoes, 2012, ISBN 978-972-752-147-0.

[11] BROCKEN, H. J. P. Moisture transport in brick masonry: the grey area between bricks, TU Eindhoven 1998, ISBN 90-6814-087-6.

Theoretical calculations of the Elastic and Thermodynamic Properties of hexagonal Lithium Phosphide

S. Lakel[1,2], M. Ibrir[3], K. Almi[1]

[1] Laboratory of Fundamentals Sciences - University of Laghouat – Algeria
[2] Laboratoire de Matériaux Semi Conducteurs et Métalliques «LMSM», Université de Biskra,
[3] Département de physique, Université de M'sila, Algérie

Abstract: *Lattice constants, elastic and thermodynamic properties of hcp structure Li3P are studied using first-principles calculations based on the plane wave pseudopotential density functional theory method within the generalized gradient approximation (GGA) for exchange and correlation. It is demonstrated that the ratio c/a of about 1.779 is the most stable structure for the hcp Li3P, which is consistent with the experimental data. Through the quasi-harmonic Debye model, in which the phononic effects are considered, the dependences of bulk modulus on pressure and temperature are successfully obtained. The variations of the Debye temperature Θ, the thermal expansion coefficient α and the heat capacity Cv with pressure P and temperature T are investigated systematically in the ranges of 0–35 GPa and 0–1000 K.*

Keywords: *DFT, elastic properties, thermodynamic properties, Debye temperature*

1. Introduction

Solid electrolytes with high ionic conductivity are required for high energy density lithium batteries. There is a growing need for high energy density batteries for application in microelectronic devices, power tools, and even large scale energy storage systems [1]. Lithium phosphide has been introduced as a good ionic conductor[2]. Advanced batteries such as, lithiated graphite/solid electrolyte/metal oxides, are very promising, nonpolluting, high energy power sources. Solid electrolytes have many advantages over liquid electrolytes in terms of design flexibility and miniaturization of the electronic devices. Solid electrolytes can be made in thin film configurations which provide a low ohmic resistance [3] .

The ionic conductivity of many available solid electrolytes is too low (at ambient temperature) to be useful for high energy power sources. Commercial development of a solid state lithium battery relies on the successful development of a solid electrolyte with high ionic conductivity [4]. During last few years, the search for new ion conducting materials has focused on a series of metallate, phosphate, sulphate, silicate and borate glasses [5]. Among these materials Li3P is one of the most important ionic conductors and it can be used for solid state lithium batteries. Nazri et al. [6] has used Li3P ionic conductor during preparation of Li3P-LiCl solid electrolyte for solid state lithium batteries.

The theoretical and experimental studies have been performed to investigate structural and electronic properties [1-4-7] of Li3P. Besides the structural and electronic properties, the study of elastic, thermodynamic and optical properties of Li3P are also important for practical applications. But there is no a detail experimental information on elastic, thermodynamic and optical properties of Li3P. The knowledge of elastic constants is essential for many practical applications related to the mechanical properties of materials, e.g. load deflection, sound velocities, internal strain, thermo elastic stress. These also offer

important information regarding the degree of anisotropy which is known to correlate with a tendency to either ductility or brittleness. The microscopic thermodynamic properties are closely related to the microscopic dynamics of atoms. Thermodynamic properties of solid materials are directly related to the quanta of lattice vibrations known as phonons. Phonons directly contribute to a number of phenomena such as the thermal expansion, temperature dependence of mechanical properties, phase transitions and phase diagrams.

In this work, the elastic properties such as independent elastic constants, Young's modulus, ratio of the shear modulus to bulk modulus (Pugh's indicator), Cauchy's pressure, Poisson's ratio, elastic anisotropy are calculated. The thermodynamic properties such as bulk modulus, specific heat capacities (CP, CV), volume thermal expansion coefficient and Debye temperature at elevated temperature and pressure are calculated and analyzed by using quasi-harmonic Debye model.

2. Method of calculation

2.1 Total energy electronic structure calculations

In the present electronic structure calculation, we apply the GGA for the exchange-correlation functional in the scheme of Perdew-Wang 1991 (PW91) [8] functions as implemented in the CASTEP code [9] . A plane-wave basis set with energy cut-off 700 eV is applied. The interactions between ion and electron are represented by norm-conserving pseudopotentials for Li, and P atoms [10]. Pseudo atomic calculations are performed for Li($2s^1$) and P($3s^2$ $3p^3$). For the Brillouin-zone sampling, we use the 8×8×6 Monkhorst-Pack mesh [11] , where the self-consistent convergence of the total energy is at 1.0×10^{-6} eV/Atom. The structures were optimized by the BFGS algorithm [12].

2.2. Elastic properties :

Elastic properties are closely related to various fundamental solid state properties such as Debye temperature, thermal expansion, Gruneisen parameter, etc. Hence, elastic constants are essential for many technological applications. Usually, elastic constants are defined by means of a Taylor expansion of the total energy $E(V, \delta)$ for the system with respect to a lattice strain δ of the primitive cell volume V. The energy of a strained system is expressed as follows [13]:

$$E(V,\delta) = E(V_0,0) + V_0\left(\sum_i \tau_i \xi_i \delta_i + \frac{1}{2}\sum_{ij} C_{ij}\,\delta_i \xi_i \delta_j \xi_j\right) \quad (1)$$

where $E(V_0, 0)$ is the energy of unstrained system with equilibrium volume V_0, τ_i is an element in the stress tensor, ξ_i and ξ_j are factors to take care of Voigt index. There are five independent elastic constants for hexagonal structure, i.e., C_{11}, C_{33}, C_{44}, C_{12}, and C_{13}. From the independent elastic constants above, the theoretical elastic modulus can be obtained. There are two approximation methods to calculate the modulus, namely the Voigt and Reuss method. For the hexagonal crystal, the Voigt (B_V) and Reuss (B_R) bulk modulus are given by:

$$B_V = \frac{2}{9}(C_{11} + C_{12} + 2C_{13} + C_{33}/2) \quad (2)$$

$$B_R = \frac{(C_{11}+C_{12})C_{33}-2C_{13}^2}{(C_{11}+C_{12})+2C_{33}-4C_{13}} \quad (3)$$

Correspondingly, the upper and the lower bounds for the shear modulus of hexagonal crystal are expressed as follows:

$$G_V = \frac{1}{30}(C_{11} + C_{12} + 2C_{33} - 4C_{13} + 12C_{44} + 12C_{66}) \quad (4)$$

$$G_R = \frac{5}{2}\frac{\left((C_{11}+C_{12})C_{33}-2C_{13}^2\right)C_{44}C_{66}}{3B_V C_{44}C_{66}+\left((C_{11}+C_{12})C_{33}-2C_{13}^2\right)(C_{44}+C_{66})} \quad (5)$$

where

$$C_{66} = \frac{1}{2}(C_{11} - C_{12}) \quad (6)$$

The arithmetic average of the Voigt and Reuss bounds is called the Voigt–Reuss–Hill (VRH) method. The VRH averages for bulk modulus (B) and shear modulus (G) are given by:

$$B = E_H = \frac{1}{2}(B_R + B_V) \quad (7)$$

$$G = G_H = \frac{1}{2}(G_R + G_V) \quad (8)$$

The Young's modulus (E) and the Poisson's ratio (ν) are then calculated from these elastic constants using the following equations:

$$E = \frac{9BG}{3B+G} \quad (9)$$

$$\nu = \frac{3B-2G}{2(3B+G)} \quad (10)$$

2.3. Quasi-harmonic Debye model

To investigate the thermodynamic properties of LiP_3, we here apply the quasi-harmonic Debye model [14-15], in which the phononic effect is considered. In the quasi-harmonic Debye model, the non-equilibrium Gibbs function G*(V ; P; T) takes the form of

$$G^*(V, P, T) = E(V) + PV + A_{vib}(\Theta(V), T) \quad (11)$$

where $E(V)$ is the total energy per unit cell, PV corresponds to the constant hydrostatic pressure condition, $\Theta(V)$ is the Debye temperature, and A_{vib} is the vibrational Helmholtz free energy that can be written as

$$A_{vib}(\Theta, T) = n k T\left[\frac{9}{8}\frac{\Theta}{T} + 3\ln\left(1 - \exp\left(-\frac{\Theta}{T}\right)\right) - D(\Theta/T)\right] \quad (12)$$

where D(Θ/T) represents the Debye integral, n is the number of atoms per formula unit. For an isotropic solid, Θ is expressed by

$$\Theta = \frac{\hbar}{k}\left(6\pi^2 V^{1/2} n\right)^{1/3} f(\nu)\sqrt{\frac{B_S}{M}} \quad (13)$$

where M is the molecular mass, B_S is the adiabatic bulk modulus and $f(\nu)$ are approximated by the static compressibility [16] :

$$f(\nu) = \left\{3\left[2\left(\frac{2}{3}\frac{1+\nu}{1-2\nu}\right)^{3/2} + \left(\frac{1}{3}\frac{1+\nu}{1-\nu}\right)^{3/2}\right]^{-1}\right\}^{1/3} \quad (14)$$

$$B_S \cong B(V) = V\left\{\frac{d^2E(V)}{dV^2}\right\} \quad (15)$$

The Poisson ν is obtained from Eq. (11). Therefore, the non-equilibrium Gibbs function $G^*(V; P; T)$ can be minimized with respect to volume V:

$$\left(\frac{\partial G^*(V,P,T)}{\partial V}\right)_{P,T} = 0 \quad (16)$$

and one could obtain the thermal equation of state and the thermal expansion coefficient α as follows:

$$\alpha = \gamma C_V/(B_T V) \quad (17)$$

where the isothermal bulk modulus B_T, the heat capacity C_V and the Grüneisen parameter γ are expressed as

$$B_T(P,T) = V\left(\frac{\partial^2 G^*(V,P,T)}{\partial V^2}\right)_{P,T} \quad (18)$$

$$C_V = 3n\,k\left[4D(\Theta/T) - \frac{3\Theta/T}{e^{\Theta/T}-1}\right] \quad (19)$$

$$\gamma = -\frac{d\ln\Theta(V)}{d\ln V} \quad (20)$$

For cubic ZrC, n=4, M=51.796 a.u. Through the quasi-harmonic Debye model, all the thermodynamic quantities of any temperature and pressure of cubic ZrC may be calculated from the calculated E-V data.

3. Results and discussion

3.1. Structural properties

Experimental studies have established that Li_3P crystallizes in hexagonal structure with space group *P*63/*mmc* (194) and has 8 atoms in one unit cell. First of all, we have performed the geometry optimization as a function of the normal stress by minimizing the total energy. Secondly, we execute a series of geometry optimization from -20 to 40 GPa, and obtain the total energy E and the corresponding primitive cell volume V. By fitting the E–V data to the numerical equation of state (EOS) [17], we can obtain the equilibrium lattices constants *a and c*, bulk modulus B_0 and its pressure derivation B'_0 at P = 0 GPa and T = 0 K, which are listed in Table I, together with the available experimental and other theoretical data [7, 18].

Table 1. Calculated lattice parameters a (Å), c (Å) and c/a ratio for Li_3P at T = 0 K.

This work	other results		
a (°A)	*4.26*	*4.23 [7]*	*4.27 [18]*
c (°A)	*7.58*	*7.56 [7]*	*7.59 [18]*
c/a	*1.779*		
B_0 (GPa)	*36.28*		
B'_0	*3.25*		

3.2. Elastic properties

To study the elastic properties of Li_3P at $T = 0$ K and $P = 0$ GPa, the elastic constants C_{ij}, bulk modulus B, shear modulus G, Young's modulus E, and Poisson's ratio ν have been calculated for the first principle based on CASTEP code . The theoretical polycrystalline moduli for Li_3P may be computed from the set of independent elastic constants. Using the formulas: (2), (3), (4), (5), (7), (8), (9) and (10), the polycrystalline Young's modulus E (in GPa) and the Poisson's ratio ν are obtained and given in Table 2. The condition for mechanical stability is that B, C_{11}-C_{12} and C_{44} are positive[19]. It is found that Li_3P is mechanically stable because B, C_{11}-C_{12} and C_{44} are positive. The ductitle-brittle nature of materials can be discussed in terms of elastic constants of the relevant material. If the Cauchy's pressure (C_{12}-C_{44}) is negative (positive), the material is expected to be brittle (ductile) [20]. In the present case this value is negative and it indicate that Li_3P is brittle. Another index of ductility is Pugh's ratio [21] and a material behaves in a ductile manner, if $G/B < 0.5$, otherwise it should be brittle. The critical number which separates the ductile and brittle was found to be 0.57 [22]. Thus the value of 0.9 for Li_3P thus indicates its brittle behavior. The elastic anisotropy of crystal, defined by the ratio $A = 2C_{44}/(C_{11} - C_{12})$ [23], yields a value of 0.59 for A. The factor $A = 1$ represents complete isotropy, while value smaller or greater than this measures the degree of anisotropy. Therefore, Li_3P shows strong anisotropic behavior. The parameter $k_c/k_a = (C_{11}+C_{12}–2C_{13})/(C_{33}–C_{13})$ expresses the ratio between linear compressibility coefficients of hexagonal crystals [23]. From our data the value of k_c/k_a (= 1.27) indicates that the compressibility for Li_3P along c axis is greater than along a axis.

Table 1. Calculated elastic constants C_{ij} (GPa), bulk moduli B (GPa), shear moduli G (GPa), Young's moduli E (GPa), Poisson's ratio ν , A and k_c/k_a for Li_3P at T = 0 K.

C_{11}	C_{12}	C_{13}	C_{33}	C_{44}	B	G	ϒ	ν	A	G/B	k_c/k_a
104.5	22.8	4.25	98.22	24.15	36.28	32.8	77.55	0.18	0.59	0.9	1.27

3.3. Thermodynamic properties

The investigation of thermodynamic properties under high temperature and high pressure requires the application of quasi-harmonic Debye approximation [14,15,16] . The thermodynamic properties of Li_3P have been investigated by using this model and for this we first derive E-V data obtained from Birch-Murnaghan equation of state [24] using zero temperature and zero pressure equilibrium values, E_0, V_0, B_0, based on DFT method.

Fig. 1(a) shows the temperature and pressure dependent of bulk modulus B. It is seen that bulk modulus decrease with increasing temperature. Fig. 1-b shows the pressure dependent of bulk modulus at 300 K. We see that B and increase with increasing pressure.

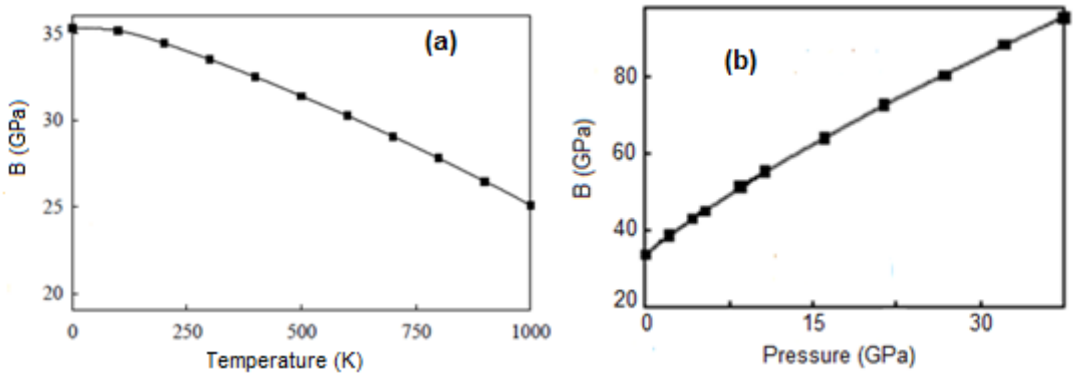

Figure 1: The temperature and pressure dependence of bulk modulus of Li_3P, at P = 0 GPa (a) ; at 300 K (b).

The Debye temperature is also one key quantity in the quasiharmonic Debye model. In Fig. 2, we show the Debye temperature Θ as a function of temperatures at P =0 GPa and pressure P at the temperatures of 300 K. For Fig. 2(a), it is shown the Debye temperature Θ decreases when the temperature changes from 0 to 1000 K. Fig. 2(b) is shown that when the temperature is constant, the Debye temperature Θ increases non-linearly with applied pressures, indicating the change of the vibration frequency of particles under pressure.

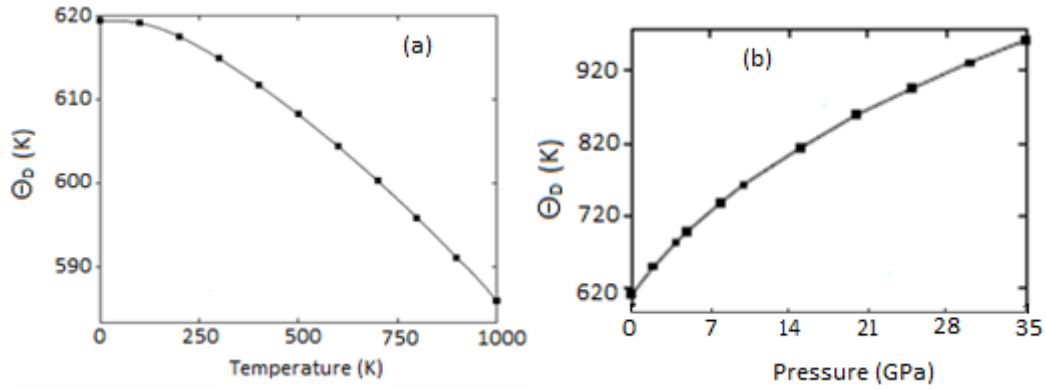

Figure 2: The temperature and pressure dependence of Debye temperature Θ_D at P = 0 GPa (a) , at 300 K (b).

The thermal effect on the heat capacities C_V, C_P of Li_3P are shown in Fig. 3 (a, b). at high temperatures ($T > \Theta_D$), the anharmonic effect on C_V is suppressed and C_V is a constant $3R$ (R is the universal gas constant), which is in accordance with the law of Dulong and Petit limit of $C_V = 3nNk_B = 99.74$ J/mol.K. In this temperature range, maximum frequency lattice waves are populated and the energy difference is less than the heat kinetic energy kT. The energy difference can be ignored in order to classical statistical theory. At sufficiently low temperature (T < 200 K) , C_V is proportional to $(T/\Theta_D)^3$. This is because only the long wavelength vibration modes of the lattice are populated and these modes could be approximated by treating the lattice as a continuum. For a given temperature, C_V decreases with increasing pressure. The difference between C_P and C_V is given by $C_P - C_V = \alpha^2(T)\, BTV$, which is due to the thermal expansion caused by anharmonicity effects. These results show the fact that the interactions between ions in Li_3P have great effect on heat capacities especially at low temperatures. There is no theoretical or experimental value of specific heat capacities of Li_3P for comparison with the present calculated results.

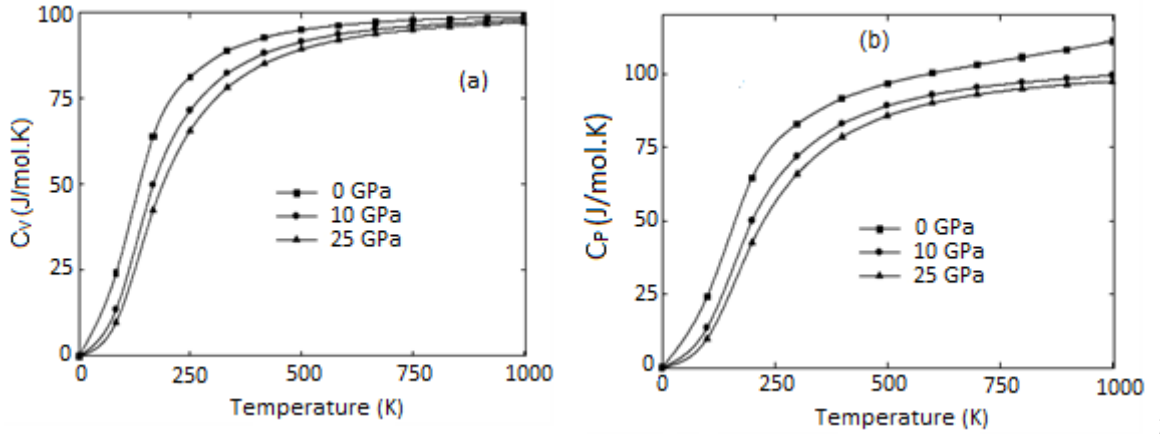

Figure 3: The temperature dependence of specific heat at (a) constant-volume C_V and (b) constant pressure C_P at different pressures 0 GPa, 10 GPa, 25 GPa.

The dependence of the thermal expansion α with the temperature and pressure are shown in Fig. 4. From Fig. 4(a) the thermal expansion coefficient of Li_3P increase as the temperature increase. it can be seen that the thermal expansion coefficient also increases with T^3 at lower temperatures and gradually approaches to a linear increase at higher temperatures. Moreover, the variation of the thermal expansion coefficient with temperature is similar to that of C_V . For Fig. 4(b), it is noted that as the pressure increases, α almost decreases exponentially. This means that there is a large thermal expansion at low pressure which is in accordance with the variation of V/V_0 with pressure.

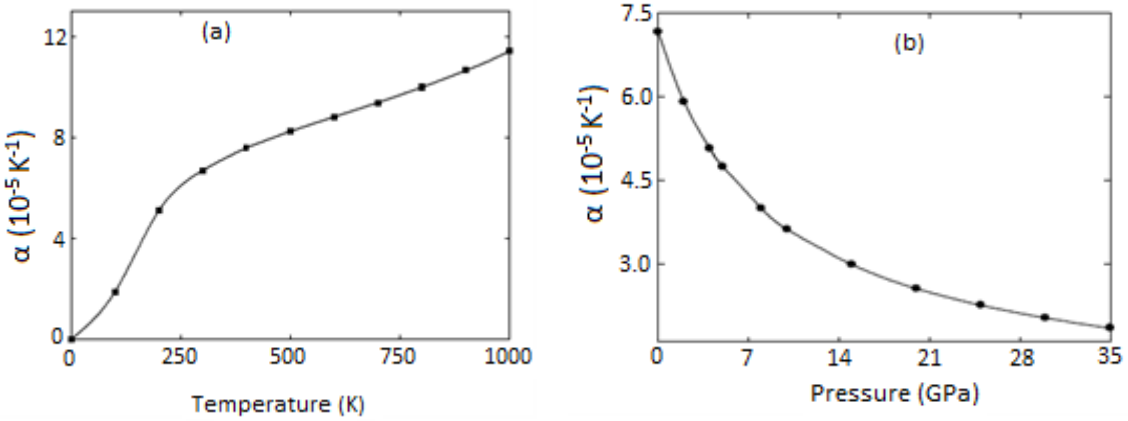

Figure 4: The thermal expansion coefficient α as a function of (a) temperature and (b) pressure at 300K.

4. Conclusion

First-principles calculations based on DFT have been used to study the elastic and the thermodynamic of Li_3P. The material is elastically anisotropic and shows brittle behavior. Through the quasi-harmonic Debye model, the thermodynamic properties, *e.g.* bulk modulus, Debye temperature, specific heats, and thermal expansion coefficient are successfully obtained , which considers the phononic contribution, and the results are analyzed. The variation of the bulk modulus B and the variation of the Debye temperature Θ_D with temperature decrease when the temperature changes from 0 to 1000 K, and increases with increasing pressure. Furthermore, when the temperature is constant, the Debye

temperature Θ increases non-linearly with applied pressures, indicating the change of the vibration frequency of particles under pressure.

Reference

[1] JULIEN C.and NAZRI G. A. , Solid State Batteries,Materials Design and Optimization (Kluwer Academic Publishers,1994).

[2] NAZRI G. , Solid State Ionics 34, 97 (1989

[3] SUZUKI S. , FUJITA H., ASAMI Y., HOMMA F. and SATO Y., New Mat. New Process 3, 264 (1985).

[4] HARVEY P. E. , In: Proc. 4th International Meeting on Lithium Batteries, Vancouver, B.C.Canada, May 24-27, 1988.

[5] Mat. Res. Soc. Symp. Proc. Vol. 135 (1989) Materials Research Society for Discussion of glassy electrolytes.

[6] NAZRI G. A. , CONELL R. A., and JULIEN C., Solid State Ionics 86-87 (Part 1), 99 (1996).

[7] NAZRI G. , Mater. Res. Soc. Symp. Pruc. 135, 117 (1989).

[8] PERDEW J.P., CHEVARY J.A., VOSKO S.H., JACKSON K.A., PEDERSON M.R., SINGH D.J., FIOLHAIS C. , Phys. Rev. B 46 (1992) 6671–6687.

[9] SEGALL M.D. , LINDAN P.J.D., PROBERT M.J., PICKARD C.J. , HASNIP P.J. , CLARK S.J. , PAYNE M.C., J. Phys.: Condens. Matter 14 (2002) 2717–2744.

[10] VANDERBILT D. , Phys. Rev. B 41, 7892 (1990).

[11] MONKHORST H.J., Pack J.D., Phys. Rev. B 13 (1976) 5188–5192.

[12] PFROMMER B.G. , COTE´ M. , LOUIE S.G., COHEN M.L., J. Comp. Physiol. 131 (1997) 233–240.

[13] FAST L., WILLS J.M., JOHANSSON B., ERIKSSON O. , Phys. Rev. B 51 (1995) 17431–17438.

[14] PERDEW J.P., BURKE K., Ernzerhof M., Phys. Rev. Lett. 77, 3865 (1996).

[15] FRANCISCO E., RECIO J.M., BLANCO M.A., MARTÍN--PENDÁS A., COSTALES A., J. Phys. Chem. 102, 1595 (1998).

[16] BLANCO M. A., FRANCISCO E., and LUAÑA V., Comput. Phys. Comm. 158, 57 (2004).

[17] POIRIER J. P. and TARANTOLA A., Phys. Earth Planet Int. 109 (1998) 1.

[18] DONG Y., and DISALVO F. J., Acta Cryst. E 63, i97 (2007).

[19] WALLACE D. C., Thermodynamics of Crystals (Wiley, New York, 1972).

[20] PETTIFOR D.. Mater. Sci. Technol. 8, 345 (1992).

[21] PUGH S. F., Philos. Mag. 45, 823 (1954).

[22] KANCHANA V. and S. RAM S., Intermetallics 23, 39 (2012).

[23] ZENER C. M., Elasticity, Anelasticity of metals (University of Chicago Press, Chicago, 1948).

[24] BIRCH F., J. Geophy. Res. 83, 1257 (1978).

Kinetics analysis of large ceramic samples using isothermal thermogravimetry

Ján Ondruška, Igor Štubňa

Department of physics, Constantine the Philosopher University in Nitra, A. Hlinku 1, 949 74 Nitra, Slovakia, e-mail: jondruska@ukf.sk

Abstract: *In the paper the dehydroxylation of large ceramic samples with two different diameters, 80 mm and 100 mm, is investigated under the isothermal conditions at 540 °C, 580 °C, and 650 °C by the thermogravimetric analysis. The kinetic parameters, activation energy, and frequency factor are evaluated from a series of thermogravimetric experimets. The activation energy and frequency factor of dehydroxylation were determined as 106 kJ mol–1 and 115 s–1 for ∅80 mm sample and 98 kJ mol–1 and 36 s–1 for ∅100 mm sample.*

Keywords: *Kaolinite, Isothermal kinetics, Dehydroxylation, TGA, Large samples*

1. Introduction

Green ceramic mixtures during heating change their physical and mechanical properties [1, 2, 3]. The first process which can be observed is the liberation of physically bonded water in the temperature region ~100 – 250 °C [2]. Another process which results in a weight loss in kaolinite crystals is called dehydroxylation. This process starts at the temperature ~450 °C and finishes at the temperature ~700 °C and is connected with the phase transformation of kaolinite into metakaolinite [1, 4]. At the end of a firing process, at ~950 °C, one can observe a reaction connected with the metakaolinite-to-spinel phase transformation [5, 6]. All these processes are connected with changes in kaolinite.

Kaolinite is an important raw material for the ceramic technology. The kaolinite structure consists of tetrahedral SiO_4 and octahedral $AlO_2(OH)_4$ layers [7]. The distance between two such layers is about 0.72 nm [8]. Dehydroxylation of kaolinite can be split into two separate processes: one is water release and the destruction of kaolinite structure and the other is the recombination of alumina and silica to the metakaolinite structure [9].

The dehydroxylation kinetics of kaolinite under isothermal conditions is mostly described by the JMAYK (Johanson-Mehl-Avrami-Yerofeyev-Kolgomorov) equation (see Eq. (1) below) with the exponent n equal to 1. This corresponds to F_1 nucleation-growth mechanism [8]. The JMAYK equation is given as

$$\alpha = 1 - \exp[-(kt)^n], \tag{1}$$

where k is the overall rate constant, t is time, and α is the transformed phase fraction (conversion coefficient). The index n, which depends on the shape of nuclei and on the dimensionality of their growth, as well as on the rate of nuclei formation, is usually known as Avrami's exponent [10].

The aim of the present paper is the determination of the pertinent kinetic parameters of kaolinite on the basis of thermogravimetric experimets in large samples.

2. Samples and Methods

The samples were prepared from a dry ceramic mixture by an isostatic pressing process by the electroceramic plant PPC Čab, Slovakia. The initial composition of samples contained 30 wt. % of kaoline, 25 wt. % of alumina, 30 wt. % of feldspar, and 15 wt. % of refractory grog. The samples have a cylindrical shape with two different diameters (80 mm and 100 mm) and a length 200 mm.

For the thermogravimetry measurements the apparatus described in [11] was used. First, the samples were preheated at temperature 400 °C for one hour to stabilize the temperature in the whole volume of samples. The main measurement was performed in the dehydroxylation interval. Isothermal heatings at 540 °C, 580 °C, and 650 °C for 6 hours were used. The isothermal temperatures were reached from 400 °C by a linear heating with a heating rate 3 °C/min.

The weight loss in isothermal curves was recalculated to the conversion coefficient α defined by the expression

$$\alpha = \frac{m_t}{m_0}, \tag{2}$$

where m_t is the weight loss after time t and m_0 is the total weight loss after complete dehydroxylation.

According to the reaction theory, the kinetic equation for decomposition of solid matter is usually written as [12]

$$\frac{d\alpha}{dt} = k(1-\alpha)^n, \tag{3}$$

where $k = A \cdot \exp(-E_A/RT)$ is the reaction rate constatnt, A is the frequency factor, E_A is the activation energy, R is the gas constant, T is the temperature, and n is the reaction order.

Assuming that dehydroxylation is the first-order reaction [13], the rate equation can be written as

$$\frac{d\alpha}{dt} = A \cdot e^{-E_A/RT}(1-\alpha). \tag{4}$$

Separation of variables and integration leads to

$$\ln(1-\alpha) = kt\,. \tag{5}$$

For the first order kinetics a plot of ln (1 – α) vs. t will yield a slope equal to $-k$. The determination of the activation energy and frequency factor is based on the logarithmic form of the Arrhenius law via plotting ln k vs. T^{-1} (see Eq. (6) below). The slope of this dependence is equal to $-E_A/R$. The intercept with the y-axis in the Arrhenius plot is equal to the equation term ln A [8].

$$\ln k = \ln A - \frac{E_A}{R}\frac{1}{T} \tag{6}$$

3. Results and Discussions

The isothermal thermogravimetric analysis was performed at temperatures 540, 580, and 650 °C. Under isothermal conditions, the temperature decreases the dehydroxylation time to reach the same extent of conversion (see Fig. 1). Due to the samples dimensions, a certain time is needed when the temperature homogeneity between the surface and the center of the sample is reached [14]. Temperature homogeneity for an isothermal heating for the sample with a diameter 80 mm was reached at 540 °C in 40 minutes, at 580 °C in 80 minutes, and at 650 °C in 55 minutes. For samples with a diameter 100 mm the temperature homogeneity was reached at 540 °C in 55 minutes, at 580 °C in 95 minutes, and at 650 °C in 70 minutes. The time t = 0 in Fig. 1 is the time when the temperature of the isothermal heating in the center of the sample was reached.

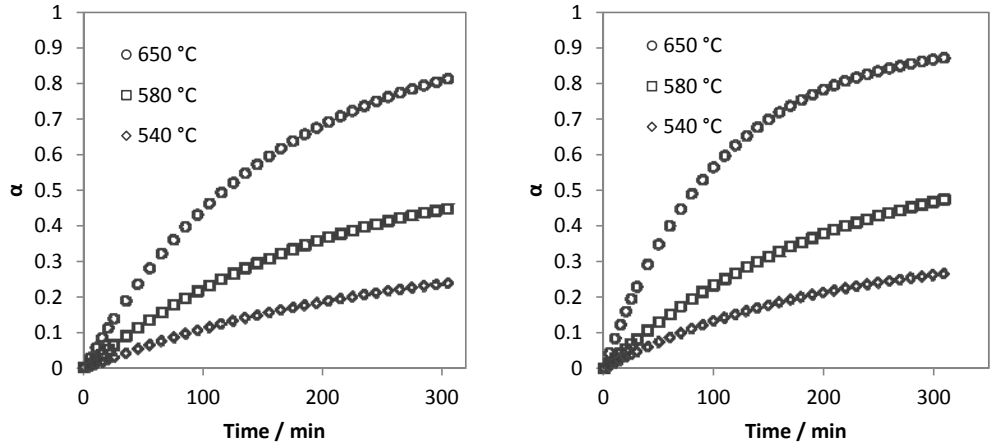

(a) (b)

Fig 1. Conversion coefficient α vs. time for samples with the diameter (a) 100 mm and (b) 80 mm

For the evaluation of the rate constant k, the experimental data of the isothermal heating were regressed linearly by Eq. (4). The results are shown in Fig. 2. The values of rate constants k and correlation coefficients R^2 are given in Table 1. The correlation coefficient of each curve exceeds 0.94, in most cases it is over 0.97. This is in good agreement with the F_1 nucleation-growth mechanism.

Table 1. The results of the isothermal analysis form Fig. 2

	100 mm diameter		80 mm diameter	
Temperature / °C	Rate constant k	Correlation coefficient R^2	Rate constant k	Correlation coefficient R^2
540	1.65×10^{-5}	0.976	1.85×10^{-5}	0.943
580	3.60×10^{-5}	0.976	3.73×10^{-5}	0.975
650	9.48×10^{-5}	0.998	1.19×10^{-4}	0.978

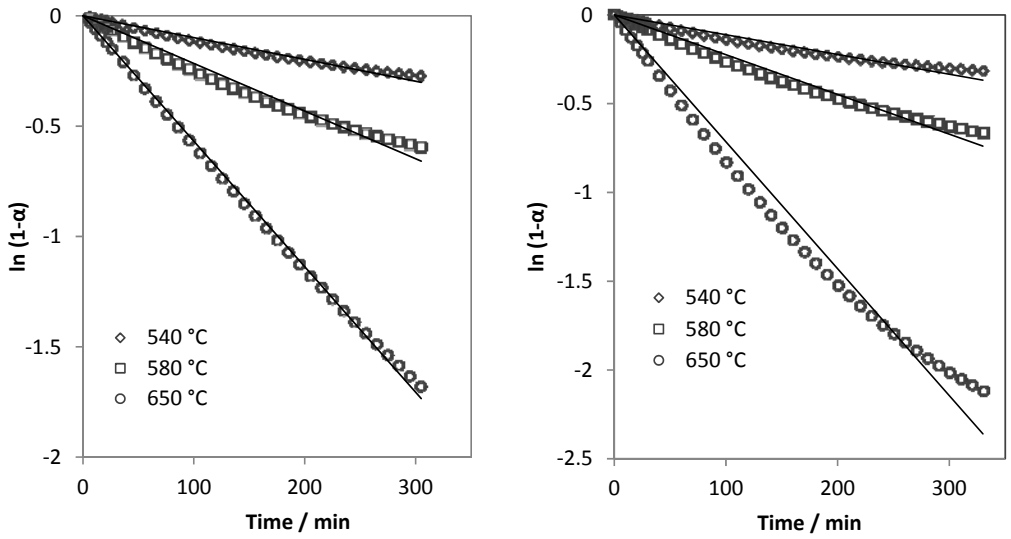

Fig 2. The ln(1 – α) vs. time at different isothermal conditions for samples with the diameter (a) 100 mm and (b) 80 mm

The activation energy and frequency factor were determined by the slope and intercept using the linear regression of ln k vs. T^{-1} plot (see Fig. 3). For 80 mm samples the activation energy of 106 kJ mol^{-1} and the frequency factor of 115 s^{-1} were obtained. For 100 mm samples the activation energy of 98 kJ mol^{-1} and the frequency factor of 36 s^{-1} were obtained.

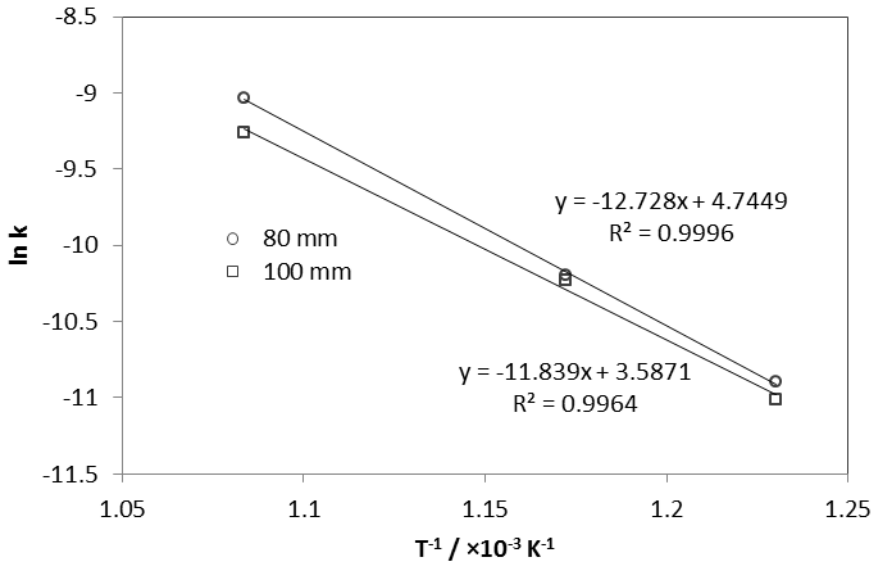

Fig. 3 The ln k vs. T^{-1} plot for samples with a 80 mm and 100 mm diameter

The most frequently published values of the activation energies and frequency factors are placed within the interval from 140 to 250 kJ mol^{-1} and from 10^8 to 10^{14} s^{-1}, respectively [8, 13, 15, 16]. The activation energy and frequency factor depend on the rate of reaction (see Eq. (3)). The lower the reaction rate, the lower the activation energy and frequency factor were obtained. The reaction rate in this contribution is lower than in [8, 13, 15]. A lower rate of

dehydroxylation is due to the samples dimensions. In large samples the temperature field is not homogenous during heating. The dehydroxylation starts on the surface of the sample and spreads towards its center [14]. During an isothermal heating a time to homogenize the temperature in the sample is needed. During this time the dehydroxylation in outer layers of the sample occurs.

4. Conclusions

The dehydroxylation of large ceramic samples with two different diameters 80 mm and 100 mm was studied by the thermogravimetric analysis under the isothermal conditions at 540 °C, 580 °C, and 650 °C. Using the F_1 nucleation-growth mechanism, the kinetic parameters, i.e., the activation energy (E_A) and frequency factor (A), were evaluated from the thermogravimetric experiments. They were determined to be 106 kJ mol^{-1} and 115 s^{-1} for ∅80 mm samples and 98 kJ mol^{-1} and 36 s^{-1} for ∅100 mm samples.

Acknowledgement

This work was supported by grants UGA VI/38/2013, VEGA 1/0646/12, VEGA 1/0869/13 and by cooperation of electro-porcelain plant PPC Čab, Slovakia, a member of the international PPC Insulators group.

References

[1] BRINDLEY, G. W.; SHARP, J. H.; PATTERSON, J. H.; NARAHARI, B. N. Kinetics and mechanism of dehydroxylation process, I. temperature and vapor pressure dependence on dehydroxylation of kaolinite. In *The American Mineralogist*. 1967.52(N1-2). p.201-211

[2] KOZÍK, T. et al. The temperature dependence of the electric conductivity of unfired porcelain mixture. In Ceramics – Silikáty. 1992.36. p. 69-72

[3] KOZÍK, T.; ŠTUBŇA, I. Mechanical strength of the ceramic material in the dehydroxylation temperature region. In Silikáty. 1981.25. p. 237-241

[4] ČÍČEL, B.; NOVÁK, I.; HORVÁTH, I. Mineralogy and crystalochemistry of clays. SAV Bratislava, 1981

[5] ŽIVANOVIČ, B.; JANOVIČ, O. Dehydroxylation of kaolinite. In Hem. Ind. 1978.32(N8). p.512-516

[6] POPPE, L.; GABOR, M.; WAJAND, J.; SZABÓ, Z. Two-step dehydroxylation of the kaolinite. In Proc. 1st Symp. Thermal Anal. Salford 1976, p.332-335

[7] VARGA, G.; TRNÍK, A. The structure of kaolinite and metakaolinite. In *Épitönayag*, 59, 2007, p. 6-9

[8] PTÁČEK, P.; KUBATOVA, D.; HAVLICA, J.; BRANDŠTETR, J.; ŠOUKAL, F.; OPRAVIL, T. Isothermal kinetic analysis of the thermal decomposition of kaolinite: The thermogravimetric study, In *Thermochimica Acta* 501 (2010) p. 24–29

[9] HEIDE, K.; FOLDVARI, M. High temperature mass spectrometric gas-release studies of kaolinite $Al_2[Si_2O_5(OH)_4]$ decomposition, In *Thermochimica Acta* 446 (2006) p. 106–112

[10] FARJAS, J.; ROURA, P. Modification of the Kolmogorov–Johnson–Mehl–Avrani rate equation for non-isothermal experiments and its analytical solution, In *Acta Materialia* 54 (2006) p. 5573–5579

[11] ONDRUŠKA, J.; MEDVEĎ, I.; SLÁVIKOVÁ, J. Termogravimetrická analýza veľkých keramických vzoriek In: *30. Mezinárodní český a slovenský kalorimetrický seminář*, 2008, Univerzita Pardubice, p. 93 – 96

[12] XIA YONGJIANG, XUE HUAQING, WANG HONGYAN, LI ZHIPING, FANG CHAOHE, Kinetics of isothermal and non-isothermal pyrolysis of oil shale, In Oil Shale, 2011, Vol. 28, No. 3, p. 415–424

[13] SAIKIA, N.; SENGUPTA, P.; GOGOI, P.K.; BORTHAKUR, P.CH. Kinetics of dehydroxylation of kaolin in presence of oil field effluent treatment plant sludge, In *Applied Clay Science* 22 (2002) 93–102.

[14] ONDRUŠKA, J.; TRNÍK, A.; VOZÁR, L.; Degree of Conversion of Dehydroxylation in a Large Electroceramic Body, In *International Journal of Thermophysics*. Vol. 32, no. 3 (2011), p. 729-735. ISSN 0195-928X

[15] NAHDI, K.; LLEWELLYN, P.; ROUQUEROL, F.; ROUQUEROL, J.; ARIGUIB, N.K.;. AYEDI, M.T. Controlled rate thermal analysis of kaolinite dehydroxylation: effect of water vapour pressure on the mechanism, In *Thermochimica Acta* 390 (2002) p. 123–132.

[16] LEVY, J.H.; HURST, H.J. Kinetics of dehydroxylation, in nitrogen and water vapour, of kaolinite and smectite from Australian Tertiary oil shales, In: *Fuel* 72 (1993) p. 873–877.

Theoretical formulas for approximation of sorption isotherms of chosen building materials

Zbyšek Pavlík[1], Igor Medveď[1], Jaromír Žumár[1], Milena Pavlíková[1], Robert Černý[1]

[1] Department of Materials Engineering and Chemistry, Faculty of Civil Engineering, Czech Technical University in Prague, 166 29 Prague, Czech Republic
e-mail: zbysek.pavlik@fsv.cvut.cz

Abstract: *Experimental measurement of water vapour sorption isotherms of three chosen building materials is done using dynamic vapour sorption device. Three popular theoretical models of moisture adsorption are applied for approximation of particular measured data. On the basis of performed computational and experimental analysis, new semi-empirical formula is proposed and its validity verified. The formulated combined formula is found to provide the best approximation of experimental data.*

Keywords: *water vapour adsorption, building materials, Brunauer–Emmett–Teller isotherm, Brunauer–Skalny–Bodor isotherm, Frenkel–Halsey–Hill isotherm, combined adsorption model, dynamic vapour sorption device.*

1. Introduction

The possible water ingress into the porous building materials is defined by materials hygric transport and storage properties, whereas the total water transfer is divided into liquid and gaseous (water vapour) phase of water. In this paper we focused on water vapour storage in building materials that is usually characterized by sorption isotherms.

Sorption isotherm describes the thermodynamic relationship between relative humidity of materials environment and its equilibrium moisture content at constant temperature and pressure. Some authors, especially in food products research, use instead of relative humidity the water activity concept [1, 2]. They introduce water activity of material equal to the relative humidity of the air divided by 100. Water adsorption is process in which water molecules progressively and partially reversibly mix with the solid constituents of porous materials via chemisorption, physical adsorption (evoked by van der Waals type forces), and multilayer condensation. The sorption isotherms are in case of building materials almost exclusively of type II, according to original work introduced by Brunauer at al. [3], i.e., with an S-shape [4].

Although many empirical and theoretical equations have been used along the years to describe moisture isotherms of different porous materials and their dependence with temperature [5, 6] none of these equations can be claimed as the ‘‘universal’’ equation to describe sorption data. On this account, three popular theoretical models of moisture sorption are tested in this paper for approximation of experimentally measured sorption isotherms of three typical building materials. On the basis of performed analysis, new semi-empirical formula is proposed and its validity verified.

2. Theoretical Formulas of Adsorption Isotherms

The Brunauer–Emmett–Teller (BET) isotherm expresses the surface concentration, C_s, by the equation [3]

$$C_s = \frac{c\theta}{(1-\theta)[1+(c-1)\theta]} C_s^{sat} \tag{1}$$

Where C_s^{sat} is the saturation surface concentration. The relative humidity θ in the pores is equal to the ratio of the bulk concentration in the pores to the bulk saturation concentration, C/C_{sat}. In chemistry, θ is usually called the coverage. The two parameters of the BET isotherm to be fitted are $c > 0$ (called the BET constant) and C_{sat}.

The Brunauer–Skalny–Bodor (BSB) isotherm (often called the three-parameter BET isotherm) is given as [7]

$$C_s = \frac{ck\theta}{(1-k\theta)[1+(c-1)k\theta]} C_s^{sat} \tag{2}$$

Here, k is the third fitting parameter and its value must be less than 1. Formally, the difference between isotherms (1) and (2) is the replacement of θ by $k\theta$.

Assuming a dependence of the adsorption potential on the distance from the surface, the Frenkel–Halsey–Hill (FHH) isotherm was proposed [8, 9]

$$C_s = \left(\frac{K}{\ln\theta}\right)^{1/\sigma} C_s^{sat} \tag{3}$$

The two fitting parameters of this isotherm are a positive coefficient K and a positive exponent σ, while the value of C_s^{sat} can be determined from the BET (or other similar) isotherm applied in a low θ regime. The exponent σ is connected to the character of the interaction between the adsorbate and the adsorbent surface, namely, σ represents the decay of surface forces with the adsorbate–adsorbent distance [10].

3. Experimental

3.1 Studied Materials

Sorption isotherms were measured for three typical porous building materials, namely lime-cement mortar (LCM), hardened gypsum and calcium silicate. The basic physical properties of researched materials are summarized in Table 1.

Table 1: Basic properties of studied materials

Material	Bulk density (kg/m³)	Matrix density (kg/m³)	Total open porosity (%)
LCM	1 545	2 625	43
Gypsum	516	2 183	76
Calcium silicite	260	2 262	89

The cement-lime mortar was produced at our laboratory. The gypsum material was product of the company Gypstrend Ltd., Czech Republic. Its official product label is MS 86. Calcium silicate was produced by Calsitherm Ltd., Germany. It is capillary active material originally developed for interior thermal insulation systems.

3.2 Measurement of Sorption Isotherms

The measurement of moisture sorption isotherms usually relies on the static gravimetric method using thermally stabilized desiccators filled with saturated salt solutions. Although this method is still commonly employed, automated humidity generating instruments have been introduced to the market for the continuous determination of sorption isotherms in a dynamic system.

In this paper, DVS-Advantage device (Surface Measurement Systems Ltd.) was used for the sorption isotherms measurement. The Dynamic Vapour Sorption (DVS) method is designed to measure the equilibrium moisture content of a material at any desired relative humidity and selected temperatures in a short period of time. The humidity range of the applied DVS instrument is 0–98% with the accuracy ±0.5%, whereas the experiments can be realized at temperature range 5-60°C. Before the measurements, samples of the studied materials were dried at first in a vacuum drier and then, during the cooling, they were kept in desiccators. After drying, the similar experimental procedure as presented in [10] proceeded. The particular samples were put into the climatic chamber of the DVS-Advantage instrument and hung on the automatic balances in a special steel tube. The experiments were performed at 25°C. The samples were exposed to the following partial pressure profile: 0; 10; 20; 30; 40; 50; 60; 70; 80; 90; and 98% relative humidity. During the experiments, the DVS-Advantage instrument was running in the dm/dt mode (the mass variation over the time variation) to decide when the equilibrium was reached. A fixed dm/dt value of 0.00004%/min was selected for all relative humidity segments.

4. Results and Discussion

Figs. 1-3 show experimentally measured adsorption isotherms for the three studied materials, together with their fits using the theoretical models described above.

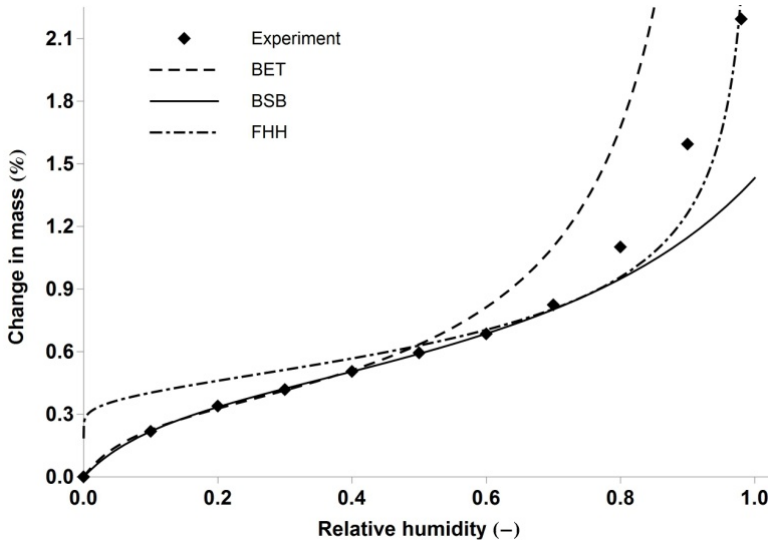

Fig. 1 Fitting of experimental data for lime-cement mortar

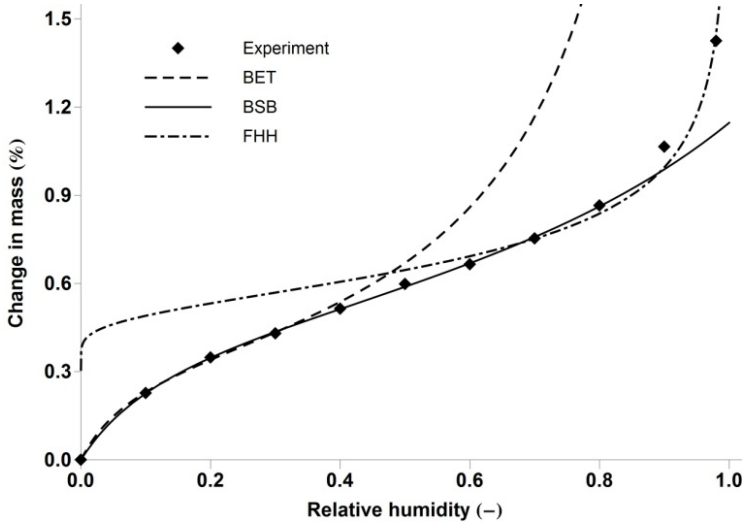

Fig. 2 Fitting of experimental data for gypsum

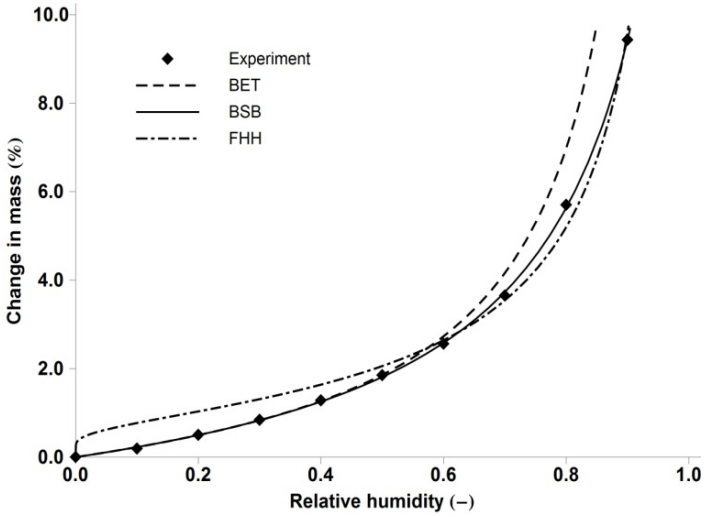

Fig. 3 Fitting of experimental data for calcium silicate

The maximal mass of adsorbed water vapour ranged from 1.4% kg/kg for gypsum to 9.8% kg/kg for calcium silicate. High water vapour adsorption exhibited also lime cement mortar.

The values of the obtained fitting parameters are given in Table 2. They were calculated from the regression analysis by finding least-squares fits to the experimental data, assuming that the data is independently and normally distributed with a common standard deviation. Here, the relative errors in % are given in the parentheses.

At low relative humidities θ, the most accurate theoretical fits resulted for the BSB isotherm. Indeed, Table 2 shows that its R2 are closest to 1 and the relative errors of the BSB fitting parameters are the smallest. Moreover, looking at Figs. 1-3, we observe that the BSB isotherm provides a very good approximation of the experimental data for θ up to 0.6–0.7 for all studied materials. For gypsum and calcium silicate it is well applicable even up to $\theta \approx 0.8$. On the similar behaviour we reported already in [10] and it clearly demonstrates the validity of the BSB isotherms for porous building materials in the presented relative humidity range. The BET isotherm was applicable for low relative humidity values, typically up to $\theta \approx 0.4$ only. As expected from the generally accepted range of applicability of the FHH equation, the latter turned out to be a very good approximation of the experimental isotherms for θ above 0.7 for all investigated materials.

Table 2: The parameters of theoretical formulas obtained at the fitting of experimental data

		LCM	Calcium silicate	Gypsum
BET	c	13.2 (13.2)	1.24 (8.7)	12.1 (12.2)
	C_s^{sat}	0.34 (2.5)	1.68 (4.6)	0.36 (3.0)
	R^2	0.99960	0.99973	0.99975
BSB	c	11.0 (4.8)	1.12 (9.8)	11.9 (4.9)
	C_s^{sat}	0.45 (3.5)	2.05 (5.7)	0.50 (2.7)
	k	0.70 (3.7)	0.91 (0.8)	0.59 (2.5)
	R^2	0.99995	0.99989	0.99993
FHH	K	1.73 (29.0)	0.70 (13.2)	2.13 (22.7)
	σ	2.70 (9.0)	1.22 (5.7)	4.35 (6.9)
	R^2	0.980073	0.996787	0.998199

Since the BSB isotherm was found the most accurate at low relative humidities and the FHH isotherm was very accurate at high relative humidities, a proper combination of these two isotherms was supposed to provide a very accurate approximation of experimental data for all values of relative humidity. This combination we presented in [10] and can be formally written as

$$C_s^{BSB+FHH} = \frac{C_s^{FHH} + C_s^{BSB}}{2} + \frac{C_s^{FHH} - C_s^{BSB}}{2} f(\theta) \tag{4}$$

where C_s^{BSB} and C_s^{FHH} are the surface concentrations obtained for the BSB and FHH isotherms, respectively, and $f(\theta)$ is a suitable function that smoothly interpolates between −1 and 1 and rapidly changes from −1 to 1 as θ crosses a value θ_0, separating the low and high humidity regimes.

We approximated $f(\theta)$ in Eq. (4) by the function $\tanh[b(\theta - \theta 0)]$ that changes within the interval $[\theta 0 - 3/b, \theta 0 + 3/b]$ of length $6/b$ from −0.995 to 0.995. The values of b and θ_0 given at Table 3 were obtained for each of the studied materials as follows.

Table 3: The parameters of Combined model obtained at the fitting of experimental data

		CLM	Calcium silicate	Gypsum
BSB+FHH	b	50.7	21.8	24.9
	θ_0	0.732	0.756	0.778

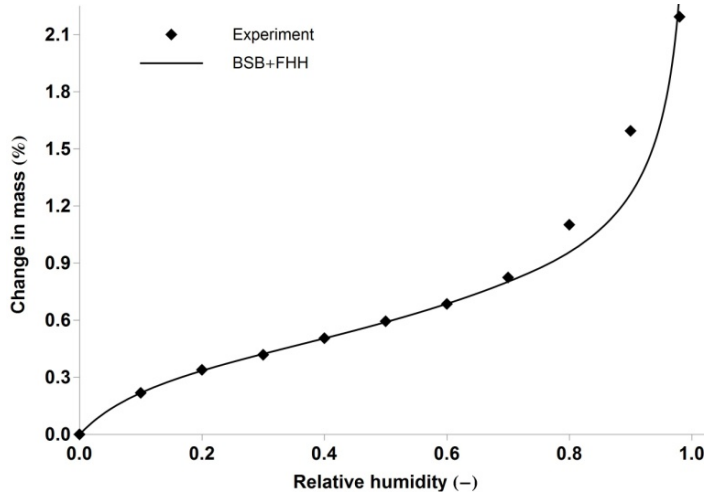

Fig. 4 Fit of experimental data for lime-cement mortar using combination of BSB and FHH formulas

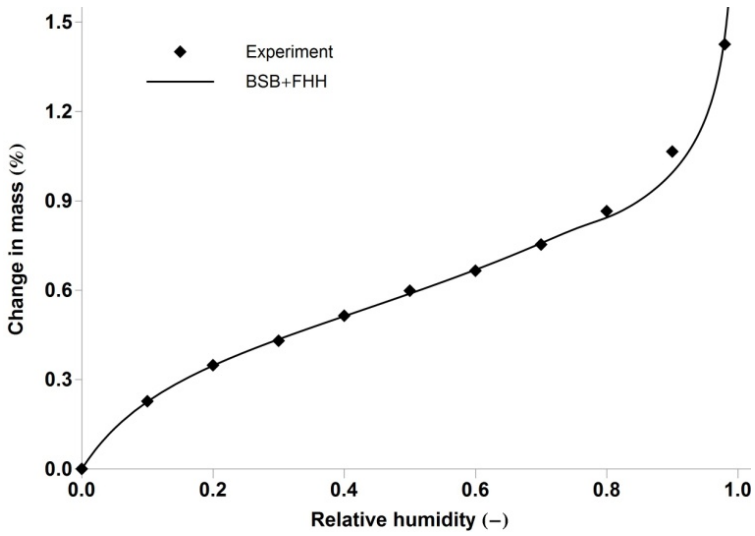

Fig. 5 Fit of experimental data for gypsum using combination of BSB and FHH formulas

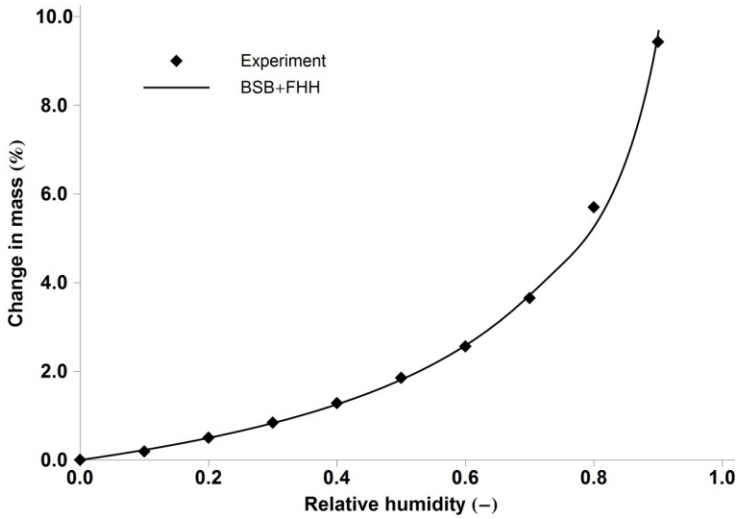

Fig. 6 Fit of experimental data for calcium silicate using combination of BSB and FHH formulas

We determined the smallest (largest) relative humidity θ_1 (θ_2) at which the difference $\left[C_s^{BSB}(\theta) - C_s^{FHH}(\theta)\right]$ is equal to 1/100 of the experimental value of the mass change measured at the relative humidity θ = 0.5. Identifying the interval [θ_1, θ_2] with the interval [$\theta 0 - 3/b$, $\theta 0 + 3/b$], the values $\theta_0 = (\theta_1+\theta_2)/2$ and $b = 6/(\theta_2-\theta_1)$ were determined. Thus, resulting combined isotherms $C_s^{BSB+FHH}$, Eq. (4), were plotted against the experimental data in separate plots, giving an excellent approximation for all studied materials and all relative humidities (see Figs. 4-6).

5. Conclusions

Experimental and theoretical analysis of water vapour adsorption in porous structure of typical building materials was presented in the paper. The obtained results showed that the shape of the measured adsorption isotherms at low relative humidities, up to about 0.6 (for some materials even up to 0.7), corresponded to the BSB isotherm and at relative humidities higher than 0.7 to the FHH isotherm. The combined BSB-FHH formula applied for characterization of sorption process of porous building materials can find use in computational modelling of coupled moisture and heat transport in building materials and structures. It can be also used for the estimation of the water vapour adsorption behaviour of building materials, where the experimental measurements are not available. However, one must take into account that the analysis presented in this paper and in [10] was performed for ten typical building materials only. Therefore, for the universal applicability of the formulated equation of water vapour adsorption, further experiments and calculations must be done.

Acknowledgments

This research has been supported by the by the Ministry of Education, Youth and Sport of the Czech Republic, under projects No SGS14/174/OHK1/3T/11 and No 7AMB14SK087.

References

[1] ANDRADE, R. D. P. – LEMUS, R. M. – PEREZ, C. E. C. Models of sorption isotherms for food: uses and limitations. In *Vitae, revista de la facultad de química farmacéutica*. 2011. 18. p. 325-334. ISSN 0121-4004.

[2] RAJI, A. O. – OJEDIRAN, J. O. Moisture sorption isotherms of two varieties of millet. In *Food Bioprod. Proces.* 2011. 89. p. 178-184. ISSN: 0960-3085.

[3] BRUNAER, S. – EMMET, P. H. – TELLER, W. E. Adsorption of gases in multimolecular layers. In *Journal of the American Chemical Society*. 1938. 60. p. 309–319.

[4] HANSEN, K. K. Sorption Isotherms-A Catalogue. *Technical report,* 162/86, TU Denmark, Lyngby. 1986.

[5] BRUNAUER, S. – SKALNY, J. – BODOR, E. E. Adsorption on Nonporous Solids. In *Journal of Colloid Interface and Science.* 1969. 30. p. 546–552.

[6] BLAHOVEC, J. – YQNNIOTIS, S. Modified classification of sorption isotherms. In *Journal of Food Engineering*. 2009. 91. p. 72–77. ISSN: 0260-8774.

[7] FURMANIAK, S. – TERZYK, A. P. – GOLEMBIEVSKI, R. – GAUDEN, P. A. – CZEPIRSKI, L. Searching the most optimal model of water sorption on foodstuffs in the whole range of relative humidity. In *Food Research International*. 2009. 42. p. 1203–1214. ISSN: 0963-9969.

[8] HILL, T. L. Thermodynamics of adsorption. In *Transactions of the Faraday Society*. 1951. 47. p. 376–380.

[9] HALSEY, G. Physical adsorption on non-uniform surfaces. In *Journal of Chemical Physics.* 1948. 16. p. 931–937.

[10] PAVLÍK, Z. – ŽUMÁR, J. – MEDVEĎ, I. – ČERNÝ, R. Water vapor adsorption in porous building materials: experimental measurement and theoretical analysis. In *Transport in Porous Media.* 2012. 91 (3). p. 939-954. ISSN: 0169-3913.

Mathematical modeling of processes proceeding in concrete during fire

Petra Rozehnalová[1], Anna Kučerová[1], Petr Štěpánek[1]

[1]Faculty of Civil Engineering, Brno University of Technology, Veveří 331/95
CZ-602 00 Brno, Czech Republic

Abstract: *Paper aims to describe and model processes in concrete during fire. Concrete is porous material, which contains water and moisture. Water in concrete is: a) in pores (from production and from outer environment), b) chemically bounded. Higher temperature releases chemically bounded water into the pores, which increases pore pressure. Increased pressure may lead to service failures. Amount of moisture in the pore structure is essential for the reliability and stability of building constructions.*

Mathematical model of this phenomenon consists of nonlinear non-stationary system of partial differential equations accompanied by the boundary conditions. From the equations a numerical scheme is derived. The numerical results are compared with data from experiment.

Keywords: *Concrete, fire simulation, finite element method.*

1. Introduction

Behavior of concrete exposed to the fire plays crucial role in the assessment of the reliability of concrete structure. There exist several mathematical models that aim to predict and simulate such a behavior. One of the first models was developed by Bažant and Thonguthai. Its improved version is described in [1] or in [2]. Another model was formulated by Majorana and Gawin [9] or by Dwaikat and Kodur [4]. These models differ in its complexity.

In the paper we introduced mathematical model which is derived from the Bažant's model [1]. Our model belongs to the simpler ones because the only one phase (free water) is assumed. But as it is shown in the end of the paper, computational results closely correspond to the experimental ones.

The paper is organized as follows. In Section 2 the physical phenomenon is described, in Section 3 mathematical model is presented and there is described time and spatial discretization. Section 4 is devoted to the computational and experimental results.

2. Physical phenomena

Concrete is noncombustible material with low thermal conductivity. Although concrete does not contribute to fire load of the structures, significant changes occur in its structure during a fire exposure. Besides reduction of mechanical, deformation and material properties also chemical composition of concrete is varied during heating [1].

Concrete, as a porous material, contains a large amount of pores, which can be filled fully (saturated concrete) or just partially with water. The water occurred in the pores is evaporable water and starts to evaporate at early beginning of the fire. The first changes of concrete structure arise at 105°C as stated in [8], when chemically bounded water is released from cement gel to the pores. Some small micro-cracks start to appear as the capillary

porosity arises. The peak of the dehydration process is reached around 270°C. The color of concrete is changed and a slight decrease of strength, modulus of elasticity and changes in material properties like thermal conductivity can be noted. Temperature of 300°C is the extreme temperature beside which the concrete structure is irreversibly damaged [7]. In range of 400°C-600°C calcium hydroxide decomposes into calcium oxide plus water (rise of amount of free water) and transition of α and β quartz, accompanied by increase in its volume, induces another creation of severe cracks in concrete.

Not only high temperature can affect adversely the load bearing capacity of concrete structures. Simultaneously with a temperature profile should be investigated also the change of mass of free water (mostly vapor) across a concrete member during fire and distributions of pore pressure. The pore pressure is one of the main reasons of concrete spalling (Figure 1), which happens at the beginning of heating (10 – 30 minutes) and is accidental. Small or grater (1 m wide and 1 m long) areas of concrete cover can be broken and cross section of the member is reduced then. Furthermore in most cases the reinforcement is exposed directly to the fire after spalling and the member is heated faster, which can lead to the total loss of loadbearing capacity of the structure.

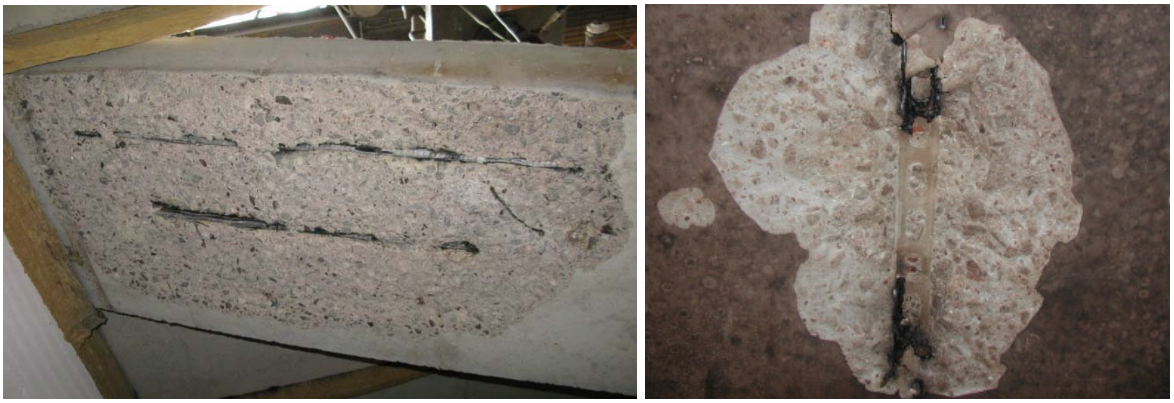

Figure 1: Areal (left) and local (right) spalling of concrete.

3. Mathematical model

In the following, we introduce mathematical model, which aims to simulate behavior described in the Section 2.

3.1 Notation and formulation of the model

In the model, vectors and vector functions are denoted by bold letters.

Let us consider $\mathbf{x} = (x_1, x_2) \in \Omega$, where Ω is a simple domain in $\mathbb{R}^2$ and let Γ be its boundary, which consist of two non-intersecting parts: Γ_N and Γ_R and it holds $\overline{\Gamma}_N \cup \overline{\Gamma}_R = \Gamma$. The part Γ_R represents pies of the boundary, which is exposed to the fire and Γ_N denotes the part exposed to the atmosphere. By $\boldsymbol{n}$ we denote outer unit normal vector of the boundary Γ. By $t \geq 0$ it is denoted time.

In the model there are three unknowns: $T = T(\mathbf{x}, t)$ temperature [°C], $w = w(\mathbf{x}, t)$ mass of all free water [kg m^{-3}] and $P = P(\mathbf{x}, t)$ pore pressure [Pa].

Furthermore, there occur several known physical quantities and constants: $C_c = C_c(T)$ specific heat of concrete [J kg^{-1} °C^{-1}], $\rho_c = \rho_c(T)$ density of concrete [kg m^{-3}], C_w specific heat of water [J kg^{-1} °C^{-1}], ΔH_{deh} enthalpy of dehydration [J kg^{-1}], $\Delta H_{\text{evap}} = \Delta H_{\text{evap}}(T)$ enthalpy of evaporation [J kg^{-1}], g gravity constant [m s^{-2}], $\mu = \mu(T, P)$ permeability of concrete [m s^{-1}], $\lambda = \lambda(T)$ thermal conductivity of concrete [W m^{-1} °C^{-1}], $e = 0.7$ emissivity of concrete [-], $\sigma = 5.67 \cdot 10^{-8}$ Stefan- Boltzmann constant [W m^{-2} K^{-4}], $\alpha = \alpha(\boldsymbol{x})$ heat transfer coefficient [W m^{-2} °C^{-1}], $\beta = \beta(\boldsymbol{x})$ coefficient of moisture transfer through the boundary [s m^{-1}].

Empirical function $m_{\text{deh}} = m_{\text{deh}}(T)$ specified in [6], represents the mass of water, which was dehydrated [kg m^{-3}]. At temperature above 100 °C, the function m_{deh} is increasing (i.e. the higher temperature the bigger amount of dehydrated water).

Model consists of two differential equations, derived from conservation law of water content and energy, accompanied by state equation. The outer conditions and the state of the system at $t = 0$ are described by the boundary and initial conditions. P_∞ denotes outer pressure, T_∞ temperature of the environment and $T_{\text{en}} = T_{\text{en}}(t)$ temperature caused by fire. We used T_{en} given by the ISO curve [4].

Now, we can formulate the model:

Conservation of water content:

$$\frac{\partial w}{\partial t} + \operatorname{div} \cdot \boldsymbol{J} = \frac{\partial m_{\text{deh}}}{\partial t}, \quad \text{in } \Omega \times (0, \infty). \tag{1}$$

Conservation of energy:

$$\rho_c C_c \frac{\partial T}{\partial t} + \operatorname{div} \cdot \boldsymbol{q} = C_w \boldsymbol{J} \cdot \operatorname{grad} T - \Delta H_{\text{deh}} \frac{\partial m_{\text{deh}}}{\partial t} + \Delta H_{\text{evap}} \frac{\partial w}{\partial t}, \quad \text{in } \Omega \times (0, \infty). \tag{2}$$

State equation:

$$w = \Phi(P, T), \quad \text{in } \Omega \times (0, \infty). \tag{3}$$

Boundary conditions:

$$\boldsymbol{q} \cdot \boldsymbol{n} = \alpha(T - T_\infty), \quad \text{in } \Gamma_N \times (0, \infty), \tag{4}$$

$$\boldsymbol{q} \cdot \boldsymbol{n} = \alpha(T - T_\infty) + e\sigma(T^4 - T_{\text{en}}^4), \quad \text{in } \Gamma_R \times (0, \infty), \tag{5}$$

$$\boldsymbol{J} \cdot \boldsymbol{n} = \beta(P - P_\infty), \quad \text{in } \Gamma \times (0, \infty). \tag{6}$$

Initial conditions:

$$P(\boldsymbol{x}, 0) = P_0, \quad \text{for } \boldsymbol{x} \in \Omega, \tag{7}$$

$$T(\boldsymbol{x}, 0) = T_0, \quad \text{for } \boldsymbol{x} \in \Omega. \tag{8}$$

In the relations above, $\mathbf{q}$ represents heat flux and is governed by Fourier law and $\mathbf{J}$ denotes flux of moisture in concrete and is proportional to the gradient of pressure, i.e.

$$\boldsymbol{q} = -\lambda \operatorname{grad} T, \quad \boldsymbol{J} = -\frac{\mu}{g} \operatorname{grad} P. \tag{9}$$

Function $\Phi = \Phi(P,T)$ is empirical and can be found in [3], page 530.

3.2 Numerical scheme

Let $0 < t_1 < t_2 \ldots < t_N$ be an equidistant partitioning of the interval $\langle 0, t_N \rangle$ with step Δt. Let n be such that $0 \le n \le N$. In the following numerical scheme we abbreviate $f(t_n)$ by f_n for any function f.

The semi-implicit difference scheme of the continuous model (1)-(8) (after incorporating (9)) is:

$$\frac{w_{n+1} - w_n}{\Delta t} - \nabla \cdot \left(\frac{\mu(T_n, P_n)}{g} \nabla P_{n+1} \right) = \frac{m_{\text{deh}}(T_{n+1}) - m_{\text{deh}}(T_n)}{\Delta t} \ , \tag{10}$$

$$\begin{aligned} &\rho_c C_c(T_n) \frac{T_{n+1} - T_n}{\Delta t} - \nabla \cdot \left(\lambda(T_n) \nabla T_{n+1} \right) = \\ &- C_w \frac{\mu(T_n, P_n)}{g} \nabla P_n \cdot \nabla T_n - \Delta H_{\text{deh}} \frac{m_{\text{deh}}(T_{n+1}) - m_{\text{deh}}(T_n)}{\Delta t} + \Delta H_{\text{evap}}(T_n) \frac{w_{n+1} - w_n}{\Delta t}, \end{aligned} \tag{11}$$

$$w_{n+1} = \Phi(P_{n+1}, T_{n+1}) \ . \tag{12}$$

The functions P_n, T_n, w_n are considered to be known.

For fixed n, (10) and (11) represent stationary partial differential equations. These equations are solved by finite element method on square conforming uniform mesh with bilinear basis and test functions. Integrals which occur in finite element method are computed by Gaussian quadrature.

Finite element method transform the equations (10) and (11) to the system of nonlinear equations. This system is solved by Newton method with residual tolerance 10^{-8}.

4. Results

4.1 Numerical results

Let us present results of our model problem. The set Ω is a rectangle 50 mm x 100 mm. Γ_R is left and upper side of the Ω and so Γ_N is right and lower side.

The data of model was set as follows: $C_w = 4180$ J kg^{-1} °C^{-1}, $\Delta H_{\text{deh}} = 2.44 \cdot 10^6$ J kg^{-1}, $g = 9.81$ m s^{-2}, $\alpha = 25$ W m^{-2} °C^{-1} on Γ_R and $\alpha = 4$ W m^{-2} °C^{-1} on Γ_N, $\beta = 20 \cdot 10^{-9}$ s m^{-1} on Γ_R and $\beta = 10 \cdot 10^{-9}$ s m^{-1} on Γ_N, $P_\infty = P_0 = 1330$ Pa, $T_\infty = T_0 = 25$ °C.

Thermal conductivity of concrete is given in [5]. $\lambda(T) = \frac{\lambda_{\text{up}} + \lambda_{\text{low}}}{2}$, where

$$\lambda_{\text{up}}(T) = 2 - 0.2451 \cdot \frac{T}{100} + 0.0107 \cdot \left(\frac{T}{100} \right)^2 , \tag{13}$$

$$\lambda_{\text{low}}(T) = 1.36 - 0.136 \cdot \frac{T}{100} + 0.0057 \cdot \left(\frac{T}{100}\right)^2 . \tag{14}$$

Following [5], density of concrete is:

$$\rho_c(T) = \begin{cases} 2500 & \text{for } 20\,°\text{C} \le \text{T} \le 115°\text{C}, \\ 2500 \cdot \left(1 - 0.02 \cdot \frac{T-115}{85}\right) & \text{for } 115\,°\text{C} \le \text{T} \le 200°\text{C}, \\ 2500 \cdot \left(0.98 - 0.03 \cdot \frac{T-200}{200}\right) & \text{for } 200\,°\text{C} \le \text{T} \le 400°\text{C}, \\ 2500 \cdot \left(0.98 - 0.07 \cdot \frac{T-400}{800}\right) & \text{for } 400\,°\text{C} \le \text{T} \le 1200°\text{C}. \end{cases} \tag{15}$$

Specific heat of concrete is given by (cf. [5]):

$$C_c(T) = \begin{cases} 900 & \text{for } 20\,°\text{C} \le \text{T} \le 100°\text{C}, \\ 900 + (T - 100) & \text{for } 100\,°\text{C} \le \text{T} \le 200°\text{C}, \\ 1000 - \frac{T-200}{2} & \text{for } 200\,°\text{C} \le \text{T} \le 400°\text{C}, \\ 1100 & \text{for } 400\,°\text{C} \le \text{T} \le 1200°\text{C}. \end{cases} \tag{16}$$

Permeability $\mu = \mu(T, P)$ can be found in [1] Enthalpy of evaporation is given as [9]:

$$\Delta H_{\text{evap}}(T) = 2.672 \cdot 10^5 (374.15 - T)^{0.38} \quad \text{for } \text{T} \le 400\,°\text{C} \ . \tag{17}$$

Results of the model are on the Figure 2.

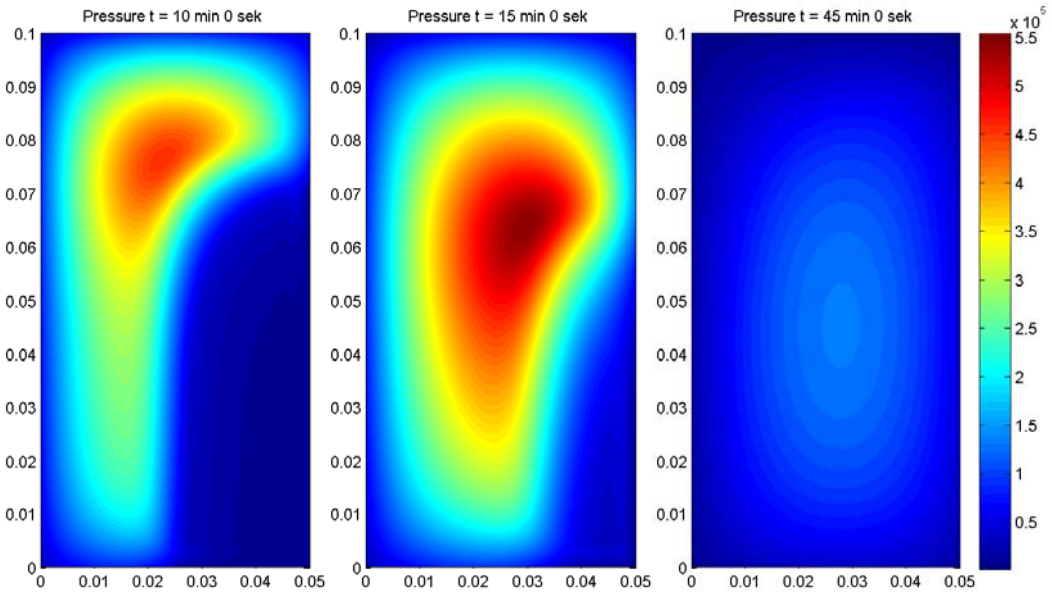

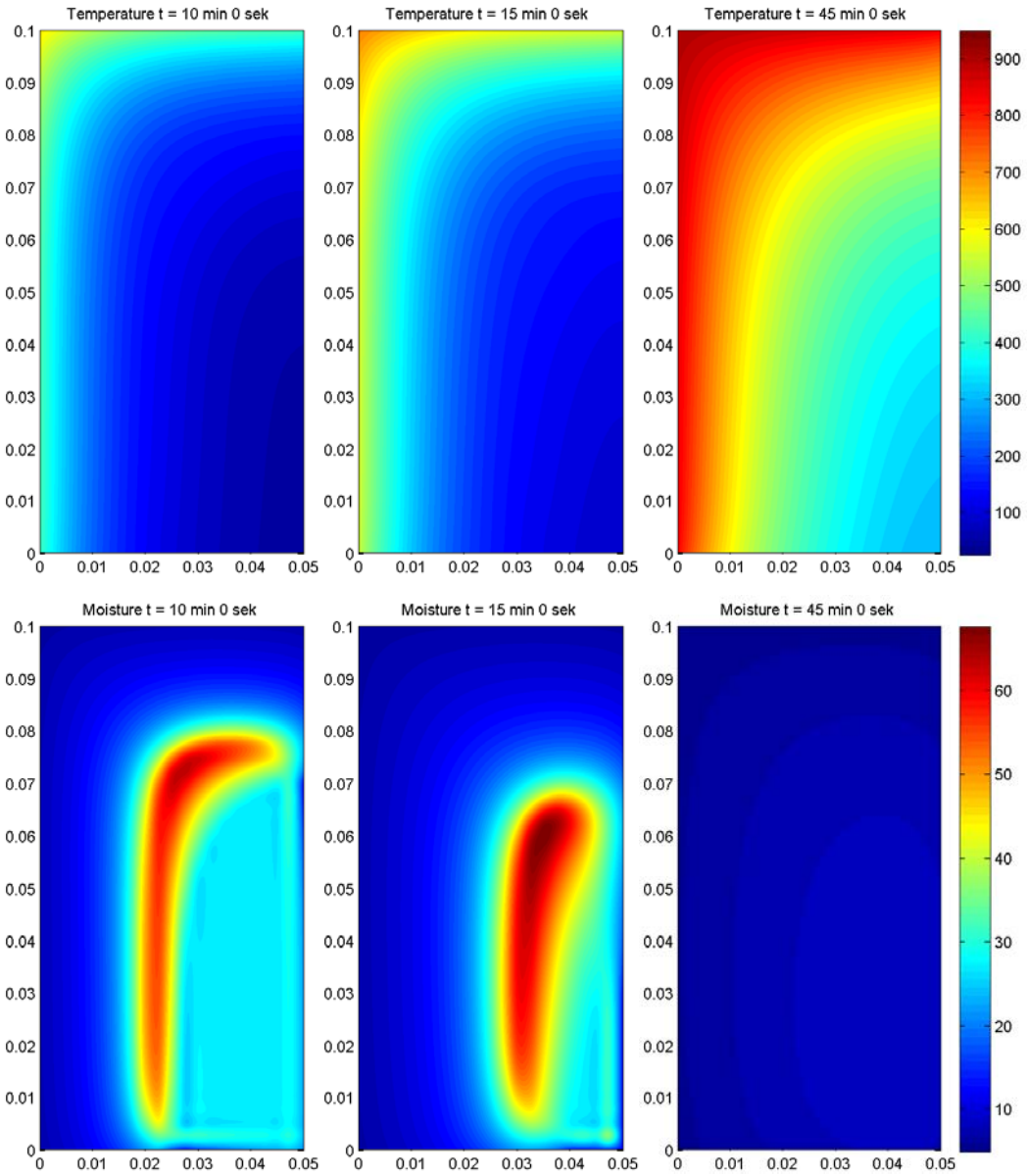

Figure 2: Pressure, temperature and moisture distribution after 10, 15, 45 min of fire.

4.2 Experimental results

The team of researchers from Brno University of Technology, Faculty of Civil Engineering completed fire load bearing test at laboratory in Veselí nad Lužnicí in September 2012. A main aim of the experiment was to investigate load bearing capacity of panels loaded by concentrated force in the middle of the panel during fire exposure. The panels were 3.6 m long, 0.5 m wide, 0.15 m thick and were reinforced with 3 FRP bars of diameter 14 mm. The applied fire load was following standard fire curve ISO 834. Accept gauges necessary for measurement of deflections and tensions of the panels, there were installed temperatures sensors inside the panels at the distance of 30 mm, 50 mm and 70 mm from exposed surface. The experimental test is on the Figure 3.

Figure 3: Load bearing test before start of fire.

The comparison of the experimental test and a numerical simulation is presented on the Figure 4. Time of fire exposure during the test was around 50 minutes. After this period one of the panel collapsed and the experiment was interrupted. The mathematical model presented above was used for a numerical simulation. The numerical simulation was done for cross section of 0.15 x 0.5 m at three aforementioned points with cover 30 mm, 50 mm and 70 mm and with material properties similar to tested concrete panels.

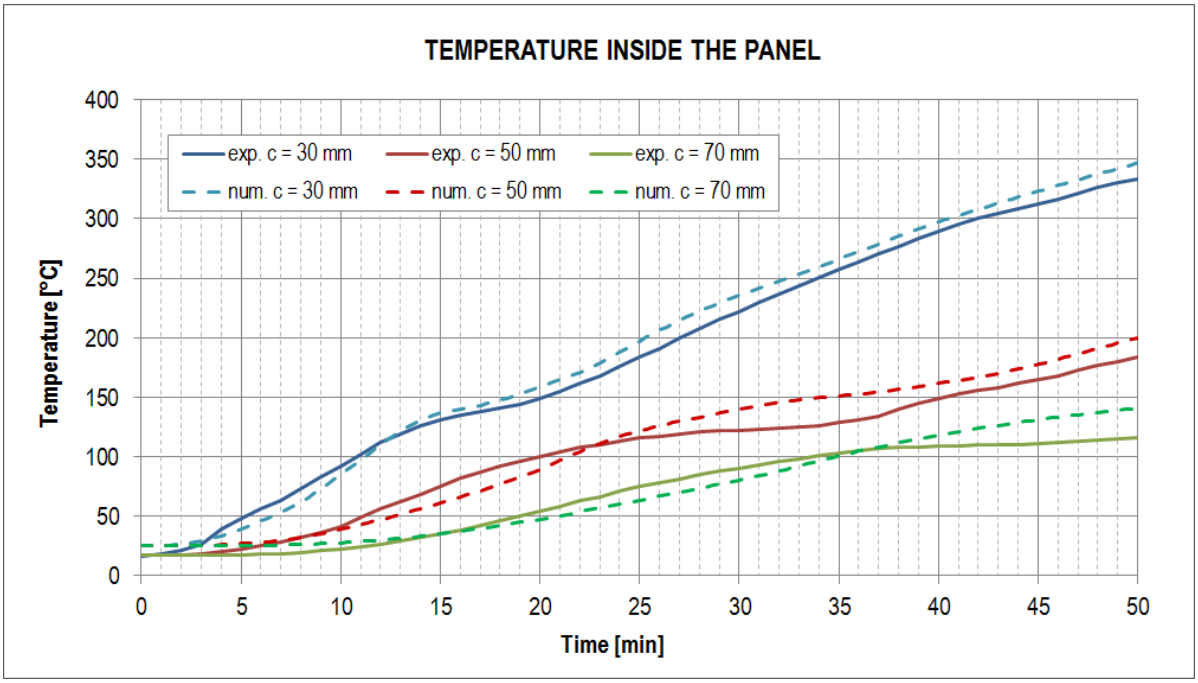

Figure 4: Dependence of temperature inside the panels on time of fire exposure at different depths for experimental test and numerical simulation.

The experimental data have close similarity to the numerical results. It can be said, that presented model has sufficient accuracy and could be used for assessment of the temperature profile, pore pressure and amount of free water in concrete cross section, which are necessary when calculated the load bearing capacity of the concrete member.

Acknowledgments

This research was supported by Brno University of Technology, Specific Research project no. FAST-J-14-2362.

References

[1] BAŽANT, Z. P. – KAPLAN, M.F. *Concrete at High Temperatures*: *Material Properties and Mathematical Models,* Concrete design and construction series. Longman Group Limited, Harlow, 1996, pp. 412, ISBN 0-582-08626-4.

[2] BENEŠ, M. – ŠTEFAN, R. – ZEMAN, J. Analysis of coupled transport phenomena in concrete at elevated temperatures. In *Applied Mathematics and Computation*. 2013. 219(13). p. 7262–7274. ISSN 0096-3003.

[3] ČERNÝ, R. – ROVNANÍKOVÁ, P. *Transport processes in concrete,* Spon Press, London, 2002, pp. 537, ISBN 0-415-24264-94.

[4] ČSN EN 1991-1-2 (730035) *Eurokód 1: Zatížení konstrukcí – Část 1-2: Obecná zatížení – Zatížení konstrukcí vystavených účinkům požáru.* Český normalizační institut, Praha, 2004, p. 56.

[5] ČSN EN 1992-1-2 (731201) *Eurokód 2: Navrhování betonových konstrukcí – Část 1-2: Obecná pravidla – Navrhování konstrukcí na účinky požáru.* Český normalizační institut, Praha, 2006, p. 26.

[6] DWAIKAT, M. B. – KODUR, V. K. R. Hydrothermal model for predicting fire-induced spalling in concrete structural systems. In *Fire Safety Journal.* 2009. 44(3). p. 425-434.

[7] HERTZ, K. *Analyses of Concrete Structures Exposed to Fire,* Department of Buildings and Energy, Technical University of Denmark, 1999, pp. 92.

[8] INGHAM, J.P. Application of petrographic examination techniques to the assessment of fire-damage concrete and masonry structures. In *Materials Characterization.* 2009. 60(7). p. 700-709. ISSN 1044-5803.

[9] MAJORANA, C. E. – GAWIN, D. – PESAVENTO, F. – SCHREFLER, B. A. Computational structures technology. In *Concrete Structures Subject to High Temperature*. Civil-Comp press, Edinburgh. 2002. p. 63–91. ISBN 1-874672-16-4.

[10] MORAN, M. J. – SHAPIRO, H. N. – BOETTNER, D. D. – BAILEY, M. *Fundamentals of engineering thermodynamics,* John Wiley & Sons, 2010, pp. 944, ISBN 0470-49590-1.

Thermal and optical properties of Cd1-xZnxSe semiconductor from photoacoustic measurement

B. K. Sarkar[1*], G. Pavlendova[2], I. BANIK[2], Deviprasadh PS[3]

[1]Department of Physics, Galgotias University, Greater Noida 201308, India

[2]Department of Physics, Faculty of CE, Slovak University of Technology, Radlinského 11, 813 68 Bratislava, Slovak Republic

[3]Department of Physics, CMS College of Engineering & Technology, Coimbatore 641032, India

Email: bks@physics.org.in

Abstract: *Diluted magnetic semiconductor $Cd_{1-x}Zn_xSe$ is used in a wide spectrum of optoelectronic devices, photovoltaic solar cells, laser screen materials and various luminescence devices, etc. This compound is important due to variation of its electronic and optical properties by changing the Cd:Zn ratio. In this paper we have reported the composition dependent absorption coefficient (α), thermal diffusivity (σ) and optical band gap (E_0) of $Cd_{1-x}Zn_xSe$ diluted magnetic semiconductor (DMS). For higher Zn composition the absorption spectrum of the $Cd_{1-x}Zn_xSe$ system consists of three regions viz. high absorption region, the exponential region and the weak absorption tail. The band gap follows a nonlinear variation with composition. The absorption spectra show that the transition is allowed and direct.*

Keywords: *Diluted magnetic semiconductor, thermal properties, optical properties, $Cd_{1-x}Zn_xSe$, photoacoustic spectroscopy.*

1. Introduction

In the recent years, II-VI semiconductors have drawn substantial due to their potential applications in a large extent starting from light emitting diodes [1,2], solar cells [3,4], displays [5,6], photovoltaic cells [7,8] to luminescence biological tags [9,10]. For example, many optoelectronic devices in the blue to near- ultraviolet spectral region are manufactured with the mixed II-VI ternary compounds [9-11]. Many X-ray, γ-ray detectors are prepared based on II-VI materials [12, 13]. It is well known that ZnSe and CdSe as member of II-VI semiconductors are used in green semiconductors lasers due to their direct and large band gap. These two compounds are characterized by their own special crystal structure. ZnSe structure exists in cubic form (zinc blende) [14,15], and CdSe compound exists both in zinc blende and wurtzite (properties of the combination of both CdSe and ZnSe as ternary compound $Cd_{1-x}Zn_xSe$ mixed crystals, theoretically [19,20] as well as experimentally [21,22]. First-principles calculations estimated the optical constants of $Cd_{1-x}Zn_xSe$ [20]. The empirical pseudo-potential method (EPM) is used for the calculation of electronic and optical properties of $Zn_xCd_{1-x}Se$. Experimental work reported the measurement of the optical properties of $Cd_xZn_{1-x}Se$ films grown on GaAs [21]. In the reflection spectroscopy study, the composition (x) dependence of the fundamental gap of $Cd_xZn_{1-x}Se$ has been described [22].

As per literature survey, we could not find thermal properties study of $Cd_xZn_{1-x}Se$. In this paper we have reported the measurement of thermal diffusivity, optical-absorption and energy band gap near the fundamental edge of $Cd_{1-x}Zn_xSe$ ($0 \le x \le 1$) type polycrystalline

alloys. We have used a high resolution photoacoustic spectrometer (PAS) [23] in the visible spectral region.

hexagonal) structures at normal conditions [16-18]. Many reports are found for the study of structural and electronic

2. Experimental

For the preparation of the samples $Cd_{1-x}Zn_xSe$ (x = 0, 0.4, 0.8, 1), CdSe and ZnSe are used as starting materials. The desired amounts of the mixture are ground to powder and pressed into thin pellets. These pellets are sealed in an evacuated quartz tube and placed inside a furnace at about 1400-1500^{0}C for several days. The ampoules were then furnace cooled at room temperature. The samples thus prepared were crystalline in nature, and their composition and structure were tested by X-ray powder diffraction (Phillips: Model PW 1710) studies with CuK_α. The energy dispersive X-ray (EDX) experiment (Kevex: Model 3600-0388, California) confirms the ratio of the constituent atoms within ±2%.

The single beam photoacoustic spectrometer used in the present investigation consists of a PA cell containing the sensitive microphone, a 1000W Xe lamp with a power supply (Muller, type SVX 1000, Germany), a monochromator (Oriel 77250), and a mechanical chopper (SR540). The PA signal is detected by a sensitive microphone (Bruel and Kjaer 4147) and processed by using a preamplifier and a lock-in amplifier (SR530). To minimize light scattering, very thin (~3-4 mm dia and ~0.3 mm thick) samples were used for the PAS studies. All spectra were recorded at room temperature using a chopping frequency of 120 Hz. The optical band gap is determined by measuring the variation of the normalized PA signal intensity with the wavelength of the incident light. The PA spectrum obtained from highly absorbing carbon black powder was used to normalize the spectrum of the samples.

3. Results & Discussions

The normalized PA spectra of $Cd_{1-x}Zn_xSe$ as a function of incident wavelength is shown in figure 1.

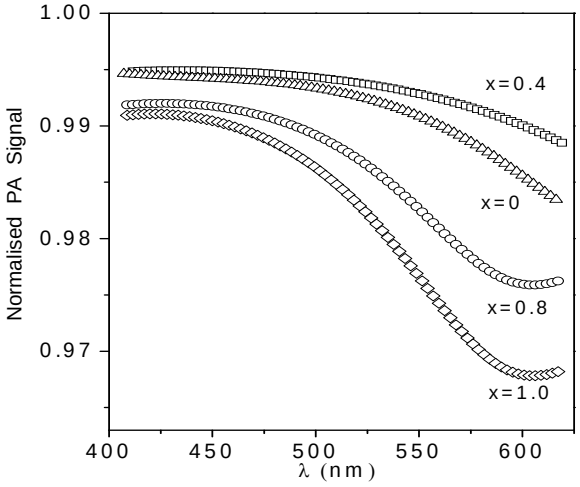

Figure1: Normalized photoacoustic (PA) spectra of $Cd_{1-x}Zn_xSe$ system with x =0.0, 0.4, 0.8 and 1.0. as a function of wavelength of incident light.

The optical absorption coefficient α for thermally thick samples is calculated from the relation [23],

$$\alpha = \frac{q^2 + q\left(2 - q^2\right)^{1/2}}{\mu\left(1 - q^2\right)} \tag{1}$$

where q is the normalized PA amplitude and μ is the thermal diffusion length (~6×10^{-3} cm). The variation of the absorption coefficient of the samples with the incident photon energy is shown in figure 2.

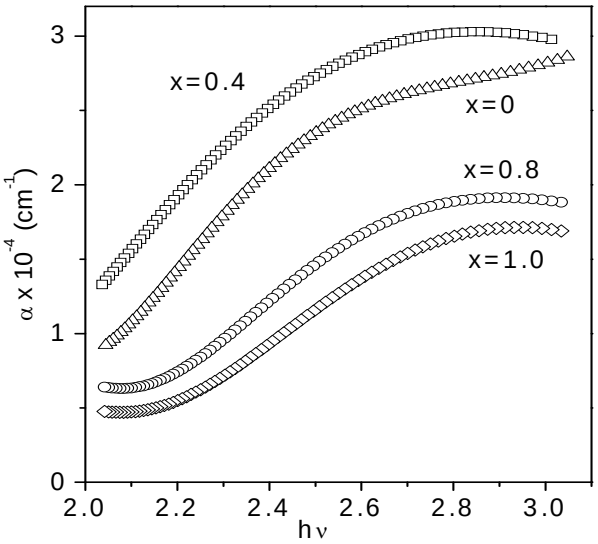

Figure2: Variation of absorption coefficient (α) of $Cd_{1-x}Zn_xSe$ as a function of incident photon energy with x =0.0, 0.4, 0.8 and 1.0. Absorption coefficient is determined using Fig.1 and Equation1.

The absorption spectrum of the $Cd_{1-x}Zn_xSe$ system consists of three distinct regions, viz., the high absorption region [$h\nu > E_0$ ($\alpha > 10^3$ cm^{-1})], the exponential region, and the weak absorption tail. Here *h* is Planck's constant, ν is the frequency of the incident radiation, and E_0 is the band gap. The type of transitions was determined by considering the relation between the absorption coefficient (α) and the photon energy ($h\nu$). They are related as:

$$\alpha h\nu = A\left(h\nu - E_0\right)^n \tag{2}$$

where, A is a constant and n is the transition power factor having values 0.5, 2, 1.5 and 3 for allowed direct, allowed indirect, forbidden direct and forbidden indirect transitions, respectively.

A plot of logarithmic $\alpha h\nu$ versus $h\nu$ (figure 3) determines the value of n for different Zn composition as shown in Table-1.

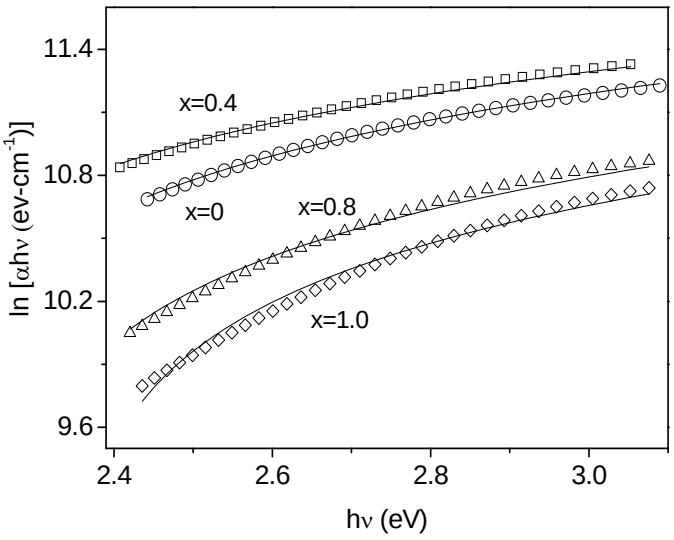

Figure3: Plot of ln(αhν) vs. hν for $Cd_{1-x}Zn_xSe$. Solid lines are theoretical curve fitting taking relation as $\ln(\alpha h\nu) = B + n\ln\left(h\nu - E_0\right)$ *using Eq.(2). Values of n for different Zn compositions are given in Table 1.*

Table 1: Characteristic parameters of the $Cd_{1-x}Zn_xSe$ ($0 \le x \le 1$) alloys

Sample	Transition power factor n (used in Eq. (2))	Thermal diffusivity σ (cm^2/sec)	E_0 (eV)
CdSe	0.467	0.0216	2.281
$Cd_{0.6}Zn_{0.4}Se$	0.503	0.0193	2.238
$Cd_{0.2}Zn_{0.8}Se$	0.492	0.0251	2.372
ZnSe	0.508	0.0256	2.431

For all the samples the value of n is approximately 0.5 which describes the transition as direct in nature in the higher photon energy region. The values of the optical band gap (E_0) are estimated from Eq.(2). It is found that the variation of E_0 with composition (x) is nonlinear in nature as shown in figure 4 obeying the relation, $E_0(x) = 2.276 - 0.209x + 0.376x^2$. The variation is not very sharp, and this might be due to the fact that mixed $Cd_{1-x}Zn_xSe$ crystals crystallize in a zinc-blend structure for x=0.19, and in a mixture of zinc-blend and wurtzite structure for 0.19 <x < 0.3. A variation of band gap with alloy composition in II–VI materials has also been reported in the literature [24]. The variation is consistent with our result.

From the variation of PA signal intensity with modulation chopping frequency, a characteristic frequency (f_C) can be found where a change in slope will occur (figure 4) such that

$$\sigma = f_c l^2 \tag{3}$$

σ is the thermal diffusivity and *l* is the sample thickness [23].

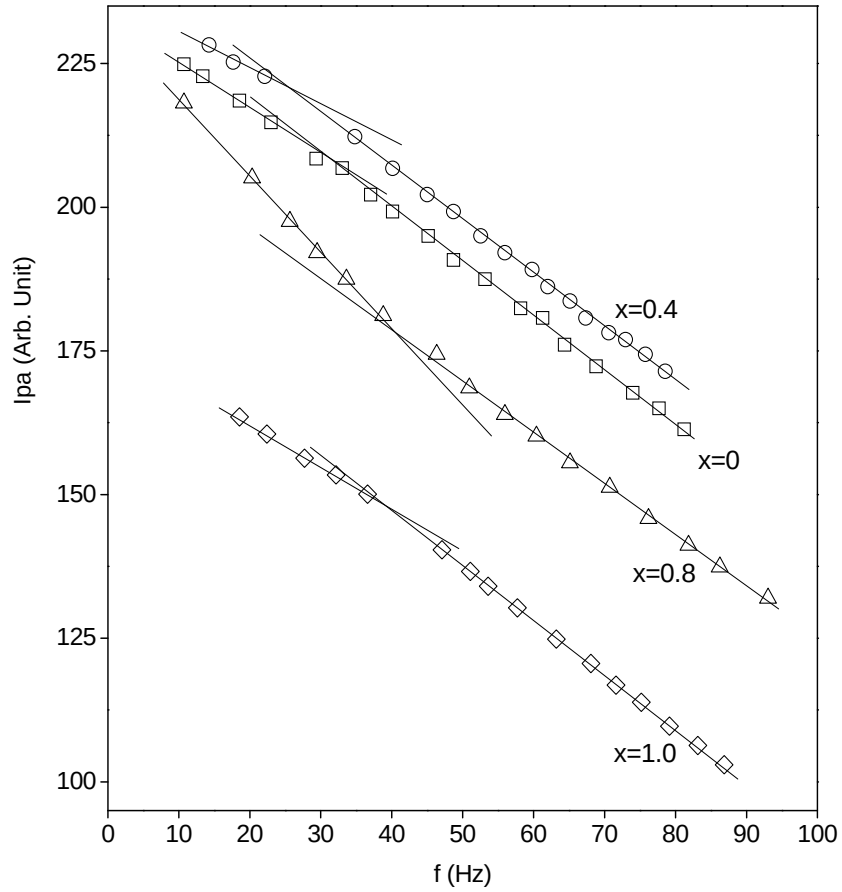

Figure 4: PA signal amplitude (Ipa) versus chopping frequency (f) for different values of x in Zn1-xZnxSe. Characteristic chopping frequency (fC) is determined from the distinct change in slope. fC has the values as 24 Hz, 31 Hz, 40 Hz and 38 Hz for x =0.0, 0.4, 0.8 and 1.0.

Thus the value of the thermal diffusivity (σ) calculated (using Eq.3) is found to vary nonlinearly with concentration (Table I). These values of σ are comparable with those of As-Se-Te (σ ~2×10^{-2} cm^2/sec) [25] and Ge_xTe_{1-x} (σ ~2×10^{-2} cm^2/sec) [26] systems.

4. Conclusion

From the PAS studies of the ternary alloys $Cd_{1-x}Zn_xSe$ we have determined Zn composition dependence of thermal diffusivity, optical absorption coefficient.and band gap. From the optical absorption spectrum the direct band to band transition has been found for high absorption region. The feature of the PAS data enabled us to determine the values of the band gap as a function of Zn composition (x). The dependence of E_0 on x is nonlinear

Acknowledgements

We acknowledge the support provided by Slovak University of Technology. One of the authors (BKS) would like to express his gratitude to Galgotias University for its support. The fourth author (DPS) is thankful to CMS College of Engineering & Technology for its assistance.

References

[1] COE, S. WOO, W.-K. BAWENDI, M. BULOVIC, V. Electroluminescence from Single Monolayers of Nanocrystals in Molecular Organic Devices. In *Nature*. 2002. 420. p. 800-803. ISSN 0028-0836

[2] TESSLER, N. MEDVEDEV, V., KAZES M. KAN S. BANIN U. Efficient Near-Infrared Polymer Nanocrystal Light-Emitting Diodes. In *Science*. 2002. 295. p. 1506-1508. ISSN 0036-8075

[3] GAL, D. HODES, G. HARISKOS, D. BRAUNGER, D. SCHOCK, H.-W. Size-Quantized CdS Films in Thin Film CuInS2 Solar Cells. In *Applied Physics Letters*. 1998. 73. p. 3135-3137. ISSN 1077-3118

[4] HUYNH, W. U. DITTMER, J. J. ALIVISATO, A. P. Hybrid Nanorod-Polymer Solar Cells. In *Science*. 2002. 295. p. 2425-2427. ISSN 0036-8075

[5] COLVIN, V. L. SCHLAMP, M. C. ALIVISATOS, A. P. Light Emitting Diodes Made from Cadmium Selenide Nanocrystals and a Semiconducting Polymer. In *Nature*. 1994. 370. 354-357. ISSN 0028-0836

[6] DABBOUSI, B. O. BAWENDI, M. G. RUBNER, O. O. Electroluminescence from CdSe Quantum-Dot/Polymer Com- posites. *Applied Physics Letters*. 1995. 66. p. 1316-1318. ISSN 1077-3118

[7] O'REGAN, B. GRÄTZEL, M. A LOW-COST, High Efficiency Solar Cell Based on Dye-Sensitized Colloidal TiO2 Films. In *Nature*. 1991. 353. p. 737-740. ISSN 0028-0836

[8] GREENHAM, N. C. PENG, X. ALIVISATOS, A. P. Charge Separation and Transport in Conjugated Polymer/Cad- mium Selenide Nanocrystal Composites Studied by Photoluminescence Quenching and Photoconductivity. In *Synthetic Metals*. 1997. 84. p. 545-546. ISSN: 0379-6779

[9] VAN DE WALLE, C. G. In Wide-Band-Gap Semiconductors. North Holland, Amsterdam. 1993. ISBN 9780444599179

[10] JAISWAL, J. K. MATTOUSSI, H. MAURO, J. M. SIMON, S. M. Long-Term Multiple Color Imaging of Live Cells Using Quantum Dot Bioconjugates. In *Nature Biotechnology*. 2003. 21. p. 47-51. ISSN 1087-0156

[11] JEON, H. DING, J. PATTERSON, W. NURMIKKO, A. V. XIE, W. GRILLO, D. C. KOBAYASHI, M. GUNSHOR, R. L. Blue- Green Injection Laser Diodes in (Zn, Cd)Se/ZnSe Quantum Wells. *Applied Physics Letters*. 1991. 59. p. 3619-3621. ISSN 1077-3118

[12] EISEN. Y. SHOR, A. CdTe and CdZnTe Materials for Room Temperature X-Ray and Gamma Ray Detectors. In *Journal of Crystal Growth*. 1998. 184-185. p. 1302- 1312. ISSN: 0022-0248

[13] HANNACHI, L. BOUARISSA, N. Electronic Structure and Optical Properties of CdSexTe1−x Mixed Crystals. In *Super lattices and Microstructures*. 2008. 44. p. 794-801. ISSN 0749-6036

[14] DURANDURDU, M. Pressure-Induced Phase Transition in Wurtzite ZnS: An *ab Initio* Constant Pressure Study. In *Journal of Physics and Chemistry of Solids*. 2009. 70. p. 645-649. ISSN 0022-3697

[15] CUI, S. HU, H. FENG, W. CHEN, X. FENG, Z. Pressure Induced Phase Transition and Metallization of Solid ZnSe. In *Journal of Alloys and Compounds*. 2009. 472. p. 294-298. ISSN 0925-8388

[16] WRIGHT, K. GALE, J. D. Interatomic Potentials for the Simulation of the Zinc Blende and Wurtzite Forms of ZnS and CdS: Bulk Structure, Properties, and Phase Stability. In *Physical Review B*. 2004. 70. Article ID: 035211. ISSN 1098-0121

[17] WEI, S.-H. ZHANG, S. B. Structure Stability and Carrier Localization in Cd*x* (*x* = S, Se, Te) Semiconductors. In *Physical Review B*. 2000. 62. p. 6944-6947. ISSN 1098-0121

[18] AL-DOURI, Y. The Pressure Effect of the Bulk Modulus Seen by the Charge Density in Cd*x* Compounds. In *Materials Chemistry and Physics*. 2003. 78. p. 625-629. ISSN 0254-0584

[19] BOUAMAMA, K. DJEMIA, P. LEBGA, N. KASSALI, K. *Ab Initio* Calculation of the Elastic Properties and the Lattice Dynamics of the Zn*x*Cd1-*x*Se Alloy. In *Semiconductor Sci-ence and Technology*. 2009. 24. Article ID: 045005. ISSN 1361-6641

[20] BENOSMAN, N. AMRANE, N. AOURAG, H. Calculation of Electronic and Optical Properties of Zinc-Blende Zn*x*Cd1-*x*Se. In *Physica B*. 2000. 275. p. 316- 327. ISSN 1098-0121

[21] KIM, Y. D. KLEIN, M. V. REN, S. F. CHANG, Y. C. LUO, H. SAMARTH, N. FURDYNA, J. K. Optical Properties of Zinc Blende CdSe and Zn*x*Cd1-*x*Se Films Grown on GaAs. In *Physical Review B*. 1994. 49 p. 7262-7270. ISSN 1098-0121

[22] SNYDER, D. W. KO, E. I. SIDES, P. J. MAHAJAN, S. Growth of CdTe by organometallic vapor phase epitaxy in an impinging jet reactor. In *Applied Physics Letters*. 1990. 56. p. 1166-1168. ISSN 1077-3118

[23] SARKAR, B. K. CHAUDHURI, B. K. International Journal of Thermophysics, **26** (2005) 295. ISSN 0195-928X

[24] EBINA, A. YAMAMOTO, M. TAKAHASHI, T. In Phys. Rev. B. 1972. 6. p. 3786-3791. ISSN 1098-0121

[25] NANDAKUMAR, K. PHILIP. In Journal of Non-Crystaline Solids. 1992. 144. p. 247-252. ISSN. 0022-3093

[26] de LIMA, J. C. CELLA, N. MIRANDA, L. C. M. CHYING AN, C. FRANZAN, A. H. LEITE, N. F. Physical Review B. 1992. 46. p. 14186-14189. ISSN 1098-0121

Mechanical properties of alumina porcelain after firing

Peter Šín[1], Anton Trník[2, 3], Rudolf Podoba[1, 4], Igor Štubňa[3]

[1]Department of Physics, Faculty of Civil Engineering, Slovak University of Technology, 81368 Bratislava, Slovakia

[2]Department of Engineering and Chemistry, Czech Technical University, Thákurova 7, 16629 Prague, Czech Republic.

[3]Department of Physics, Faculty of Natural Sciences, Constantine of Philosopher University, 94974 Nitra, Slovakia

[4]Institute of Materials Research, Slovak Academy of Sciences in Košice, Watsonova 47, 04001 Košice, Slovakia

Abstract: *Mechanical strength and Young's modulus of green alumina porcelain (50 wt. % of kaolin, 25 wt. % of Al_2O_3, and 25 wt. % of feldspar) were measured after heating up to 1250 °C. We used the three point-bending method and modulated force thermomechanical analysis (mf-TMA). The liberation of the physically bound water (20 – 250 °C) strengthens the sample, however, after firing the sample regains the moisture and therefore Young's modulus remains at the same value. The dehydroxylation, i.e., the transformation of kaolinite into metakaolinite, taking place in the range 400 – 650 °C, causes a very slight increase in mechanical strength. On the other hand, Young's modulus remains the same increases in this temperature range. Beyond the dehydroxylation range, above 650 °C, both Young's modulus and mechanical strength increase exponentially up to 1250 °C. The sharp increase of Young's modulus and mechanical strength above 950 °C is caused by solid-state sintering This was compared with plenty of different analyses and measurements after firing. Vickers hardness measured at room temperature at samples fired at dehydroxylation temperature region (400 – 700 °C) is increasing with the firing temperature. From 900 °C it increases exponentially which is caused by the solid-state sintering. The sample therefore gains better mechanical properties after dehydroxylation and solid-state sintering. Shore hardness follows the same patterns, just the increase is not exponential but linear. Vickers hardness increases 130 times during the whole temperature interval, Shore hardness increases only 4 times.*

Keywords: *alumina porcelain, mechanical strength, Young's modulus, firing*

1. Introduction

Alumina porcelain as a material with exceptional properties is intensively studied. Since a development of the properties during firing is predominantly given by phase changes in kaolonite, a research was most often focused on the phase transformations of kaolinite during heating. A lot of different experimental techniques were used to reveal characteristic features of the phase transformations kaolinite → metakaolinite → mullite under different conditions, see for example [1–7]. This transformation can be also experimentally studied after heating of the green samples at selected temperatures. Changes of the structure and composition which were reached during such thermal treatment are saved in the cooled samples and can be measured at room temperature.

When a dry alumina porcelain sample comes into contact with the ordinary air, the sample starts to chemically and physically combine with atmospheric moisture. This causes a mass

increase and expansive strain [8]. The process is reversible and the sample loses this physically bounded water during heating at temperatures lower than 300 °C [4]. MOR and YM increase in his temperature interval, as dehydration increases those two quantities [9].

The next important reaction is dehydroxylation, where kaolinite transforms in metakaolinite and the water vapor is released from a crystal, see e.g. [1, 3, 9]. Metakaolinite is highly defective structure and its porosity is higher than those of the parent kaolinite [2, 3, 10]. At the beginning of dehydroxylation there is a slight decrease of YM and MOR at 425 °C, as the kaolinite structure becomes deffective. After this temperature, YM and MOR increases during the dehydroxylation as the structure is modified [10]. Vickers hardness [11], fracture toughness [12] and Shore hardness [13] follows the similar trend as YM and MOR – they slightly increase at samples fired at the dehydroxylation temperature interval.

The first high-temperature process in metakaolinite begins at ~950 °C. Its product is spinel and amorphous SiO_2 or, according another authors, the product is γ-alumina and amorphous SiO_2 [1]. At higher temperatures, not less than 1100 °C, the formation of mullite occurs [3, 4]. Both reactions cause dramatic increase of MOR and YM [9]. The same trend occurs for Vickers hardness [11], fracture toughness [12] and Shore hardness [13] – these quantities dramatically increase during this temperature interval.

A heating rate during firing of the ceramic products is limited by YM, MOR, and some thermophysical quantities. Therefore, it is evident practical value of these mechanical quantities as functions of the firing temperature.

The goal of the paper is experimental study of MOR and YM of the green alumina porcelain samples after their heating at selected temperatures and to relate the obtained results to structural changes caused by dehydration, dehydroxylation and high-temperature reactions.

2. Experimental

Alumina porcelain samples (50 wt. % of kaolin, 25 wt. % of Al_2O_3 and 25 wt. % of feldspar) were prepared from a wet plastic mass (75 wt. % of alumina porcelain mixture and 25 wt. % of distilled water) using a laboratory extruder with a circular muzzle. The samples were dried in open air for one week. After drying, the samples contained ~1.5 wt. % of the physically bounded water and their diameter was 11 mm. The samples were preheated at selected temperatures with heating rate of 5 °C/min and all analyses were performed at room temperature.

MOR was measured by the three-point-bending method with magazine for 8 samples. Ten sample of the size ∅11×120 mm was subjected to loading force, which increased with a rate of 2 N/s.

YM was measured by a resonant method [14] that served as a base of the modulated force thermomechanical analysis (mf-TMA). Dimensions of the sample were ∅11×140 mm.

For fracture toughness test, samples with dimensions 5×5×30 mm were used, for Vickers and Shore hardness test, their dimensions were 5×35×35 mm.

Vickers hardness was measured using the 4-sided diamond pyramid was pressed into the sample for certain time under certain loading force. The dimensions of the imprint were

measured by a microscope. From the loading force and area of imprint the Vickers hardness was calculated.

Shore hardness was measured –the steel ball fell from the height *H*on the sample which was tilted in height *h* from support. Steel ball rebounded from the sample and fell to the distance *l* from the support. From measured values *h*, *H*, *l* the Shore hardness was calculated.

Fracture toughness was measured by 3-point-bending method on the sample with crack. This crack was made by the apparatus used for Vickers hardness measurement.

3. Results and discussion

In green alumina porcelain mixture the three processes are presented, which are visible in Fig. 1. The first process is liberation of physically bound water until 200 °C. Since this process is reversible and the samples were not measured immediately after heating, no changes of the sample mass and dimensions were registered. The second process is dehydroxylation at 420 – 680 °C. The mass loss of this material is almost 6 wt. % whereas the relative contraction 0.4 %. The third process is spinel formation at 950 °C Relative mass loss gains it maximal value whereas relative contraction starts growing rapidly after this temperature. The maximal relative contraction is about 9 wt. % at the temperature 1250 °C [15, 16, 17].

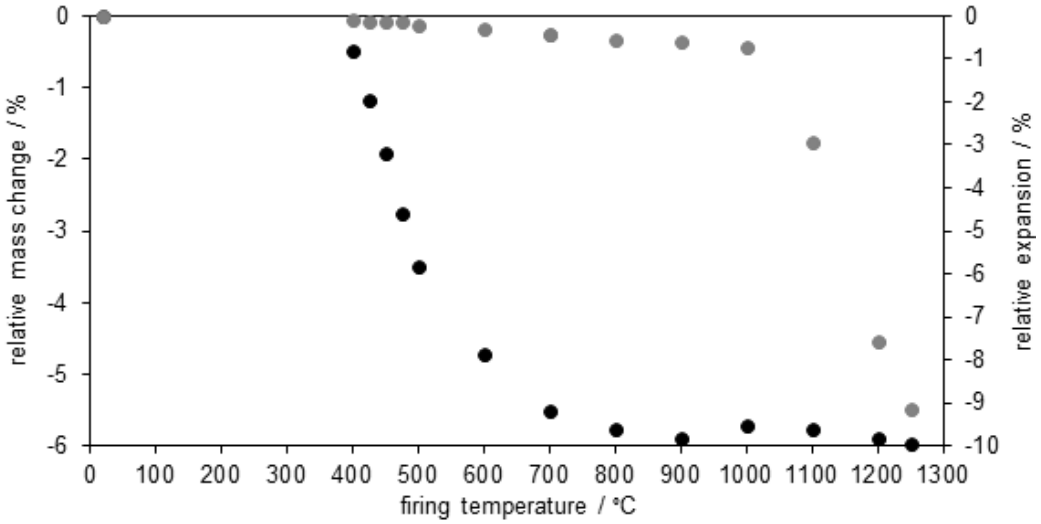

Figure 1: Relative mass change (black, left y-axis) and relative linear expansion (grey, right y-axis) after firing

Next valuable results which can explain the development of mechanical properties are results of bulk density, Fig. 2. Until 300 °C, the liberation of physically bounded water is present which results to relative expansion of the sample. Therefore the bulk density decreases. But sample regains the moisture after the firing so this could be verified only immediately after firing the sample. The volume mass decreasing continues also at samples fired at the dehydroxylation temperature interval (400 – 700 °C), which is connected with liberation of chemically bounded water and with rebuilding of kaolinite structure. At samples fired at 950 °C formation of spinel (or $\gamma - Al_2O_3$) occurs. At samples fired at 1100 °C formation of mullite occurs. These two processes are accompanied by strong increase of bulk density.

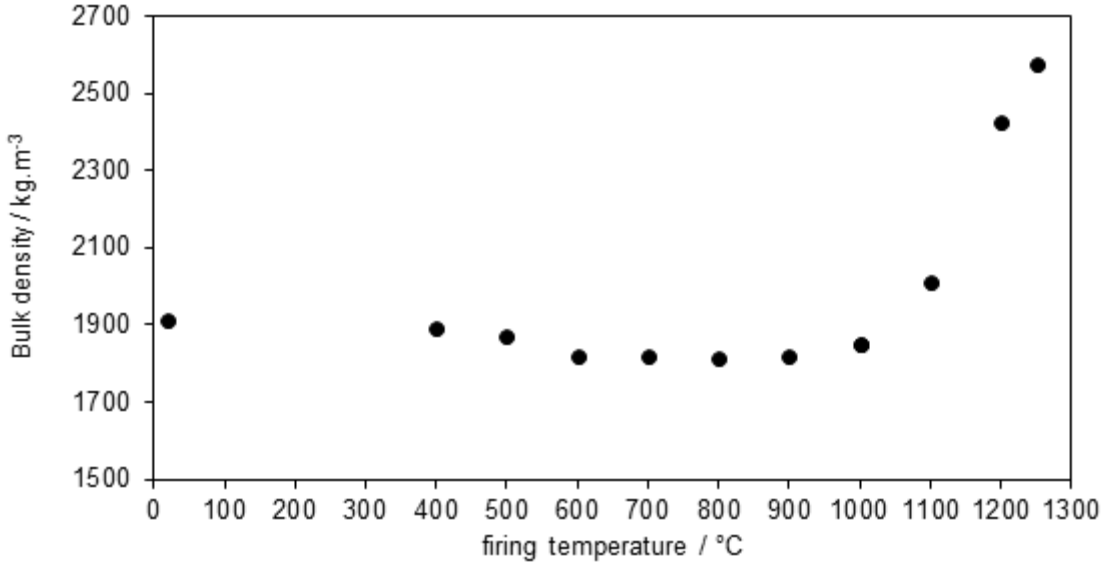

Figure 2: Bulk density as a function of the firing temperature

MOR of alumina porcelain fired at different temperatures is depicted in Fig. 3. During dehydroxylation and beginning of the sintering it increases only moderately and over 800 °C it increases exponentially what is caused by solid-state sintering. We assume that sintering, as a process induced by heat, is dependent on Boltzmann's factor $\exp(-E/kT)$. This dependence is the same as for pure kaolin samples [18]. YM has the same course as MOR and therefore the explanation is the same.

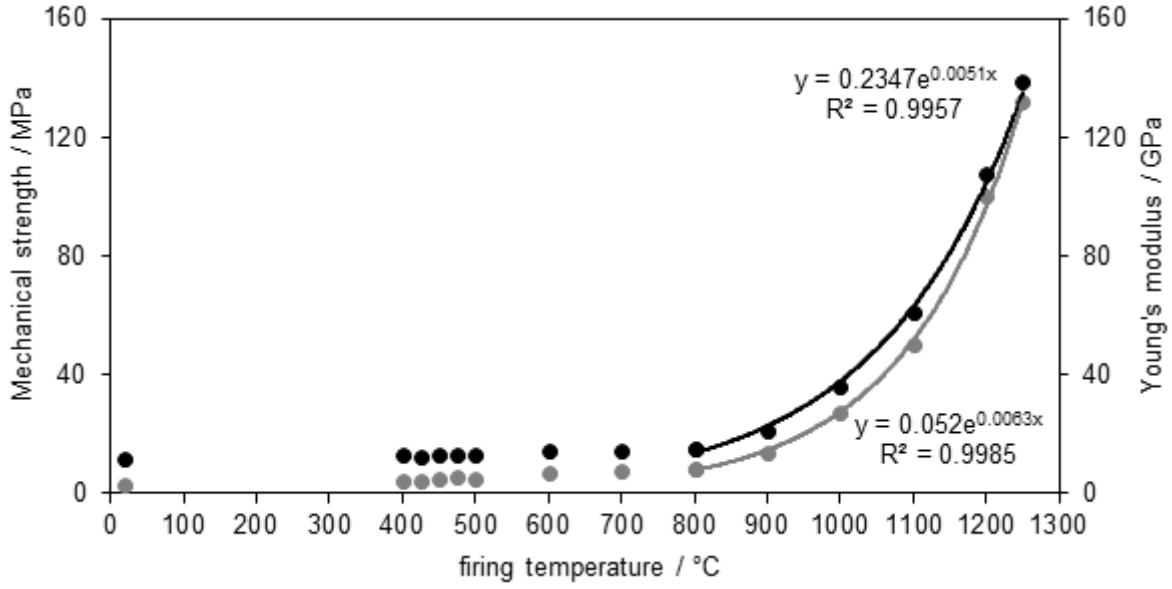

Figure 3: Mechanical strength (grey) and Young's modulus (black) after firing

Vickers hardness measured at room temperature at samples fired at dehydroxylation temperature region (400 – 700 °C) is increasing exponentially with the firing temperature. From 900 °C it increases exponentially that is caused by sintering (Fig. 4). Therefore, the sample gains better mechanical properties after dehydroxylation and sintering [19]. Shore

hardness follows the same course just the increase is not exponential but linear. Vickers hardness increases 130 times during the whole temperature interval, Shore hardness increases only 4 times.

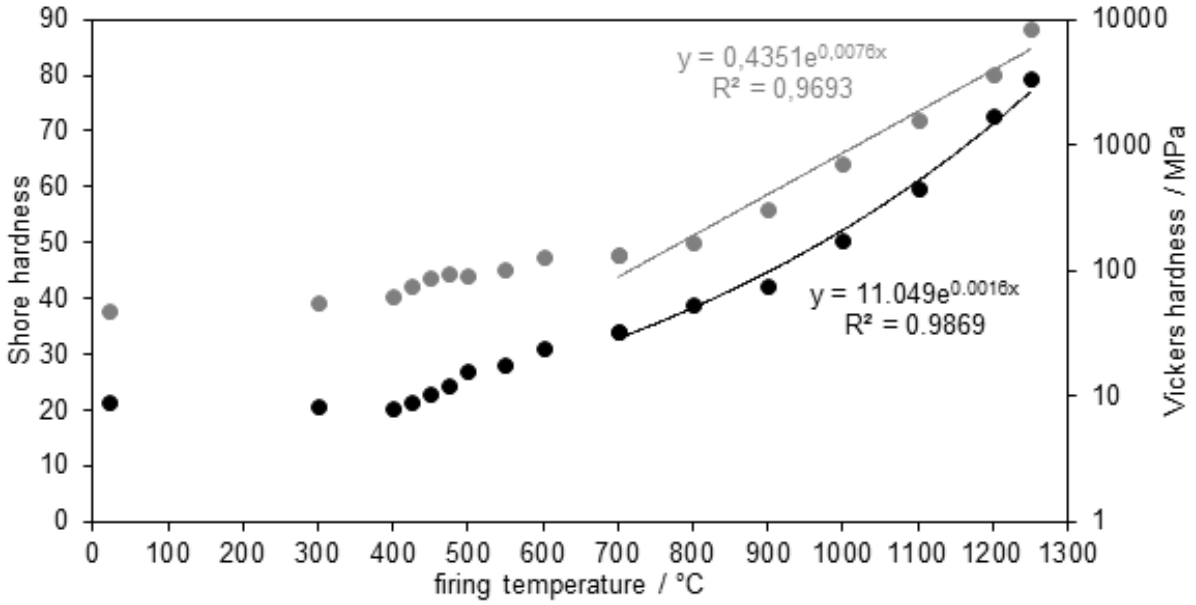

Figure 4: Vickers (grey) and Shore (black) hardness after firing

Fracture toughness (Fig. 5) very slowly increases with temperature until 900 °C. Over 900 °C it has exponential dependence what is caused by solid state sintering [20]. Sintering closes the micro cracks and therefore increases the fracture toughness.

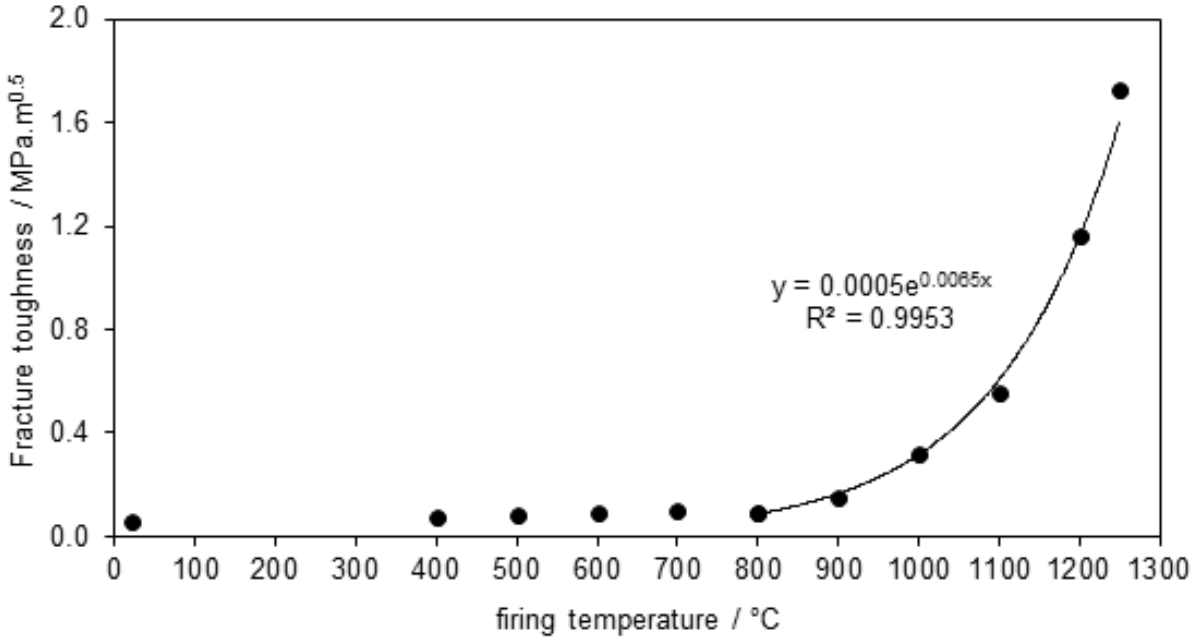

Figure 5: Fracture toughness after firing

4. Conclusion

To reveal the influence of the heating on the mechanical strength and Young´s modulus of alumina porcelain, the three-point-bending method, modulated-force thermomechanical analysis (mf-TMA), bulk density measurements, relative mass loss and relative contraction after firing was performed. The previous firing was made at chosen temperatures with the heating rate of 5 °C/min.

These measurements were supplemented by: Vickers hardness (HV), Shore hardness (HSC) and fracture toughness (KIC).

The both quantities, MOR and YM slightly increase their values in the dehydroxylation region (400 – 650 °C). The increase is only moderate, as dehydroxylation rebuilds the structure. When dehydroxylation is finished, a formation of spinel occurs at 950 °C. Above 1100 °C, the formation of mullite occurs. As a consequence, the YM and MOR increases exponentially with temperature in this temperature interval.

Relative mass loss gradually increases for the samples fired at dehydroxylation temperature interval. On the other side, contraction of the sample fired at this temperature is very low. At 950 °C where the formation of spinel occurs, the mass loss has its maximum value (6 wt. %) and sample fired at this temeprature starts to contract significanlty. This also applies for the temperature 1100 °C – the mullite formation temperature. At 1250 °C the relative contraction has its maximum value – about 9 %.

Bulk density decreases at samples fired at dehydration (up to 400 °C) and dehydroxylation (400-700 °C) temperature region because sample loses physically and chemically bounded water. From 950 °C when spinel forms the density starts to increase and this continues also at mullite formation temperature – 1100 °C.

Vickers hardness at the samples fired at dehydroxylation temperature region (400 – 650 °C) is increasing with the firing temperature. From 900 °C it increases exponentially that is caused by the sintering. Shore hardness follows the same course.

Fracture toughness very slowly increases with temperature until 900 °C. Over 900 °C it has exponential dependence which is caused by the solid state sintering. Sintering closes the microcracks and therefore increases the fracture toughness.

Acknowledgments

This work has been supported by the grant VEGA 1/0464/12 and by the Estonian target financed grant SF0140091s08. This work has been supported by the grant VEGA 1/0689/13 – Hygric Deformation of Building Materials at the Slovak University of Technology. This work has been supported by the Project "PROMATECH" IMTS: 26220220186. This research was supported by European Social Fund's Doctoral Studies and Internationalisation Programme DoRa". The authors are indebted to ceramic plant PPC Čab, Slovakia, for a green alumina porcelain mixture.

References

[1] CHEN, C. Y. – LAN, G. S. – TUAN, W. H. Microstructural evolution of mullite during the sintering of kaolin powder compacts. In *Ceramics International*. 2000. 26. p. 715 - 720. ISSN 0272-8842

[2] FREUND, F.Kaolinite-metakaolinite, a model of a solid with extremely high lattice defect concentration. In *Ber. Deutsche Keram. Ges.* 1967. 44(N4). p. 5 - 13. ISSN 0365-9542

[3] NORTON, F. H. *Fine Ceramics – Technology and Applications.* Ed. Mc. Graw Hill Book Co., New York, 1970. ISBN 0-88-275582-X

[4] HANYKÝŘ, V. – KUTZENDORFER, J. *Technology of Ceramics*. Ed. SilisPraha a Vega, Hradec Králové, 2000. ISBN 978-80-86821-48-1

[5] VARGA, G. Structure of kaolinite and metakaolinite. In *Épitoanyag*. 2007. 58(N1). p. 6 - 9. ISSN 0013-970X

[6] GUALTIERI, A. – BELLOTTO, M. – ARTIOLI, G. – CLARK, S. M. Kinetic study of the kaolinite-mullite reaction sequence, Part II: Mullite formation. In *Physics and Chemistry of Minerals.* 1995. 22(N4). p. 215 - 222. ISSN 0342-1791

[7] SONUPARLAK, B. – SARIKAYA, M. – AKSAY, I. Spinel phase formation during the 980 °C exothermic reaction in the kaolinite-mullite reaction series. In *J. Amer. Ceram. Soc.* 1987. 70. p. 837 - 842. ISSN 1551-2916

[8] MESHBAH, H. – WILSON, M. A. – CARTER, M. A. The role of the kaolinite-mullite sequence in moisture mass gain in fired kaolinite. In *Advances in Science and Technology.* 2010. 68. p. 38 – 43. ISSN1662-0356

[9] Štubňa, I. – Šín, P. – Trník, A. – Veinthal, R.: Mechanical Properties of Kaolin during Heating. In: *Proceedings of Baltmattrib 2012 Conference 18.-19.10.2012, Tallinn, Estonia.*

[10] ŠTUBŇA, I. – KOZÍK, T. Permeability of the electroceramics to gas and its dependence on the firing temperature. In *Ceramics International.* 1997. 23. p. 247 – 249. ISSN0272-8842

[11] ŠÍN, P. – VEINTHAL, R. – SERGEJEV, F. – ANTONOV, M. – STUBNA, I. Vickers hardness of ceramic fired at different temperatures. In: *Young Researchers 2011 : PhD Students, Young Scientists and Pedagogues Conference Proceedings.* 2011. p. 565-570. ISBN 978–80–8094–946–4

[12] ŠÍN, P. – VEINTHAL, R. – SERGEJEV, F. –ANTONOV, M. – STUBNA, I. Fracture Toughness of Ceramic Fired at Different Temperatures. In: *Materials Science (Medžiagotyra)*. 2012. 18. p. 90 – 92. ISSN 1392-1320

[13] ŠTUBŇA, I. – ŠÍN, P. – VOZÁR, L. Hardness of alumina porcelain fired at different temperatures. In: *DIDMATTECH 2012 – Conference proceedings.* 2012. p. 28-34. ISBN 978-80-8122-060-0

[14] ŠTUBŇA, I. – TRNÍK, A. – VOZÁR, L. Determination of Young's modulus of ceramics from flexural vibration at elevated temperatures.In: *ActaAcustica + Acustica.* 2011. 97. p. 1 – 7. ISSN1610-1928

[15] BOUDNIKOV, P. P. et. al. *Technologie keramiky a žáruvzdorního prostředí.* Ed. SNTL, Praha, 1960. ISBN 8-07-080568-4

[16] ŠTUBŇA, I. – ŠÍN, P. – TRNÍK, A. – VEINTHAL, R. Mechanical properties of kaolin during heating. In *Key Engineering Materials*. 2013. 527. p. 14 - 19. ISSN 1662-9795

[17] RIEDLMAJER, R. – ŠTUBŇA, I. – VARGA, G. Thermoelectric and thermodilatometric analysis of English kaolins. In *Silika*. 2006. 16. p. 119 - 121. ISSN 1213-3930

[18] ŠÍN, P.*Strength Characteristics of Kaolin – Based Material up till 1350 °C – Doctoral Thesis*. Ed. Constantine the Philosopher University, Nitra, 2013

[19] ŠÍN, P. – VEINTHAL, R. – SERGEJEV, F. – ANTONOV, M. – ŠTUBŇA, I. Vickers hardness of ceramics fired at different temperatures. In *Young Researchers.* 2011. p. 565 - 570. ISSN 1211-4669

[20] ŠÍN, P. – VEINTHAL, R. – SERGEJEV, F – ANTONOV, M. – ŠTUBŇA, I. Fracture toughness of ceramics fired at different temperatures. In *Materials Science.* 2012. 18(1). p. 90 - 92. ISSN 0137-1339

Dilatometric investigation of the phase transition in the high strength steel S960QL

Tomasz Ślęzak[1], Janusz Zmywaczyk[2], Piotr Koniorczyk[2], Lucjan Śnieżek[1]

[1]Department of Construction Machinery, [2]Faculty of Mechatronics and Aerospace, Military University of Technology, Kaliskiego 2, 00-908 Warsaw, Poland, email: piotr.koniorczyk@wat.edu.pl

Abstract: *Thermal expansion measurement for microalloyed high strengh steel is reported. The investigation concentrated on the linear expansivity in the region of the second order phase transision. Experiments have been carried out using the High Temperature Dilatometer DIL 402C (Netzsch). Initially a copper sample was tested within temperature range of 50-340 °C in order to verify technical thermal expansion with the literature values given by NBS. As a tested material a sample from the high strengh steel S960QL was used within temperature range of 50-900 °C. Investigations have revealed the thermal hysteresis of the linear expansivity in the region of the second order magnetic phase transision in the S960QL steel. A brief description of the experimental apparatus and measurement technique is also given.*

Keywords: *high strength steel S960QL, coefficient of linear thermal expansion (CLTE)*

1. Introduction

Despite many years of investigations the problem of microalloyed high strength steels anomalies of thermophysical properties still remains very interesting. This is mainly because of the anomalous thermal expansivity near the Curie point region. The anomaly is of magnetic origin and vanishes after the ferromagnetic to paramagnetic state transition. The steel S960QL has been recently used in manufacturing of various types of cranes, high speed rotors, road and rail vehicles, airplanes, ships, rocket and space technology [1, 2]. Due to lack of sufficient data on thermal expansivity of that steel and keeping in mind potential risks of failure, there is a need for more detailed research and contributions to the field of optimization of structure elements.

Measurements were performed with a pushrod dilatometer DIL 402C manufactured by Netzsch (Germany) for samples with 25 mm of the length and 6 mm of the sample diameter. The horizontal design of the dilatometer with motorized pushrod and easy to move furnace make it simple to place samples on the special sample supports in the recess of the tube-type sample carrier – Fig. 1. A thermocouple in direct proximity to the sample (1-2 mm) yields reproducible temperature measurements. During the measurement of tested material one should take into account that the sample carrier and pushrod also change their length. For that reason calibration using alumina or other reference material is necessary to obtain reliable and more accurate results of tested material. In our case the alumina reference material made by Netzsch in a form o cylinder (25 mm long, 6 mm of diameter) was used keeping the same temperature program like in tested material (standby at 25^{0}C – heating to 950^{0}C at 1K/min rate – isothermal at 950 ^{0}C for 5min – cooling down to 25 ^{0}C at 1K/min – isothermal at 25 ^{0}C for 5 min)

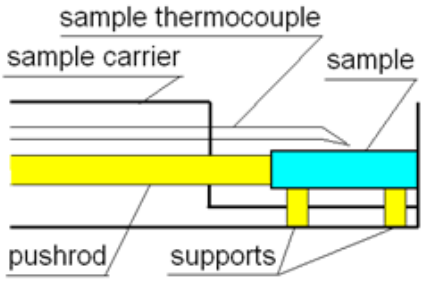

Figure 1: Tube-type sample holder of the High Temperature Dilatometer DIL 402C.

For the detection of the specimen length changes a contact force of the pushrod (between pushrod and sample) can be adjusted on the value of 15cN. All specimen were investigated in the as-received condition and were not annealed. Liquid nitrogen flowing at 60ml/min was used as an inert gas. Chemical composition of tested high strength steel S960QL is presented in the Table1.

Table 1: Composition of the S960QL steel [1, 2].

C	Si	Mn	P	S	Cr	Mo	Ni	Nb	V	Cu	Ti
0.17	0.47	1.42	0.008	0.003	0.59	0.56	0.79	0.02	0.05	0.03	0.01

In order to avoid of a potential misunderstanding of the Coefficient of Linear Thermal Expansion (CLTE) notion the physical alpha (CLTE α^*) is defined as [3]:

$$\alpha^*(T) = \frac{1}{L(T_o)}\frac{dL(T)}{dT} = \frac{1}{L_o}\frac{dL(T)}{dT} \tag{1}$$

which is in accordance with Netzsch DIL 402C manual.

In addition to this by dL is signed increase of the length of the sample involving correction resulting from taking into account the pushrod and the sample carrier thermal expansion.

2. Experimental results for copper

In order to check the accuracy of our own measurements sample made of electrolytic copper was used and the results were next compared with the reference values of copper NBS standard material. Our copper sample is available commercially and it isn't of such purity as a NBS reference material. Thermal expansivity measurements of copper were carried out in the temperature range 25 ÷ 400 ^{0}C with the heating/cooling rate 1 K/min and 2 K/min, respectively but the results of CLTE α^* for copper can be accepted physically in the range 50÷ 320 ^{0}C. The given heating/cooling rates were chosen so that to study their influence on the CLTE α^* results. The thermal characteristics of the dL and the CLTE α^* curves are shown in figure 2 and 3. In Fig. 3 the values of CLTE α^* were given as average ones from heating and cooling.

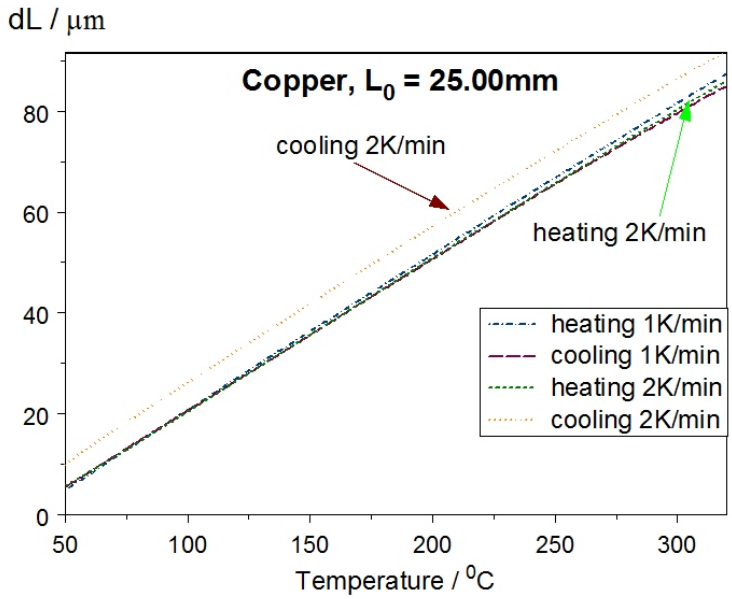

Figure 2: Temperature dependences of the dL of the S960QL steel.

It is shown in Fig. 2 that at heating/cooling rate 2 K/min there are bigger discrepancy between heating and cooling curves than at heating/cooling rate 1 K/min. Despite this the results of CLTE α^* visible in Fig. 3 are quite close to the NBS reference data and the maximum discrepancy do not exceed 2%. However, at heating/cooling rate 2 K/min one can observe bigger discrepancy of CLTE α^* values near temperature 130 °C.

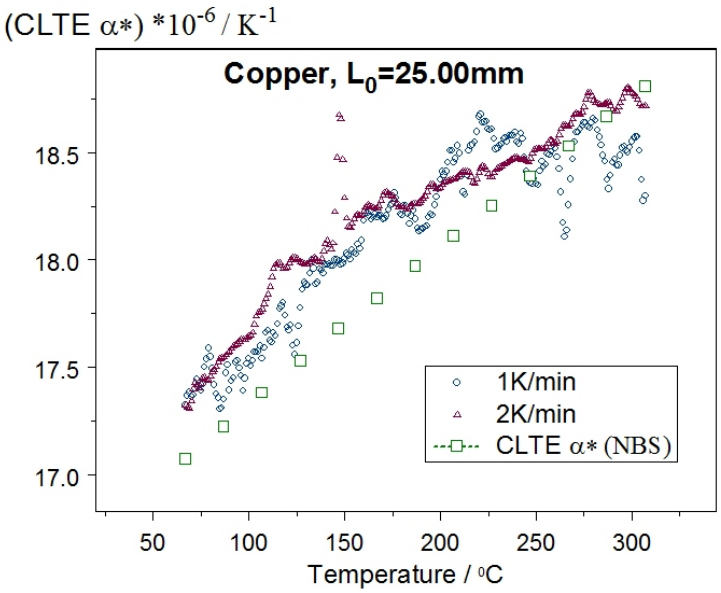

Figure 3: Temperature dependences of the CLTE α^* of the Copper

3. Experimental results for the S960QL steel

Thermal expansivity measurements were carried out in the temperature range 25÷950 ^{0}C with the heating/cooling rate 1 K/min. At temperatures 25 ^{0}C and 950 ^{0}C the sample was thermostated for 5 min. In Fig. 4 there are given results for S960 QL sample steel with respect to length change dL and linear expansion dL/L_0 (LE). Despite of similarity of these figures one can easily find analyzing the left Fig. 4 what was the change of the sample length in [μm] within the whole temperature range. One can easily observed (see Fig. 4) than after annealing at 950 ^{o}C the shape of linear expansion curve of S960QL sample while cooling down is quite different to the one during heating up.

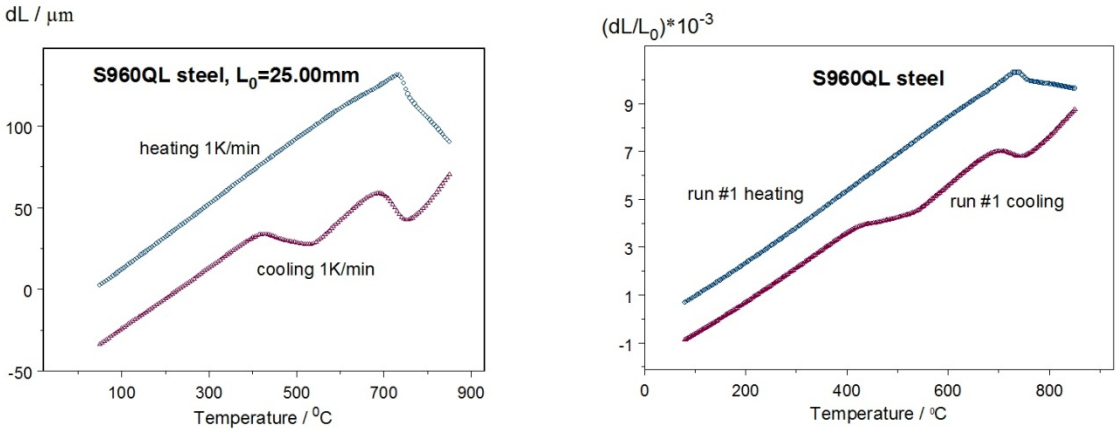

Figure 4: Temperature dependences of the dL and dL/L$_0$ of the S960QL steel.

The thermal hysteresis in α^* - T curves is shown in Fig. 5. The discrepancy between the Curie temperature of heating and cooling processes amounts to 16.3 ^{0}C (745.7 ^{o}C - heating, 729.4 ^{0}C – cooling). It is worth to notice that the Curie temperature of pure iron is equal to 770 ^{0}C [4].

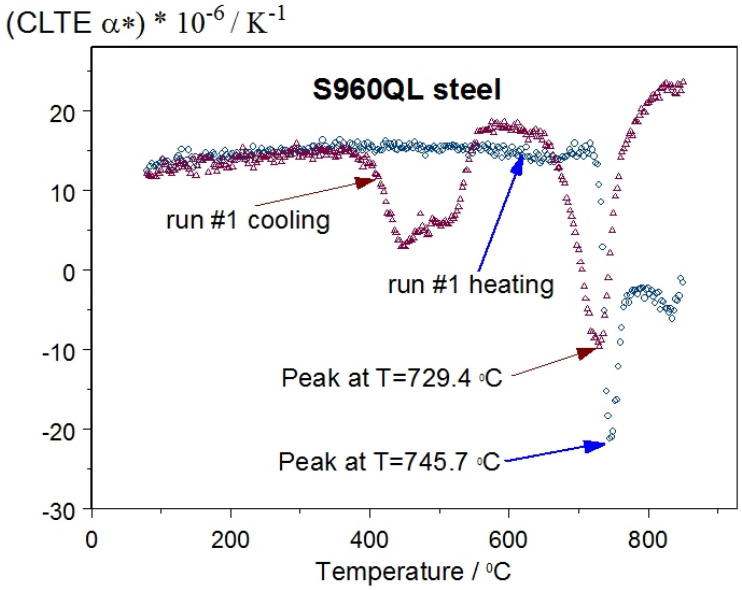

Figure 5: Temperature dependences of the CLTE α^* of the S960QL steel.

In case of high strength steel S960QL being tested we obtained that the Curie temperature was shifted with respect to the pure iron. At the moment we didn't know if in this case the thermal hysteresis is reversible in the next heating/cooling processes – Fig. 5. Before CLTE measurements, e.g. in the as-received condition, the S960QL sample steel exhibited fine-grained structure of tempered martensite and bainite [2]. The sample heated to 700 ^{0}C did not cause significant changes (temperature of tempering was 680 ^{o}C) in structure. The sample heated to 800 ^{0}C exhibited increase in grains [1, 2]. Heating to 900 ^{0}C caused even greater increase in grains. The was separation of precipitates observed in the samples heated to higher temperatures (1100 ^{0}C and 1300 ^{0}C). The heat affected an increase in structural transformations into martensitic-bainite structure [2]. According to literature the S960QL sample steel heated to 800 ^{0}C and above exhibited increase in grains and decrease of hardness [1, 2]. Confirmation of this above mentioned statement is visible in Fig. 5 difference in thermal expansion of the sample during its heating and cooling running. In order to explain the character of minimum CLTE α^* near 400 ^{0}C (see Fig. 5) it is necessary to conduct the further metallographic investigations.

4. Conclusions

In this paper CLTE α^* temperature characteristics were obtained experimentally for the high strength S960QL sample steel using Netzsch dilatometer DIL 402 C. Preliminary studies of CLTE α^* for electrolytic copper have revealed a good agreement with their tabled values given by NBS (accuracy of the measurements did not exceed 2%). The measurements were time consuming due to low heating and cooling rate equals 1 K/min. The results of CLTE α^* investigations revealed phase transition of the second kind for S960QO steel at 745.7 ^{o}C during heating and at 729.4 ^{o}C during cooling..

Acknowledgement

This work was supported by university grant RMN 08-878.

References

[1] DUNDER M., VUHERER T., SAMARDIC I., Weldability of microalloyed high strength steels TStE 420 and S960QL, *Metalurgija 53 (2014) 3, pp.335-338* (in English)

[2] DUNDER M., VUHERER T., SAMARDIC I., Weldability prediction of high strength steel S960QL after weld thermal cycle simulation, *Metalurgija 53 (2014) 4, pp.627-630* (in English)

[3] PANAS A. J., High thermal resolution dilatometric investigation of the phase transitions in the binary iron-nickel alloys, *High Temperatures-High Pressures, 1998, volume 30, pp. 683-688*

[4] MILLS K. C., Recommended values of thermophysical properties for selected commercial alloys, NPL, *Woodhead Publishing Limited, Cambridge England 2002 (ISBN 0-87170-753-5*

Samples preparation for calorimetric measurement of hydration heat using solid/solid mixing

Vratislav Tydlitát[1], Zbyšek Pavlík[1], Viviana F. Rahhal[2], Edgardo F. Irassar[2]

[1]Faculty of Civil Engineering, Czech Technical University in Prague, Thákurova 7, CZ-166 29 Prague, Czech Republic, email: tydlitat@fsv.cvut.cz

[2]Facultad de Ingenieria, Universidad Nacional del Centro de la Provincia de Buenos Aires, B7400JWI Olavarría, Argentina

Abstract: *Theoretical limits of the accuracy of the mixture composition achieved by solid/solid mixing in preparation of dry blended silicate samples for measurement of their hydration heat power are studied in the presented paper.*

Keywords: *Solid/solid mixing, variation in particle composition, variation in mass composition*

1. Introduction

In the building industry, the binder is usually prepared by mixing of dry solids with water. In case of the presence of batch water in the mixture, the mixing of the binder is easier than mixing of two solids only, whereas the mixture exhibits properties similar to a thick liquid.

In our previous research work we met many cases, where it was necessary to prepare inorganic binders in the dry form on the basis of two solid components. For these binders we observed hydration kinetics and measured the hydration power. In order to realize the planned experiments, there was necessary to prepare binders samples of sufficient homogeneity. To provide good solid/solid mixing the segregation must be avoided. Segregation occurs when mixed solid particles have different physical properties: sizes, shapes, densities, etc., whereas the particles movement can cause their accumulation into the layers of different physical and chemical properties. On the other hand, motion of miscible liquids and gases makes possible quality mixing due to the convection. Molecular diffusion completes the mixing in micro-dimensions. The influence of gravitation field shall not be excluded and must be considered in case of mixing two particulate sets of particles with different densities. In connection with above given facts we studied the theory of solid/solid mixing using simplest models.

2. Mixing of two components

Let us have 113 light and 101 dark coloured beads in different state of mixing. The overall proportion of dark beads is 0.472 (i.e. 101/214). If we have distributed the mixture into many different samples wit n beads, we have found for n = 21 samples the lowest proportion of dark beads 0.1 and highest 0.78. The mean value of the proportion of black beads p_i calculated over all samples according to Eq. (1) is $\underline{p}$ = 0.472.

$$\underline{p} = (p_1 + p_2 + ... + p_n)/n \tag{1}$$

Standard deviation σ_R (0.195) around the mean value of proportion of black and white beads is given by expression (2)

$$\sigma_R = \sqrt{\frac{\sum(pi - \underline{p})^2}{n-1}} \tag{2}$$

with variance of 0.0382 calculated as σ_R^2.

We suppose that the proportion of dark and light beads of chosen samples follow the normal distribution. On this account we expect that 68.2% samples have the proportion of dark and light beads in the limits 0.472 +/- standard deviation (i.e. 0.472+/-0.195).

In more common conception let us consider a set of identic particles of a substance that vary in colour only (A black, B white). In the set we indicate by $\underline{a}$ proportion of A particles. If we analyse the mixing state of the set we must take m samples every containing identical number n of particles. The possible values $\underline{a}$ of black particles in the sample of n particles are 0, 1/n, 2/n, 3/n, … ,1. Totally, there are n+1 different values of $\underline{a}$. P_i is the probability of occurrence of each possible value of $\underline{a}$ in the sample formulated as

$$\sum_{i=0}^{n} P_i = 1, \tag{3}$$

$$\sum_{i=0}^{n} P_i a_i = \underline{a}, \tag{4}$$

where $a_i - \underline{a}$ is the deviation in composition from the mean.

In this case, quadrat of standard deviation is expressed as

$$\sigma_R{}^2 = \sum_{i=0}^{n} P_i (a_i - \underline{a})^2, \tag{5}$$

where

$$\sum_{i=0}^{n} P_i (a_i - \underline{a})^2 = \sum_{i=0}^{n} P_i a_i{}^2 - 2\underline{a}\sum_{i=0}^{n} P_i a_i{}^2 + \underline{a}^2 \sum_{i=0}^{n} P_i \,. \tag{6}$$

Then

$$\sigma_R{}^2 = \sum_{i=0}^{n} P_i a_i{}^2 - 2\underline{a}\underline{a} + \underline{a}^2 \tag{7}$$

or

$$\sigma_R{}^2 = \sum_{i=0}^{n} P_i a_i{}^2 - \underline{a}^2. \tag{8}$$

The expression $\sum_{i=0}^{n} P_i a_i{}^2$ can be rewritten by multiplying of every of n+1 terms of the row for P_i by terms 0, (1/n)^2 , (2/n)^2 ,

$$\left(\frac{1}{n}\right)^2 \left\{0 + n(1-\underline{a})^{n-1}\underline{a} + \frac{n(n-1)}{1}(1-\underline{a})^{n-2}\underline{a}^2 + \frac{3n(n-1)(n-2)}{1.2}(1-\underline{a})^{n-3}\underline{a}^3 + \ldots + \underline{a}^n\right\} \tag{9}$$

or

$$\left(\frac{\underline{a}}{n}\right)\left\{(1-\underline{a})^{n-1}\frac{2(n-1)}{1}(1-\underline{a})^{n-2}\underline{a}+\frac{3n(n-1)(n-2)}{1.2}(1-\underline{a})^{n-3}\underline{a}^{2}+\ldots\right\} \tag{10}$$

It may be written also in two rows as

$$\begin{aligned}&\left(\frac{\underline{a}}{n}\right)\left\{(1-\underline{a})^{n-1}\frac{(n-1)}{1}(1-\underline{a})^{n-2}\underline{a}+\frac{(n-1)(n-2)}{1.2}(1-\underline{a})^{n-3}\underline{a}^{2}+\ldots\right\}+\\&\left(\frac{\underline{a}}{n}\right)\left\{(0+\frac{(n-1)}{1}(1-\underline{a})^{n-2}\underline{a}+\frac{2(n-1)(n-2)}{1.2}(1-\underline{a})^{n-3}\underline{a}^{2}+\ldots\right\}.\end{aligned} \tag{11}$$

The first of the above two series in brackets is the binomial expansion of $((1-\underline{a})+\underline{a})^{(n-1)}=1$. The second series is the same one with successive terms multiplied by 0, 1, 2, 3…., i.e. by successive values of (n-1)a (n terms in all), i.e. (n-1)$\underline{a}$, and its sum is therefore the mean value of (n-1)a, i.e. (n-1)$\underline{a}$.

Thus

$$\sum_{i=0}^{n}P_i a_i^{\,2}=\frac{\underline{a}}{n}\{1\}+\frac{\underline{a}}{n}\{(n-1)\underline{a}\}=\frac{\underline{a}}{n}(1+(n-1)\underline{a}), \tag{12}$$

and

$$\sigma_R^{\,2}=\sum_{i=0}^{n}P_i a_i^{\,2}-\underline{a_i}^{\,2}=\frac{\underline{a}}{n}(1+(n-1)\underline{a}-n\underline{a})=\frac{\underline{a}}{n}(1-\underline{a}), \tag{13}$$

$$\sigma_R=\sqrt{\frac{\underline{a}(1-\underline{a})}{n}}. \tag{14}$$

We consider again a set of identical particles of different colour (particles A are black, particles B are white) that are not mixed. We take samples containing every time n particles. a is the number of black particles in a sample divided by the whole number of particles in sample. Every sample can reach value of a = 1 or a = 0. In not mixed set, there were taken m samples. If the number m is high enough, we will found that contents a = 1 is in $\underline{a}m$ samples and a = 0 in $(1-\underline{a})m$ samples. The variance is then

$$\sigma_R^{\,2}=\frac{((m\underline{a}(1-\underline{a})^2)+m(1-\underline{a})\underline{a}^2))}{(m-1)}=\frac{m\underline{a}(1-\underline{a})(1-\underline{a}+\underline{a})}{(m-1)}=\frac{\underline{a}(1-\underline{a})m}{(m-1)}. \tag{15}$$

For high number of samples m is $\sigma_R^2=\underline{a}(1-\underline{a})$. So we have an instrument for evaluation the mixing quality, if we test the mixed set of identic (with exception of colour) particles taking m samples of n particles. The worst (largest) measure of mixing quality is $\sigma_R^2=\underline{a}(1-\underline{a})$, and the best (smallest) attainable value of $\sigma_R^{\,2}=\frac{\underline{a}}{n}(1-\underline{a})$.

3. Two components mixing – practical example

For the assessment of the variance as mixing quality, the work with the number of particles in the mixed set is difficult. Much easier is to take m samples of identical mass from a mixed

set of two components (P) and (Q), where P is the relative mass of component (P) and Q is the relative mass of component (Q), $P + Q = 1$. Here we need and have to evaluate mean mass of particles w_P and w_Q and dimensionless variation numbers C_P and C_Q formulated as

$$C_P = \frac{\sigma_P}{w_P}, \tag{16}$$

$$C_Q = \frac{\sigma_Q}{w_Q}. \tag{17}$$

The variance for testing samples of mass g was in detail derived by Stange [4] using a statistical method (Einflußgrößenrechnung). The result is in the form

$$\sigma_Z{}^2 = \frac{PQ}{g}\left[Pw_Q(1 + C_Q{}^2) + Qw_P(1 + C_P{}^2)\right]. \tag{18}$$

The quality measure σ_Z^2 of random mixture depends on masses (P; Q), on mean masses of particles w_P and w_Q, and variation numbers C_P and C_Q in the mixture containing parts (P) and (Q). The two mean values w_P and w_Q are a measure of the trituration, the two variation numbers C_P and C_Q are the measure of the uniformity of the pulverizing. Altogether is the variance σ_Z^2 at given mixture proportional to reciprocal value of the sample mass g contrary to Eq. (13), where is variance for set of particles proportional to reciprocal number of particles in the sample n.

In Tables 1a, b, c, there are given examples of characteristics of three different two-components mixing tests performed with uncoloured sand (P) and coloured sand (P). Tests marked 2W and 3W were performed with 2 and 3 mass% of water in order to avoid the particles segregation. For this tests was used a good mixing device, described in [4]. There are presented mass characteristics of the mixture. Here, practical examples of powder data for calculation by Eq. (19)

$$\sigma_Z{}^2 = \frac{PQ}{g}(Pw_Q + Qw_P) \tag{19}$$

are presented.

Table 1a: Characteristics of tested mixtures

Test No.	**Total mass [g]**	**Component P**			
		Grain size [mm]	**Abs. mass of component [g]**	**Rel. mass of component P [g]**	**Mean grain mass w_P [10^{-6}g]**
1	250	0.4 – 0.6	150	0.6	177.0
2W	250	0.2 – 0.3	175	0.7	24.2
3W	250	0.1 – 0.15	175	0.7	2.8

Table 1b: Characteristics of tested mixtures

Test No.	Total mass [g]	Component Q			
		Grain size [mm]	Abs. mass of component [g]	Rel. mass of component Q [g]	Mean grain mass w_Q [10^{-6}g]
1	250	0.4 – 0.6	100	0.4	190
2W	250	0.4 – 0.6	75	0.3	190
3W	250	0.4 – 0.6	75	0.3	190

Table 1c: Characteristics of tested mixtures

Test No.	Sample mass [10^{-3}g]	Measure of mixing quality σ_Z^2 x 10^4 [-]	Standard deviation σ_Z [%]
1	71	6.25	2.50
2W	65	4.53	2.13
3W	66	4.26	2.06

In last two columns of above given tables there are presented the measures of mixing quality, variance σ_Z^2 and standard deviation σ_Z. In Eq. (19), the variance numbers C_P and C_Q are neglected. Stange [4] shows that the values of variation number quadrates C_P^2, C_Q^2 used in Eq. (18) are in this calculation less than 0.1.

4. Conclusions

In the part about particles mixing we have derived with Lacey [1] the lowest limit for the measure of quality of mixing using binomial statistic, the variance σ_R^2 (Eq. (13)). In this case, the upper limit is expressed by Eq. (15). Mixing quality σ_Z^2 determined from mass measurement (see Eq. (18)) was derived by Stange [4] and the theory was successfully applied by Poole et al. [3] and by Poux et al. [6]. Table 1 illustrates the calculation of three examples of tests with two coloured sands. The theory and verification is instructive for our methods of mixing dry plasters and binders used at material research and for preparation samples for hydration kinetics measurement.

Acknowledgments

This research has been supported by the Ministry of Education, Youth and Sports of the Czech Republic under project No. 7AMB13AR01, by the Czech Science Foundation under project No. 14-04522S, and by the Ministry of Science, Technology and Production Innovation of the Argentine Republic within the scientific and technical cooperation ARC-12/12.

References

[1] LACEY, P.M.C. The mixing of solid particles. In *Transactions of the Institution of Chemical Engineers*. 1943. 21. p. 53-59.

[2] LACEY, P.M.C. Developments in the theory of particulate mixing. In *Journal of Applied Chemistry*. 1954. 4. p. 257-268. DOI: 10.1002/jctb.5010040504

[3] POOLE, K.K. – TAYLOR, F.R. – WALL, P.G. Mixing powders of fine-scale homogeneity: studies of batch mixing. In *Transactions of the Institution of Chemical Engineers*. 1964. 42. p. T305-T315.

[4] STANGE, K. Die Mischgüte einer Zufallsmischung als Grundlage zur Beurteilung von Mischversuchen. In *Chemie Ingenieur Technik*. 1954. 26. p. 331-337.

[5] HOLDIG, R.G. *Fundamentals of Particle Technology*, Midland Information Technology and Publishing, Leicestershire, Shepshed, 2002, pp. 173. ISBN 0-9543881-0-0

[6] POUX, M. – FAYROLLE, J. – BERNARD, J. – BRIDOUX, D. – BOSQUET, J. Powder mixing: some practical rules applied to agitated systems. In *Powder Technology*. 1991. 68. P. 213-234. DOI: 10.1016/0032-5910(91)80047-M

Computational evaluation of thermal conductivity and diffusivity using the boundary integral technique

Jiří Vala, Petra Jarošová

Faculty of Civil Engineering, Brno University of Technology,
Veveří 95, 602 00 Brno, Czech Republic,
e-mail: vala.j@fce.vutbr.cz, jarosova.p@fce.vutbr.cz

Abstract: *Evaluation of thermal conductivity and diffusivity (or capacity, alternatively) from direct non-stationary measurements relies i) on the experimental arrangement of a nearly closed physical system, avoiding other relevant physical processes, ii) on some very special geometrical configuration, iii) on a sufficiently simple, exact and robust computational algorithm, supporting just i) and ii). Since iii) contains contradictory requirements, the proper analysis of identification problems with reduced dimension is needed. The paper demonstrates an approach of such type, exploiting fundamental solutions in cylindrical coordinates together with the boundary integral technique on material interfaces.*

Keywords: *Heat conduction, inverse problems, fundamental solutions, boundary integral method.*

1. Introduction

The progress in computational mechanics of last decades leads to numerical modelling and simulation of still more complicated multi-physical problems, containing a lot of serious problems in several areas, e.g. a) in their transparent physical formulation, utilizing available micro-structural data, b) in the mathematical analysis of existence and uniqueness of solutions in some appropriate abstract function spaces, c) in the convergence of sequences of approximate solutions from iterative numerical algorithms, including errors coming from practical hardware and software implementations. However, the validity of all numerical results depends in all cases d) on the reliable values of all (mostly empirical or semi-empirical) material characteristics, suggested by a) end utilized (usually under some additional assumptions on their range, behaviour, etc.) in b) and c). The development of new materials, structures and technologies makes d) more difficult, because of the absence of practical experience and simple algebraic evaluation formulae.

Unlike the complex simulation tools, the numerical simulation of both laboratory and in situ experiments, with the aim to identify d), should avoid multi-physical phenomena, being related to sufficiently simple, namely in geometrical configuration, and (nearly) physically closed systems, as explained in [5]. In this paper we shall pay attention namely to the identification of basic thermal characteristics of non-stationary heat conduction, considered as constant in a macroscopically homogeneous and isotropic material specimen in some acceptable temperature range, with a priori known constant initial temperature is constant. Most of such assumptions could be removed, or at least partially reduced, but this would generate very complicated reader-unfriendly formulations, obtained from formal manipulations with MAPLE software. However, most ideas can be applied to more general problems of heat transfer also to mass transfer – cf. [17].

The proper physical formulation of thermomechanical problems comes from the balance equations of selected scalar quantities, as mass, (linear and angular) momentum, energy, etc. Under above sketched simplifying assumptions (for more details see lower), following [1], the complete system of equations of evolution degenerates to just one, coming from the balance of (thermal) energy, with the (absolute) temperature T as an only unknown space- and time-dependent variable. If the values of both needed material characteristics, namely the thermal capacity κ, related to the unit volume, and the thermal conductivity λ, are prescribed, for certain (very special) classes of volume and surface loads the fundamental solutions are known; their overview in [6] relies on their derivation in [3], namely for the case of the formal volume load represented by the Dirac distribution both in the time and in the space variable. The thermal diffusivity $\alpha = \lambda/\kappa$ is used instead of κ frequently. In some special geometrical configuration, especially in the hot-ball method with a (theoretically) infinitely small ball, explicit formulae for the evaluation of time redistribution of T can be derived, which can be applied to the inverse problem of setting λ and α, too. Apart from some technical difficulties, the same is allowed to be done for the hot-wire method, considered in cylindrical coordinates: the evaluation of λ, recommended in [7], exploits just the first two terms in corresponding decompositions to Taylor series, whereas the more precise analysis of [8] makes it possible to determine also α, as demonstrated in [14] with help of [16]. However, the hot-plate approaches simplify all their considerations to one-dimensional heat conduction typically, as in [15], offering various configurations: i) with a (sufficiently large) specimen located between two plates, at least one heated, ii) with a specimen replaced by some massive building structure (which is useful for measurements in situ) and only one heated plate, etc., in all such cases respecting the own thermal conductivity and diffusivity of plate(s). The idea of upgrade of such evaluations to more realistic three-dimensional configurations, seems to be simple, but brings remarkable technical difficulties, sketched and discussed in this paper. Unfortunately, they cannot be overcome easily using the general results and algorithms of [11] or [4]; [9] is still restricted to one-dimensional problems, as well as the analysis of needed Tikhonov regularization by [18], [12] applies the Laplace transform to the three-dimensional determination of an unknown heat source only, which can be expressed by integration of above mentioned Dirac distributions easily.

The standard iterative numerical solution of an initial and boundary value problem of heat conduction with step-by-step updated λ and α, e.g. that using the finite element, finite volume, finite difference or some usual mesh-free approaches, is clearly the most general alternative, frequently used in commercial software packages, but is rather expensive; even the potential reduction of dimension due to a special experimental configuration may not be effective. The boundary integral method, exploiting the knowledge of some form of a fundamental solution, developed in [2], [13] and [10], is able to transfer most or all numerical calculations from the three-dimensional sets to their two-dimensional boundaries, with possible further reduction of dimension for a special configuration. This paper tries to apply this approach to certain simple version of the above introduced hot-plate problem, to obtain a robust computational support of measurements in situ, using a rather simple and inexpensive direct measurement equipment.

2. Fundamental solutions of heat conduction equation

Let us consider an open set Ω in the 3-dimensional Euclidean space R^3, whose boundary consists of 2 disjoint parts Γ and Θ. The time development of the temperature T, as well as of further physical quantities, can be studied on the time interval I, starting from zero time. The Cartesian coordinate system $x = (x_1, x_2, x_3)$ is considered on Ω, together with the time t on I. The standard notation of Hamilton operators $\nabla = (\partial/\partial x_1, \partial/\partial x_2, \partial/\partial x_3)$, of central dots for scalar products in R^3, of Laplace operators $\Delta = \nabla \cdot \nabla = (\partial^2/\partial x_1^2, \partial^2/\partial x_2^2, \partial^2/\partial x_3^2)$ and of upper dots for partial derivatives with respect to t will be used here, as well as that of unit (formally) outward local normal vectors $n(x) = (n_1(x), n_2(x), n_3(x))$ on Γ. All introduced sets need to be smooth enough to admit such definitions; this is assumed to be valid for a reasonable geometrical configuration.

The proper physical formulation of thermo-mechanical problems comes from the balance equations of selected scalar quantities, as mass, (linear and angular) momentum, energy, etc. Under above sketched simplifying assumptions, following [1], the complete system of equations of evolution degenerates to just one, coming from the balance of (thermal) energy,

$$\kappa \dot{T} + \nabla g = f \text{ on } \Omega \times I \tag{1}$$

where, in addition to the (absolute) temperature $T(x,t)$, $g(x,t) = (g_1(x,t), g_2(x,t), g_3(x,t))$ denotes the thermal flux and $f(x,t) = (f_1(x,t), f_2(x,t), f_3(x,t))$ and the volume heat source,

$$g + \lambda \nabla T = 0 \text{ on } \Omega \times I \tag{2}$$

represents the Fourier constitutive law,

$$g \cdot n = q \text{ on } \Gamma \times I \tag{3}$$

the boundary condition of Neumann type, with the prescribed surface heat source $q(x,t) = (q_1(x,t), q_2(x,t), q_3(x,t))$, and finally

$$T - T_e \text{ on } \Theta \times I \tag{4}$$

the boundary condition of Dirichlet type; here (for simplicity) we shall consider the temperature T_e of the external environment as a constant, such that $T = T_e$ is satisfied everywhere on Ω in the initial time $t = 0$, too. Let us notice that g can be eliminated from the system (1) – (4) easily: (1) and (2), using the notation $f_* = f/\kappa$, yield

$$\dot{T} - \alpha \Delta T = f_* \text{ on } \Omega \times I, \tag{5}$$

whereas (2) and (3) result

$$-\lambda \nabla T = q \text{ on } \Gamma \times I; \tag{6}$$

both constants λ and α still remain in (5) and (6).

Assuming $f_*(x,t) = Q\delta_y(x)\delta_0(t)$ where Q is an arbitrary constant, $\delta_y(x)$ dentotes the Dirac distribution in the variable x with its unit impulse in some point $y \in R^3$ and $\delta_0(t)$ the Dirac

distribution in the variable t with its unit impulse in zero time, the fundamental solution of (5) for is

$$T(x,t) = (Q/(4a\pi t)^{3/2}) \exp(-(x-y)\cdot(x-y)/(4at)) ; \quad (7)$$

This can be verified easily using e.g. MAPLE software or *symbolic* toolbox from MATLAB environment, as alternatives of long formal calculations. This is also just the formula, useful (supplied by an initial conditions and integrated in time, coming from the formal Dirac source distribution to the Heaviside function) in the hot-ball considerations, but it is not quite easy to adopt this to significantly more general boundary (and initial) conditions, as needed in our situation.

3. Implementation of special boundary conditions

Our design of the measurement equipment will be very simple. Its technical solution is similar to that described in [15], including practical examples, with the following innovations: i) no massive plates are implemented, only one very thin heating layer of the annulus shape, ii) the temperature sensor is located in the annulus centre, iii) the proper three-dimensional computational analysis should be performed (no artificial one-dimensional simplification, neglecting all heat flux components except e.g. $q_1(x)$, is needed). The right axonometric scheme of Figure 1 can be understood in the following sense: the plane $x_3 = 0$ represents the contact between a massive specimen (an analyzed part of a building structure) and a massive insulation layer belonging to the measurement equipment; the annulus surface heat source generates, starting from the initial time, certain constant surface heat flux q to both adjacent layers. The time interval should be not too long, to avoid the heat transfer to the environment from some of these layers. Consequently we are allowed to take $\Omega - R^3$, only with one boundary condition of the type (6) on $\Gamma - R^2$, with $n = (0,0,1)$ everywhere. Thus we are able, applying the cylindrical coordinate system (ρ,ϕ,z) with $x_1 = \rho\cos\phi, x_2 = \rho\sin\phi$, $x_3 = z$ (thus $0 \leq \rho$ and $0 \leq \phi \leq 2\pi$), to convert (7) into its slightly modified form

$$T(r,z,\rho,\phi,\varsigma,t) = (Q/(4a\pi t)^{3/2}) \exp((-(r-\rho\cos\phi)^2 - (r-\rho\cos\phi)^2 - (z-\varsigma)^2)/(4at)) \quad (8)$$

where the evaluation of temperature is done in certain point $(r,0,z)$ with $r \geq 0$ (0 here can be inserted without loss of generality, because of the cylindrical shape everywhere) for the Dirac source distribution $(\rho,\phi,0)$. The new constant $\varsigma \geq 0$, interpretable even as a function of ρ, does not disturb the property of fundamental solution of (5) (this can be verified e.g. using MAPLE again), although (6) is not satisfied.

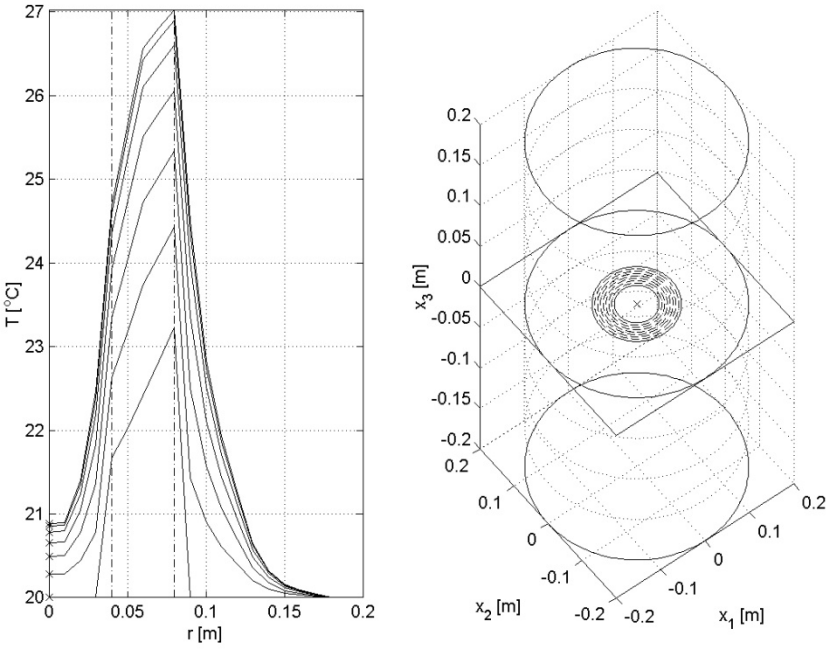

Figure 1: Radial symmetrical geometrical configuration of the measurement equipment (right scheme). Example of redistribution of temperature from a computational simulation attempt (left graph).

Assuming that the values of λ and α are given (or can be at least estimated, as a starting point for some iterative process), for the reasonable evaluation of T for any triple (r, z, t) it remains only to adopt (7) to satisfy (6) on Γ. However, this is the most difficult step in our considerations. In the first place, we must come from the Dirac source distributions, aside from Q, to the constant value of q for any ϕ and for every ρ between certain values ρ_1 and ρ_2, maintained during realistic experiments, as evident from the right scheme of Figure 1. Integrating over ϕ and ρ (the Jacobi determinant is just equal to ρ, for $0 \leq \phi \leq \pi$ and $\pi \leq \phi \leq 2\pi$ there are identical results) and also over t with $t - \tau$ in (8) instead of t where $\tau \in I$, we come to the result

$$T(r,z,t) - T_0 + 2\int_0^t (Q/(4\alpha(t-\tau))^{3/2}) \int_0^\infty \rho\, T_r(r,\rho,t)\, T_z(r,z,\varsigma,t)\, d\rho\, d\tau\,, \tag{9}$$

making use of the notations

$$T_r(r,\rho,t) = \int_0^\pi \exp((-r^2 - \rho^2 + 2\rho r\cos\phi)/(4\alpha t))\, d\phi\,, \tag{10}$$

$$T_z(z,\rho,\varsigma,t) = \exp(-(z-\varsigma)^2/(4\alpha t))\,; \tag{11}$$

the dependence of ς on ρ should be discovered from (6).

For the sake of brevity, for the first time step let us reformulate (9), together with (10) (where the numerical integration with respect to ϕ is also required) and (11), in the discrete form, namely for the rectangular quadrature rule, applying the Einstein summation rule to indices $i, j \in \{1, \ldots, N\}, h = H/L$ where L is the length of I, $N \to \infty$, as

$$T(r,z,h) - T_0 = (2Q/(4\alpha h)^{3/2})\, h\, \eta_j\, T_r(\eta_i,\eta_j,h)T_z(\eta_i,\eta_j,\varsigma_j,h)\,. \tag{12}$$

Consequently, thanks to (11), we have

$$\lambda\, \partial T_z/\partial z(z,\rho,\varsigma,t) = -2\lambda\,((z-\varsigma)/(4\alpha t))\, T_z(z,\rho,\varsigma,t)\,, \tag{13}$$

which is needed, in particular for zero-valued z, in (6).

Now we need to distinguish between two constant values of λ: for $z \geq 0$, denoted by λ_1, and for $z \leq 0$, denoted by λ_2; the same is true also for α and κ, thus we have also (in general) different T_{r1} and T_{r2}, T_{z1} and T_{z2}, etc. Using the simplifying notation (for both such cases again) $A_{ij} = (2Q/(4\alpha h)^{3/2})$ h $\eta_j T_r(\eta_i,\eta_j,h)$ and $C_j = \exp(-\varsigma_j^2/(4\alpha_j h))$, we are able to introduce

$$F_{i1} = A_{ij1}C_{j1} - A_{ij2}C_{j2}\,, F_{i2} = (\varsigma_{j1}\lambda_1/(2\alpha_1 h))A_{ij1}C_{j1} + (\varsigma_{j2}\lambda_2/(2\alpha_1 h))A_{ij2}C_{j2} - q\chi(\eta_i) \tag{14}$$

where χ means the characteristic function of the radius interval $[\rho_1,\rho_2]$. Let us notice that all conditions $F_{i1} = 0$ guarantee (for discrete points) the continuity of T on Γ, whereas all conditions $F_{i2} = 0$ force just the validity of our modification of (6). Since ς_{j1} and ς_{j2} are hidden in C_{j1} and C_{j2}, but not in A_{ij1} or A_{ij1}, (14) with some estimated values ς_{j1} and ς_{j2} occurring in F_{i2} explicitly represents a system of $2N$ linear algebraic equations with $2N$ variables only. It is then easy to calculate the derivatives of F_{i1} and F_{i2} with respect to variables ς_{j1} and ς_{j2}, i.e.

$$F_{i1,j1} = -(\varsigma_{j1}/(2\alpha_1 h))A_{ij1}C_{j1}\,,\; F_{i1,j2} = (\varsigma_{j2}/(2\alpha_1 h))A_{ij2}C_{j2}\,. \tag{15}$$

$$F_{i2,j1} = \lambda_1(1/(2\alpha_1 h) - (\varsigma_{j1}/(2\alpha_1 h))^2)A_{ij1}C_{j1}\,,\; F_{i2,j2} = \lambda_1(1/(2\alpha_2 h) - (\varsigma_{j2}/(2\alpha_2 h))^2)A_{ij2}C_{j2}\,, \tag{16}$$

thus the classical Newton iterative procedure reads $\boldsymbol{DF}(\boldsymbol{\sigma} - \tilde{\boldsymbol{\sigma}}) = \boldsymbol{F}$ where $\boldsymbol{DF}$ refers to the matrix with the first N lines compound from $F_{i1,j1}$ and $F_{i1,j2}$ by (15) and the remaining N lines compound from $F_{i2,j1}$ by (16), whereas $\boldsymbol{F}$ refers to the vector consisting of F_{i1} and F_{i2} by (14); similarly $\boldsymbol{\sigma}$ is the vector including ς_{i1} and ς_{i2} and $\tilde{\sigma}$ its improved value.

To cover the whole interval I, the second, third, etc. time steps can be performed in the same way, to cover the whole interval I, corresponding to the left side of (12) $T(r,z,2h) - T(r,z,h)$, , $T(r,z,3h) - T(r,z,2h)$, etc., instead of $T(r,z,h) - T_0$. This completes the deterministic way (although so system numerical errors occur for a finite N in practical computations) of the analysis of time redistributions of $T(r,z,3h)$, evidently under the assumption (only theoretical here) of a priori perfect knowledge of all values of applied material characteristics.

4. Least squares algorithm for identification of material characteristics

For simplicity, let us suppose that we have only one temperature sensor, recording (in the centre of the annulus in Γ) the temperature $T(0,0,t)$ for $t \in \{0,h,2h,3h,\ldots\}$, as sketched (by daggers) on the left edge of the left graph of Figure 1; such values will be denoted by $\vartheta(t)$. Clearly

$$\vartheta(0) = T_e, \vartheta(h) \approx T(0,0,h),\ \vartheta(2h) \approx T(0,0,2h), \vartheta(3h) \approx T(0,0,3h), \tag{17}$$

Neglecting the above mentioned system errors of the evaluation of $T(0,0,t)$, with some reasonable estimate of material characteristics, we can modify their values to satisfy (17) in the best way in the least squares sense. This can be done using the minimization of the formally simple cost function, relying on the weighted norm in the Euclidean space R^N with certain weight $w(h), w(2h), w(3h), \ldots,$

$$F(\lambda_1, \alpha_1) = \sum_{s=1}^{N} w(sh) \left(\vartheta(sh) - T(0,0,sh)\right)^2. \tag{18}$$

Clearly all evaluations of T on the right side of (18) need both λ_1, α_1 and λ_2, α_2 as input values. The left side of (18) respects the standard situation: λ_1, α_1 refer to the specimen (whose thermal characteristics need to be identified) and λ_2, α_2 to the insulation layer (whose thermal characteristics must be guaranteed). The weights should express, similarly to [7], the different reliability of particular measurements: the first ones are affected by the (theoretically) immediate change of the surface load from zero to its final value, the last ones may be disqualified by the heat transfer into the environment, neglected in our calculations.

Although (18) cannot be handled using linear regression, because of the complicated non-linear algorithm of evaluations of T, it represents finally only a function of two positive variables, which can be handled in a rather efficient and robust way, using appropriate functions of the *optimization* toolbox from the MATLAB environment. This makes our approach practicable, although its implementation involves a lot of technical difficulties, not discussed in this paper in more details: e.g. the passage from (9) to (12) performs the numerical evaluation of improper integrals and the convergence of the Newton algorithm cannot be guaranteed without sufficiently good estimates of λ_1, α_1.

5. Conclusions

An alternative approach to the identification of thermal conductivity and diffusivity of building materials, making use of the evaluation of boundary integrals, has been presented in this paper. Both the software development in MATLAB and the optimal composition of the measurement equipment is still in progress. The approach seems to be applicable to practical data from well-considered measurement, but some its properties, namely the analysis of uncertainty and separation of errors of measurements and system and approximation errors from numerical simulations, need deeper analysis.

Acknowledgement.

This research has been supported by the project of specific university research of Brno University of Technology, No. FAST-S-14-2346.

References

[1] BERMÚDEZ DE CASTRO, A. *Continuum Thermomechanics*. Birkhäuser, Basel, 2005.

[2] BROŽ, P., PROCHÁZKA P. *Metoda okrajových prvků v inženýrské praxi (Boundary Element Method in Engineering Practice)*. SNTL, Prague, 1987. (In Czech.)

[3] CARSLAW, H. S., JAEGER, J. C. *Conduction of Heat in Solids*. Clarendon Press, Oxford, 1959.

[4] COLA, M. J., ORLANDE, H. R. B., DULIKRAVICH, G. S. Inverse and optimization problems in heat transfer. *Journal of the Brazilian Society of Mechanical Sciences and Engineering* 28 (2006), pp. 1–24.

[5] ČERNÝ, R., et al. *Complex Systems and Methods for Directed Design and Assessment of Functional Properties of Building Materials: Assessment and Synthesis of Analytical Data and Construction of the System*. Czech Technical University in Prague, 2010.

[6] DAVIES, M. G. *Building Heat Transfer*. J. Wiley & Sons, Hoboken, 2004.

[7] EN ISO 8894-1. *Refractory materials – Determination of thermal conductivity – Part 1: Hot-wire methods (cross-array and resistance thermometer).* CEN (European Committee for Standardization), 2010.

[8] GUTIERREZ-MIRAVETE, E. Heat conduction in cylindrical and spherical coordinates. In: *Conduction Heat Transfer*, Chapter 3. Hartford University, 2006.

[9] HON, Y. C., WEI, T. *A fundamental solution method for inverse heat conduction problem*. Engineering Analysis with Boundary Elements, 2004, vol. 28, p. 489-495.

[10] HSIAO, G. C., Wendland, W. L. *Boundary Integral Equations*. Springer, Berlin, 2008.

[11] ISAKOV, V. *Inverse Problems for Partial Differential Equations*. Springer, Berlin, 2006.

[12] MIERZWICZAK, M., KOŁODZIEJ, J.A. J.A. Application of the method of fundamental solutions with the Laplace transformation for the inverse transient heat source problem. *Journal of Theoretical and Applied Mechanics*, 2012, vol. 50, p. 1011-1023.

[13] SLÁDEK, J., SLÁDEK V. *Singular Integrals in Boundary Element Method*. Computational Mechanics Publications, Southampton, 1998.

[14] ŠŤASTNÍK, S.; VALA, J. Identification of thermal characteristics of a high-temperature thermal accumulator. *Thermophysics 2012 – Conference Proceedings*, in Podkylava (Slovak Republic), Slovak Academy of Sciences, Bratislava, 2012, p. 214-222.

[15] ŠŤASTNÍK, S., VALA, J., KMÍNOVÁ, H. Identification of thermal technical characteristics from the measurement of non-stationary heat propagation in porous materials. *Kybernetika*, 2007, vol. 43, p. 561-576.

[16] VALA, J. Least-squares based technique for identification of thermal characteristics of building materials. *International Journal of Mathematics and Computers in Simulation*, 2011, vol. 5, p. 126-134.

[17] VALA, J., JAROŠOVÁ, P. Identification of the capillary transfer coefficient in porous building materials. *11th International Conference on Numerical Analysis and Applied Mathematics (ICNAAM*), in Rhodos (Greece), American Institute of Physics, Melville, 2013, p. 1004-1007.

[18] ZHAO, Z., XIE, O., MENG, Z., YOU, L. Determination of an unknown source in the heat equation by the method of Tikhonov regularization in Hilbert scales. *Journal of Applied Mathematics and Physics*, 2014, vol. 2, p. 10-17.

Thermal properties of colloids

Lucie Trhlikova, Lenka Dohnalova, Katerina Valentova, Oldrich Zmeskal

Brno University of Technology, Faculty of Chemistry, Purkynova 118, CZ-612 00 Brno, CZECH REPUBLIC, zmeskal@fch.vutbr.cz

Abstract: *The article discusses the use of transient methods to study the thermal properties of liquids. More specifically it is devoted to studying the properties of colloids based on oil and water. The result is the dependence of thermal diffusivity, thermal conductivity and specific heat as the function of temperature and ratio of both components.*

Keywords: *transient method, fractal model of heat transport, thermal diffusivity, thermal conductivity, specific heat*

1. Introduction

The basic principle of transient methods is based on supplying energy to the substance, in our case to liquid, from heat source which is in direct contact with the measured substance. From the heat source is spread thermal response, measured by the temperature sensors placed at a certain distances from the thermal source. Advantage of transient method consists in that the surface of the sample material does not affect the measurement, since the thermal response occurs inside the sample.

There are a few heating methods of sample, which was based for these measurements; these methods have been described in article thermal properties of building materials [1]. The step-wise method was selected for our research.

The main difference between the previous measurements of solids to measuring of colloids is that the heat in liquids is not only spreads heat conduction, but also by flow [2]. In the article were measured as separate liquids (water, oil) and colloids, which consisted in varying ratio water and oil.

2. Studied materials

2.1 Colloids

Colloidal substance comprises two each other immiscible components. The liquid dispersed in liquid, the resulting system is called an emulsion. The emulsion was divided in two basic types according to the polarity of the dispersion medium and dispersed material. One is oil in water emulsion (o / w) and second is water in oil emulsion (w / o).

In this work are presented results of measurement of basic components colloids (water and oil) and their mixtures. The oil was mixed with water in different volumetric ratio (o : w = 25 : 75, 50 : 50, 75 : 25). The total volume of the emulsion was 650 ml. Thermal properties were measured in all these systems.

2.2 Water and oil

Water is commonly known liquid. Its parameters are measured and we can compare these values. The dependence of the thermal conductivity on the temperature is shown in Figure 1 [9], [10].

In our measurements was used sunflower oil, which was mixed with water. This system was chosen because we can use oil not only in the food industry but also in the cosmetic and pharmaceutical industries. Sunflower oil, which we used in experimental part, contains mainly linoleic acid in triglyceride form.

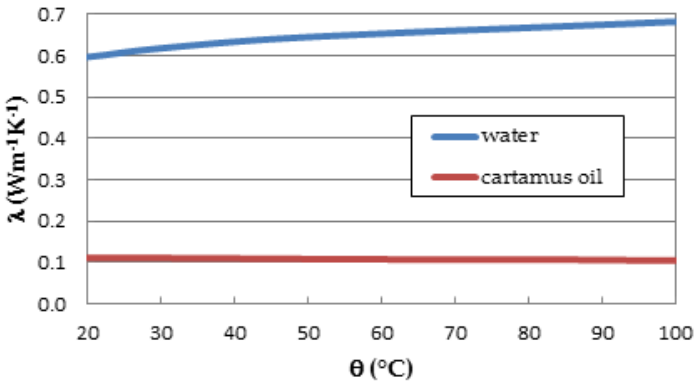

Figure 1: Temperature dependences of thermal conductivity of water and cartamus oil

3. Measured methods

3.1 Experimental equipment

Thermal properties were measured in Dewar´s container (thermos bottle, diameter $d = 7{,}8\ \text{mm}$) on Figure 2. Temperature sensors were placed in a bottle (thermocouple, RTD - platinum thermometers). Heat was supplied to the system through the resistor (HSA25 22R) built-in to metal planar source. Ideal planar heat source has dimension $D = 2$.

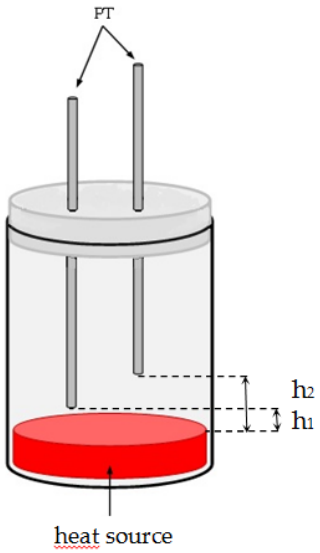

Figure 2: Experimental equipment for measuring of thermal properties of liquids

3.2 Experimental measurement

The experiment was set up for step-wise [5], [6], [7] . The measurement was realized for 10 cycles. The measurement was realized for 10 cycles. One cycle was 4 hours, when the first heating was realized for 2 hours and then cooling was carried out same time. The total duration of the experiment therefore amounted to 40 hours (see on Fig. 3).

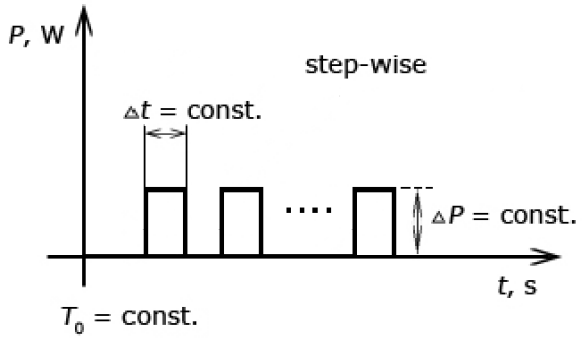

Figure 3: Principal of step-wise, ramp-wise and combined way of measurement

Default parameters have been set in the EMA program and start the measurement. Measured data contain time, voltage and current through the heat source (Agilent 6622) and a temperature corresponding to the thermocouple voltage, measured using the Agilent 34420. Data were processed and evaluated.

3.3 Principal of evaluation of experimental results

Evaluation of experimental data was performed using the relationship

$$\Delta T(t) = At^{\alpha} \exp\left(-\frac{t_{\mathrm{D}}}{t} - \frac{t}{t_{\mathrm{R}}}\right), \quad (1)$$

where A is absorption coefficient determined as $A = P(4\pi a)^{\alpha} / 4\pi a \alpha \lambda$, relaxation time determined as $t_{\mathrm{R}} = R^2/4a$, diffusion time determined as $t_{\mathrm{D}} = h^2/4a$, where $h = c\sqrt{t_0^2 - t_{\mathrm{T}}^2}$ is the sample thickness, $R = 2ct_0/\alpha$ is a heat losses parameter and $a = c^2 t_0/2\alpha$ is thermal diffusivity.

A parameter characterizing the properties of the heat source α can also be calculated from the term

$$\alpha = \alpha_0 - s = \alpha_0 + \frac{D-E}{2}, \quad (2)$$

where D is the dimension of the heat source (ideal for surface becomes a source of value) $D = 2$), E is the dimension of the space in which the heat spread (for 3D space $E = 3$). The parameter α depends on the type of experiment (the value of the coefficient α_0). For pulse method the coefficient $\alpha_0 = 0$, , for step wise method the coefficient will be $\alpha_0 = 1$, and for ramp-wise method $\alpha_0 = 2$ [3], [4].

Data was analyzed and temperature parameters were obtained using regression methods

$$y(t) = \ln\Delta T(t) = \ln A + \alpha \ln t - \frac{t_D}{t} - \frac{t}{t_R} = m_0 + m_1 x_1 + m_2 x_2 + m_3 x_3 , \quad (3)$$

where $x_1 = \ln t$, $x_2 = 1/t$ a $x_3 = t$. From parameters m_0 , m_1 , m_2 a m_3 we can obtain parameter α, $\alpha = (D - E + 2)/2 = m_1$ (or fractal dimension D from heat source on 3D space, E=3), heat loss parameter, which is directly proportional to the diameter of the sample $R = h\sqrt{t_R / t_D} = h/\sqrt{m_2 m_3}$, thermal diffusivity $a = h^2/4t_D = -h^2/4m_2$ and thermal conductivity $\lambda = P/(4\pi\alpha A)\cdot(4\pi\alpha)^{\alpha} = P/\left(4\pi m_1 e^{m_0}\right)\cdot\left(-\pi h^2/m_2\right)^{m_1}$. The heat capacity can be calculated from the previous parameters and known density $c_p = \lambda/\rho a$.

The results of extrapolation for 3D space E = 3, ideal planar heat source with fractal dimension D = 2 and step-wise method of measurement $(\alpha_0 = 1)$ using the equation (**Error! Reference source not found.**. We obtain parameter ⌾ = 0,5. Measurement was performed on sections of data. Data was reduced by 1 to 9 point (time interval). We obtain 10 groups of parameters, which were based on uncertainly.

The result of approximation of absorption coefficient, diffusion time and relaxation time determined parameters for this condition, when we use linear regression.

4. Results and discussion

Thermo physical parameters were determined on the basis of extrapolated dependent parameters (diffusion, absorption, relaxation).

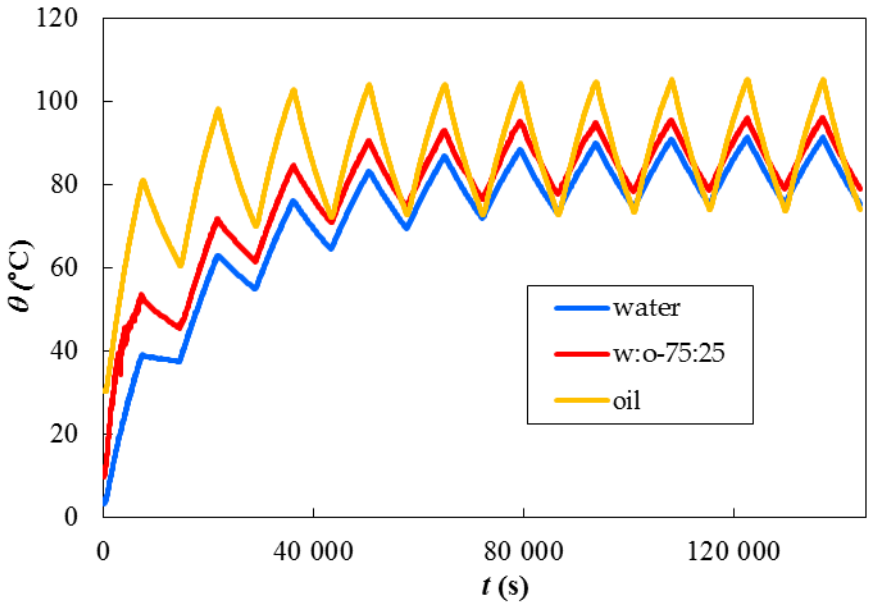

Figure 4: Thermal responses of measured colloids

In Fig. 4 is comparison extrapolated data of thermal diffusivity water, emulsion and oil. Water and oil are approaching tabulated value. Deviation from tabulated data was caused by loss heat around cover of bottle. We expected thermal diffusivity of emulsion between tabulated data (water, oil). But results are different. It was caused by heat transfer, which is

realized conduction and convection. Final data deviate from the trend, because heat transfer was mainly convection.

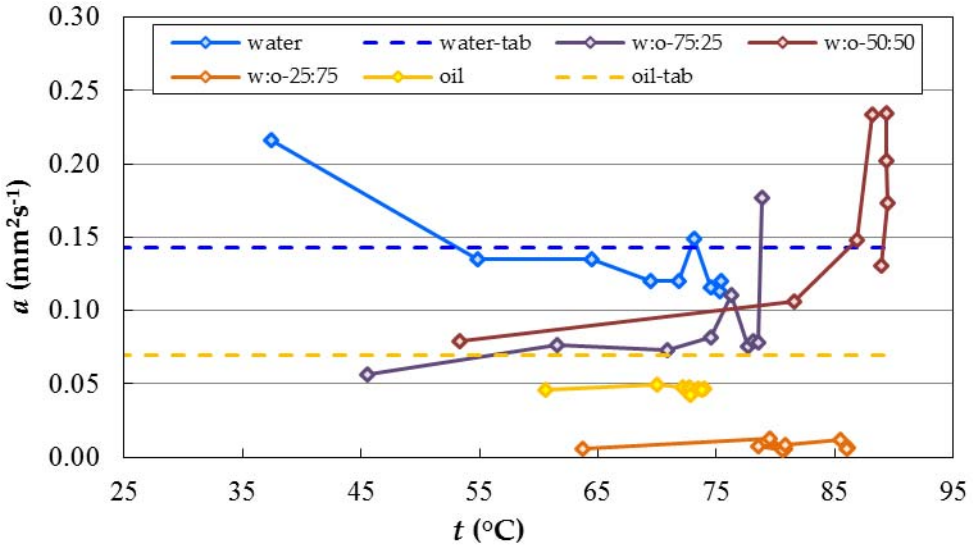

Figure 5: Comparison extrapolated data of thermal diffusivity (tabulated value for 20°C)

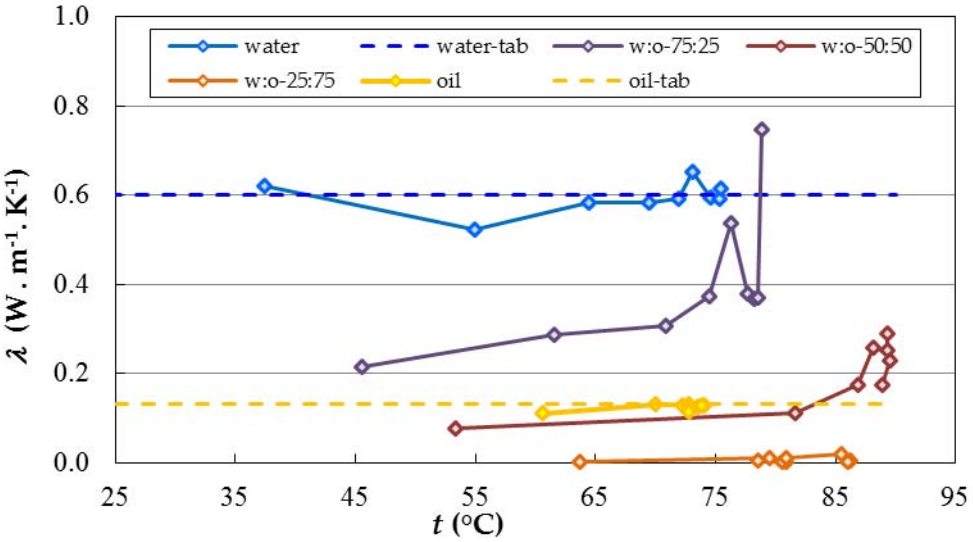

Figure 6: Temperature dependences of thermal conductivity (tabulated value for 20°C)

In Fig. 6 water and oil are around tabulated value. Conductivity of emulsions decreases with the change their concentration. With the addition of oil to water, thermal conductivity is lower.

Measured data of water and oil are around tabulated value how demonstrate Fig. 7. Specific heat declines with ratio water to oil. When we add more oil, it is go down. Points that are not depending were caused by convection transfer of heat.

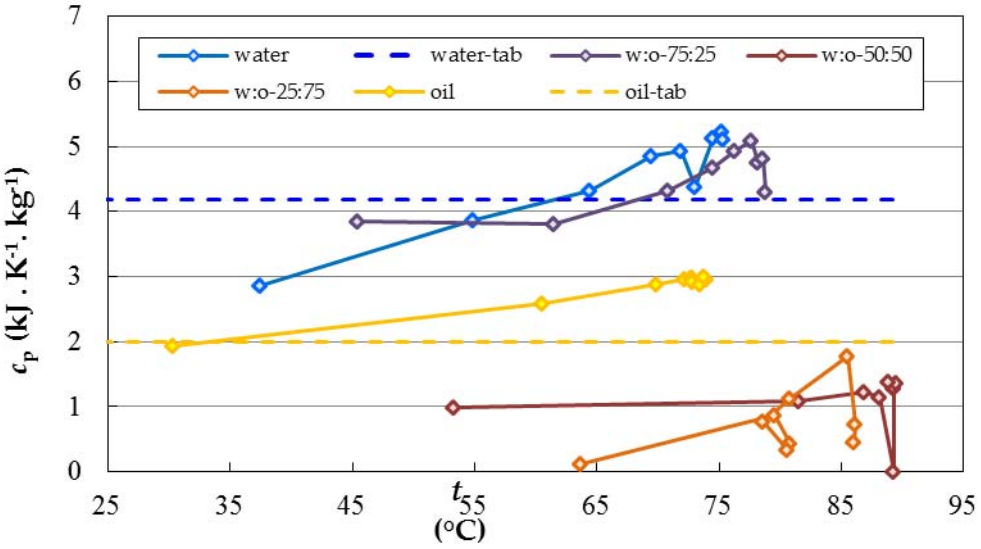

Figure 7: Temperature dependences of specific heat (tabulated value for 20°C)

Table 1: The results of thermophysical parameters for measured colloids for temperature 20 °C

	ratio	a (mm^2·s^{-1})	λ (W·m^{-1}·K^{-1})	c_p (kJ·kg^{-1}·K^{-1})
water		0.135	0.592	1.833
water – tab.		0.143	0.600	4.180
oil		0.046	0.112	1.737
oil – tab.		0.070	0.130	2.000
emulsion 1	1:3	0.058	0.231	3.021
emulsion 2	1:1	0.077	0.072	0.627
emulsion 3	3:1	0.005	0.001	0.004

5. Conclusion

In this work were studied and characterized thermophysical parameters of water, oil and its emulsions, namely the thermal diffusivity, thermal conductivity and specific heat. In addition, optimal conditions were determined by extrapolation of the production of the ideal planar heat source.

The Table 1 shows the results of the thermophysical parameters measured samples at 20 °C. From the table it can be seen that the lowest value of thermal conductivity at 20 ° C the emulsion 3 which also achieves the lowest values for the thermal conductivity and thermal capacity.

Determined values of water and oil were compared with tabulated values, were in approximate agreement with experimental data. Most close to the case were the heat and thermal conductivity results for water, when the tabulated values obtained with different values in both cases less than 10%, the results were affected by the specific heat of greater error (around 50%).

Also the thermal conductivity and heat capacity of the oil showed a good agreement between the experimental results and tabulated (less than 15%), the difference was more

pronounced for thermal conductivity. These variations could be due to different characteristics of different types of oils (about 35%). Values emulsions lies between the values of the basic liquids (water, oil).

Acknowledgments

Authors thank to Ministry of Education, Youth and Sports of Czech Republic for support by national project COST LD14131 and for support by project Sustainability and Development REG LO1211 addressed to Materials Research Centre at FCH BUT.

References

[1] ZMESKAL. O., TRHLIKOVA. L., DOHNALOVA. L. Temperature dependence of thermal parameters of building materials. *In Thermophysics 2013 – conference proceeding.* FCH BUT in Brno: SAS Bratislava. BUT in Brno. 2013. p. 194-207. ISBN: 978-80-214-4801-8.

[2] ZMESKAL, O., BUCHNICEK, M., VALA, M.: Thermal properties of bodies in fractal and cantorian physics. *Chaos. Solitons and Fractals*. 2005. 25(5), p. 941-954.

[3] KUBICAR, L., VRETENAR, V., STOFANIK, V., BOHAC, V.: Hot-Ball Method for Measuring Thermal Conductivity. *Int. J. Thermophys. p. 1904-1918 DOI 10.1007/s10765-008-0544-4 (2010*).

[4] KUBICAR, L.: Pulse Method of Measuring Basic Thermophysical Parameters. 1. vyd. Bratislava: VEDA, vydavatel'stvo Slovenskej akadémie vied, 1989. 344 p. ISBN 80-224-0085-8

[5] ZMESKAL, O., STEFKOVA, P., HŘREBENOVA, L., BARINKA, R.: Pulse Transient Method as a Tool for the Study of Thermal Properties of Solar Cell Laminating Films. *Int. J. Thermophys.* 2009. 30(6), p. 1891-1901, ISSN: 0195- 928X.

[6] ZMESKAL, O., HREBENOVA, L., STEFKOVA, P.: *A new Differential Method for Evaluation Step Wise and Pulse Transient Measurements*. Brno: BUT, 2009.

[7] ZMESKAL, O., HREBENOVA, L., STEFKOVA, P.: Use of step wise and pulse transient methods for the photovoltaic cells laminating films thermal properties study. In *Thermophysics 2009- conference proceeding*. Brno. FCH BUT in Brno. 2009. p. 200 - 207. ISBN 978-80-214-3986-3.

[8] ZMESKAL. O., NESPUREK. S., DOHNALOVA. L. Study of PCM material diffusivity. In *Thermophysics 2012 - conference proceeding.* Brno: SAS Bratislava. BUT in Brno. 2012. p. 258-264. ISBN: 9788021445994.

[9] Table of physical constants. Online. Cit.: [2014–07–15]. Available on www: http://fyzika.fce.vutbr.cz/doc/vyuka_schauer/tabulky.pdf.

[10] Thermal conductivity of vegetable oils in a of wide range of temperatures, pressures and concentration solvents. 2008. Online. Cit.: [2014-06-23]. Available on www: http://works.bepress.com/mahmadali_mahmadievich_safarov/1/

Thermo-mechanical analysis of selected solid rocket propellant

Janusz Zmywaczyk[1], Piotr Koniorczyk[1], Marcin Cegła[2], Jacek Borkowski[2]

[1]Faculty of Mechatronics and Aerospace, Kaliskiego Street 2, 00-908 Warsaw, POLAND

[2]Military Institute of Armament Technology, Wyszyńskiego Street 7, 05-220 Zielonka, POLAND e-mail[1] : janusz.zmywaczyk@wat.edu.pl

Abstract: *This paper presents results of Dynamic Mechanical Analysis (DMA), Thermal Expansion (TE) and temperature characteristics of thermal conductivity k, thermal diffusivity D, and specific heat C_p within temperature range from -20 ^{0}C to +80 ^{0}C of a heterogeneous solid rocket propellant sample GM II with density ρ=1.77 g/cm^3 at room temperature. GM II is manufactured by special production plant "GAMRAT" Ltd. in Poland. Mechanical properties such as storage modulus (E'), loss modulus (E'') and tan(δ) were measured using Netzsch (Germany) DMA 242C analyzer within temperature range from -120 ^{0}C to +80 ^{0}C at 2 K/min of heating rate. The test sample in a shape of rectangle of dimensions 54.0mm length, 9.0mm width and 1.52mm thickness was subjected to the dual cantilever mode with frequency f = 1Hz recommended by the NATO 4540 standard. The Coefficient of Linear Thermal Expansion (CLTE) of GM II sample was determined using Netzsch DIL 402C dilatometer within temperature range from 30 ^{0}C to 80 ^{0}C at 1 K/min of heating and cooling rate, respectively. The thermophysical properties of GM II sample were determined using KD2 Pro apparatus. Special attention was devoted to determining the glass transition temperature and softening temperature of solid rocket propellants. The obtained experimentally temperature values during DMA studies are very important for safe usage of solid rocket propellants under operating conditions.*

Keywords: *DMA, solid rocket propellant, mechanical properties, thermal expansion, thermophysical properties*

1. Introduction

Solid rocket propellants are substances that are able to burn in the absence of ambient air generating during combustion a large number of gaseous molecules at high temperature from the range 2300 K - 3800 K. Taking into account the condition in which their ingredients are connected one can distinguish two general types which are called homogeneous and heterogeneous (composite) solid rocket propellants, respectively. The homogeneous propellants have a uniform physical structure consisting of chemically bonded fuel and oxidizer ingredients forming a single chemical structure whereas in heterogeneous ones, the oxidizer and fuel are physically mixed but do not have chemical bonds between them. Double base rocket propellants, which are mostly used, consist mainly of nitrocellulose (NC) 50-60% and nitroglycerine (NG) 30-39% which deliver energy to the system and other plasticizers (DEP: diethylphtalate, PU: polyurethane, TA: triacetine), stabilizers (EC: ethyl centralite, 2NDPA: 2-nitrodiphenilamine), burning rate catalyst (PbSa: lead salicylate, CuSa: copper salicylate, etc.), high-energy additive (RDX: cyclotrimethylene trinitramone, NGD: nitroguanidine), opacifier (carbon black), flame suppressant, metal fuel (Al: aluminum) [1].

Heterogeneous solid rocket propellants are mixture of a solid oxidizer (mainly ammonium perchlorate: AP) and liquid combustible substances (binders) mostly synthetic rubber with functional groups, a cross-linking agent and various kinds of plasticizers as well as additives that when curing at elevated temperature form a consistent mass with the corresponding physico-mechanical properties [4]. The addition of aluminum powder in composite propellants plays role of a secondary but highly energetic fuel component. Solid rocket propellants should be characterized by: high gas temperature and/or low molecular mass of products, high density, good mechanical and bond properties, good aging characteristics, low-hazard manufacturing and handling, low thermal expansion coefficient, low absorption of moisture, minimum sensitivity of burning velocity to pressure, initial temperature and gas velocity [1].

Due to the nature of solid rocket propellants belonging to the group of viscoelastic polymeric materials it is important to know their thermal and mechanical properties which may affect the proper operation of the rocket engines leading up even to its explosion. Changing of mechanical properties for such materials are caused by physical processes (e.g. migration of plasticizers and humidity), chemical reactions (e.g. oxidative cross-linking like decomposition of nitrates to nitrogen oxides) and mechanical processes (e.g. acceleration, rotation, mechanical vibration, fast increase of pressure, etc.) under conditions of their storage and operation. A powerful technique for determining mechanical properties of solid rocket propellants such as dynamic storage modulus E' which represents the elastic properties of material, dynamic loss modulus E'' which represents the viscous properties of material and $\tan(\delta) = (E''/E')$ which represents the damping of material [2] is the dynamic mechanical analysis [8]. In DMA technique the input signal is a sinusoidal oscillating force with a small amplitude of several newtons subjected to the investigated sample. As a result, the sample begins to deform in an oscillating manner generating in-phase and out- of-phase strains (output signal). The difference between the applied stress and the resultant strain is an angle, δ. The storage E' and the loss E'' moduli in this experimental technique can be measured as a function of time, frequency of oscillation and temperature according to a program of investigation set by the user. Mušanić et al [7] have studied influence of heating rate, frequency and length to thickness ration on DMA results. Wani et al [4] have found that as the temperature increases the storage modulus, loss modulus, and $\tan(\delta)$ curves with respect to the frequency shift towards the lower side. Mušanić and Sućeska [3] have studied the dynamic mechanical properties of double base rocket propellant artificially aged at temperatures of 80, 85 and 90 °C, in order to detect and quantify changes in the dynamic mechanical properties caused by ageing, and to investigate the possibilities for the prediction of service lifetime. While testing solid rocket propellant samples using DMA technique one can specify the strength of the material under dynamic loads and its ability to irreversible dissipation and conservation of mechanical energy supplied during the periodic loads. This is of particular interest in order to be able to predict rocket motors behavior during possible operational use. This paper presents the results of DMA and thermal expansion investigations of the heterogeneous solid rocket propellant GM II. For comparison purposes also the results of DMA for sample S4 [5] which is an example of a homogeneous solid double-base rocket propellant are given. In addition to this the thermal conductivity k, thermal diffusivity D and specific heat C_p within temperature range from -20 ^{0}C to +80 ^{0}C were shown for GM II. The thermophysical properties for GM II were obtained using KD2 Pro thermal analyser manufactured by Decagon Devices, Inc. from USA.

2 Experimental

2.1 DMA experiment

Sample of heterogeneous solid rocket propellant GM II with density $\rho = 1.77$ g/cm^3 at room temperature (T=25^{0}C) were used as an object of DMA investigations within temperature range from -120 ^{0}C to +80 ^{0}C. Density of the sample was measured by means of analytical balance RADWAG XA 60/220/X with readability 0.01/0.1 mg using the method of double weighing of the sample (in air and in water) by applying specific gravity measurement kit. The GM II test sample was a cuboid at the time of delivery and her primary dimensions in [mm] were (length x width x thickness) (54.0 x 9.0 x 2.0). Then, the sample thickness was reduced to a value of 1.52 mm using sand paper and manual processing. Next the sample was subjected to DMA investigations using Netzsch DMA 242C analyzer with sample holder 2 x 16 mm in dual cantilever mode. The frequency f = 1Hz, recommended by the NATO standard STANAG 4540, and the heating rate at 2 K/min were chosen. In table 1 are given DMA parameters used for experimental research. Temperature range of measurements from -120 ^{0}C up to +90 ^{0}C was feasible by using the liquid nitrogen.

Table 1: DMA input parameters for dual cantilever mode

Specimen	Thickness, width, length / mm	Temp. range / ^{0}C	Heating rate / K/min	Static force /N	Dynamic force / N	Amplitude / μm
GM II	1.52, 9.0, 54.0	-120 ÷ +80	2	0	7.5	30.0
S4 [5]	1.15, 10.0, 60.0	-120 ÷ +90	1	0	7.5	50.0

2.2 DIL 402C experiment

Thermal expansion of GM II in the temperature range from 30 ^{0}C to 80 ^{0}C at 1 K/min of heating/cooling rate was studied using Netzsch contact horizontal dilatometer DIL 402 C. The main parts of the dilatometer are: furnace, sample carrier with platinum platinum-rhodium thermocouple (type S), pushrod and inductive displacement measurement system. Dilatometer has two thermocouples. One of them is a control thermocouple placed in the furnace, and the second one is located in the direct vicinity of the test sample. According to manufacturer's declaration the dilatometer is characterized by the following parameters: temperature range -180 ^{0}C ÷ 2000 ^{0}C, heating rate 0.01 ÷ 50 K/min, temperature precision 0.1K, measuring range 500/5000 μm, ΔL resolution 0.125 nm/digit, 1.25 nm/digit. Test sample dimensions (diameter d=5.00mm and length L_0=25.00mm) were measured at room temperature T=25 ^{0}C using micrometer screw. Measurements of thermal expansion for GM II were carried out in accordance with Netzsch procedure. At the beginning the standard sample from high purity polycrystalline Al_2O_3 (6.0mm diameter, 25.0mm length) was tested applying the same temperature program (standby at 25^{0}C for 5 min, heating to 120^{0}C at 1 K/min, isothermal at 120^{0}C for 5 min, cooling down to 25^{0}C at 1 K/min, isothermal at 25^{0}C for 5 min) as for GM II sample. After that the standard sample was replaced by GM II one. In both cases high purity argon with flow rate 60ml/min was used as an inert gas. To obtain high accuracy for CLTE measurement a correction procedure is implemented in software. In

general the correction of $\Delta L(T)=L(T)-L(T_0)$ is connected with the measurement system ΔL_{sys} (thermal expansion of sample carrier and pushrod) and the tested sample ΔL_{sample_meas}

$$\Delta L_{sys} = \Delta L_{std\_table} - \Delta L_{std\_meas} \tag{1a}$$

$$\Delta L_{sample} = \Delta L_{sample\_meas} + \Delta L_{sys} \tag{1b}$$

where ΔL_{sys} is the system correction, ΔL_{std_table} and ΔL_{std_meas} are the tabulated values of ΔL for standard material issued by National Bureau of Standards Certificate (NBS) and obtained experimentally for the same standard material (e.g. Al_2O_3, fused silica, inconel600, pyroceram9606, platinum, tungsten), respectively, T_0 is the reference temperature (recommended value is 293.15K (20^0C)). The calibration corrected data $\Delta L/L_{0,c}$ are calculated automatically based on the formula (2) given by Netzsch

$$\frac{\Delta L}{L_{0,c}}(t,T_1) = \frac{\Delta L - s_m}{L_{0,m} + s_{SL}}(t,T_1) + \left[\frac{\Delta L}{L_{0,std}}(T_1) - \frac{\Delta L - s_{CAL}}{L_{0,CAL}}(t,T_2)\right] \tag{2}$$

where s_m, s_{CAL} stand for the offset of: the sample measurement at $T_1(t)=20^0$C and the calibration standard at temperature $T_2(t)$ for the current time t, respectively, s_{SL} is the sample length correction and $L_{0,m}$, $L_{0,CAL}$ stand for the length of the measured and the calibration standard (mm) at temperature 20^0C, respectively.

While investigating thermal expansion coefficient of solids relative expansion of sample $\varepsilon(T)=(L(T)-L_0)/L_0$, ($L_0=L(T_0)$), is measured according to the user setting of heating/cooling temperature program. Knowing the temperature dependence of sample relative expansion $\varepsilon(T)$ the mean $\alpha^*(T)$ and integral mean $\alpha_{tech}(T)$ CLTE are determined as follows [9, 10]

$$\alpha^*(T) = \frac{1}{L_0}\left(\frac{\partial L}{\partial T}\right)_p = \left(\frac{\partial \varepsilon}{\partial T}\right)_p \tag{3a}$$

$$\alpha_{tech}(T) = \frac{1}{L_0}\frac{L(T)-L_0}{T-T_0} = \frac{\varepsilon(T)}{T-T_0} \tag{3b}$$

It is easy to prove that the following relationship between α^* and α_{tech} is satisfied

$$\alpha^*(T) = \alpha_{tech} + \left(\frac{\partial \alpha_{tech}}{\partial T}\right)_p (T-T_0) \tag{3c}$$

2.3 KD2 Pro experiment

Experimental studies of temperature characteristics of the thermal conductivity, thermal diffusivity and specific heat were carried out using fully portable thermal analyser KD2 Pro. The range of measurement and declared accuracy of estimated thermophysical parameters are as follows: thermal conductivity $k \subset (0.02\div4.0)$ W/m/K ±5%, thermal diffusivity $D\subset$ (0.1÷1.0) mm^2/s ±10%, volumetric heat capacity $C \subset (0.5\div4.0)$ $MJ/m^3/K$ ±10%, operating environment for sensor from -50^0C to $+150^0$C. It uses the transient line heat source method. The test sample in a shape of cylinder with diameter d=25.0mm and length H=35.0mm was made of GM II material. In order to put 30mm dual-needle sensor SH-1 into tested sample two holes of diameter 1.3 mm, depth 30mm and spaced r=6mm from each other were drilled in it. One needle of SH-1 sensor is the heater and the other one is the temperature sensor.

Knowing the temperature readings of the sensor and the heat per unit length, q, the resulting data T^* are fit to the following equations using a non-linear least squares procedure

$$T^*(t) = b_0 t + b_1 Ei\left(\frac{b_2}{t}\right) \tag{4}$$

where b_0, b_1 and b_2 are the constants to be fit, $Ei(x)$ is the exponential integral, $T^*=4\pi(T-T_0)/q$, here T_0 is the initial temperature.
Then the unknown thermophysical parameters k, D, C are calculated as

$$k = 1/b_1, \quad D = r^2/4b_2, \quad C = \rho c_p = k/D \tag{5}$$

Temperature characteristics of thermophysical parameters for GM II in the range from -20 ^{0}C to +80 ^{0}C were obtained by stabilizing the sample's temperature in laboratory oven SLW 115 STD for 2-3 hours at a given positive temperature or in refrigerator for negative temperature range. After reaching the set temperature measurements were made using KD2 Pro thermal analyser.

3. Results and discussion

In figure 1 the results of DMA investigations for heterogeneous GM II and (for comparison) homogeneous S4 solid rocket propellants are presented. The accepted amplitude values (A=30μm or A=50μm) given in table 1 for each tested sample were reached in the whole temperature range for dynamic force less than F_{dyn}=2.6 N which is about one-third of the set value of F_{dyn}=7.5 N. Temperature of the glass transition (T_g) for GM II is equal to T_g =-56.6 ^{0}C and for S4 is equal to T_g =-45.0 ^{0}C (peak on E'' curve following the NATO Standardization Agreement – STANAG 4540). The second maximum on E'' at T=31.4 ^{0}C for S4 sample

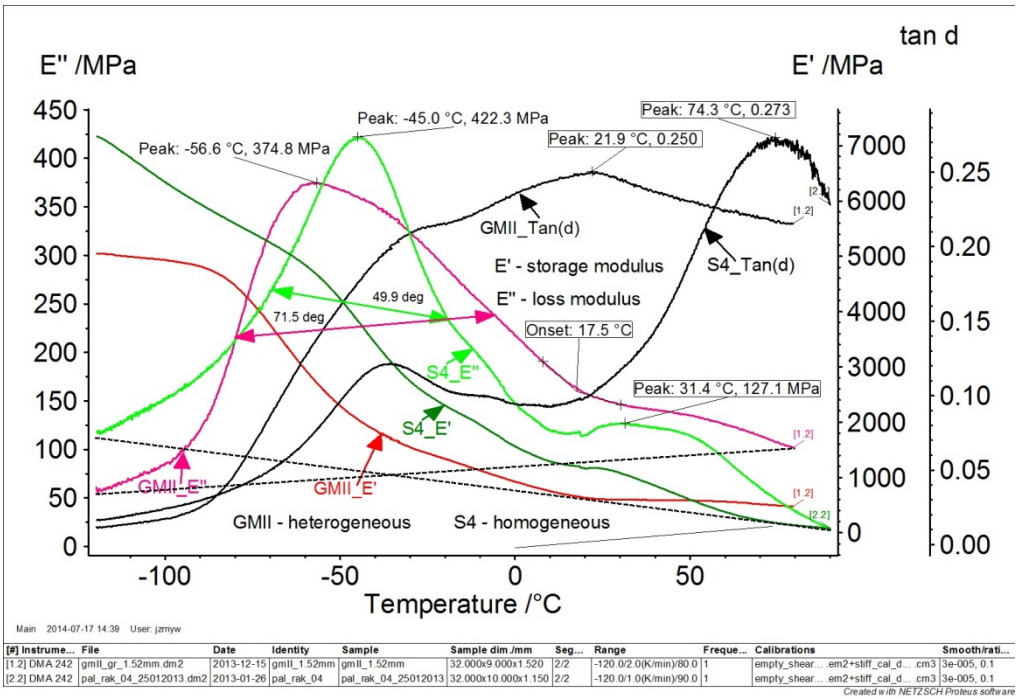

[#] Instrume...	File	Date	Identity	Sample	Sample dim./mm	Seg...	Range	Freque...	Calibrations	Smooth/rati...
[1.2] DMA 242	gmII_gr_1.52mm.dm2	2013-12-15	gmII_1.52mm	gmII_1.52mm	32.000x9.000x1.520	2/2	-120.0/2.0(K/min)/80.0	1	empty_shear....em2+stiff_cal_d... cm3	3e-005, 0.1
[2.2] DMA 242	pal_rak_04_25012013.dm2	2013-01-26	pal_rak_04	pal_rak_04_25012013	32.000x10.000x1.150	2/2	-120.0/1.0(K/min)/90.0	1	empty_shear....em2+stiff_cal_d... cm3	3e-005, 0.1

Figure 1: Results of DMA investigations of heterogeneous GM II and homogeneous S4 solid propellants

corresponds to the softening temperature [3]. In case of GM II sample there is only one maximum lying on *E''* curve but the onset at 17.5 ^{0}C can be regarded as the end of the glass transition region. The peak width at half height on *E''* curves which is equal to 49.9 ^{0}C for S4 and to 71.5 ^{0}C for GM II, respectively is related to molecular weight variability in NC for S4 [3] and maybe in AP for GM II. Information about flexibility of macromolecules is involved in tan(δ) curve. The first maximum on tan(δ) curve for S4 is at *T*=-35.6 ^{0}C and the second one at *T*=74.3^{0}C whilst for GM II one can observe the first peak for GM II at *T*=21.9^{0}C. The visible in figure 1 increase of tan(δ) values between these two maximum for S4 is connected with the increase of flexibility of NC macromolecules [3] which proves that the method of DMA has a great ability to detect changes in the viscoelastic properties of the tested material.

Results of thermal expansion measurements for GM II solid propellant is visible in figure 2. In order to be certain of the obtained results a sample made of electrolytic copper was used and preliminary investigation of CLTE (α*) have confirmed a good agreement with the literature data [6]. In the temperature range from 30 ^{0}C to 80 ^{0}C the relative expansion ($\Delta L/L_0$) of GM II and mean coefficient of linear thermal expansion obtained during heating and cooling differ significantly from one another. This can be explained by the shift of the sample and the oven temperature. In the temperature range from 40 ^{0}C to 50 ^{0}C there is observed a slight shrinkage of the material which does not occur during the cooling

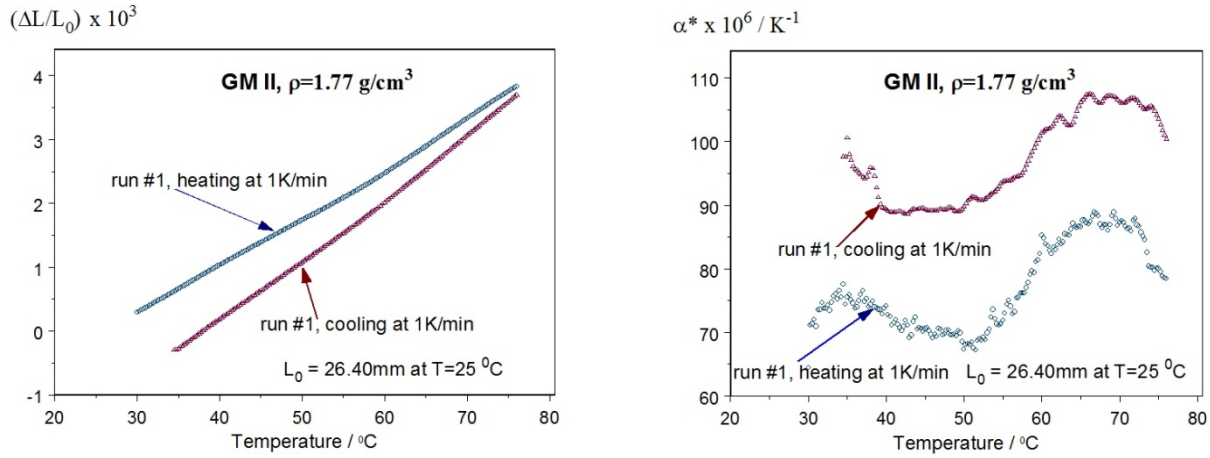

Figure 2: Results of thermal expansion measurements of hererogeneous solid propellant GM II

Table 2: Results of thermal properities measurements for GM II solid propellant

T / ^{0}C	*k* / Wm^{-1}K^{-1}	*D* / mm^{2}s^{-1}	*C* / MJm^{-3}K^{-1}	α* ·10^6/ K^{-1}	C_p / Jkg^{-1}K^{-1}
-19.08	0.432	0.173	2.506	-	1416
15.68	0.415	0.163	2.539	-	1434
29.23	0.425	0.156	2.704	66.5	1529
38.78	0.412	0.157	2.629	73.9	1490
48.40	0.414	0.154	2.679	69.8	1521
58.11	0.417	0.154	2.703	77.7	1539
76.92	0.403	0.153	2.635	76.5	1506

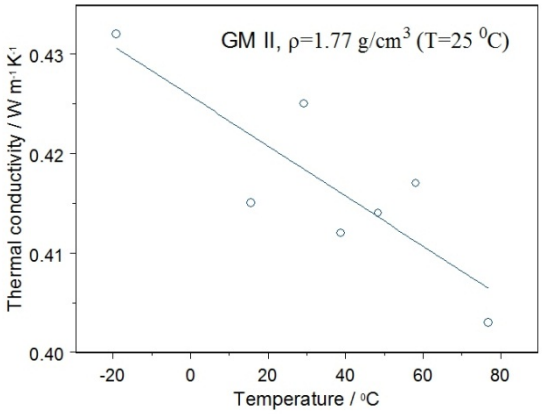

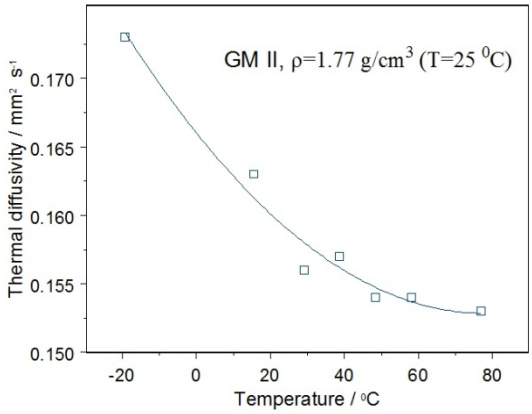

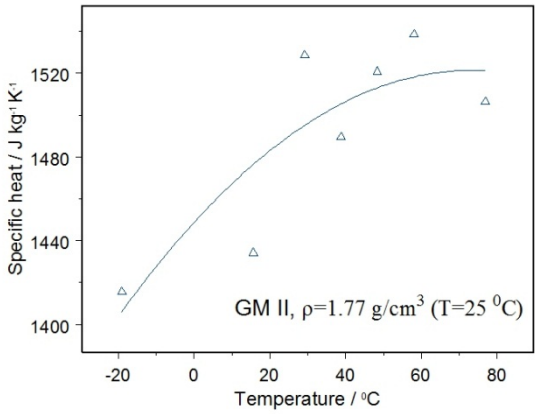

Figure 3: Results of thermopysical properties of GM II obtained by KD2 Pro thermal analyser.

The results of the thermal conductivity, thermal diffusivity and specific heat for GM II are given in table 2 and shown in figure 3. The specific heat values were calculated from the volumetric heat capacity as C_p=C/ρ taking into account the variability of density with temperature in form

$$\rho(T) \cong \frac{\rho(T_0)}{1+3\alpha^*(T)(T-T_0)} \tag{6}$$

4. Conclusions

In the relevant literature there is rather hard to find publications in which the results of thermo-mechanical properties of solid rocket propellants are given. In this paper the heterogeneous GM II and homogeneous S4 solid rocket propellant materials were studied using Netzsch DMA 242C analyser to determine their mechanical properties and Netzsch DIL 402C dilatometer as well as KD2 Pro thermal analyser were used to determine thermophysical properties of GM II. Mechanical properties test by DMA method allow to determine temperature range for safe usage of solid rocket propellants under operating conditions. In case of GM II the glass transition temperature was determined to be T_g= -56.6

^{0}C whilst for S4, T_8= -45.0 ^{0}C. In the near future, further study of thermo-mechanical properties for other solid fuel rocket propellants are planned.

Acknowledgments

This work was supported by the European Regional Development Fund under the Operational Programme Innovative Economy 2007-2013, POIG.02.02.00-14-022/09

References

[1] Solid propellants and their combustion characteristics, http://media.johnwiley.com.au/product_data/excerpt/60/11181275/1118127560-46.pdf

[2] HERDER G., WETERINGS, F.P., de KLERK W.P.C., Mechanical Analysis on Rocket Propellants, *Journal of Thermal Analysis and Calorimetry*, 2003, Vol. 72, p. 921-929

[3] MUŠANIĆ S.M., SUĆESKA M., Dynamic mechanical properties of artificially aged double base rocket propellant and the possibilities for the prediction of their service lifetime, *Central European Journal of Energetic Materials*, 2013, 10(2), pp. 225-244

[4] WANI V., MEHILAL V.W., PRAVEEN PRAKASH SINGH S.J., BHATTACHARYA B., Studies of the influence of testing parameters on dynamic and transient properties of composite solid rocket propellants using a dynamic mechanical analyzer, *J. Aerosp. Technol. Manag*., Sao Jose dos Campos, 2012, Vol. 4, No 4, p.443-452. DOI: 10.5028/jatm.2012.04044012

[5] CEGŁA M., ZMYWACZYK J., KONIORFCZYK P., Dynamic Mechanical analysis of double base solid rocket propellant with addition of soot, *Thermophysics* 2013, *Conf. Proc*. 13-15 Nov. 2013, Podkylava, Slovak Republik, pp. 208-215, **ISBN**: 978-80-214-4801-8

[6] ŚLĘZAK T., ZMYWACZYK J., KONIORFCZYK P., ŚNIEŻEK L., Dilatometric investigation of the phase transition in the high strength steel S960QL, *Thermophysics* 2013, *Conf. Proc*. 8-10 Oct. 2014, Podkylava, Slovak Republik

[7] MUŠANIĆ, S.M.; SUĆESKA M., SANKO B., Influence of testing conditions on results of dynamic mechanical analysis of double base rocket propellants, *New Trends in Research of Energetic Materials* / Svatopluk Zeman (ed). - Pardubice : Univeristy of Pardubice , 2002. p. 223-234

[8] MENARD K.P. *Dynamic mechanical analysis. A practical introduction*, 2nd ed., 2008 Taylor & Francis Group, LLC, Boca Raton London New York, ISBN 978-1-4200-5312-8

[9] STANKUS S.V. , YATSUK O.S., ZHMURIKOV E.I., TECCHIO L., Thermal expansion of artificial graphites in the temperature range 293−1650 K, *Thermophysics and Aeromechanics*, 2012, Vol. 19, No. 3, pp. 463-468

[10] STANKUS S.V., KOZLOVSKY Yu.M., YATSUK O.S., VERBA O.I., Thermal expansion of ChS-139 steel in temperature range 20 –720 °C, *Thermophysics and Aeromechanics*, 2013, Vol. 20, No. 3, pp. 355-358

Analysis of the Measurement Regime for the Tuff Stones Using Cylindrical Geometry for Pulse Transient Method.

Vlastimil Boháč[1], Peter Dieška[2], Viliam Vretenár[1], Danica Fidríková[1]

[1]Institute of nuclear and Physical engineering, FEI - STU, Ilkovičova 3, Bratislava, Slovakia of Physics, Slovak Academy of Sciences, Bratislava, Slovakia
Email: bohac@savba.sk

Abstract: *The problems regarding the specimen size on one side and the set-up of experimental parameters like the total time for the measurement on the other side is critical for any type of method that investigate thermophysical properties of materials. In this paper we discuss the model for the sample having the cylindrical geometry. The effects of heat loss from the surface of the sample as well as temperature stabilized sinks on the both ends of specimen set-up are including. The specimen size of rock gathered from the nature locality is limited because the shape of tools for the specimen sampling. Usually the drill bit with drilling pipe is used (see Figure). Finally the tuff cores drilled out in this way from the nature have the limited dimensions. This causes the additional effect of heat losses from the sample surface that takes place during the measurement and influences the results. The two-dimensional cylindrical model including the heat transfer coefficient from the sample surface to the surrounding was tested by mathematical methods resulting in the uncertainty analysis based on theory of sensitivity coefficients. The results of the uncertainty analysis help to set-up range of experimental conditions under which the model is valid at acceptable uncertainty for results. The uncertainty of estimated parameters is low in the range of reasonable high sensitivity coefficients.*

Figure: One part of the drilling pipe (up) with diamond crown to cut out the rock cores used for the experiments.

Keywords: *transient pulse method, cylindrical sample, heat transfer coefficient and heat losses*

1. Introduction - Principle of pulse transient method

Pulse Transient method [5] belongs to a group of dynamic methods for measurement of thermophysical parameters. In principle the planar heat source is generating the heat pulse. A temperature response to the heat pulse is recorded by thermocouple placed apart of the heat source (Fig. 1). The model initial and boundary conditions are given in Fig. 2.

Mechanism of deformation of planar temperature equipotential by heat losses effect is drawn on Fig. 1. This effect is evident for specimens having bigger thicknesses or using longer times of the temperature response measurements. The area that is not influenced by this effect during a measurement is depicted in white rectangle in Fig. 1. For the case of heat losses from the sample surface it was derived a model for cylindrical geometry that accounting the heat transfer coefficient α [1, 2, 3, 4].

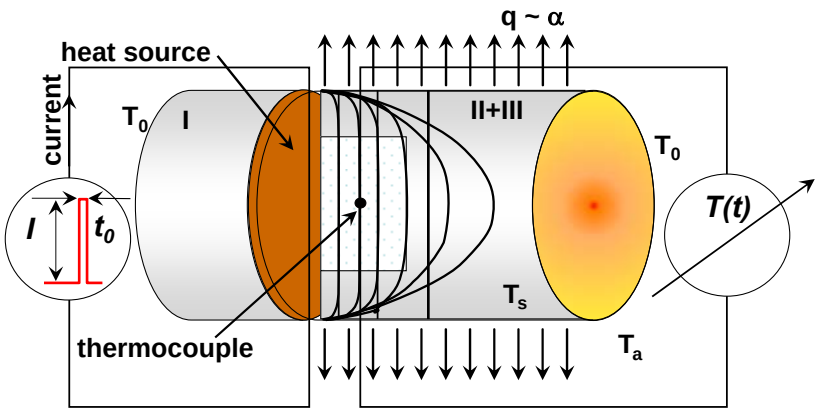

Figure 1. Wiring diagram and the sample set. In between first and second part of a sample set a planar heat source is inserted. The thermocouple for the measurement of temperature response to the heat pulse is inserted in between second and third part. In the sample cut it is illustrated a problem with deformation of planar isotherms. They are deformed in time by the radial heat flow q represented by α - the heat transfer coefficient between the sample surface and ambient. T_s and T_a are surface and ambient temperatures, T_0 is the temperature of the heat sinks – the thermally stabile blocks of sample holder.

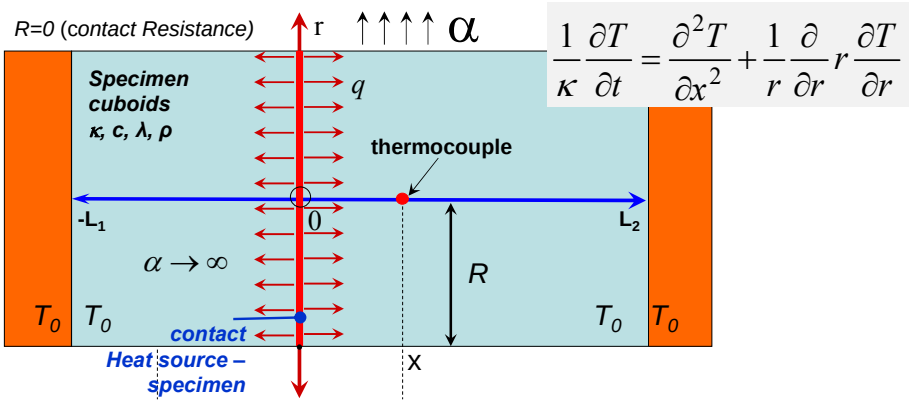

$$\frac{1}{\kappa}\frac{\partial T}{\partial t}=\frac{\partial^2 T}{\partial x^2}+\frac{1}{r}\frac{\partial}{\partial r}r\frac{\partial T}{\partial r}$$

Figure 2. Initial and boundary conditions for heat transfer equation the model assuming asymetrical arrangement of specimen in a form of finite cylinders of different length ($L_1 \neq L_2$). The circle shaped heat source having zero thermal capacity is placed in between, the heat transfer between the heat source and specimen is ideal ($a \to \infty$). T_0 is the temperature before shooting heating pulse

The solution of the heat transfer equation for given initial and boundary conditions drawn in Fig. 2 in the form of temperature response is the following:

$$T(t,x,r=0)=T_0\frac{R}{x}\sum_{\xi}\frac{\beta}{\xi(\xi^2+\beta^2)}\frac{1}{J_0(\xi)}\sum_{j=-\infty}^{\infty}\left[F(u_{1j},\upsilon_{nm})-F(u_{2j},\upsilon_{nm})\right] \qquad (1)$$

where $F(u,\upsilon)=\left[e^{-2uv}\Phi^*(u-\upsilon)-e^{2uv}\Phi^*(u+\upsilon)\right]$, $u_{1j}=\frac{|z+4Lj|}{2\sqrt{kt}}$, $u_{2j}=\frac{\left||z|+4L_j+2L_1\right|}{2\sqrt{kt}}$,

meaning of next variables are the following: $T_0=\frac{qL}{\lambda}$, $a=\frac{\lambda L}{C\kappa}$; $\beta=\frac{R\alpha}{\lambda}$; $v=\xi\frac{\sqrt{\kappa t}}{R}$; T is temperature increase, t is time, x Cartesian coordinate, $L_{1,2}$ are the thickness of sample, q heat

flow density at source, λ thermal conductivity, κ thermal diffusivity, ν is a root of the equation $a\cos\upsilon - \upsilon\sin\upsilon = 0$ and k is the Stefan-Boltzmann constant. Initial and boundary conditions for heat transport equation. T_s, T_a are surface and ambient temperatures, T_0 heat sink temperature. ξ is a root of the equation $\beta J_o(\xi) - \xi J_1(\xi) = 0$. Heat loss H from the specimen surface to the surrounding is considered by heat transfer coefficient α. $\Phi^*(x) = 1 - \Phi(x)$ is complementary error function $\Phi(x) = \frac{2}{\sqrt{\pi}} \int_0^x e^{-t^2} dt$. The relation (1) characterizes the step-wise measuring regime. After the duration of the heat pulse t0, the temperature is expressed by the relation

$$T^*(t,x) = T(t,x) - T(t - t_o, x) \tag{2}$$

The relation (2) characterizes the Pulse Transient Regime.

2. Uncertainty analysis

The uncertainty analysis was developed in respect with experimental data set $\{t_n, T_n\}_{n=1}^N$, where N is the number of measurements. In the case of reasonably large statistical number of measurements the measurements are statistically independent when the mean quadratic deviation in between average values and measured mean values is zero, e.g. no correlation exists between the subsequent measurements of temperature response T_n as well as measurement of other constant parameters $\langle b_j \rangle$ determined by independent measurements. There is estimated the moment for the parameter estimation $\langle a_i \rangle$ in the space of possible solutions of equation (2). Model is described by the temperature function $T_{model} = f(t,a,b)$ that represents the temperature response in time and depends on variables that are represented by set of free parameters $a = \{a_i\}_{i=1}^{N_a}$ evaluated by fitting procedure and constants $b = \{b_j\}_{j=1}^{N_b}$ presented in model and determined by different independent measurements. We used least square optimization and looking for $\min\left\{ \sum_{n=1}^N [T_n - f_n(a,b)]^2 \right\}$, where $f_n(a,b) = f(t_n,a,b)$, t_n is deterministic parameter, $b, \{T_n\}_{n=1}^N$ are independent random variables, a - dependent random variables. The least square optimization (fitting procedure) gives the system of non-linear equations $\sum_{n-1}^{N} (T_n - f_n) \frac{\partial f_n}{\partial a_i} = 0, \quad for\ i = 1,2,\ \ldots N_a$

For the case of uncertainty analysis we assuming, hat statistically mean values <.>

$$\left\langle \left(b_j - \langle b_j \rangle\right)\left(b_k - \langle b_k \rangle\right) \right\rangle >\sim \delta_{jk} u(b_j)^2 \tag{3}$$

$$\langle T_n \rangle >\sim f_n(\langle a \rangle, \langle b \rangle) \tag{4}$$

$$\left\langle \left(T_n - \langle T_n \rangle\right)\left(T_m - \langle T_m \rangle\right) \right\rangle >\sim \delta_{nm} u(T)^2 \tag{5}$$

$$\left\langle \left(T_n - \left\langle T_n \right\rangle\right)\left(b_k - \left\langle b_k \right\rangle\right)\right\rangle >\sim 0 \tag{6}$$

are independent, we estimate the uncertainty

$$u(a_i)^2 \sim \left\langle \left(a_i - \left\langle a_i \right\rangle\right)^2 \right\rangle = \left\langle (\Delta a_i)^2 \right\rangle \sim \left\langle (da_i)^2 \right\rangle \tag{7}$$

Differentiating equation of temperature function (2) according dependent random variables, we obtain system of equations (sensitivity coefficients [6])

$$\sum_{i=1}^{N_a} A_{ki} da_i = \sum_{n=1}^{N} dT_n \frac{\partial f_n}{\partial a_k} + \sum_{j=1}^{N_b} B_{kj} db_j, \qquad k = 1,2, \ \ldots N_a \tag{8}$$

where

$$A_{ki} = \sum_{n=1}^{N} \left[\left(f_n - T_n\right) \frac{\partial^2 f_n}{\partial a_k \partial a_i} + \frac{\partial f_n}{\partial a_k} \frac{\partial f_n}{\partial a_i} \right] \cong \sum_{n=1}^{N} \frac{\partial f_n}{\partial a_k} \frac{\partial f_n}{\partial a_i} \tag{9}$$

$$B_{kj} = \sum_{n=1}^{N} \left[\left(f_n - T_n\right) \frac{\partial^2 f_n}{\partial a_k \partial b_j} + \frac{\partial f_n}{\partial a_k} \frac{\partial f_n}{\partial b_j} \right] \cong -\sum_{n=1}^{N} \frac{\partial f_n}{\partial a_k} \frac{\partial f_n}{\partial b_j} \tag{10}$$

Now we can estimate uncertainty contribution of any particular measurement of involved parameters like $\boldsymbol{T}$ or $\boldsymbol{b}$. Solution of equations (8) has the form

$$da_k = \sum_{i=1}^{N_a} A_{ki}^{-1} \left(\sum_{n=1}^{N} dT_n \frac{\partial f_n}{\partial a_i} + \sum_{j=1}^{N_b} B_{ij} db_j \right), \qquad k = 1,2,\ldots N_a \tag{11}$$

Then, the uncertainty of $\boldsymbol{a_k}$ with respect to equation (3-7) should be written in a form

$$u^2\left(a_k\right) = \sum_{i=1}^{N_a} \sum_{i'=1}^{N_a} A_{ki}^{-1} A_{ki'}^{-1} \left[A_{i'i} u^2(T) + \sum_{j=1}^{N_b} \sum_{j=1}^{N_b} B_{ij} B_{i'j} u^2\left(b_j\right) \right] \tag{12}$$

$$u^2\left(a_k\right) = C_{kT}^2 u^2(T) + \sum_{j=1}^{N_b} C_{kj}^2 u^2\left(b_j\right)$$

where for the contribution quotients of particular variables and constants we can express as the sensitivities

$$\mathrm{C_{kT}} = \sqrt{A_{kk}^{-1}} \tag{13}$$

and

$$\mathrm{C_{kj}} = \sum_{ki}^{N_a} A_{ki}^{-1} B_{ij} \tag{14}$$

the elements of matrix ***A*** and ***B*** are defined with equations 9 and 10. It is seen that ***A~N***, and ***B~N***, therefore $C_{kT} \sim \frac{1}{\sqrt{N}}$ and C_{kj} is ***N***-independent. For power-like dependences it is useful to define indices

$$\nu_{kj} = \frac{\partial \log a_k}{\partial \log b_i} = \frac{b_j}{a_k} C_{kj} \tag{15}$$

Then for relative uncertainties we can write the equation

$$u_r\left(a_k\right)^2 = C_{kT}^2 \frac{uT^2}{a_k^2} + \sum_{j=1}^{N_b} \nu_{kj}^2 u_r\left(b_j\right)^2 \tag{16}$$

Then for relative and absolute uncertainties we can write the equation

$$u_r\left(a_k\right)^2 = C_{kT}^2 \frac{u(T)^2}{a_k^2} + \sum_{j=1}^{N_b} \nu_{kj}^2 u_r\left(b_j\right)^2 \; ; \; U_j = \frac{u_j\left(a_{kj}\right)}{a_j} . \frac{1}{u(T)} .100\% \tag{17}$$

3. Numerical calculations

The normalized sensitivity coefficients were calculated for real values of thermophysical parameters. The density is 888 kg/m^3, thermal diffusivity 1.1487x10^{-6} m^2/s thermal conductivity 0.2235 W/ (m·K) found from experimental measurements at the temperature around 26°C. The heat transfer coefficient was set to 7 W/ (m^2·K). Geometry of the specimen set-up for tuff stone was set for 50 mm in diameter. The thickness of a middle part of specimen set-up covered a series 0.002, 0.004, 0.006, 0.008, 0.01, 0.015, 0.02, 0.025, 0.03, 0.035, 0.04 m. The thickness of the guides was calculated as 1.3 times of middle part. The theoretical temperature responses, sensitivity coefficients and uncertainties were calculated for the heat pulse widths 2, 3, 4, 6, 9, 12, 15, 18, 21, 24, 27.and 30 seconds. All the calculations were done for region of dimensionless time F (Fourier number) from 0 up to 4F value where F=k·t/ (2·x^2).

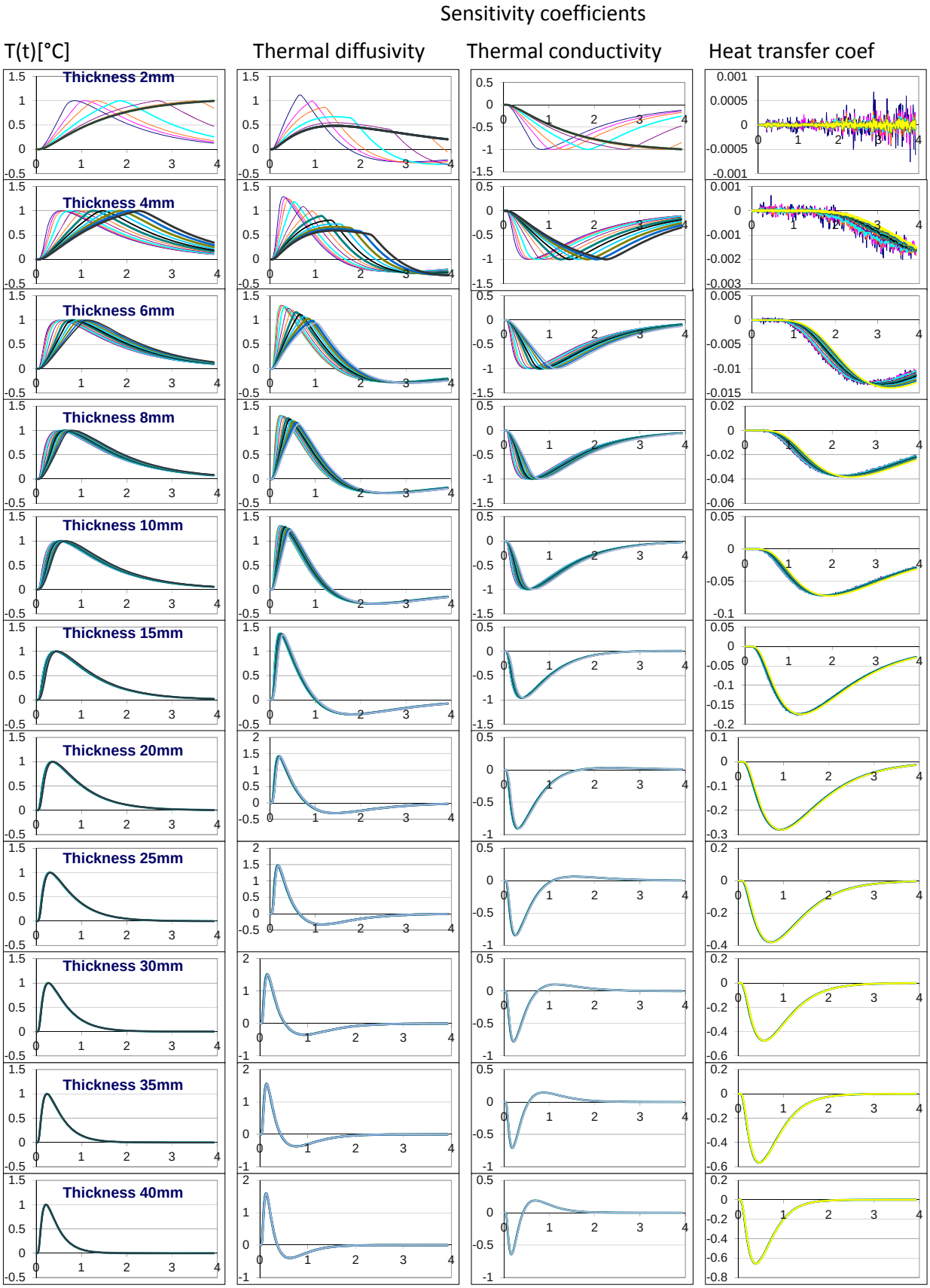

Figure 3. Calculated temperature response and sensitivity coefficients for free parameters cylindrical model e.g. thermal diffusivity, thermal conductivity and heat transfer coefficient.

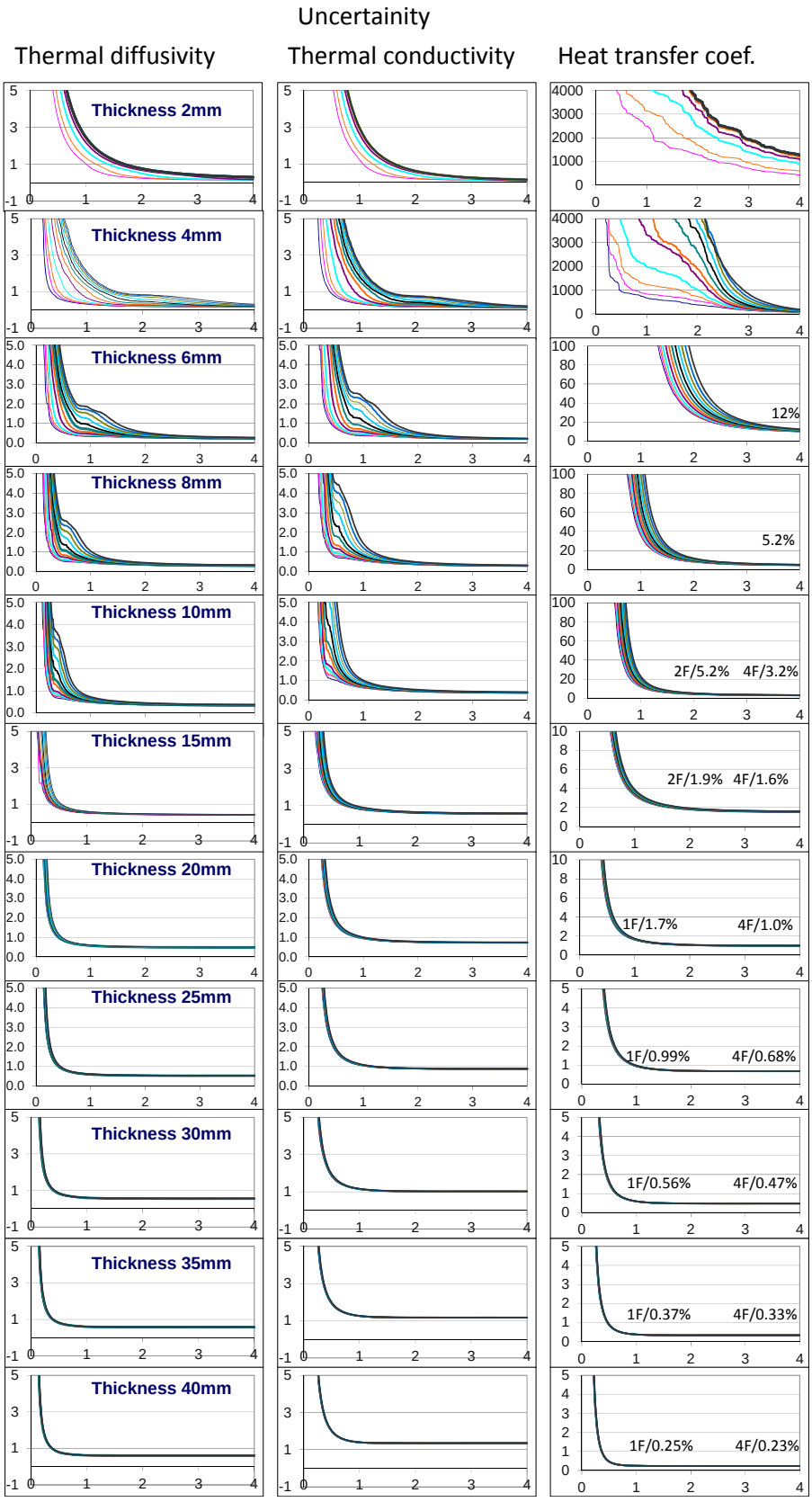

Figure 4. Calculated uncertainties for thermal diffusivity, thermal conductivity and heat transfer coefficient.

The grid of the results of the temperature response, sensitivity coefficients of thermal diffusivity, thermal conductivity and heat transfer coefficient for the given range of thicknesses and pulse widths is plotted in the time scale from 0 up to 4F in the figure 3. The figure 4 show the plot of uncertainties for all free parameters in the model, e.g. thermal diffusivity, thermal conductivity and heat transfer coefficient for the specified grid of thicknesses and pulse widths.

4. Conclusions

The sensitivity coefficient for estimated free parameters in the model usually has the maximums in a case of the thermal conductivity and thermal diffusivity and is increasing with measurement time in a case of the heat transfer coefficient. The total time of transient recording have to be long enough to include the corresponding effect to estimate this parameter unambiguously by the fitting procedure. For the small thicknesses and longer duration of pulse the regime is changed from pulse to step-wise. The model is able to evaluate measurements measured also in this regime. While the thermal conductivity and the thermal diffusivity are estimated with uncertainty less than 2-3% in all range of tested parameters, the uncertainty for the heat transfer coefficient α depends on the total time of measurement of temperature response. The sensitivity coefficient for α is very low or zero up to thicknesses of 6 mm. In this case we can conclude that there is no influence on the measurement at this thickness. The influence of this parameter start to influence the measurement at the thicknesses above 8 mm and uncertainties have the values about 5% only on the cost of very long measurements up to 4F that satisfy to about more than 600seconds in real time. For the thicknesses of 10 mm the uncertainty value is lowered to 5% even for the time 2F. Uncertainty of α for the thickness between 15-20mm is 5.2 and 1.9% for 2F and for the thickness more than 25mm drop down below 1% even for the times 1F.

The uncertainty analysis of the pulse transient model for cylindrical samples of finite length in respect to the heat transfer coefficient was performed and illustrated in the Figures 3 and 4. The accuracy of the results depends on the uncertainty of measured temperature response and in the presence of the effect of the heat losses from the sample free surface depend on the time of the measurement as well as geometry of the specimen. This parameter is affecting the measurement with increasing time of the measurement at larger thicknesses of the sample. The ideal model overestimates values of thermophysical parameters more than ten percent. The heat transfer coefficient is not possible to estimate unambiguously for short times of the measurement and thin sample thicknesses because of low sensitivity. The described method of uncertainty analysis is applicable to any kind of the physical model. The presented analysis helps to improve the accuracy of measurements. Cylindrical model was used for data evaluation of thermophysical parameters measured on the tuff stone taken from locality Brhlovce, the Museum of Rock Dwellings that received the Europa Nostra award as the first organization at the Slovak Republic. Estimation procedure based on new model was tested on real experimental data.

Acknowledgements

This work was supported by the Slovak Research and Development Agency under the contract No. APVV-0641-10, Study of rocks properties and investigation of structural and

textural characteristic in correlation with thermophysical and physico-mechanical properties and by Scientific Grant Agency of the Ministry of Education, science, research and sport of the Slovak Republic and the Slovak Academy of Sciences under the contract No. 2/0182/12 Development and testing of physical models for the pulse transient method.

References

[1] BOHÁČ, V., DIEŠKA, P., VRETENÁR, V. Uncertainty Analysis of Pulse Transient Method for Cylindrical Samples, In MEASUREMENT 2013, Proc. of the 9th International Conference on Measurement, Smolenice, Eds: Jan Maňka, Milan Tyšer, Viktor Witkovský, Ivan Frollo, ISBN 978-80-969-672-5-4, pp 227

[2] BOHÁČ, V., DIEŠKA, P., VRETENÁR, V., GREIF, V. Model for Cuboid Shape Samples and its Analysis Used for Measurements of Thermophysical Properties of Sandstone, Measurement Science Review 01/2011; 11(6), pp 192-197.

[3] BOHÁČ V, DIEŠKA P, VRETENÁR V, GREIF V, Model for Cuboid Shape Samples and its Analysis Used for Measurements of Thermophysical Properties of Sandstone, MEASUREMENT SCIENCE REVIEW, Volume 11, No. 6, 192-197, 2011.

[4] BOHÁČ V, DIEŠKA P, VRETENÁR V, The measurement of thermophysical properties of sandstone by pulse transient method using model for cuboid form samples and influence of heat loss effect, Conference Proceedings 17th International Meeting of Thermophysical Society -Thermophysics 2012. 31st October to 2th November 2012, Podkylava, Slovak Republic, ISBN: 978-80-214-4599-4

[5] KUBIČÁR Ľ, 1990, Pulse Method of Measuring Basic Thermophysical Parameters. in Comprehensive Analytical Chemistry Vol. XII Thermal Analysis Part E Ed Svehla G, Amsterdam, Oxford, New York, Tokyo: Elsevier, pp 350.

[6] BECK, J.V., ARNOLD, KENNETH J., Parameter Estimation in Engineering and Science, ISBN: 9780471061182, Better World Books (Mishawaka, IN, U.S.A.) John Wiley & Sons, 1977

Investigation of luminophores for high spatial and temporal resolution thermometry

Olena Kraieva[1,2,3], Carlos M. Quintero[1] , Gábor Molnar[2], Michel Mortier[4], Lionel Aigouy[5] and Christian Bergaud[1]

[1]LAAS-CNRS & Université de Toulouse III, 7 Av de Colonel Roche, 31077 Toulouse, France
[2]LCC, CNRS & Université de Toulouse III, 205 route de Narbonne, 31077 Toulouse, France
[3]Kyiv Polytechnic Institute, National Technical University of Ukraine, 37 Prospect Peremogy, Kiev 03056, Ukraine
[4]CNRS Chim ParisTech, Inst Rech Chim Paris, F-75005 Paris, France
[5] Ecole Super Phys & Chim Ind Ville Paris, LPEM, UMR CNRS 8213, F-75231 Paris 05, France

Abstract: *We describe the properties of selected fluorescent probes (Rhodamine B, Rhodamine 110 and PbF2:Er3+,Yb3+) for luminescence thermometry on the surface of an electrical circuit. We report on the stability, temperature sensitivity and general photophysical properties of these probes. As a model circuit we use in this work a Joule-heated gold microwire based heating platform providing fast and well confined temperature control.*

Keywords: *Nanothermometry, luminescence, nanowire heater*

1. Introduction

The reduced dimensions of electrical conduction channels in micro- and nanoelectronic circuits lead to high densities of components in such a way that the Joule heating effects become increasingly important to manage. The knowledge of the exact location of "hot spots" is crucial to avoid circuit damage and temperature mapping can help to improve the device design. Unfortunately, thermal characteristics are not always easy to predict, since they depend not only on the device design, but also on the quality of fabrication. Thus nanothermometry is becoming an important tool for the investigation of the thermal properties in integrated circuits during real operating conditions.

Frequently, the easiest way to perform a temperature measurement is using a contact method. However, the probe can easily modify the temperature of the sample as soon as it touches its surface. Non-contact methods are thus desirable to avoid the typical problems found with contact methods. A variety of non-contact techniques have been described in the literature enabling both non-invasive or semi-invasive temperature measurements, such as infrared thermography, thermoreflectance, Raman microspectroscopy, optical interferometry, luminescence thermography, etc [1].

Luminescence micro- and nanothermometry aims to extract knowledge of the local temperature of a given system with high spatial resolution using a temperature-sensitive luminescent probe. This method exploits the relationship between temperature and temperature dependent luminescence properties of the material (intensity, spectral band shape, lifetime, polarization, etc.). When thermal sensing is achieved through the analysis of the luminescence intensity, the temperature change provokes an overall change in the number of emitted photons per second such that the emission spectra becomes less (or more)

intense. Temperature induced changes in the luminescence intensity are generally caused by the thermal activation of non-radiative decay channels. The thermal sensitivity of luminescence intensity depends obviously on the selected luminescent probe and important efforts are thus devoted to the investigation of these latter. The probes can be either incorporated in the sample [2] to be studied or deposited on its surface, often in the form of a thin film of a polymer host containing the probes [3], [4]. Several parameters must be taken into account when selecting a luminescent probe for a particular application such as sensitivity, stability, spatial resolution and temporal resolution. The spatial resolution in luminescence thermometry is limited primarily by the diffraction of light. Nonetheless, using short wavelength and appropriate optics sub-micrometer resolution has been reported [3], [5]. The temporal resolution of this technique is mostly limited by the luminescence lifetime of the probe.

This paper describes the properties of selected fluorescent probes for luminescence nanothermometry on the surface of an electrical circuit. The investigation of the probes includes stability issues, e.g. photostability, temperature sensitivity and general photophysical properties. As a model circuit we use in this work a metallic microwire based platform (Fig.1) [3]. This simple device allows to create thermal perturbation via Joule effect in different types of samples with a sub microsecond response time and a high spatial confinement.

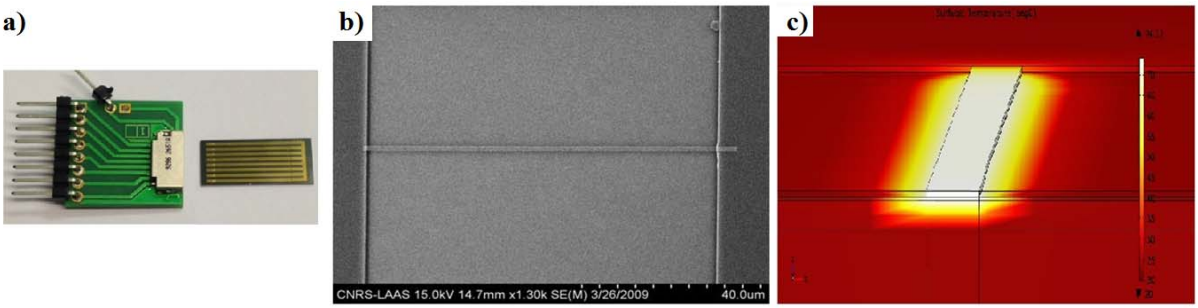

Figure 1: Gold microwires for localized heating purposes. a) Au micro heaters embedded on a chip and its electrical connector, b) Scanning electron microscopy image of 50 nm x 1 µm x 80 µm gold wire and c) finite element simulation of the temperature distribution in this wire using COMSOL MULTIPHYSICS.

2. Experimental

Three fluorescent probes have been investigated. The primary choice was the use of the commercial organic molecular dyes Rhodamine B, which was already explored by Löw et al. [6], and Rhodamine 110. We also investigated PbF2 nanocrystals codoped with erbium (Er) and ytterbium (Yb) ions, which are further described in ref. [7]. The fabrication and characterization of gold microwires have been described elsewhere [8].Fluorescence microscopy images have been recorded with an Olympus BX51 upright microscope equipped with a halogen lamp. Fluorescence imaging was realized using a CCD image sensor (Clara, Andor Technology) and a ×5 magnification objective (numerical aperture, NA = 0.1) or a ×50 magnification objective (NA = 0.5). In the case of the luminophore Rhodamine B the excitation and collected light beams were separated by a dichroic mirror (cutting edge at 590 nm) and band-pass filters centered at 550 nm (full width at half maximum, FWHM = 45 nm) and 610 nm (FWHM = 45 nm), respectively. In case of rare earth ions we have used a

dichroic mirror with a cutting edge at 510 nm band-pass filters centered at 450 nm (FWHM = 45 nm) and at 550 nm (FWHM = 50 nm). All experiments were carried out inside the chamber of a variable-temperature cryostage (Linkam THMS600) under nitrogen or air atmosphere. Analysis of the acquired fluorescent images was performed using the Solis software from Andor. Further processing of the images was done using MATLAB.

3. Results

3.1 Rhodamine B

Rhodamine B is one of the most commonly applied organic dyes in fluorescent thermometry due to its strong temperature dependence and high quantum yield. It absorbs green light and fluoresces in the red-orange part of the visible spectra. Figure 2 shows the temperature dependence of the luminescence of a thin layer of Rhodamine B. The thin film was elaborated by spin-coating of an aqueous solution of Rhodamine B on a silicon substrate. The fluorescence intensity decreases with increasing temperature at a rate of ca. 0.5 % per °C. However, following a complete cooling-heating temperature cycle the intensity of the luminescence decreased irreversibly by ca. 5 %, which we can attribute to the photochemical degradation of the molecules (photobleaching). Obviously this degradation of the luminescent probes makes impossible (or at least very difficult) the use of this luminophore for thermometry purposes.

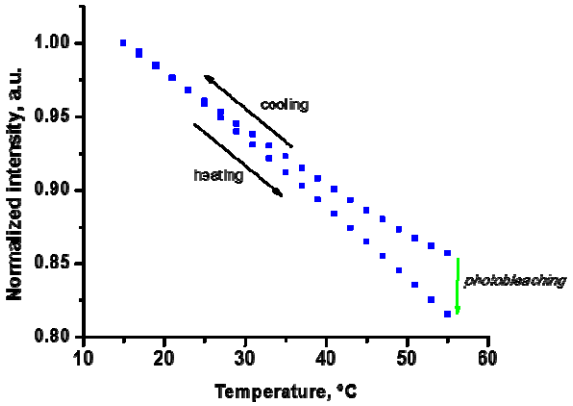

Figure 2: Temperature dependence of the luminescence intensity (excitation 550 nm, emission 610 nm) of a Rhodamine B thin film through a complete cooling - heating cycle.

In order to investigate the impact of ambient air (i.e. oxygen molecules and humidity) on the photochemical degradation of the Rhodamine B, we have prepared two identical thin film samples of Rhodamine B. Then, we have recorded the temporal variation of the luminescence of the two films at a constant temperature (20°C) and under identical light exposure conditions in two different atmospheres: in ambient air and in dry nitrogen. Figure 3a shows the photobleaching rate of Rhodamine B for the two cases. After 70 min exposure to light we observe ca. 0.9 % decrease of the Rhodamine B luminescence intensity under nitrogen atmosphere, which is significantly smaller than the decrease (~3.3 %) observed in air. Besides the presence of oxygen and humidity the degradation rate of the luminophore depends also on the temperature. To investigate the influence of temperature on the photostability of Rhodamine B we prepared three identical samples and studied their

luminescence intensity at different temperatures. The three samples were exposed to light excitation at 20, 15 and 5 °C under ambient air atmosphere. Figure 3b shows the variation of the luminescence intensity of these samples over 50 min. As it can be expected the photobleaching rate decreases with the decrease of the sample temperature (1.2 % at 20 °C, 0.7 % at 15 °C and 0.2 % at 5 °C).

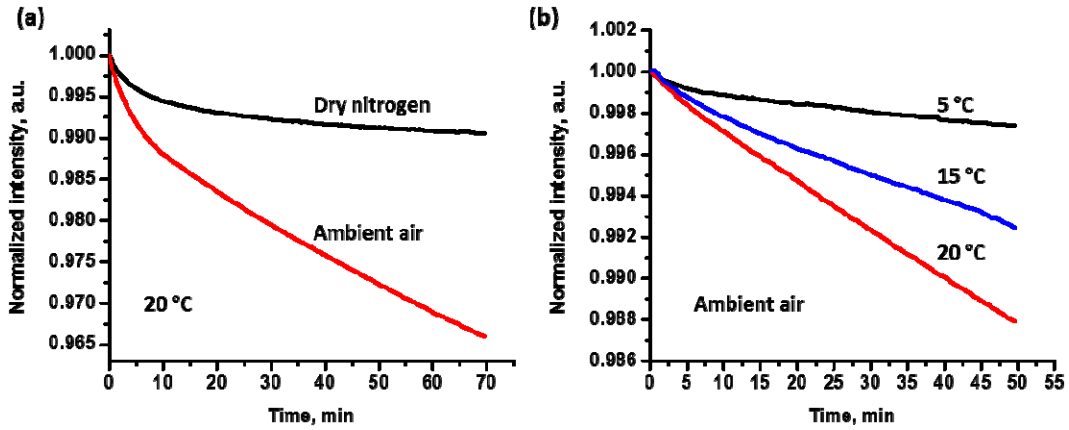

Figure 3: Temporal variation of the luminescence of Rhodamine B thin films in different atmospheres (a) and at different temperatures (b).

Another problem with Rhodamine is its tendency to self-quench. It is well known that the brightness of a Rhodamine solution does not increase linearly with the increase of concentration. Actually, dry Rhodamine films are not much fluorescent in comparison with diluted solutions. In a highly concentrated system, the separation between centers is small and the chance of having energy transfer (either radiative or non-radiative) between the molecules increases dramatically. To separate the molecules and thus avoid self-quenching the molecules are often diluted in different matrices. We have explored this idea and we have used a silica powder (Silica gel Si 60, 40-63 μm, from Merck) which was impregnated by an aqueous solution of both Rhodamine B (RhB) and Rhodamine 110 (Rh110). The simultaneous use of two fluorescent probes allows for a more accurate temperature measurement. To separate the luminescence signal from the two types of Rhodamines we resolved the two emission bands using a spectrograph (Fig. 4a). The luminescence spectra was recorded over the 90°C-60°C-90°C temperature range. Figure 4b shows the plot of the luminescence intensity as a function of temperature at 515 nm for Rhodamine 110 and at 580 nm for Rhodamine B (excitation 450 nm) embedded in the silica powder. The luminescence intensity of RhB and Rh110 shows a linear thermal variation of 0.77 % per °C and 0.19 % per °C, respectively. We observed a strong luminescent signal with this system and even more importantly after a complete high temperature cooling-heating cycle in ambient air the luminescence intensity of both luminophores remained stable. (One should note that prior to the measurement the sample was annealed at 100°C for 15 min in air in order to remove humidity. This treatment is necessary in order to avoid the photobleaching.) From a photophysical point of view this RhB&Rh110@SiO2 system presents thus a significant interest for thermometry purposes. However, the silica particles we used are rather big (≈ 50 μm) to be used as a high spatial resolution temperature probe. Further work will be necessary to develop this system in the form of a thin film.

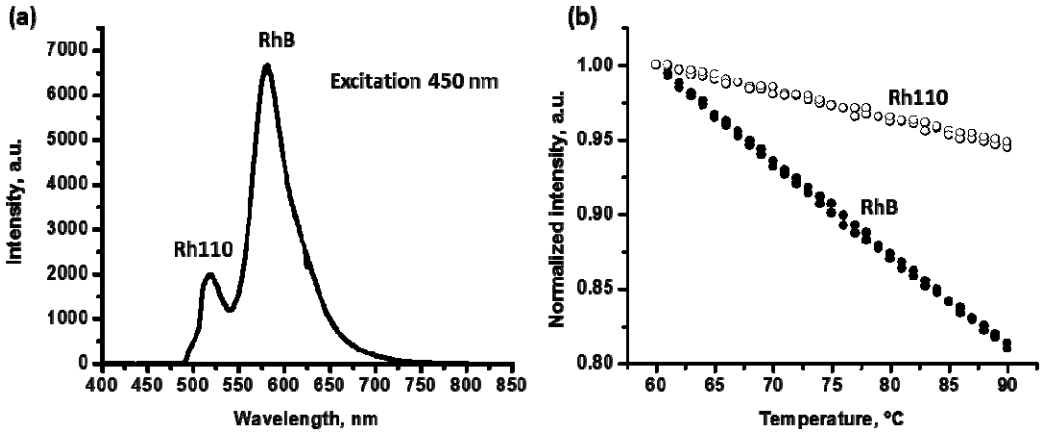

Figure 4: (a) Emission spectra of the mixture Rhodamine B & Rhodamine 110 in silica matrix (excitation 450 nm); (b) temperature dependence of the luminescence intensity at 515 nm (Rh110) and at 580 nm (RhB) over a complete cooling – heating cycle in air.

3.2 Rare earth ions

Rare earth ions (lanthanides) are also interesting candidates for luminescence thermometry. Indeed, lanthanide complexes have often been used in temperature sensors as they do not suffer much from photobleaching when compared to organic dyes [9]. We used PbF_2 nanocrystals codoped with erbium (Er^{3+}) and ytterbium (Yb^{3+}) ions [7]. The photoluminescence spectra (both excitation and emission) of these nanocrystals are represented in Fig. 5.

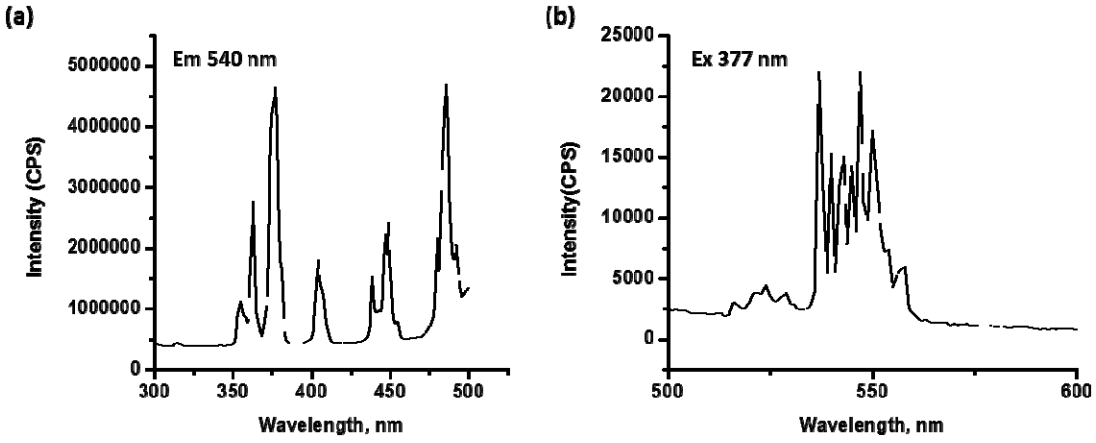

Figure 5: Excitation (a) and emission (b) spectra of PbF_2 nanoparticles co-doped with Er^{3+} and Yb^{3+} ions.

The emission spectrum is composed of sharp lines grouped into two zones: a high energy zone between 517–531 nm and a low energy zone between 538–556 nm. The populations of the two groups of levels are in thermal equilibrium. At a given temperature T, the luminescence intensities at 520 nm and 550 nm are given by:

$$I_{520}(T) = p_{520}(T)N_{520}(T) \; ; \; I_{550}(T) = p_{550}(T)N_{550}(T)$$

where the parameters p_i are related to the radiative recombination rates and N_i are the populations of the levels. If the levels are in thermal equilibrium, then N_{520} and N_{550} are related by

$$\frac{N_{520}}{N_{550}} = exp\left(-\frac{\Delta E}{kT}\right)$$

where ΔE is the energy difference between the two levels and k is the Boltzmann constant.
We have recorded the temperature dependence of the luminescence intensities at 520 nm and 550 nm. Figure 6 shows the temperature dependence of the quantity I_{520}/I_{550}. After three complete thermal cycles (20°C-40°C-20°C) virtually no photobleaching is observed. The temperature dependence of the luminescence intensity ratio (0.85 % per °C) is also fairly high. However, when working with small quantities of the powder, the luminescence intensity was rather low. This is chiefly related to the fact that with our current experimental setup we cannot excite the luminescence in the near IR spectral region where a very efficient (upconversion) excitation was reported for this system [4]. Future work will address this technical issue. Let us note also that a major inconvenience of lanthanide luminescence thermometers is the rather long luminescence decay (ms – μs range) when compared to the organic dyes (ns decay times), which is obviously a key issue for high temporal resolution thermometry.

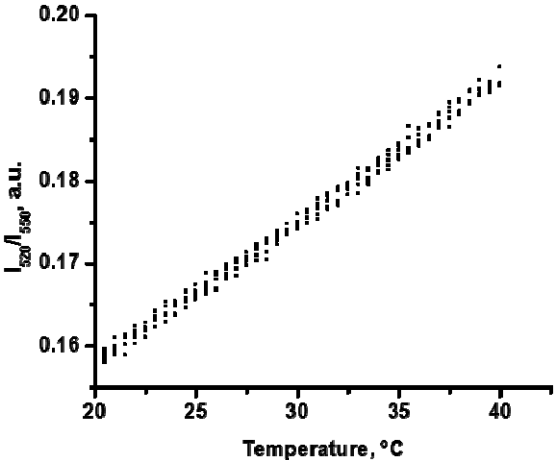

Figure 6: Temperature dependence of the ratio I_{520}/I_{550} for the 520 nm and 550 nm emission lines of PbF_2:Er,Yb through 3 complete thermal cycles.

3.3 Application

The main idea of the experiments described below consist in employing one of studied luminescence thermal probe as a temperature sensor on the surface of a simple electronic circuit, which consists of 5 Joule-heated gold microwires separated by 1.5 μm (Fig. 7a). Once the layer of the Rhodamine B is deposed on the chip, fluorescence images are taken from the circuit with different bias. The reduced cross section of the wire (in conjunction with the Si substrate, which acts as an efficient heat sink) allows for a local confinement of the heating along its axis when passing an electrical current through the device. As the current (and thus the temperature) increases the luminescence intensity of RhB from the heated area will decrease. With a precise calibration of the luminescence dependence on temperature, a given change in intensity can be converted to temperature. Figure 7b displays the luminescence images obtained in the off-state (I=0 mA) and in the on-state (15 mA, 25 mA and 35 mA) of the microwire heaters. One can observe a significant decrease of the luminescence intensity when current flows through the wires. This change of luminescence intensity is tightly confined to the wires, which are clearly resolved in the luminescence images. When we plot

the luminescence intensity along the wire (fig. 7c) we can observe the sharp decrease of luminescence intensity at the two edges of the wire. As expected the luminescence (and thus the temperature) profile is flat along the wire between the edges. Figure 7d shows the variation of the luminescence intensity recorded on the wires under bias over two complete thermal (i.e. bias) cycles between 20 °C (0 mA) and 74 °C (35 mA). According to our calibration, the change of luminescence (ca. 10 %) corresponds to a temperature change of 50 °C, which is in good agreement with our COMSOL simulations [8]. One may note also that this change is well reproducible and the effect of photobleaching remains fairly negligible (ca. 1%) in this experiment.

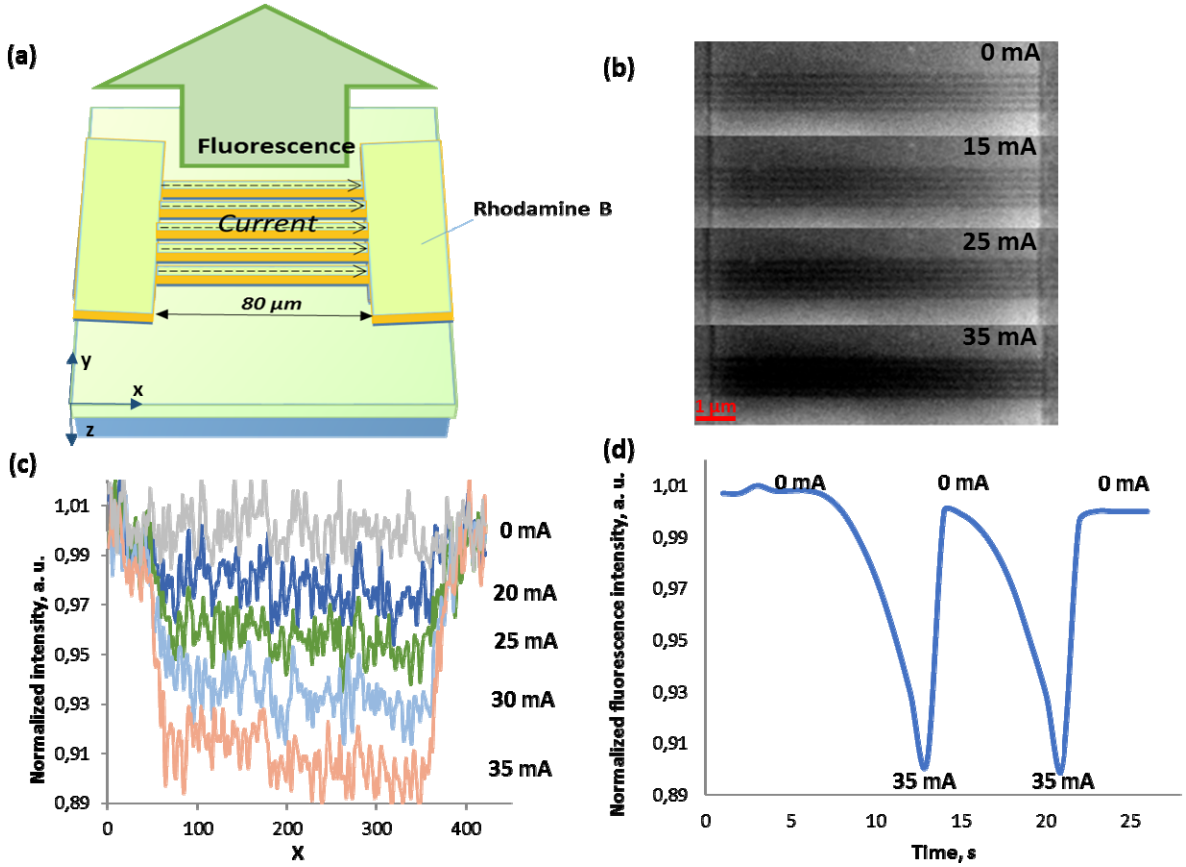

Figure 7: (a) Schematic image of the luminescence thermal imaging experiment with the microwire heater device. (b) Fluorescence microscopy images of the microwires covered by a thin film of Rhodamine B at different applied current bias. (c) Cross-section image of the luminescence intensity along a wire at different bias. (d) Variation of the luminescence intensity recorded above the microwires through two bias cycles (0 – 35 mA).

4. Conclusions

We have investigated the properties of organic and rare earth based luminescent probes with the aim of using them for thermal imaging of micro- and nanoelectronic circuits. We demonstrate that thin films of organic dye Rhodmaine B can be used for high spatial resolution thermal imaging thanks to its strong luminescence and its relatively good thermal sensitivity. (N. B. It also allows for high temporal resolution thermometry, which we discuss separately in ref. [10].) The application field of this probe is limited by its rather high

photobleaching rate in usual experimental conditions. Different ideas have been studied to reduce this effect, including the use of inert atmosphere, low temperature work and the dilution of the luminophore into silica matrix. Alternatively, rare earth based probes can be also used with negligible photobleaching.

Acknowledgments

This research was supported by the ANR project Thermospin.

References

[1] C. D. S. BRITES, P. P. LIMA, N. J. O. SILVA, A. MILLÁN, V. S. AMARAL, F. PALACIO, and L. D. CARLOS, "Thermometry at the nanoscale," Nanoscale, vol. 4, no. 16, p. 4799, 2012.

[2] C. QUINTERO, G. MOLNÁR, L. SALMON, A. TOKAREV, C. BERGAUD, and A. BOUSSEKSOU, "Design of fluorescent spin-crossover nanoparticles for thermometry applications," in Thermal Investigations of ICs and Systems (THERMINIC), 2010 16th International Workshop on, 2010, pp. 1–5.

[3] P. LÖw, B. KIM, N. TAKAMA, and C. BERGAUD, "High-Spatial-Resolution Surface-Temperature Mapping Using Fluorescent Thermometry," Small, vol. 4, no. 7, pp. 908–914, Jul. 2008.

[4] L. AIGOUY, E. Sai□Di, L. LALOUAT, J. LABÉGUERIE-EGÉA, M. MORTIER, P. Lo□W, and C. BERGAUD, "AC thermal imaging of a microwire with a fluorescent nanocrystal: Influence of the near field on the thermal contrast," J. Appl. Phys., vol. 106, no. 7, p. 074301, 2009.

[5] C. D. S. BRITES, P. P. LIMA, N. J. O. SILVA, A. MILLÁN, V. S. AMARAL, F. PALACIO, and L. D. CARLOS, "A Luminescent Molecular Thermometer for Long-Term Absolute Temperature Measurements at the Nanoscale," Adv. Mater., vol. 22, no. 40, pp. 4499–4504, Oct. 2010.

[6] P. LÖW, B. KIM, N. TAKAMA, and C. BERGAUD, "High-Spatial-Resolution Surface-Temperature Mapping Using Fluorescent Thermometry," Small, vol. 4, no. 7, pp. 908–914, Jul. 2008.

[7] J. LABÉGUERIE, G. DANTELLE, P. GREDIN, AND M. MORtier, "Luminescence properties of PbF2:Yb–Er nanoparticles synthesized by two different original routes," J. Alloys Compd., vol. 451, no. 1–2, pp. 563–566, Feb. 2008.

[8] O.KRAIEVA, C. QUINTERO, G. MOLNÁR, AND C. BErgaud, "Metallic Micro- and Nanowires for High Spatial and Temporal Resolution Thermal Investigations,"THERMINIC, submitted.

[9] A.-L. GASSNER, C. DUHOT, J.-C. G. BÜNZLI, and A.-S. CHAUVIN, "Remarkable Tuning of the Photophysical Properties of Bifunctional Lanthanide tris(Dipicolinates) and its Consequence on the Design of Bioprobes," Inorg. Chem., vol. 47, no. 17, pp. 7802–7812, Sep. 2008.

[10] C. QUINTERO, O.Kraieva, G. MOLNÁR, and C. BERGAUD, submitted.

Wireless device for monitoring the temperature-moisture regime in situ

Ján Hudec[1], Vladimír Štofanik[1], Ľudovít Kubičár[1]

[1]Institute of Physics SAS, Dúbravská cesta 9, 845 11 Bratislava, Slovakia

Abstract: *This contribution presents the wireless device for monitoring the temperature-moisture regime in situ. The monitoring is performed by means of the hot-ball method. It is based on measuring thermal conductivity, thermal diffusivity and specific heat. The measured parameters are influenced by moisture content. One of the biggest advantages of this method is a possibility of in situ application and low material invasion. These features make it very suitable for monitoring of objects of historical and cultural significance and monuments. The hot-ball method belongs to a class of transient methods. The measuring process consists of energizing the hot-ball sensor and simultaneously measuring a response of the sensor. A new electronic device that includes wireless module has been designed. The device covers all operations needed for a measurement. It includes energizing of the hot-ball sensor, measuring its response, storing of the obtained data and wireless data communication. Measured data and set parameters can be transferred via wireless connection. Wireless access, possibility of solar charging and small dimensions of the unit permits application on cultural objects and places with limited accessibility. The contribution includes description of the wireless measurement system and its basic features. Possibilities and functionality of the system is demonstrated by actual monitoring of the St. Martin's Cathedral in Bratislava. Correlations with surrounding meteorological conditions are presented. Some of the conditions can also be measured by our system, directly where the monitoring process is taking place.*

Keywords: *monitoring, wireless, hot-ball, moisture sensor, thermal conductivity*

1. Introduction

Different type of sensors and methods for measuring thermophysical properties of materials are being designed and constructed at the Institute of Physics SAS. These methods are used in various areas of human activities. The hot-ball method and its practical use also belong to the most promising ones. [1]

The hot-ball sensor is patented invention of the Institute of Physics, SAS. It consists of two main electrical parts: heating element and a thermometer. The heater is used as a source of thermal field. The thermometer is used for measuring temperature response to this heating. Both these parts are glued into small ball of very good conductive putty or implanted in a metallic ball. Electrical parts are wired by four thin wires. Diameter of the ball is up to 3 mm. Simple schematic of the hot-ball sensor's structure is shown in Fig. 1 left. Example of how a real hot-ball sensor can look is in Fig. 1 right.

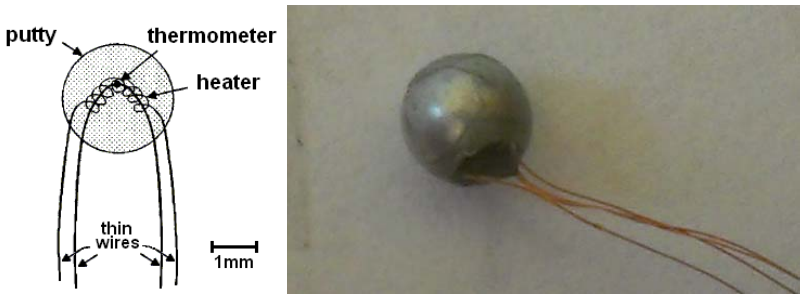

Figure 1: Hot-ball sensor, simple schematic (left), real one (right)

The main principle of the method is measuring temperature response to the heat produced in the ball by electric current. It is typical transient process. Based on the shape of the obtained curve representing response and on physical model of the system a set of thermophysical parameters is then found (mathematically fitted). The ratio between the heating power and the temperature increase caused by the power, in a steady state, is a parameter that is simpler and faster to obtain. However it is only informative, not so precise. This parameter represents a measure of thermal conductivity of sensor's surroundings.

The hot-ball method is often used in connection with so-called moisture sensor (Fig. 2) [2]. It is a cylinder of porous material, ca 2 cm high, with diameter of ca 2 cm, with hot-ball sensor placed in its centre. The moisture sensor should be constructed of a material that is as similar to the material of the monitored object as possible, especially regarding its porosity. Such moisture sensor is calibrated for dry and water saturated states. This enables us to find the absolute value of moisture content according to physical parameters of the calibrated cylinder measured by hot-ball sensor inside.

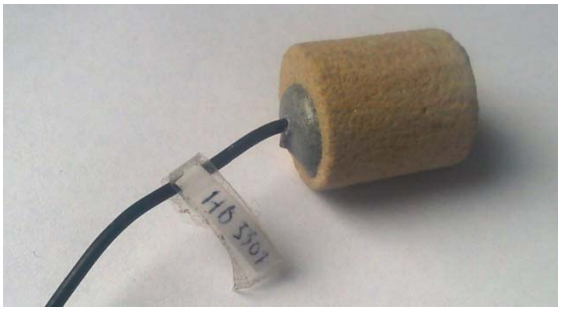

Figure 2: Moisture sensor

The most advantageous aspects of this method are: low invasion, portability, low cost for large quantities, suitability for long-term operation and small size. These characteristics make it very suitable for long-term monitoring of buildings, cultural objects, monuments, insulating materials, etc. Applying several sensors simultaneously enables us to investigate heat and moisture flows in monitored objects as well. In long-term view we can detect degradation of material.

The sensor is completed by electronic measuring system performing necessary operations, such as managing the electro-physical hot-ball sensor, timing the measurements, storing data, wireless communication, and user-friendly representation of measured values and parameters of settings, etc.

2. Measuring unit

Development of a new measuring unit considers previous simplified version and experiences with hot-ball sensors [3]. The primary version consisted of controlling processor, memory for data and parameters of settings, analog to digital and digital to analog converters for driving one hot-ball sensor, and wired communication channel for managing the device by user using a laptop. The new version is enhanced by multiple things. It has wireless communication for managing settings and measured data downloading, a I2C port for optional connecting of air temperature and humidity sensor (for inquire correlations with weather conditions), two measuring channels for connection of two hot-ball sensors (enables the investigating of heat and moisture flow's directions), more efficient controlling processor, much larger memory for storing measured data, battery under voltage protection, possibility for solar charging, current (not voltage) source for driving the heater of the hot-ball sensor, that prevents influence of unstable resistance of sensor's wires and enables measuring the heating power precisely, ability of using one or two AA sized batteries as power source, a real time circuit for reducing power consumption even more while measuring unit's sleeping regime, more user friendly graphical user interface for managing of the measuring unit. Fig. 3 shows a block schematic of the measuring unit.

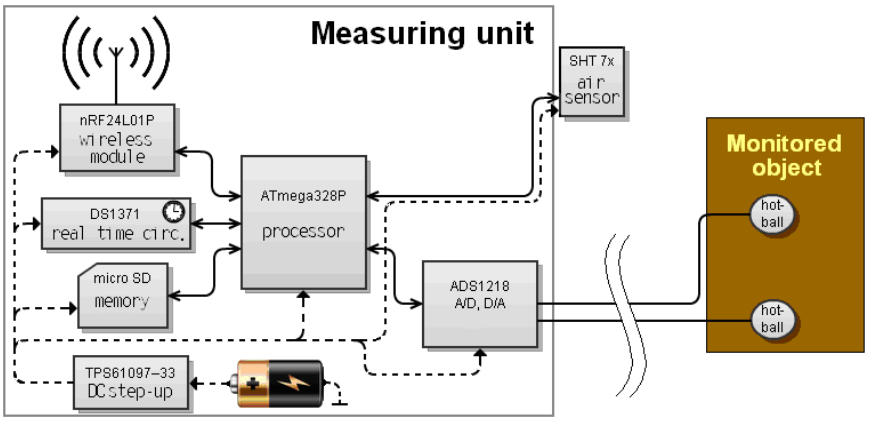

Figure 3: Block schematic of the measuring unit

Fig. 4 shows the measuring unit mounted at the belfry of the St. Martin's Cathedral in Bratislava. The thing sticking up from the measuring unit is the sensor for measuring temperature and humidity of surrounding air.

Figure 4: Photo of mounted measuring unit (uncovered)

Module next to batteries in Fig. 4 is the module for wireless communication. Using appropriate antenna we can access the measuring unit in distance of up to several kilometres (verified for direct visual). Fig. 5 illustrates wireless data downloading from St. Martin's Cathedral.

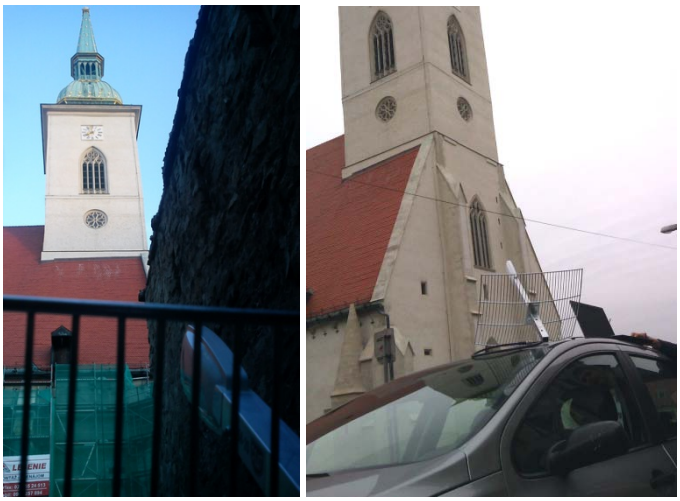

Figure 5: Wireless communication using laptop and antenna

3. Monitoring process

Fig. 6 illustrates the monitoring process [4]. Each curve of response to the heating gives us set of thermophysical parameters. Before the heating a background (baseline) temperature is measured. It enables us to suppress the unstable temperature trend of monitored object caused by weather's temperature changes and to evaluate heater's influence only. If the measuring of responses is repeated we can say object is continually monitored.

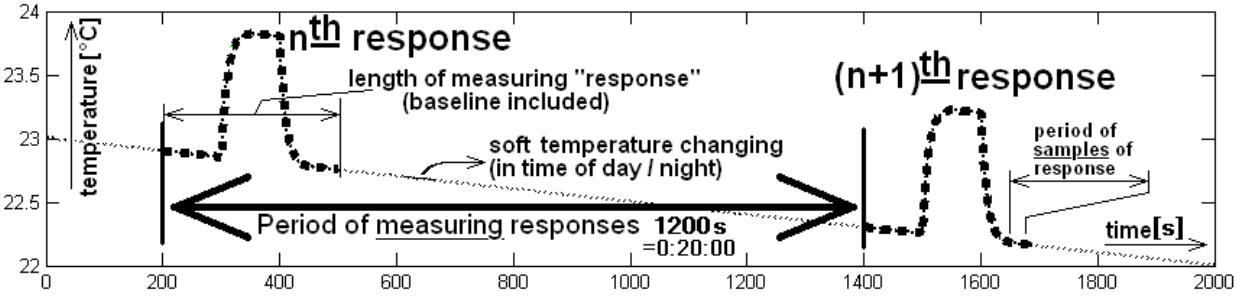

Figure 6: Wireless communication using laptop and antenna

All the counts and periods of the samples, start time of measuring, heating powers and additional parameters are wirelessly adjustable.

4. Experimental data

Basic software makes outputs to binary data files and to MS Excel format. In Excel table basic information, state of batteries, settings of measurement, and all temperature samples of each response are printed. The binary files contain all information about each read measurement. In the present more sophisticated programs for processing binary files (fitting thermophysical parameters) are being developed. Fig. 6 shows behaviour of air humidity

and measure of thermal conductivity (parameter q/dT, q – heating power, dT – temperature increase) of moisture sensors built in plaster and wall's core of St. Martin's Cathedral during two months. q/dT of wall's core is shifted for purpose of comparison. Note area around 30. 5. 2013, it is period of middle-European floods 2013.

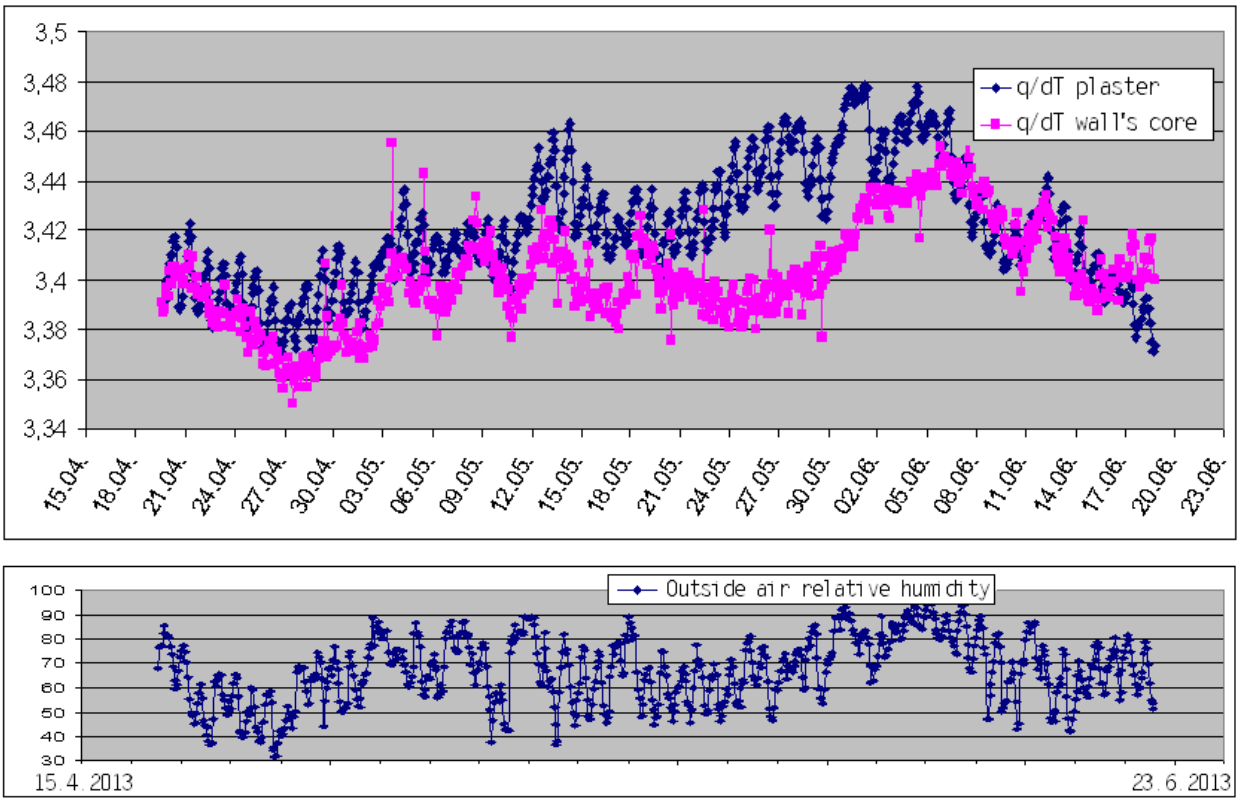

Figure 7: Humidity and measure of thermal conductivity (moisture) during two months, measured by the measuring unit at St. Martin's Cathedral

5. Conclusion

This contribution confirms the new measuring unit's capabilities for monitoring of buildings based on measuring its thermophysical properties. This method has a wide utilization. We can investigate heat and moisture flows that have a big influence on thermal insulation and degradation of building materials. We can use this method for evaluating long-term changes, for example as a result of reconstruction or water or thermal insulation of buildings. There is a lot of simulation software for studying behaviour of buildings but a few methods to compare with real data. This method is suitable for that. Simulations extended by practical measurements by this method can give us good ideas to avoid unwanted influences. Then we can continuously watch and verify its effect.

Acknowledgments

The authors thank M. Markovič and I. Peller for their technical assistance. Special thanks also belong to the Bratislava Archdiocese, especially to Mons. Thurzo for his help and kindness during this demonstration experiment. This work was supported by the Slovak Research and Development Agency under contracts No. LPP APVV 0442-09 and No. APVV 2/190/12.

References

[1] KUBIČÁR, Ľ., VRETENÁR, V., ŠTOFANIK, V., BOHÁČ, V., TIANO, P., *Monitoring of thermal moisture regime of cultural objects*, In Proc. of conference: In situ Monitoring of Monumental Surfaces - SMW08, Florence, 2008, p. 53 – 62

[2] FIDRÍKOVÁ, D., VRETENÁR, V., ŠIMKOVÁ, I., GREIF, V., VLČKO, J., DIEŠKA, P., KUBIČÁR, Ľ., *Sensor for Monitoring the Moisture in Porous Materials*, International Journal of Thermophysics, 2013, 34:1918–1929

[3] ROELS, S., CARMELIET, J., HENS, H., ADAN, O., BROCKEN, V., CERNY, V., PAVLIK, V., ELLIS, A.T., HALL, V., KUMARAN, V., PEL,V., PLAGGE, V. (2004), *A comparison of different techniques to quantify moisture content profiles in porous building materials*, Journal of Thermal Envelope and Building Science, 2003, 27: 261–270

[4] FIDRÍKOVÁ, D., GREIF, V., DIEŠKA, P., ŠTOFANIK, V., KUBIČÁR, Ľ., VLČKO, V., *Monitoring of the temperature-moisture regime in St. Martin's Cathedral tower in Bratislava*, Environmental Earth Sciences, 2013, 69:1481–1489

[5] SASS, O., VILES, H. A., *How wet are these walls? Testing a novel technique for measuring moisture in ruined walls*, Journal of Cultural Heritage, 2006, 7:257–263

Preparation and Calibration of Moisture Sensors for the In-situ Monitoring of Temperature-Moisture Regime of Rocks Situated in Volcanic Tuff Massive in Brhlovce Village

Vlastimil Boháč[1], Viliam Vretenár[1], Danica Fidríková[1], Peter Dieška[2], Lenka Kralovičová[3], Tatiana Durmeková[3], Ján Vlčko[3]

[1]Institute of Physics, Slovak Academy of Sciences, Dúbravská cesta 9, 84511 Bratislava, Slovakia

[2]Institute of Nuclear and Physical Engineering, FEI - STU, Ilkovičova 3, Bratislava, Slovakia

[3]Department of Engineering Geology, Faculty of Natural Sciences, Comenius University in Bratislava, Mlynská dolina, 842 15 Bratislava, Slovakia

e-mail: vlastimil.bohac@savba.sk

Abstract: *The basic research is based on the monitoring of the temperature-moisture regime of natural rock mass (volcanic tuffs) directly in the nature. The influences of the temperature and moisture changes are the control parameter that influences deterioration process of rock massive. Depending on thermodynamic conditions, the moisture sensor utilizes changes of thermal conductivity of porous structure when pores are filled by air/vapour, water or ice. In the principle the correlation between thermophysical properties and water content in pore material is used. The behaviour of different moisture content in dependency on temperature needs to be known. Therefore it's necessary to calibrate the moisture sensor and determine change of thermal conductivity of tuff pore material in dry and water saturated states in the temperature range that is typical for the climate of Brhlovce locality. The calibration is carried out in a temperature range at dry and moisture saturated states.*

The construction of moisture probe is based on hot ball sensor in combination with rock cylinder drilled out of tuff massive and assembled in a proper way. The probe can be used for the measurement in quasi steady-state regime or in transient regime. The new probes were calibrated in transient regime that is more sensitive for the moisture changes and the results improved accuracy of measurement. The difference in between the values of thermal conductivity in dry and moisture saturated sates is about 50%. It is big sensitivity for monitoring of relative changes of moisture content. The four probes were constructed and calibrated for the in-situ monitoring of temperature and moisture. They were installed at four different distances from the tuff massive surface and covered the depths from 9 cm up to 182 cm. The results are discussed.

Keywords: *Moisture sensor, thermal properties, monitoring, preservation of historical monuments*

1. Introduction

The massive rock materials in natural conditions are exposed in time to the climate changes like the sun radiation, precipitation and evaporation, freezing and thawing causes deterioration processes of rocks.

In the nature the water phases are always present in pores in different forms as gas, liquid, or solid when frozen. The resulting thermal conductivity of a porous material is a function of the water content in pores.

The problem of thermal transport phenomena when moisture content is present in porous materials are in high interest of building industry as well as in the area of preservation of historical buildings and monuments. The recent methods are based on various principles, like the measurement of electrical resistivity, microwave techniques with measurement of permittivity, measurement of relative air humidity in material cavities or drilled holes. The problem is in monitoring of moisture at different depths of rock massive in the free nature or in the masonry sub-surface of building that is exposed to climate changes. In our case the moisture probes are placed at the depths of 9, 37, 57, and 182cm from the free rock surface. It is problematic to place any other kind of probes at these depths. The solution of the problem is to use the laboratory calibrated moisture probes based on rock cylindrical bodies drilled out directly from the monitored place in rock dwellings in Brhlovce (preserved as historical heritage). The hot ball probe is inserted into a small cylinder of tuff (Figure 1).

2. Theory

The principle of hot ball probe is based on generation of the heat pulse in the step-wise form and recording the temperature response to this heat pulse. Model of the hot ball method assumes a constant heat flux q from the empty sphere of radius rb (radius of hot ball probe) into the infinitive medium that starts to be generated for times t > 0 (Figure 1 right). Then the temperature distribution within the medium is characterized in [1, 2].

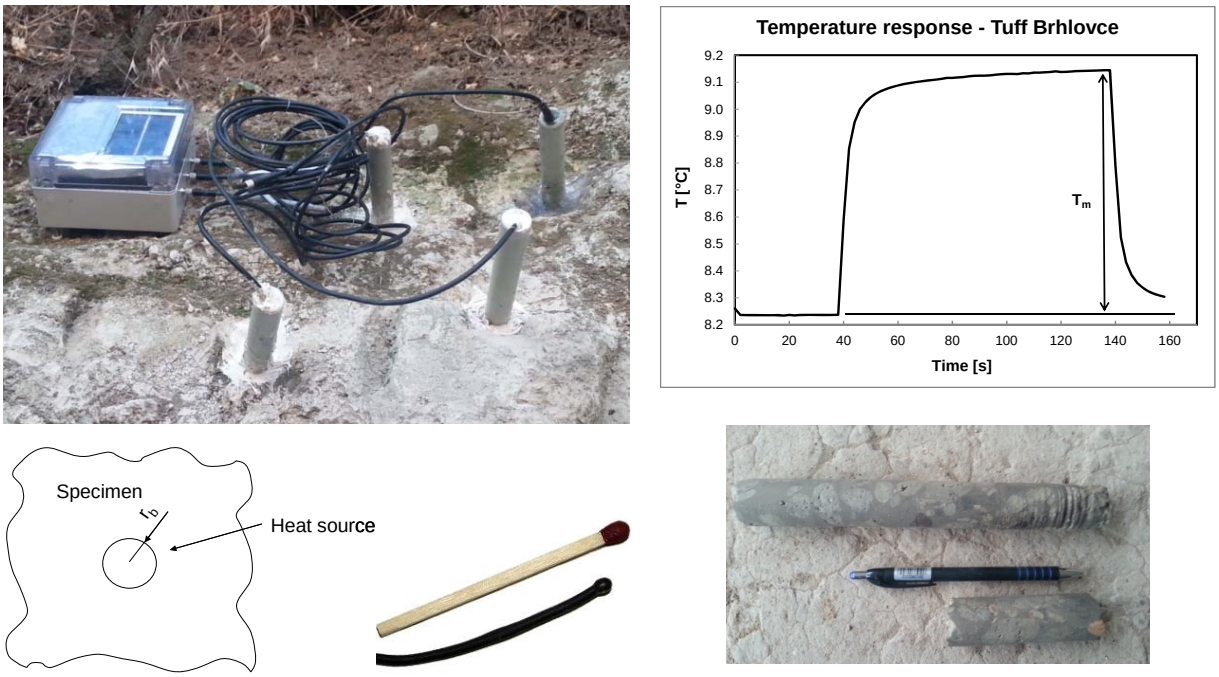

Figure 1. The electronic instrument RTM powered by solar unit in connection with the moisture probe (up), model of the hot ball (down left) and probe real size picture (down right). The temperature response measured for tuff (right up). Drilled core of tuff (right down).

The solution of the partial differential equation that describe the heat conduction for this experimental technique and describe the shape of temperature response (Fig. 1), is described according the equation (1) derived for the initial $T(0,r)=0$ and the boundary condition

$$-\lambda \frac{\partial T}{\partial r}_{r=r_0} = ql(t)$$

$$T(r,t) = \frac{q}{4\pi\lambda r}\left\{erfc\left(\frac{r-r_b}{2\sqrt{\alpha t}}\right) - \exp\left(\frac{r-r_b}{r_b} + \frac{\alpha t}{r_b^{\,2}}\right) erfc\left(\frac{r-r_b}{2\sqrt{\alpha t}} + \frac{\sqrt{\alpha t}}{r_b}\right)\right\}$$

$$\text{erfc(x)} \equiv 1 - \frac{2}{\pi}\int_0^x \exp(-\zeta^2) d\zeta \tag{1}$$

where erfc(x) is the complementary error function and λ is thermal conductivity, κ is thermal diffusivity of the surrounding medium, q is heat flux, λ is thermal conductivity. The long-time approximation ($t \to \infty$) solution of function (1) was derived as the working relation of the measuring method and the equation (2) is used for the case of steady state measurement regime

$$T_m = \frac{q}{4\pi r_0 \lambda} \tag{2}$$

Thus for the thermal conductivity λ we can write

$$\lambda = \frac{q}{4\pi r_b T_m} \tag{3}$$

where Tm is the stabilized value of the temperature. The thermophysical parameters are calculated from the temperature response by fitting procedure using model (1) or calculated from maximum (2).

3. Experiment

The Tuff rock used forexperiment have high porosity (40-60%). It's thermal conductivity is changing depending on water content in pores. The laboratory calibration of standard output parameters measured for dry and water saturated material sets the maximum range that serve as the prediction of long term measurements in nature rock massive. The Hot ball probes were calibrated in different baths before inserting to the stone cylinder. This primary calibration is used to obtain the basic probe parameters to calculate thermal conductivity and thermal diffusivity from the temperature response.

The cores drilled out from holes in massive were uset to construct the moisture sensors. The cylinders carved in tuff from Brhlovce rock dwellings having diameter 32 mm were drilled out in a middle and hot ball probe having 2.5 mm in diameter was inserted into a centre of such a hole in rock cylinder and cables were supported by cage made of nickel wires (Fig. 2.). The reason for the choice of the lithological rock types was the existence or the preparation of monitoring procedure on the temperature - moisture regime, and related laboratory research as well.

Volcanoclastic tuffs from Brhlovce belong to complex of andesite neovolcanism. In terms of descriptive characteristics of the material the color is light grey, the grain size is ranging from 0.063 to 2.0 mm, and has the porous structure with cryptopcrystallic matrix. Physical properties of tuff from Brhlovce locations are the following: specific gravity – 2.569 g.cm-3,

volume density – 1.500 g.cm-3, porosity – 31.8 %, water absorption – 16.4 % and uniaxial compression strength – 17 MPa.

Figure 2. Tuff body of moisture sensor with hot ball (left) and complete set with wire connections to RTM-solar before inserting into rock massif.

3.1 Calibration procedures

Series of hand-made Hot-ball sensors were tested for reliability and calibrated in bath liquids of water and glycerol to have two calibration points for thermal conductivities in a range of thermal conductivity values that will be measured by probe. This procedure shows also the sensitivity of the probe to thermal conductivity changes. The calibration bath liquids have different but known value of thermal conductivity and diffusivity. In this case the water and glycerol were used, so one can calculate thermal conductivity from measured temperature response characteristics according a given equations 1÷3.

The moisture sensors based on tuff stone with hot ball probes inserted in a core from drilling of holes in Fig. 1. (usually carved in a form of cylinder of porous tuff stone) and moisture sensor is ready (Fig. 2.). It is important to use the same tuff stone drilled out from massive to have the same thermophysical properties and the same porosity as the surroundings material in hole where the moisture sensor will be arranged.

The first calibration was started with the drying of the specimen that was kept at the temperature 104°C and weighting to determine the stabile dry state. This state is defined as the 0% of moisture in the sample. Into a dry stone cylinder the hot ball probe was inserted to make a moisture sensor (Fig.2.). In the next, the calibration was done for the real use of the probe as a moisture sensor. The measured value of heat flux and temperature maximum q/Tm inside the moisture sensor represents thermal conductivity that is changing in dependency of moisture content (Fig. 3.). The probe sensitivity should be high enough to register the moisture content change during moisturizing process in between dry and moisture saturated state (from 0 up to 100 % of moisture content). This change is measured as the difference of ⊚. The difference – the maximum and minimum values of ⊚ is the sensitivity and in the case of this probe it was about 0.5 Wm-1K-1. These probes were calibrated just at the temperature range from -20 up to 40°C. This calibration serves for calculation of thermal conductivity from temperature response calculated by fitting procedure.

After calibration the moisture sensors were inserted in the tuff massif at Brhlovce. Previously manufactured sensors were used for the in-situ monitoring started from October 31st 2011 [4]. The reason for their recent replacement by recently calibrated sensors is better accuracy of new ones that are able to offer all thermophysical parameters by fitting procedures. The old probe was not temperature calibrated, but the results show us how to improve methodology of the measurement of the thermal conductivity temperature dependence in regard with moisture content by this type of sensors.

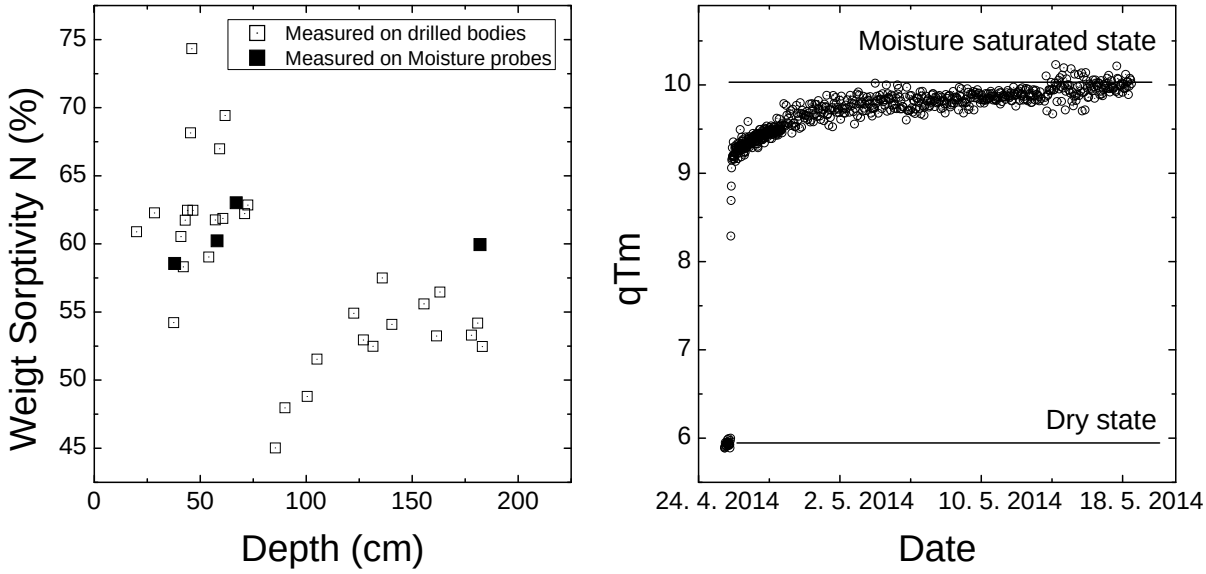

Figure 3. Sorptivity that is related to the pores volume is on the (left). Weight change from dry to moisture saturated state represents the processes of sorption of water (Right). Change of signal q/Tm for the probe made of tuff stone during the sorption process (right). The change of q/Tm from dry to moisture saturated state is about 40%. The difference of q/Tm represents 100% humidity scale in between dry and fully saturated content of pores by water [4].

For the next future, monitoring in tuff massive in depths at 10, 38, 67 and 190 cm with the new series of probes was started to run. Such moisture sensors were calibrated in dependence of temperature in both – the dry and moisture saturated regime. The new probes have the sensitivity 0.5 $Wm^{-1}K^{-1}$ calculated for dry and saturated state in a given temperature range. For different moisture content a linear dependency is valid, so one can recalculate measured values of λ to the moisture content from this calibration. The dry-moisture calibration was performed in laboratory conditions for the range of temperatures from -20 up to 40 °C (Fig.4).

3.1 Calibration results

The first calibration was carried out on moisture probes dried at 105 °C till the constant weight. Constant weight was below maintenance of using silica gel in re-closable bags.

The second calibration was done for water-saturated condition when stone cylinder was packed using Parafilm. Drying process and the saturation of the samples by water was carried out according to the applicable technical standard [3].

Humidity sensors (rock bodies with hot ball probe) exposed to temperatures from -20 °C up to +40 °C in the thermostat controlled chamber RTB 1.02. Measurements of thermal conductivity at stabilized temperatures were performed every hour inside rock bodies to keep enough time for temperature stabilization in between the heat pulses. Temperature in the chamber was set in several steps to 25, 40, 17, 10, -13, -8, -5, -1 and the back to 25 °C to check the repeatability as well as the state of water saturation. The given temperatures were always lasts for 24 hours to get perfect stability of results. An experiment was conducted on cylindrical test samples (moisture sensors) of length 32 mm and diameter 20 mm with built-in hot-ball probe. Overall, the samples were calibrated in heating-freezing-heating cycle.

Subsequently, the experimental results were statistically processed. Result of the calibration experiment with first period of data monitoring is shown in Fig. 4. The figure represent the calibrated values of thermal conductivity calculated by fitting procedure from (1) that is changing in dependency of temperature for the materials studied in dry and moisture saturated conditions during freezing-thawing cycle. The temperature dependency of measured mean values of thermal conductivity of rock in dry as well in water saturated state is linear. The calibrated temperature dependency of the thermal conductivity for the moisture saturates state is negative for the temperatures above 0 and negative for the temperatures below the freeze point (Fig. 4.). Besides this probe a next 3 probes were calibrated simultaneously.

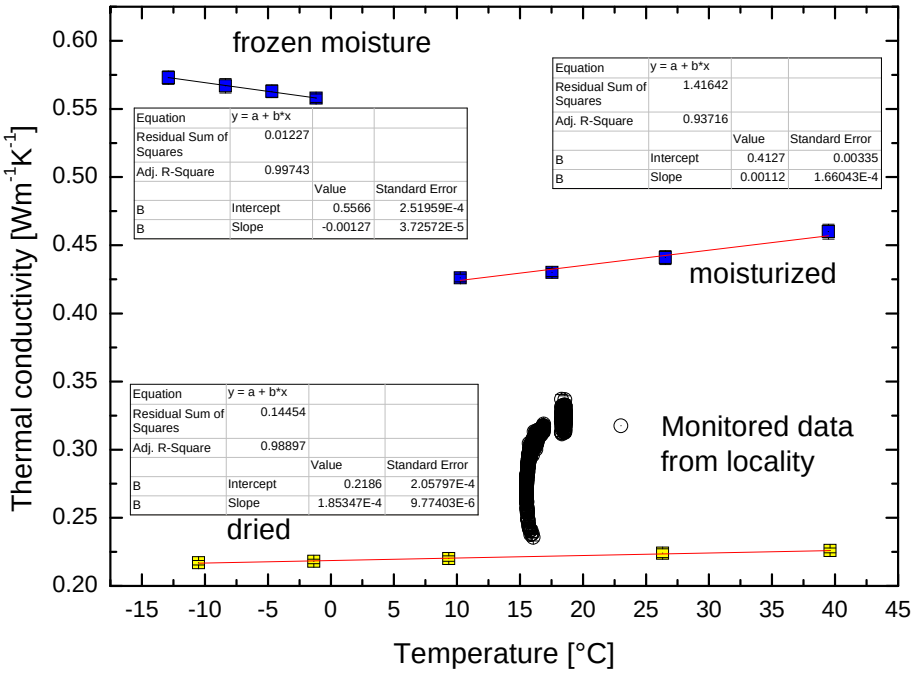

Figure 4. Temperature dependency of ⌯ calculated from (1) by fitting procedure. Calibration data were measured for tuff in dry and water saturated conditions within the temperature range from -13 up to 40°C. Data were statistically averaged for a given temperature. The tuff cylinder for moisture sensor was drilled out from the massif depth of 182cm. The monitored data collected in first period of measuremnets at locality satisfy to process of moisturing.

The values of thermal conductivity λ in the case of water saturated probes are much higher than the dried one. The high difference in the values of the thermal conductivity for the dry and reached water-saturated state of tuff also proves its high water absorption (45-65%).

According to the difference of thermal conductivity in dry and water saturated conditions at different temperatures it was confirmed the relationship between water absorption and increase of thermal conductivity for the positive temperatures. For the temperatures below the freezing point the monitoring of moisture content change is more complicated, as the frozen water will probably block the next diffusion of the water as well as the snow precipitation is expected for in-situ measurement at this temperatures.

The moisture sensor data collected within first month are in the Fig. 5 as a temperature dependency of measured parameter q/Tm recalculated to thermal conductivity as well as the in time dependency of moisture development in Fig. 6. Process of water absorption reflects the thermal conductivity changes according (3) and thus the change of moisture content. Data in Fig. 5. and Fig. 6. illustrate the time changes within this period.

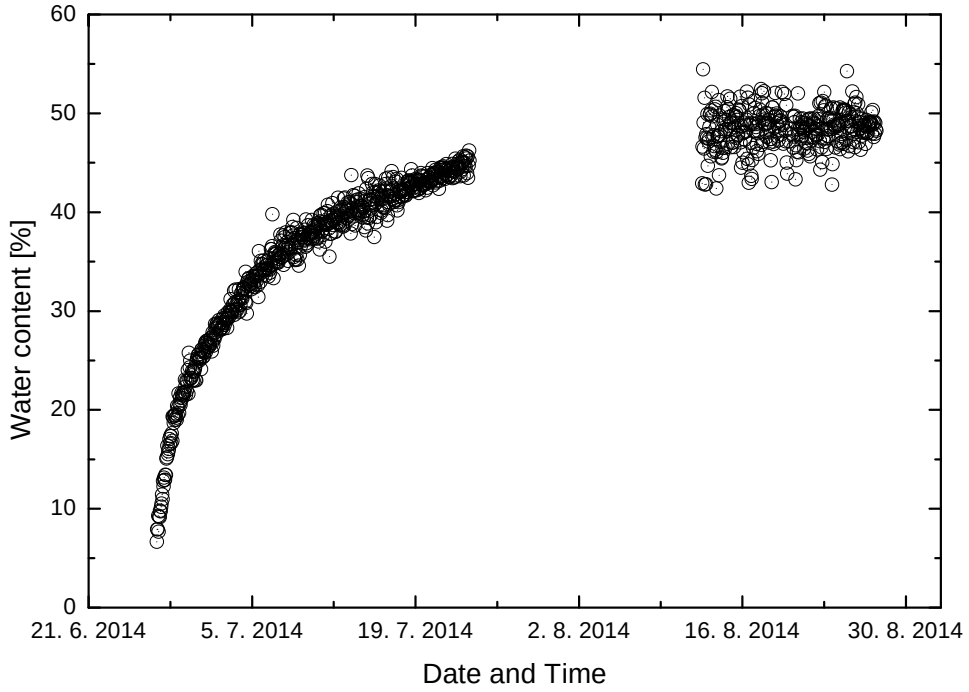

Figure 5. Data collected in one-month period from locality Brhlovce [4]. Graph show moisture changes during this period.

4. Conclusions

The calibration data in dependency of the temperature for the moisture sensors made of tuff stone cylinders in dry and moisture saturated states are presented. The thermal conductivity values of moisture probes which correspond to change of moisture content in temperature-moisture dependency calibration procedure were measured in measurement chamber RTB 1.02 [5]. Four moisture sensors will be placed into the tuff massif at locality in Brhlovce rock for the purpose of in situ monitoring of temperature–moisture regime. This kind of measurement is necessary for the geology engineers to calculate the deterioration risks as there were some collapses of the rock marquis appeared over the dwellings in years 2011 - 2013 [4]. The data values of q/T_m 0 raised from 5.85 up to 9.85 W K^{-1} were measured for the temperature 25 °C. At the initial three days of monitoring the rapid increase is evident and gives an image on difference between the dry and probably near-moisture saturated state.

For the calibrated moisture sensors the variation of λ with variation of moisture content as a parameter, the temperature dependency was found. Based on observed physical properties such as porosity, water absorption and thermal conductivity of studied materials; it can be assumed relationship between water absorption and increases of thermal conductivity. The experiment was carried out for the needs of correlations between laboratory and field research. This experiment will be helpful in monitoring the moisture in field research, because values of thermal conductivity are defined in extreme dry and wet conditions (Fig. 5). On the basis of the experiment we could better eliminate linear increase in thermal conductivity due to the increase of temperature at the given moisture content and thus determine the actual moisture in rock massif from the equations obtained by linear fit in dry and moisture saturated state as well as in the case of moisture frozen state. All new calibrated moisture probes were inserted into a massif and monitoring of moisture content has been started. In this way we would be able get more accurate data and better possibility for calculation of moisture content from measured values of thermal conductivity. The data measured by new probes have a laboratory limit that was found at calibration for dry and moisture saturated state.

Acknowledgments

This work was supported by the Slovak Research and Development Agency under the contract No. APVV-0641-10, „Study of rocks properties and investigation of structural and textural characteristic in correlation with thermo-physical and physic-mechanical properties"

References

[1] CARSLAW, H.S. & JAEGER, J.C. 1986. Conduction of heat in solids, Oxford, Clarendon Press, Second edition, p. 348.

[2] KUBIČÁR, Ľ., VRETENÁR, V., ŠTOFANIK & V. BOHÁČ, V. 2010. Hot-Ball Method for Measuring Thermal Conductivity, International Journal of Thermophysics, 31, 10, p. 1904-1918.

[3] EN 13755: 2008. Natural stone test methods. Determination of water absorption at atmospheric pressure.

[4] EKKERTOVÁ, P., ŠIMKOVÁ, I., BRČEK, M., DURMEKOVÁ, T. & BOHÁČ, V. 2012. Influences of temperature change and moisture content on the thermal conductivity of rocks. Thermophysics 2012 - Conference Proceedings, 17th International Meeting of Thermophysical Society, 31st October to 2th November 2012, Podkylava, Slovak Republic, org. Institute of Physics, Slovak Academy of Science in Bratislava, Printed by: Brno University of Technology, Faculty of Chemistry, ISBN: 978-80-214-4599-4, p.33-40.

[5] Patent No.SK 285834 B6, producer www.transientms.com

List of participants

1. **prof. Ivan Baník, PhD.,** Slovak University of Technology, Faculty of Civil Engineering, Radlinského 11, Bratislava, SLOVAKIA
2. **prof. Jerzy Bodzenta, Ph.D.,** Silesian University of Technology, Institute of Physics-Centre for Science and Education, Krzywoustego 2, 44-100, Gliwice, Poland, Jerzy.Bodzenta@polsl.pl
3. **Ing. Vlastimil Boháč, PhD.,** Slovak Academy of Sciences, Institute of Physics, Dúbravská cesta 9, 84511, Bratislava, SLOVAKIA, vlastimil.bohac@savba.sk
4. **Mr. Marcin Cegła, MSc,** Military Institute of Armament Technology, Wyszyñskiego Street 8, 05-220, Zielonka, POLAND, ceglam@witu.mil.pl
5. **prof. Ing. Robert Černý, DrSc.,** Czech Technical University, Faculty of Civil Engineering, Thákurova 7, 166 29, Prague 6, CZECH REPUBLIC, cernyr@fsv.cvut.cz
6. **doc. Abdelkader Djebli, Maitre Assistant,** University of Mascara, Sciences and Technology, Mascara, 29000, Mascara, ALGERIA, djebliabdelkader@yahoo.fr
7. **res. asst. Tuba Evgin,** Dokuz Eylül University, Faculty Mechanical Engineering Department, 35397 Tinaztepe Buca Izmir, 35397, Izmir, TURKEY, tuba.evgin@deu.edu.tr
8. **Ing. Lukáš Fiala, Ph.D.,** Czech Technical University, Faculty of Civil Engineering, Thákurova 7, 166 29 Praha 6 - Dejvice, 16000, Praha, CZECH REPUBLIC, fialal@fsv.cvut.cz
9. **Ing. Danica Fidríková, Ph.D.,** Slovak Academy of Sciences, Institute of Physics, Dúbravská cesta 9, 84511, Bratislava, SLOVAKIA, danica.fidrikova@savba.sk
10. **Ing. Jan Fořt,** Czech Technical University, Civil Engineering, Department of Material Engineering and Chemistry, Thákurova 7, 16000, Prague, Prague - the Capital (Praha - hlavni mesto), CZECH REPUBLIC, jan.fort.1@fsv.cvut.cz
11. **prof. Olivier Fudym, Ph.D.,** Université de Toulouse, Mines Albi; CNRS; Centre RAPSODEE, Campus Jarlard, F-81013 Albi cedex 09, Albi, France, olivier.fudym@mines-albi.fr
12. **Dr. Silas E Gustafsson, D Sc,** Thermetrol AB, Klyvsagagatan 29, SE-41679, Gothenburg, SWEDEN, silas.gustafsson@thermetrol.se
13. **CEO Mattias Gustavsson, Ph.D.,** Hot Disk AB, R&D, Sven Hultins gata 9 A, SE-41288, Gothenburg, SWEDEN, mattias.gustavsson@hotdiskinstruments.com
14. **Dr.-Ing. Wolfgang Hohenauer, Ph.D.,** Austrian Institute of Technology GmbH AIT, Donau-City-Strasse 1, 1220, Vienna, AUSTRIA, wolfgang.hohenauer@ait.ac.at
15. **Mgr. Matúš Holúbek, Ph.D.,** Slovak Academy of Sciences, Institute of Construction and Architecture, Dúbravská cesta 9, 84503, Bratislava, SLOVAKIA, matus.holubek@savba.sk

16. **Ing. Ján Hudec,** Slovak Academy of Sciences, Institute of Physics, Dúbravská cesta 9, 841 04, Bratislava, SLOVAKIA, ing.janhudec@gmail.com
17. **Mgr. Tomáš Húlan,** Constantine the Philosopher University, Tr. A Hlinku 1, 94974, Nitra, SLOVAKIA, tomas.hulan@ukf.sk
18. **doc. Ing. Marian Kubliha, Ph.D.,** Slovak University of Technology, Faculty of Civil Engineering, Radlinského 11, 813 68 Bratislava, SLOVAKIA, marian.kubliha@stuba.sk
19. **prof. Piotr Koniorczyk, DSC.,** Military University of Technology, Faculty of Mechatronics and Aerospace, Kaliskiego 2, 00-908, Warsaw, POLAND, piotr.koniorczyk@wat.edu.pl
20. **prom. fyz. Oľga Koronthályová, CSc.,** Slovak Academy of Sciences, Dúbravská cesta 9, 84503, Bratislava, SLOVAKIA, usarkoro@savba.sk
21. **Dr. Olena Kraieva,** Laboratoire de chimie de coordination, CNRS, 205 route de Narbonne, 31400, Toulouse, FRANCE, olena.kraieva@lcc-toulouse.fr
22. **Ing. Ľudovít Kubičár, DSc,** Slovak Academy of Sciences, Institute of Physics SAS, Dúbravská cesta 9, 84511, Bratislava, SLOVAKIA, kubicar@savba.sk
23. **Ing. Anna Kučerová,** Brno University of Technology, Faculty of Civil Engineering, Veveří 331/95, 602 00, Brno, CZECH REPUBLIC, kucerova.a@fce.vutbr.cz
24. **Dr. Ing. Daniel Lager, Ph.D.,** Austrian Institute of Technology GmbH AIT, Donau-City-Strasse 1, 1220, Vienna, AUSTRIA, wolfgang.hohenauer@ait.ac.at
25. **Ing. Peter Matiašovský, PhD.,** Slovak Academy of Sciences, Institute of Construction and Architecture, Dúbravská cesta 9, 84503, Bratislava, SLOVAKIA, peter.matiasovsky@savba.sk
26. **doc. RNDr. Igor Medveď, Ph.D.,** Constantine the Philosopher University, Department of Physics, A. Hlinku 1, 94974, Nitra, SLOVAKIA, imedved@ukf.sk
27. **Ing. Peter Mihálka, Ph.D.,** Slovak Academy of Sciences, Institute of Construction and Architecture, Dúbravská cesta 9, 84503, Bratislava, SLOVAKIA, usarmipe@savba.sk
28. **doc. Ibrir Miloud, Ph.D.,** M'SILA UNIVERSITY, Sciences, M'SILA UNIVERSITY, 28000, M'SILA, ALGERIA, ibrirmiloud@yahoo.fr
29. **Mgr. Ján Ondruška, Ph.D.,** Constantine the Philosopher University, Faculty of Natural Sciences, Tr. A. Hlinku 1, 94974, Nitra, SLOVAKIA, jondruska@ukf.sk
30. **Ing. Gabriela Pavlendová, Ph.D.,** Slovak University of Technology, Faculty of Civil Engineering, Radlinského 11, 813 68, Bratislava, SLOVAKIA, Gabriela.pavlendova@stuba.sk
31. **prof. Ing. Zbyšek Pavlík, Ph.D.,** Czech Technical University, Faculty of Civil Engineering, Department of Materials Engineering and Chemistry, Thákurova 7, 16629, Prague, CZECH REPUBLIC, pavlikz@fsv.cvut.cz
32. **Ing. Petra Rozehnalová, Ph.D.**, Brno University of Technology, Faculty of Civil Engineering, Veveří 331/95, 602 00, Brno, CZECH REPUBLIC, rozehnalova.p@fce.vutbr.cz

33. **doc. Lakel Said, Ph.D.,** University of Biskra, Faculté des Sciences Exactes et des Sciences de la Nature et de la Vie, Biskra, 07000, Biskra, Biskra, ALGERIA, s.lakel@yahoo.fr
34. **prof. Bimal K. Sarkar, Ph.D.,** Galgotias University, Department of Physics, Plot 2, 17A Yamuna Expressway, 201308, Greater Noida, Uttar Pradesh, INDIA, bks@physics.org.in
35. **RNDr. Peter Sin, PhD.,** Slovak University of Technology, Faculty of Civil Engineering, Radlinského 11, 813 68, Bratislava, SLOVAKIA, peter.sin@stuba.sk
36. **Mr. Tomasz Ślęzak, MSc.,** Military University of Technology, Department of Construction Machinery, Faculty of Mechatronics and Aerospace, Gen. S. Kaliskiego 2 Str., 00908, Warsaw, POLAND, tslezak@wat.edu.pl
37. **prof. Dr. Ismail H. Tavman, Ph.D.,** Dokuz Eylul University, Mechanical Engineering Department, 35397 Tinaztepe Buca Izmir, 35397, Izmir, TURKEY, ismail.tavman@deu.edu.tr
38. **prof. Dr. Sebnem Tavman, Ph.D.,** EGE University, Food Engineering Department, 35100 Bornova-Izmir, Turkey, sebnem.tavman@ege.edu.tr
39. **Ing. Lucie Trhlíková,** Brno University of Technology, Faculty of chemistry, Purkyňova 464/118, 61200, Brno, CZECH REPUBLIC, xctrhlikova@fch.vutbr.cz
40. **doc. RNDr. Anton Trník, Ph.D.,** Constantine the Philosopher University, Faculty of Natural Sciences, Tr. A Hlinku 1, 94974, Nitra, SLOVAKIA, atrnik@ukf.sk
41. **RNDr. Vratislav Tydlitát, CSc.,** Czech Technical University, Faculty of Civil Engeneering, Thákurova 7, 16629, Prague 6, CZECH REPUBLIC, tydlitat@fsv.cvut.cz
42. **prof. Ing. Jiří Vala, CSc.,** Brno University of Technology, Faculty of Civil Engineering, Veveří 95, 60200, Brno, CZECH REPUBLIC, vala.j@fce.vutbr.cz
43. **Ing. Viliam Vretenár, PhD.,** Slovak Academy of Sciences, Institute of Physics, Dúbravská cesta 9, 84511, Bratislava, SLOVAKIA, viliam.vretenar@savba.sk
44. **Mr. Tuncay Yilmaz, Ph.D. candidate,** Celal Bayer University, Engineering Faculty, Food Engineering Department, CBU, MURADIYE, MANISA, IZMIR, 45140, Manisa, Muraiye, TURKEY, tuncay.yilmaz@cbu.edu.tr
45. **prof. Ing. Oldřich Zmeškal, CSc.,** Brno University of Technology, Faculty of Chemistry, Purkyňova 118, 61200, Brno, CZECH REPUBLIC, zmeskal@fch.vutbr.cz
46. **Assoc. Prof. Janusz Zmywaczyk, Ph.D.,** Military University of Technology, Faculty of Mechatronics and Aerospace, Military University of Technology, Kaliskiego 2, 00-908, Warsaw, POLAND, jzmywaczyk@gmail.com
47. **Ing. Jaromír Žumár,** Czech Technical University, Faculty of Civil Engineering, Thákurova 7, 16629, Prague 6, CZECH REPUBLIC, zumarj@tpm.fsv.cvut.cz

Title	Thermophysics 2014 – Conference Proceedings
Editors	Oldřich Zmeškal, Vlastimil Boháč
Publisher	Institute of Physics, Slovak Academy of Science in Bratislava
	Dubravská cesta 9, SK-845 11 Bratislava
Print	Brno University of Technology, Faculty of Chemistry
	Purkynova 464/118, CZ-612 00 Brno
Edition	first
Year of first edition	2014
Number of pages	188
Number of copies	50

ISBN: ISBN 978-80-214-5034-9